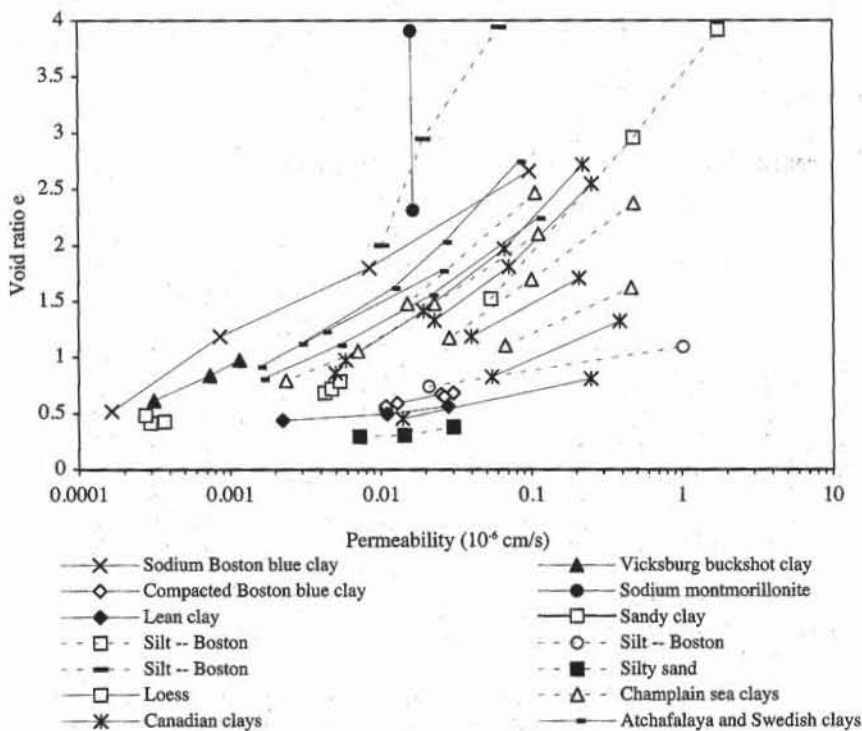
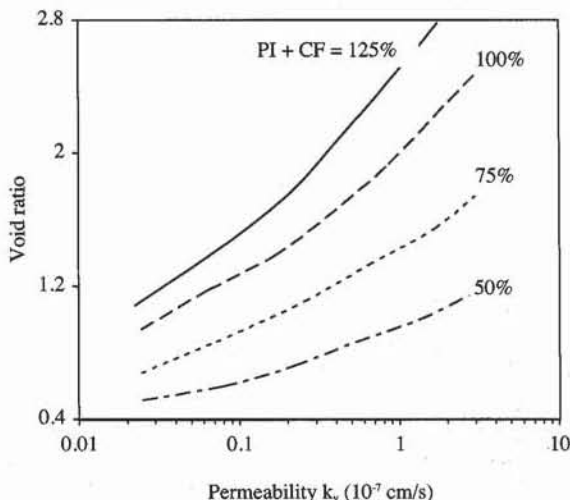


**Figure 10** Permeability data on various soils in range 1 to  $10^{-7}$  cm/s (data after Lambe and Whitman, 1979).



**Figure 11** Permeability data on various soils in range  $10^{-5}$  to  $10^{-10}$  cm/s (data after Lambe and Whitman, 1979; and Tavenas et al., 1983).



**Figure 12** Variation of vertical coefficient of permeability with void ratio, plasticity index PI, and clay fraction CF for clay (after Tavenas et al., 1983).

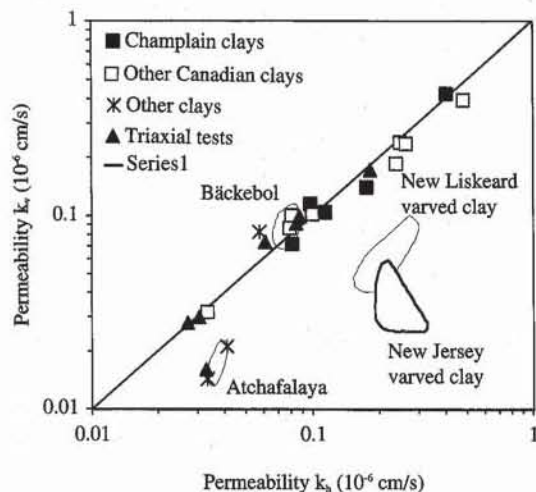


**Figure 13** Permeability anisotropy for various natural clays (Tavenas and Leroueil, 1987).

## REFERENCES

- CARMAN, P. S., 1939, "Permeability of saturated sands, soils, and clays," *J. Agric. Sci.*, Vol. XXIX, No. 11.
- DARCY, H., 1856, *Les Fontaines Publiques de la Ville de Dijon*, Dalmont, Paris.
- HANSBO, S., 1960, "Consolidation of clay with special reference to influence of vertical sand drains," *Proceedings No.18, Swedish Geotechnical Institute*, pp. 45-50.
- HAZEN, A., 1892, "Some physical properties of sands and gravels with special reference to their use in filtration," *24th annual report, Massachusetts State Board of Health*, USA.
- KULHAWY, F. H., and P. W. MAYNE, 1990, *Manual on Estimating Soil Properties for Foundations Design*, Report EL-9800 to Electric Power Research Institute, Cornell University, Ithaca, New York.
- KOZENY, J., 1927, "Über kapillare leitung des wassers in boden," *Ber. Wien. Akad.*, pp. 136-271.
- LAMBE, T. W., and R. V. WHITMAN, 1979, *Soil Mechanics, SI Version*, John Wiley & Sons, Inc., New York, 553 p.
- LANE, K. S., and D. E. WASHBURN, 1946, "Capillary tests by capillarimeter and by soil filled tubes," *Proceedings of Highway Research Board*.
- LOUDON, A. G., 1952, "The computation of permeability from simple soil tests," *Géotechnique*, Vol. 28, No. 3.
- NAVFAC, 1982, *Soil Mechanics (Design Manual 7.1)*, Naval Facilities Engineering Command, Alexandria, 355 p.
- TAVENAS, F., P. JEAN, P. LEBLOND, and S. LEROUEIL, 1983, "The permeability of natural soft clays. Part II, Permeability characteristics," *Canadian Geotech. J.*, Vol. 20, No. 4, pp. 645-660.
- TAVENAS, F., and S. LEROUEIL, 1987, "State-of-the-Art on laboratory and in-situ stress-strain-time behavior of soft clays," *Proceedings of the International Symposium on Geotechnical Engineering of Soft Soils, Mexico City*, pp. 1-46.

TAYLOR, D. W., 1948, *Fundamentals of Soil Mechanics*, John Wiley & Sons, New York, 700 p.

TERZAGHI, K., and R. B. PECK, 1967, *Soil Mechanics in Engineering Practice*, 2nd Ed., John Wiley & Sons, New York, 729 p.

## REVIEW QUESTIONS

1. Define the total head in terms of water pressure, elevation, and unit weight of water. What is the physical meaning of total head?
2. Why do we use the hydrostatic definition of total head instead of the Bernoulli definition of total head?
3. Why do we neglect the term  $v^2/2g$  in defining the total head in soil? ( $v$  is the fluid velocity and  $g$  is the earth gravity.) Justify your answer with numbers.
4. Define *soil permeability*. What are the dimensions and units of permeability?
5. Does the permeability increase or decrease with temperature?
6. Name two laboratory tests used for determining soil permeability. For which types of soils are they used?
7. Is the fluid velocity larger or smaller than the discharge velocity? What is the relationship between these velocities?
8. What is the critical hydraulic gradient?
9. Can you name several empirical relationships that relate soil permeability to physical parameters?
10. Derive the expression for permeability in a constant head test.
11. Derive the expression for permeability for a falling head test.
12. What is a typical range of permeability for gravels, sands, silts, and clays?

## EXERCISES

- 1.. Plot permeability versus void ratio for the silts of Table E1, and define the coefficient of the Kozeny-Carman equation.

TABLE E1

Soil type	$k$ (cm/s)	Void ratio $e$
Silty sand	7.E-09	0.29
	1.E-08	0.30
	3.E-08	0.38
Silt, Boston	2.E-08	0.74
	1.E-06	1.09
	1.E-08	2.00
	2.E-08	2.95
	6.E-08	3.94
	5.E-08	1.52
	5.E-07	2.96
	2.E-06	3.92
Silt, North Carolina	6.E-07	0.67
	2.E-06	0.79
	3.E-06	0.70
	3.E-05	0.89
	8.E-05	0.89

2. Same as Exercise 1 but for Table E2.
3. Same as Exercise 1 but for Table E3.

**TABLE E2**

Soil type	<i>k</i> (cm/s)	Void ratio <i>e</i>
Beach sand	8.E-02	0.65
	1.E-01	0.75
	1.E-01	0.75
	1.E-01	0.76
	1.E-01	0.79
	2.E-01	0.83
Ottawa sand	5.E-03	0.63
	6.E-03	0.66
Sand, Franklin Falls	9.E-04	0.78
	1.E-03	0.86
	1.E-03	0.78
Sand, Scituate	4.E-03	0.54
	5.E-03	0.54
	7.E-03	0.59
	8.E-03	0.67
Sand, Plum Island	2.E-02	0.69
	2.E-02	0.74
Sand, Fort Peck	2.E-03	0.63
	3.E-03	0.65
	3.E-03	0.67
	3.E-03	0.67
Sand, Union Falls	4.E-02	0.49
	6.E-02	0.57
	9.E-02	0.69
Sand from dike	2.E-04	0.68
	2.E-03	1.20

**TABLE E3**

Soil type	<i>k</i> (cm/s)	Void ratio <i>e</i>
Sandy clay	3.E-10	0.41
	4.E-10	0.42
	3.E-10	0.48
Compacted Boston blue clay	1.E-08	0.53
	1.E-08	0.56
	3.E-08	0.67
Vicksburg buckshot clay	3.E-08	0.68
	3.E-08	0.65
	1.E-09	0.97
Sandy clay	7.E-10	0.84
	3.E-10	0.61
	5.E-05	1.08
Loess	9.E-05	1.16
	2.E-04	1.18
	2.E-04	1.31
Lean clay	4.E-09	0.68
	5.E-09	0.72
	5.E-09	0.78
Sodium Boston blue clay	2.E-09	0.44
	1.E-08	0.49
	3.E-08	0.56
Calcium kaolinite	2.E-10	0.51
	9.E-10	1.18
	8.E-09	1.80
Sodium montmorillonite	1.E-07	2.66
	2.E-06	1.24
	7.E-06	1.51
	1.E-05	1.68
Sodium montmorillonite	2.E-08	2.31
	2.E-08	3.91

## 4-2 Constant Head Permeability Test

### SCOPE

The constant head permeability test (Fig. 1) is used for determining the permeability of samples of coarse-grained soils. Here we describe the constant head permeability test for sand and gravel samples.

### EQUIPMENT

The equipment for the constant head permeability test includes:

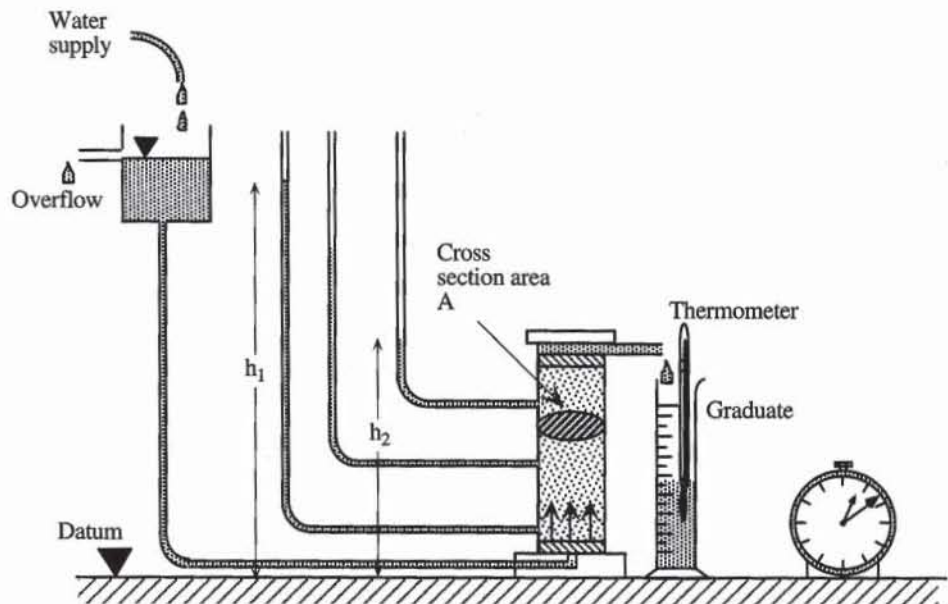
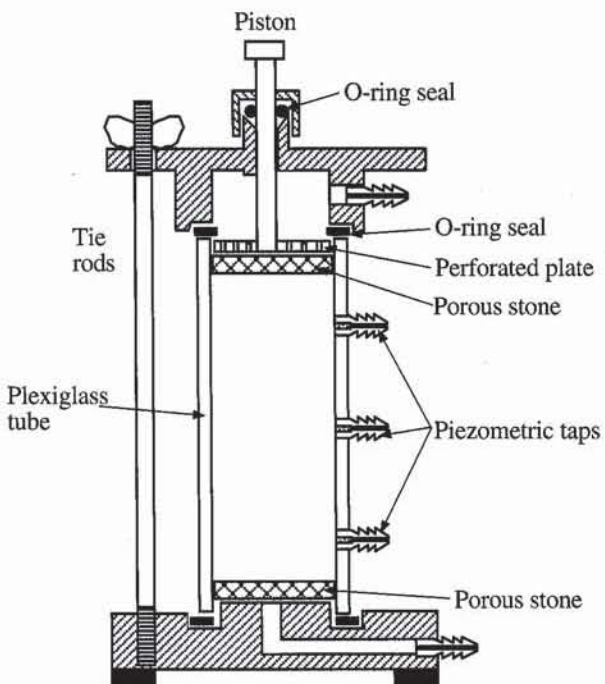
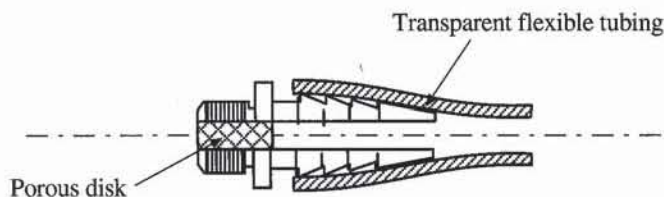


Figure 1 Experimental setup for constant head permeability test.



**Figure 2** Permeameter cell.



**Figure 3** Piezometric tap of Fig. 1.

- Permeameter cell similar to that shown schematically in Fig. 2. Its cylinder is transparent to allow observation of the sample and to permit checking the saturation. As shown in Fig. 3, piezometer taps are located along the side of the permeameter cell for measuring the total head loss along a given sample length. This type of permeameter which encases the soil sample in a rigid cylinder is called a fixed wall permeameter. There is also another type of permeameter with a flexible wall to examine the effect of confining pressure on permeability. Its experimental setup is similar to the one of the triaxial test (see Chapter 7-6).
- Perforated metal or plastic disks, porous stones, or circular wire screens, cut for a close fit inside the permeameter.
- Glass tubing 2 to 4 mm in diameter (piezometer) mounted on a panel.
- Flexible transparent hoses and screw clamps necessary to connect piezometers and water supply.
- Constant-pressure supply device for water supply, as described later.
- Deaired distilled water prepared as described later.
- Timing device.
- Graduated cylinder, 100 mL.
- Thermometer, range 0 to 50°C, accurate to 0.1°C.
- Silicon or vacuum grease.

- Balance sensitive to 0.1 g.
- Oven.
- Ruler.

### **PREPARATION OF WATER FOR PERMEABILITY TEST**

Ideally, the water used in the permeability test should be identical to that of the soils in the field. Since such water is rarely available, deaired tap water is generally used. When flowing between soil particles, untreated tap water would release air bubbles that would impede the flow of water, thereby giving erroneously low measurements of permeability. Figure 4 shows an arrangement for deairing water. A fine spray of water is sent into the vessel under internal vacuum. The vacuum pump is protected from water inflow by a water trap. Deraired water can also be prepared by boiling it on a heat source, and cooling it in a vessel sealed from the atmosphere to prevent it from dissolving air again.

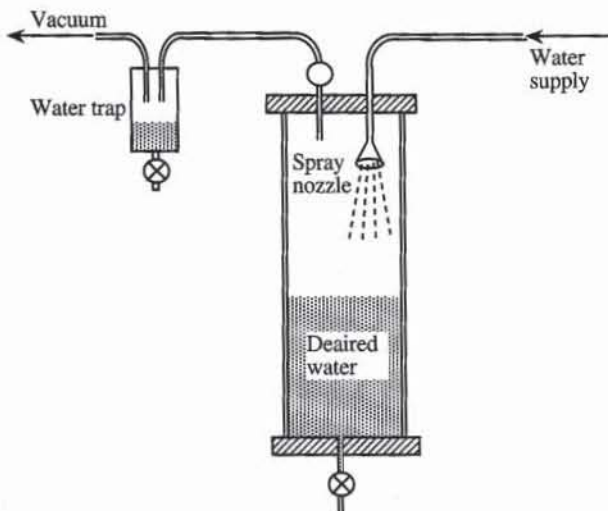


**Figure 4** Derairing water with vacuum.

### **WATER SUPPLY AT CONSTANT PRESSURE**

Figures 5 and 6 show two types of devices which can be used to supply water to the permeameter cell at a constant pressure. As shown in Fig. 5, the overflow maintains the level *A* constant, and therefore the pressure at *B* does not depend on the water level in the main supply tank.

As shown in Fig. 6, a tube is inserted and lowered to a selected depth in the container, which is hermetically sealed. When the water attempts to flow, the water level goes down in the tube and stops at point *A*. The water pressure at point *A* stays at atmospheric pressure, independently of the water level in the rest of the tank, provided that this level remains above point *A*. Therefore, the tank delivers water at constant pressure, which is controlled by the position of point *A*. Point *A* is chosen as low as possible to maximize the tank capacity. A constant pressure tank uses less deaired water than the device of Fig. 5.

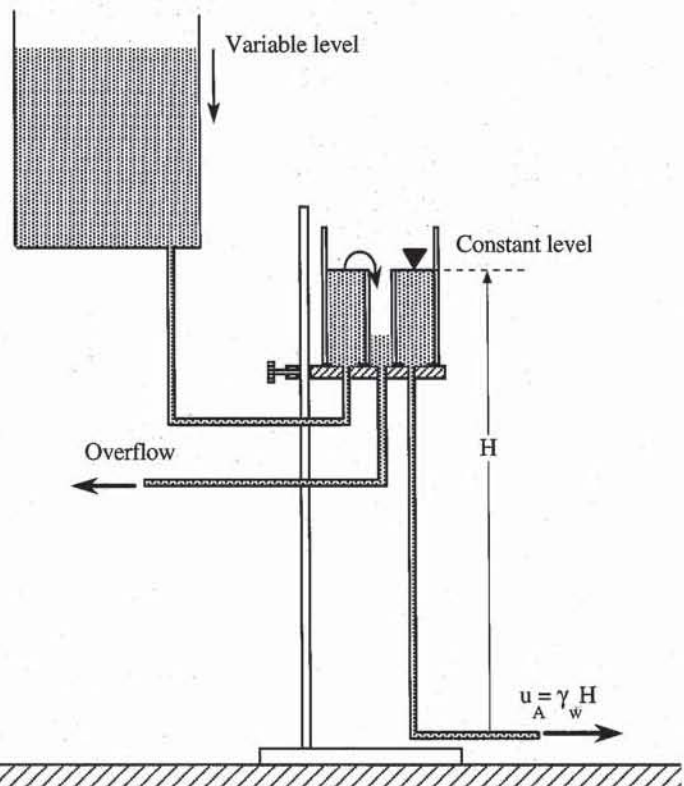


**Figure 5** Suspended tank with constant water level for supplying water at constant pressure.

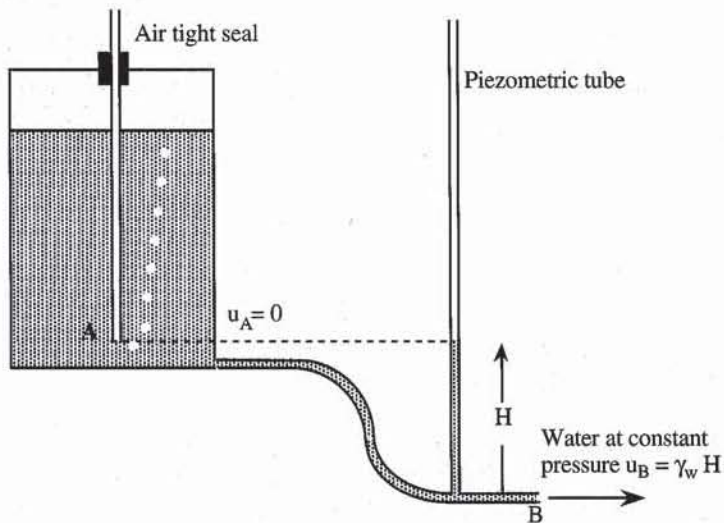


**Figure 6** Constant-pressure tank.

## PROCEDURE

1. Measure the inside diameter of the permeameter cell and the distance between piezometer taps.
2. Clean the cell base, apply silicon or vacuum grease on the lower gasket, place a porous stone on the base, and mount the permeameter cylinder.



**Figure 7** A loose specimen is obtained by using a funnel and a flexible nozzle. Denser specimens are obtained by tapping or vibrating loose samples.

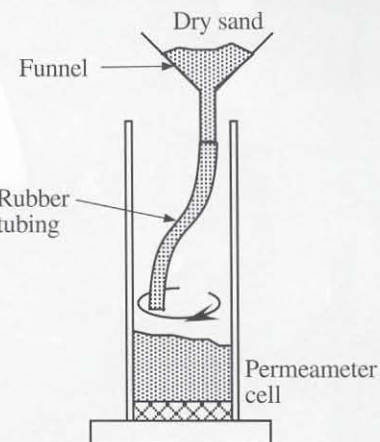


**Figure 8** Dry, loose specimens are prepared by using a funnel and flexible tubing.

**3.** Mix the dry soil material to be tested in a large pan, and measure its weight. The specimen can be prepared using dry or wet pluviation. In the *dry pluviation method* the soil is poured in the permeameter as shown in Figs 7 and 8. It falls from a constant height through the flexible tubing and funnel system, making a specimen of uniformly low density. The specimen density may be controlled by measuring its height and weight of soil left over in the pan. Denser specimens are obtained by tapping the sample sides. In the *wet pluviation method*, the permeameter cell is first filled with a few centimeters of water. Then by using a spoon, the soil is gently poured a few centimeters away from the water surface, which is gradually raised. Wet pluviation produces saturated specimens of uniformly low density, the density of which can be controlled and increased as in the dry pluviation method.

**4.** Measure the weight of material left over in the pan to compute the specimen weight.

**5.** Apply vacuum or silicon grease to the top rubber gasket, mount the permeameter cap, and tighten its bolts. As shown in Fig. 9, lower the permeameter piston so that it slightly touches the specimen. During the test, the piston will maintain the sample in place and fix its height.

**6.** As shown in Figs. 10 and 11, connect the permeameter inlet valve to the constant pressure tank with a flexible hose, and attach a 50-cm-long transparent hose to each permeameter tap. Two permeameter taps are usually sufficient.

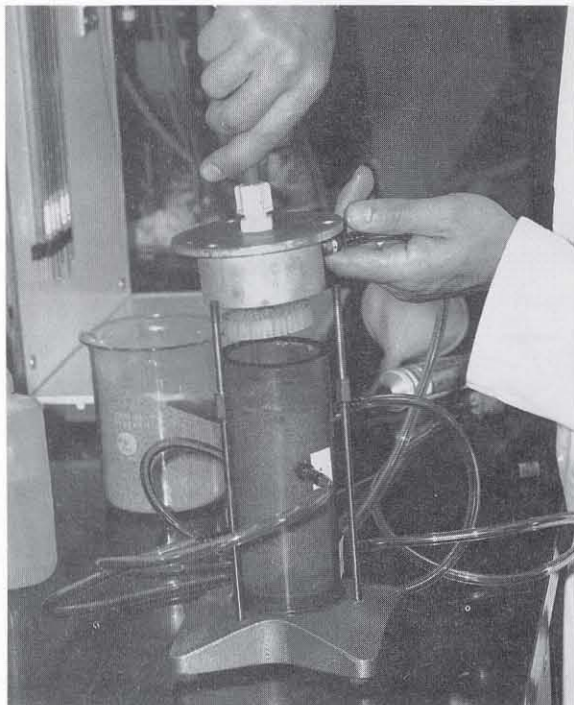


**Figure 9** The permeameter cell is closed.

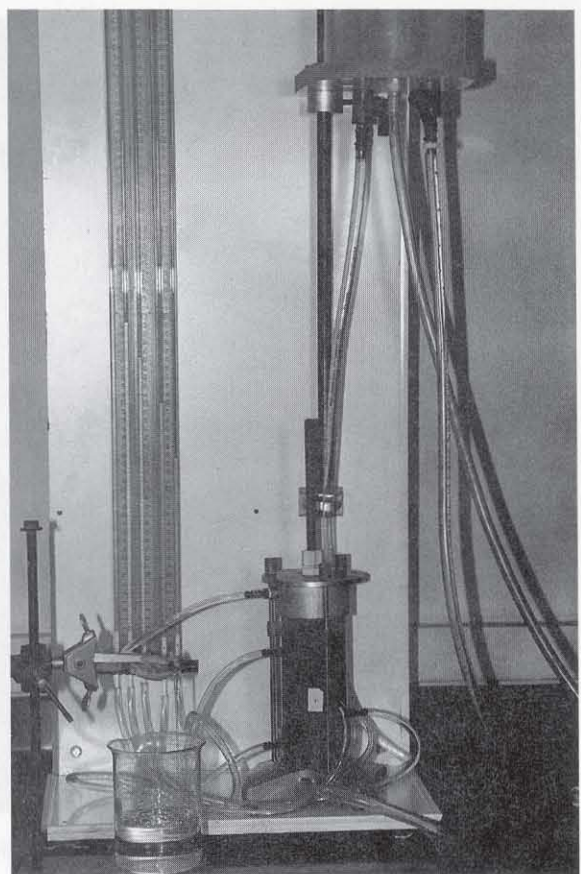


**Figure 10** Constant head permeability test in progress.

Open the inlet valve to create a gentle upward flow of water inside the sample. The water flow should displace and flush the air within the sample and piezometer hoses. When there are no more air bubbles in the hoses, connect them to the piezometric tubes. The piezometric tubes are glass tubes with an internal diameter of 2 to 4 mm. The sand specimen should be fully saturated, and no air bubbles should be seen in the transparent hoses. After saturation, measure the sample height through the transparent cylinder.

7. When the permeameter outlet valve is closed, there should be no flow inside the sample, and the water levels in all the piezometric tubes should be identical. The elevation of their water column gives the total heads at the permeameter taps. When the outlet is opened, the piezometric levels should first fall, then stabilize. When the piezometer levels stop moving, measure the vertical distance between their meniscus bottoms. This distance is equal to the total head drop.

8. Adjust the outlet valve and/or the water pressure of the supply tank to obtain the desired head drop. While the water flows at a steady rate and the piezometer levels are constant, collect water in a container at convenient intervals. Measure the water temperature and the weight of the water collected to determine its volume.

9. Repeat step 8 for various head drops. Compute the coefficient of permeability for each measurement.

10. After the test is completed, turn off the water supply and remove the sample from the apparatus. Place a porous stone on the base, and mount the permeameter cylinder.

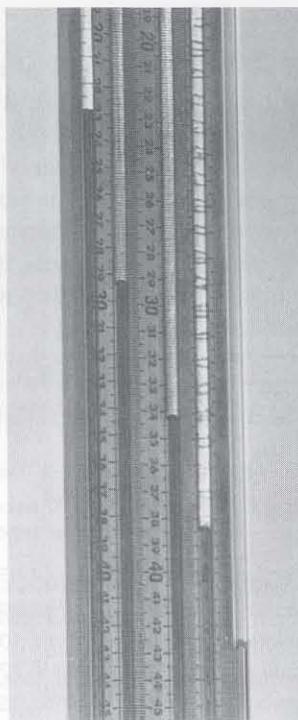


**Figure 11** Close-up view of piezometric tubes of Fig. 10.

## COMPUTATIONS

The dry unit weight  $\gamma_d$  and void ratio  $e$  of the soil specimen are

$$\gamma_d = \frac{W}{(\pi/4) D^2 H} \quad \text{and} \quad e = \frac{G_s \gamma_w}{\gamma_d} - 1 \quad (1)$$

where  $H$  is the sample height,  $D$  the sample diameter,  $W$  the dry sample weight,  $G_s$  the soil specific density, and  $\gamma_w$  the water unit weight. The discharge velocity  $v$ , hydraulic gradient  $i$ , and coefficient of permeability  $k_T$  at temperature  $T$  are

$$v = \frac{Q}{A_t}, \quad i = \frac{\Delta h}{L}, \quad \text{and} \quad k_T = \frac{v}{i} \quad (2)$$

where  $L$  is the distance between piezometer taps,  $\Delta h$  the distance between free surfaces in the piezometer tubes,  $A_t = \pi D^2/4$  is the cross-sectional area of the specimen, and  $Q$  the volume of water collected during time  $t$ . The coefficient of permeability  $k$  at  $20^\circ\text{C}$  is

$$k_{20^\circ\text{C}} = \frac{\eta_T}{\eta_{20^\circ\text{C}}} k_T \quad (3)$$

where  $\eta_{20^\circ\text{C}}$  is the viscosity of water at  $20^\circ\text{C}$  and  $\eta_T$  is the viscosity of water at temperature  $T$ .

**EXAMPLE**

Figures 12 and 14 show the results of a constant head permeability test. As shown in Fig. 12, the input data are italicized. Figure 13 lists the formulas used in Fig. 12, and Fig. 14 shows the variation of the discharge velocity  $v$  versus the hydraulic gradient  $i$ . Darcy's law is verified in the range of applied hydraulic gradient, because  $v$  varies linearly with  $i$ . The slope of the linear  $v-i$  relation is equal to the permeability coefficient  $k$  at ambient temperature. The permeability coefficient is then calculated at 20°C to compensate for the change in water viscosity with temperature.

	A	B	C	D	E	F
1	<b>Constant Head Permeability</b>					
2	Analyst Name: <i>Kary P. Tiel, J. S. Tkach, E. Davidson, and H. Guapo</i>					
3	Test Date: <i>3/1/93</i>					
4	Soil Sample: <i>Loose sand mixture</i>					
5	Specific gravity $G_s =$ <i>2.65</i>					
6	Specimen dry mass $M_d =$ <i>674.00 g</i>					
7	Specimen height $H =$ <i>14.50 cm</i>					
8	Specimen diameter $D =$ <i>6.22 cm</i>					
9	Piezometer tap distance $L =$ <i>10.35 cm</i>					
10	Initial void ratio $e =$ <i>0.73</i>					
11	Dry unit weight $\gamma_d =$ <i>14.99 kN/m³</i>					
13	Trial					
14	Piezometer level distance (cm) $\Delta h$					
15	Duration of sampling (s) $t$					
16	Mass of water collected & container (g) $M_{wc}$					
17	Mass of container (g) $M_c$					
18	Water temperature (°C) $T_e$					
19	Hydraulic gradient $i$					
20	Discharge velocity (cm/s) $v$					
21	Permeability at ambient temperature (cm/s) $k_T$					
22	Permeability at 20°C (cm/s) $k$					
23	Average permeability at ambient = <i>0.094 cm/s</i>					
24	Average permeability at 20°C = <i>0.090 cm/s</i>					

Figure 12 Example of data set for the constant head permeability test.

	A	B	C
10	Initial void ratio $e =$ $=G_s/gd*9.81-1$		
11	Dry unit weight $\gamma_d =$ $=M_d/H/PI()^4*D^2*9.81$ $kN/m^3$		

	A	B	C
19	Hydraulic gradient $i = Dh/L$		
20	Discharge velocity (cm/s) $v = (M_{wc}-M_c)/t/(PI()^4*D^2/4)$		
21	Permeability at ambient temperature (cm/s) $k_T = v/i$		
22	Permeability at 20°C (cm/s) $k = kT*VISCO(Te)/VISCO(20)$		
23	Average permeability at ambient = $=AVERAGE(kT)$ $cm/s$		
24	Average permeability at 20°C = $=AVERAGE(k)$ $cm/s$		

Figure 13 Formulas used in Fig. 12.

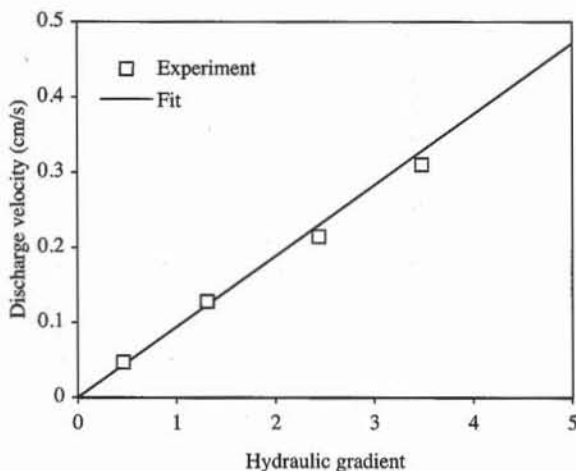


Figure 14 Variation of discharge velocity versus hydraulic gradient.

### Indirect Calculation of Permeability from Grain Size Distribution Curve

Figures 15 and 16 show the variation of the permeability coefficient  $k$  versus the void ratio  $e$  for the same material. The permeability decreases with the void ratio.

A grain size distribution is required to calculate  $k$  with Hazen's or Kozeny-Carman's equations (Eqs. 9 and 10 of Chapter 4-1). The grain size analysis results for the soil tested in Fig. 16 are reported in Figs. 17 and 18 (see Chapter 1-2 for details). Hazen's formula neglects the effect of void ratio on  $k$ , which corresponds to a vertical dashed line in Fig. 16, and overestimates the measured values. For Kozeny-Carman's formula, as shown in Fig. 17, we assume that grains larger than 0.25 are subrounded (i.e.,  $f = 1.25$ ) and those smaller than 0.25 mm are rounded (i.e.,  $f = 1.1$ ). The total value of  $fS^2$  is the weighed sum of  $fS^2$  which is calculated independently for each grain size range. Figure 19 shows the details of these calculations. Kozeny-Carman's formula is slightly in better agreement with measured values than is Hazen's formula. It accounts for the decrease in permeability with void ratio.

$k$ (cm/s)	$e$
0.0943	0.73
0.0428	0.61
0.0140	0.75
0.0045	0.44
0.1934	0.77
0.1033	0.62

Figure 15 Measured variation of permeability with void ratio.

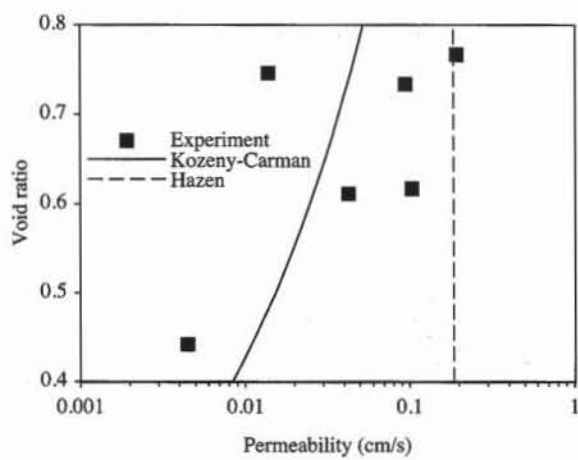


Figure 16 Measured variation of permeability with void ratio and values of permeability predicted by Hazen's and Kozeny-Carman's equations.

	A	B	C	D	E	F	G							
1	<b>Calculation of permeability coefficient with empirical relations</b>													
2														
3	Analyst: J. S. Tkach													
4	Test date: 2-Feb-93													
5	Soil type: Sand Mixture													
6														
7	Grain size (mm)	Percent finer by weight pf	Frequency p	Specific surface ( $\text{mm}^{-1}$ ) S	Angularity factor f									
8	d													
9	0.42	100.0	35.%	16.90	1.25									
10	0.3	65.2	11.%	21.91	1.25									
11	0.25	53.9	22.%	28.52	1.10									
12	0.177	32.0	7.%	36.82	1.10									
13	0.15	25.2	16.%	56.57	1.10									
14	0.075	9.2	9.%											
15	$D_{10} = 0.078 \text{ mm}$		$C_u = 3.558$											
16	$D_{30} = 0.169 \text{ mm}$		$C_c = 1.328$											
17	$D_{60} = 0.276 \text{ mm}$ Kozeny-Carman $C_k = 0.185 \text{ cm/s}$													
18	<b>Permeability coefficient</b>													
19	Hazen, k (cm/s)	0.006												
20	Void ratio e	0.730	0.610	0.440	0.750	0.770	0.620							
21	Kozeny-Carman, k (cm/s)	0.042	0.026	0.011	0.045	0.048	0.027							

Figure 17 Results of grain size analysis and calculation of permeability coefficient with Hazen's and Kozeny-Carman's equations.

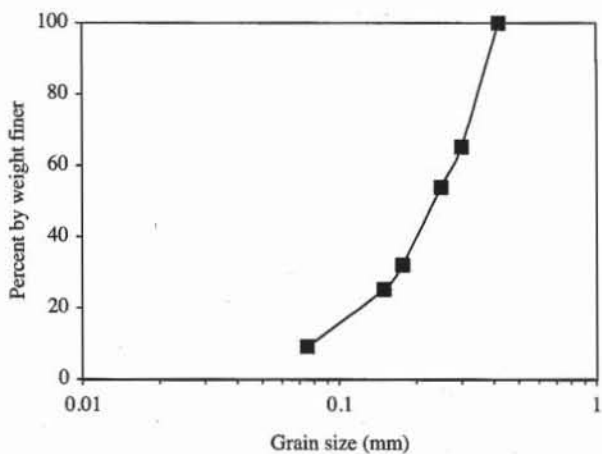


Figure 18 Grain size distribution curve of materials tested in Fig. 16.

## REVIEW QUESTIONS

- What is the purpose of the constant head permeability test?
- What is the smallest value of permeability coefficient that can be measured in the constant head permeability test? What other test do you apply to the soils of smaller permeability?
- Is the permeability coefficient of sands influenced by their void ratio? What is the trend?

	C	D
7	Frequency	Specific surface (mm <sup>-1</sup> )
8	p	S
9	= $(B_9 - B_{10})/100$	= $6/\text{SQRT}(A_9 \cdot A_{10})$
10	= $(B_{10} - B_{11})/100$	= $6/\text{SQRT}(A_{10} \cdot A_{11})$
11	= $(B_{11} - B_{12})/100$	= $6/\text{SQRT}(A_{11} \cdot A_{12})$
12	= $(B_{12} - B_{13})/100$	= $6/\text{SQRT}(A_{12} \cdot A_{13})$
13	= $(B_{13} - B_{14})/100$	= $6/\text{SQRT}(A_{13} \cdot A_{14})$
14	= $(B_{14}/100)$	

	A	B	C	D
19	Hazen, k (cm/s)	= $100 \cdot (D_{10}/10)^2$		
20	Void ratio e	0.73	0.61	0.44
21	Kozeny-Carman, k (cm/s)	= $C_k \cdot e^3 / (1+e)$	= $C_k \cdot e^3 / (1+e)$	= $C_k \cdot e^3 / (1+e)$

	A	B	C	D	E
15		$D_{10} = \text{INTER}(10, p_f, d)$	$C_u = D_{60}/D_{10}$		
16		$D_{30} = \text{INTER}(30, p_f, d)$	$C_o = D_{30}^2/D_{10}/D_{60}$		
17		$D_{60} = \text{INTER}(60, p_f, d)$	Kozeny-Carman $C_k = (9.81/(5 \cdot \text{VISCO}(20)) \cdot \text{SUMPRODUCT}(p, f, S, S))$		

Figure 19 Formulas used in Fig. 17.

4. Can you give a relation that accounts for permeability change versus void ratio?
5. Explain the principle of the constant-pressure tank shown in Fig. 6.
6. Why do you use deaired water instead of tap water for the permeability test?
7. How do you remove air from water?
8. Does the measurement of permeability increase or decrease with the air content of the test water?
9. What technique do you use to get a loose specimen of sand in the permeameter cell?
10. Does the permeability coefficient increase or decrease with water temperature? Why?

**EXERCISES**

1. Calculate the void ratio and average permeability coefficient from the test results in Table E1. Verify that the discharge velocity varies linearly with the hydraulic gradient.

**TABLE E1**

Specific gravity	2.65			
Specimen dry mass (g)	674.00			
Specimen height (cm)	13.48			
Specimen diameter (cm)	6.22			
Piezometer tap distance (cm)	10.35			
Trial	1	2	3	4
Piezometer reading, inlet (cm)	89.90	57.40	44.90	22.00
Piezometer reading, outlet (cm)	42.70	27.70	23.00	15.50
Duration of sampling (sec)	60	60	60	60
Mass of water collected and container (g)	766.0	614.0	560.0	438.0
Mass of container (g)	396.0	390.0	398.0	390.0
Water Temperature (°C)	21.8	21.9	21.9	22.2

2. Same as Exercise 1 but for Table E2.

TABLE E2

Specific gravity	2.65			
Specimen dry mass (g)	712.00			
Specimen height (cm)	15.50			
Specimen diameter (cm)	6.21			
Piezometer tap distance (cm)	10.33			
<hr/>				
Trial	1	2	3	4
Piezometer reading, inlet (cm)	54.60	16.60	63.90	74.80
Piezometer reading, outlet (cm)	9.10	5.50	10.20	11.30
Duration of sampling (s)	150	150	90	90
Mass of water collected and container (g)	670.0	470.0	594.0	620.0
Mass of container (g)	396.8	396.8	396.8	396.8
Water temperature (°C)	22.5	22.5	22.5	22.5

3. Same as Exercise 1 but for Table E3.

TABLE E3

Specific gravity	2.65			
Specimen dry mass (gr)	712.00			
Specimen height (cm)	12.80			
Specimen diameter (cm)	6.21			
Piezometer tap distance (cm)	10.33			
<hr/>				
Trial	1	2	3	4
Piezometer reading, inlet (cm)	86.90	67.20	48.40	25.40
Piezometer reading, outlet (cm)	6.40	5.90	5.70	5.50
Duration of sampling (s)	90	90	180	180
Mass of water collected and container (g)	494.0	468.0	492.0	448.0
Mass of container (g)	396.8	396.8	396.8	396.8
Water temperature (°C)	22	22	22	22

4. Same as Exercise 1 but for Table E4.

TABLE E4

Specific gravity	2.65			
Specimen dry mass (g)	698.00			
Specimen height (cm)	15.30			
Specimen diameter (cm)	6.22			
Piezometer tap distance (cm)	10.30			
<hr/>				
Trial	1	2	3	4
Piezometer reading, inlet (cm)	19.10	46.40	62.40	72.20
Piezometer Reading, outlet (cm)	11.50	30.00	41.80	48.70
Duration of sampling (s)	60	90	60	60
Mass of water collected and container (g)	656.0	1214.0	1094.0	1174.0
Mass of container (g)	390.0	390.0	390.0	390.0
Water temperature (°C)	21	21	21	21

5. Same as Exercise 1 but for Table E5.

TABLE E5

	Trial	1	2	3	4
Specific gravity		2.65			
Specimen dry mass (g)		698.00			
Specimen height (cm)		14.00			
Specimen diameter (cm)		6.22			
Piezometer tap distance (cm)		10.30			
Piezometer reading, inlet (cm)		18.20	52.10	64.80	80.40
Piezometer reading, outlet (cm)		7.20	22.10	28.30	35.90
Duration of sampling (s)		60	60	60	60
Mass of water collected and container (g)		608.0	936.0	1034.0	1146.0
Mass of container (g)		390.0	390.0	390.0	390.0
Water temperature (°C)		21	21	21	21

# **4-3 Falling Head Permeability Test**

## **OBJECTIVE**

The falling head permeability test is used for determining the permeability of soil samples that have a permeability less than about  $10^{-3}$  cm/s.

## **EQUIPMENT**

The equipment for the falling head permeability test includes:

- Permeameter similar to that shown schematically in Fig. 1.
- Perforated metal or plastic disks, circular wire screens, or porous stones.
- Glass standpipe with its support.
- Transparent flexible hoses, screw clamps, and so on.
- Deaired distilled water.
- Watch or clock.
- Thermometers, range 0 to 50°C, accurate to 0.1°C.
- Balance sensitive to 0.1 g.
- Oven.
- Ruler.

## **PROCEDURE**

1. Dry specimens are prepared as for the constant head test. Wet specimens may be trimmed and fitted into the permeameter mold as described in Chapter 7-2.
2. Measure the specimen height, diameter, and dry weight. Determine the standpipe internal diameter by measuring the volume of water contained in a standpipe section of given height.

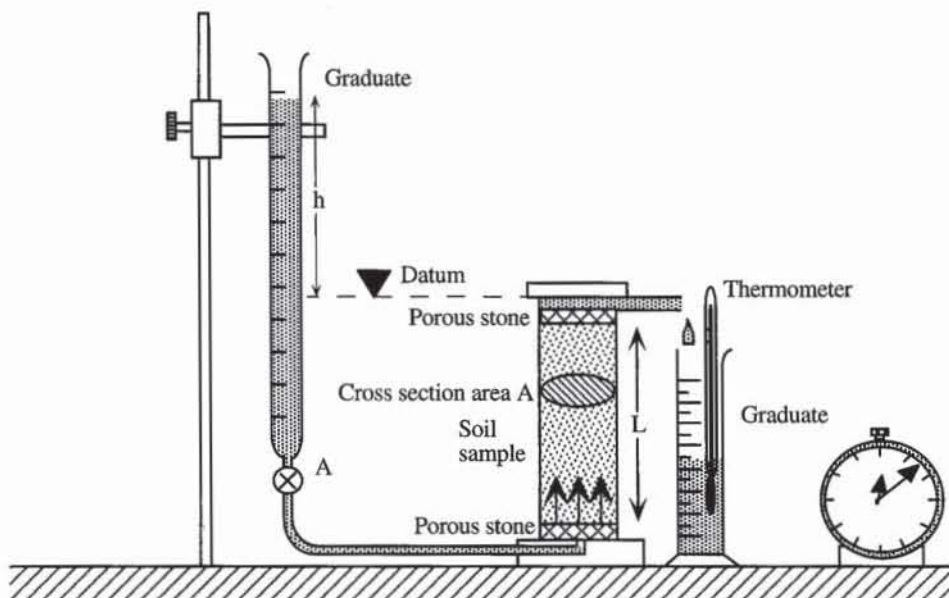


**Figure 1** Setup of falling head permeability device.

**3.** Saturate the specimen by immersing it in water for several days. It is important that the specimen be fully saturated; otherwise, the falling head test will give erroneous results.

**4.** Fill the standpipe with deaired water well above the discharge level of the permeameter cell. If the water level falls slowly and the test lasts a few days, it is recommended that a few drops of oil be added on the water surface in the standpipe to prevent water from evaporating.

**5.** Begin the test by opening the inlet valve A simultaneously and starting the timer. As the water flows through the specimen, measure the water elevation above the datum and the water temperature at various times  $t$ .

## PERMEABILITY TEST WITH CONSOLIDOMETER

Soil permeability can also be measured during the consolidation test by using either the falling head method or the rate of settlement. The former method is described below, the latter in Chapter 7-2.

Figure 2 shows the falling head permeability test during a consolidation test. The specimen in the rigid container is squeezed by a constant vertical load. The standpipe is attached to the consolidation cell and forces water through the specimen. The specimen is subjected to the falling head test after being consolidated. The permeability is computed using Eq. 1.

## COMPUTATIONS

For dry samples, the void ratio and dry unit weight are calculated as for the constant head test. For wet samples, the water content is and dry sample weight is obtained as in Chapter 7-2.

The coefficient of permeability  $k_T$  is calculated as follows:

$$k_T = \frac{aL}{At} \log \frac{h_0}{h_f} \quad (1)$$

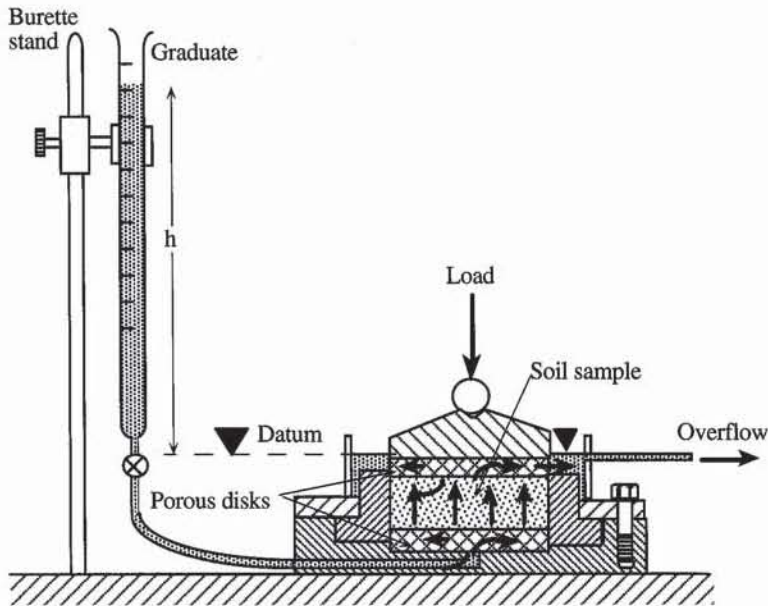


**Figure 2** Falling head permeability test during consolidation test.

where  $a = \pi d^2/4$  is the inside area of the standpipe,  $A = \pi D^2/4$  is the cross-sectional area of the specimen,  $L$  the length of the specimen,  $d$  the internal diameter of the standpipe,  $D$  the diameter of the sample,  $h_0$  the elevation of water in the standpipe above the discharge level at time  $t = 0$ , and  $h_f$  the elevation of water in the standpipe above the discharge level at time  $t$ . The coefficient of permeability  $k_{20^\circ\text{C}}$  is calculated as for the constant head test.

For small-diameter standpipes, the capillary rise  $h_c$  may not be neglected compared to  $h_0$  and  $h_f$ . In this case, Eq. 1 becomes

$$k_T = \frac{aL}{At} \log \frac{h_0 - h_c}{h_f - h_c} \quad (2)$$

### EXAMPLE

Figure 3 shows the results of a falling head permeability test. The formulas used in Fig. 3 are listed in Fig. 4. Figure 5 shows the variation of  $k$  computed by using Eq. 1 for different times and also shows the mean value of  $k$  calculated by using average and linear regression. The average method consists of averaging the values of  $k$  calculated at each sampling time. The linear regression method consists of fitting the variation of water height for the complete test duration. By using Eq. 1, the water column height  $h_t$  varies with time  $t$  as follows:

$$\ln(h_t) = \ln(h_0) - \frac{kA}{aL} t \quad (3)$$

The value of  $k$  can therefore be computed from the slope  $S$  of the linear regression passing through the data points  $(t_i, \ln(h_i))$ ,  $i = 1, \dots, n$ :

$$k = -\frac{SaL}{A} = -\frac{d^2}{D^2} SL \quad (4)$$

where  $d$  is the diameter of the standpipe and  $D$  is the diameter of the sample. As shown in Fig. 6, the average and regression methods give similar results.

	A	B	C	D	E	F	G
1							
2							
3							
4							
5							
6							
7							
8							
9							
10							
11							
12							
13							
14	Time (min)	Height of water in standpipe (cm)	Temperatur e ('C)	Permeability (cm/s)	Permeability at 20 ° C (cm/s)	Height predicted by average (cm)	Height predicted by regression (cm)
15	t	$h_t$	$T_a$	$k_T$	$k$		
16	1	134.1	16.5	1.02E-04	1.11E-04	134.47	134.66
17	2	127.3	16.5	9.77E-05	1.07E-04	127.43	127.79
18	3	120.7	16.5	9.71E-05	1.06E-04	120.76	121.27
19	4	114.3	16.5	9.73E-05	1.06E-04	114.44	115.08
20	5	108.3	16.5	9.73E-05	1.06E-04	108.44	109.21
21	6	102.8	16.5	9.67E-05	1.06E-04	102.77	103.64
22	7	97.7	16.5	9.60E-05	1.05E-04	97.39	98.35
23	8	92.7	16.5	9.58E-05	1.05E-04	92.29	93.33
24	9	88.2	16.5	9.51E-05	1.04E-04	87.46	88.57
25	10	83.7	16.5	9.50E-05	1.04E-04	82.88	84.05
26	11	79.4	16.5	9.50E-05	1.04E-04	78.54	79.76
27	Permeability calculated by average $k_{Ta}$ =				9.68E-05	cm/s	
28	Permeability calculated by regression $k_{Tr}$ =				9.43E-05	cm/s	
29	Permeability calculated by average $k_{20^{\circ}C}$ =				1.06E-04	cm/s	

**Figure 3** Example of data set for the falling head permeability test.

	C	D	E
1 1	Initial void ratio $e = G_s/gd^3 \cdot 9.81 - 1$		
1 2	Dry unit weight $\gamma_d = M/H/PI()^4/D^2 \cdot 9.81$		$kN/m^3$

	D	E	F	G
1 4	Permeability (cm/s)	Permeability at 20 ° C (cm/s)	Height predicted by average (cm)	Height predicted by regression (cm)
1 5	$k_T$	$k$		
1 6	$=ds^2*H/D^2/(t*60)*LN(h0/ht)$	$=kT*VISCO(Te)/VISCO(20)$	$=h0*EXP(-kTa*D^2/ds^2/H*t*60)$	$=h0*EXP(-kTr*D^2/ds^2/H*t*60)$
1 7	$=ds^2*H/D^2/(t*60)*LN(h0/ht)$	$=kT*VISCO(Te)/VISCO(20)$	$=h0*EXP(-kTa*D^2/ds^2/H*t*60)$	$=h0*EXP(-kTr*D^2/ds^2/H*t*60)$
2 7	Permeability calculated by average $k_{Ta} = =AVERAGE(kT)$			cm/s
2 8	Permeability calculated by regression $k_{Tr} = =-SLOPE(LN(ht),t)*ds^2/D^2*H/60$			cm/s
2 9	Permeability calculated by average $k_{20°C} = =AVERAGE(k)$			cm/s

**Figure 4** Formulas used for the falling head test.

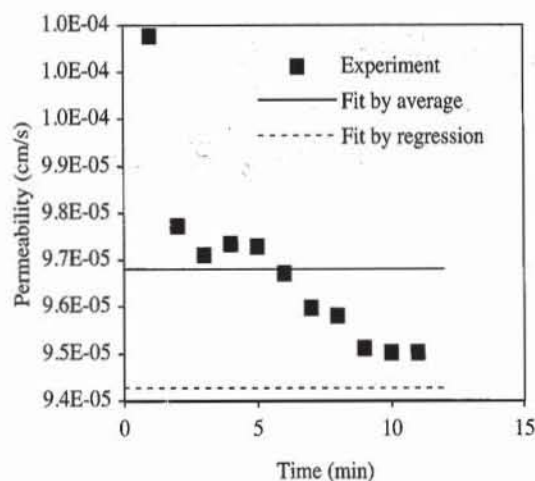


**Figure 5** Permeability coefficient computed at various time intervals, and average permeability coefficient calculated by average and linear regression.

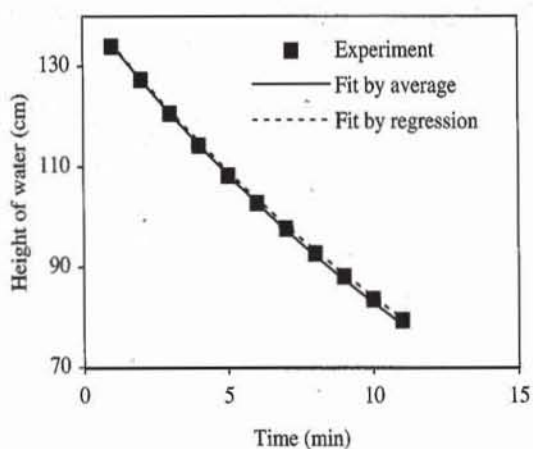


**Figure 6** Variation of height of water column versus time predicted by the average and linear regression methods.

## 4-4 Electrical Analogy of Seepage Problems

### DEFINITION

The steady-state flow of a fluid through a porous medium is analogous to the steady-state flow of an electric current through a current-conducting medium. The electrical analogy method solves seepage problems by constructing an analog problem with resistive papers and by measuring voltage instead of total head.

### ELECTRICAL ANALOGY OF WATER FLOW

#### Seepage Theory

When water flows steadily through a two-dimensional saturated soil of isotropic permeability, the distribution of total head  $h(x,y)$  obeys Laplace's equation:

$$\frac{\partial^2 h}{\partial x^2} + \frac{\partial^2 h}{\partial y^2} = 0 \quad \text{or} \quad \nabla^2 h = 0 \quad (1)$$

where  $x$  and  $y$  are spatial coordinates. Laplace's equation is not only found in the steady-state flow of water but in many other branches of engineering and physics. In particular, it describes the steady flow of electricity through resistive paper.

#### Conduction Theory

**One-dimensional Ohm's law.** As shown in Figs. 1 and 2, if two electrical potentials  $V_1$  and  $V_2$  are applied to the extremities of resistance  $R$ , the current  $i$  obeys Ohm's law:

$$i = -\frac{1}{R} (V_2 - V_1) \quad (2)$$

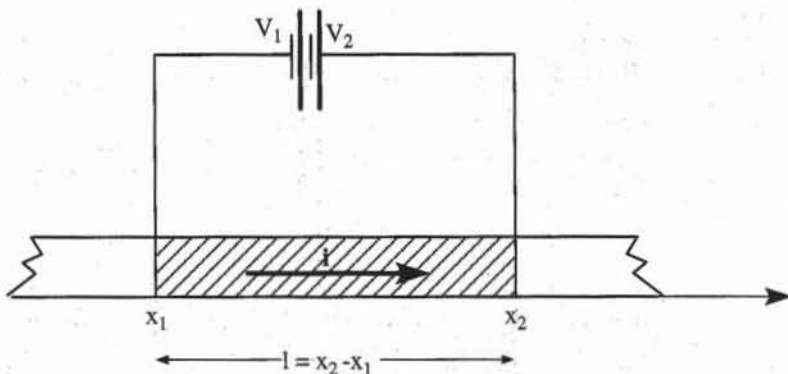


Figure 1 One-dimensional resistance of finite length.

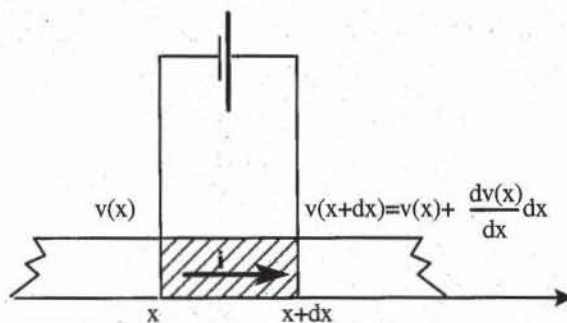


Figure 2 One-dimensional resistance of infinitesimal length.

The resistance  $r$  per unit of length is

$$r = \frac{R}{l} = \frac{R}{x_2 - x_1} \quad (3)$$

where  $l = x_2 - x_1$  is the resistance length. The conductivity  $\sigma$  is the inverse of  $R$  (i.e.,  $\sigma = 1/R$ ). When  $l \ll 1$ :

$$\frac{V_2 - V_1}{x_2 - x_1} = \frac{dV(x)}{dx} \quad (4)$$

and Ohm's law becomes

$$i = -\frac{1}{r} \frac{dV}{dx} = -\sigma \frac{dV}{dx} = -\sigma \text{grad } V \quad (5)$$

**Ohm's law for two-dimensional flow of electricity.** For the two-dimensional flow of current in an isotropically resistive paper, Ohm's law becomes

$$i_x = -\sigma \frac{\partial V}{\partial x}, \quad i_y = -\sigma \frac{\partial V}{\partial y} \quad (6)$$

where  $i_x$  and  $i_y$  are components of current intensity in the  $x$  and  $y$  directions,  $\sigma$  is the conductivity of the resistive paper, and  $V(x, y)$  is an electric potential depending on the  $x$  and  $y$  coordinates. When no electricity is stored or lost in the infinitesimal element of Fig. 3, the conservation of electricity implies that

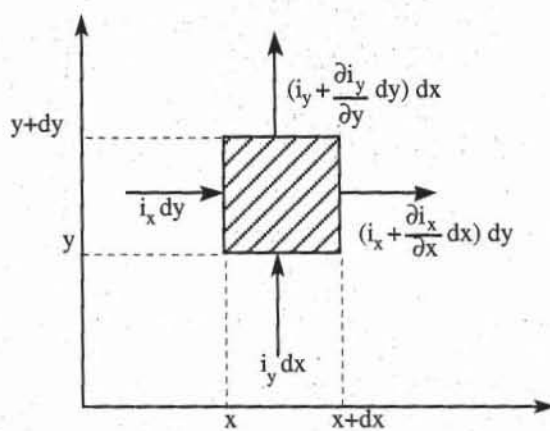


**Figure 3** Flow of current through an infinitesimal element of two-dimensional resistance.

$$\left(i_y + \frac{\partial i_y}{\partial y} dy\right) dx - i_y dx + \left(i_x + \frac{\partial i_x}{\partial x} dx\right) dy - i_x dy = 0 \quad (7)$$

Equation 7 simplifies to

$$\frac{\partial i_x}{\partial x} + \frac{\partial i_y}{\partial y} = 0 \quad (8)$$

By substituting Eq. 6 into Eq. 8,  $V(x, y)$  also satisfies Laplace's equation:

$$\frac{\partial^2 V}{\partial x^2} + \frac{\partial^2 V}{\partial y^2} = 0 \quad \text{or} \quad \nabla^2 V = 0 \quad (9)$$

#### Analogy between Seepage and Conduction Theories

Table 1 presents the correspondence between the variables and relations of water seepage in soils and electric current flow in resistive papers. Although the flow of water through a porous medium and the flow of electrons through a resistive medium are different in nature, they are described by similar variables and governing equations. These two physical phenomena are said to be analogous. The analogy between seepage flow and current flow permits us to determine the total head  $h(x, y)$  in soils by measuring  $V(x, y)$  directly on resistive paper.

**TABLE 1**

Correspondence between seepage and flow of electrical current

Flow of water	Flow of electrical current
$h$ total head	$V$ voltage
$k$ coefficient of permeability	$\sigma$ conductivity ( $\sigma = 1/r$ )
$v$ discharge velocity	$i$ current
Darcy's law: $v = -k \operatorname{grad} h$	Ohm's law: $i = -\sigma \operatorname{grad} V$
$\nabla^2 h = 0$	$\nabla^2 V = 0$
Equipotential lines: $h = \text{constant}$	Equipotential lines: $V = \text{constant}$
Impervious boundary: $\frac{\partial h}{\partial n} = 0$	Insulated boundary: $\frac{\partial V}{\partial n} = 0$

### APPLICATION OF ANALOGY TO SEEPAGE PROBLEM

Figures 4 to 6 show a seepage problem and its electrical analog. In Figs. 5 and 6, the electrical analog is cut out in a large sheet of resistive paper. Compared to the seepage problem of Fig. 4, the electrical analog has the same geometric proportions but is 100 times smaller. One meter in the field corresponds to 1 centimeter in the analog model. The thin slot in the resistive paper is an electric barrier representing the impervious sheet-pile wall. The conductive electrodes A and B represent the equipotential lines on the upstream and downstream boundaries of Fig. 4. The 6-V differential voltage applied between A and B corresponds to the total head drop of 6 m in Fig. 4. Each volt in Fig. 5 conveniently corresponds to 1 m of total head in Fig. 4. One voltmeter pin is connected to electrode B, which is equivalent to choosing the datum along the downstream surface of Fig. 4. The voltmeter indicates 6 V and 0 V on electrodes A and B, respectively. The equipotential line along which the total head is equal to 5 m can therefore be constructed point by point by tracking the places on the resistive paper where the voltmeter probe indicates 5 V. The equipotential lines for  $h = 1, 2, 3$ , and 4 m can be drawn in a similar way.

The flow lines can be obtained either by sketching the flow net by hand or by using the complementary electrical analog. In the former case, the flow lines are sketched by hand over the equipotential lines by ensuring that equipotential and flow lines intersect at right angles and generate curvilinear squares. In the latter case, the complementary electrical analog must be defined. In the complementary problem, boundary flow lines become equipotential boundaries, while

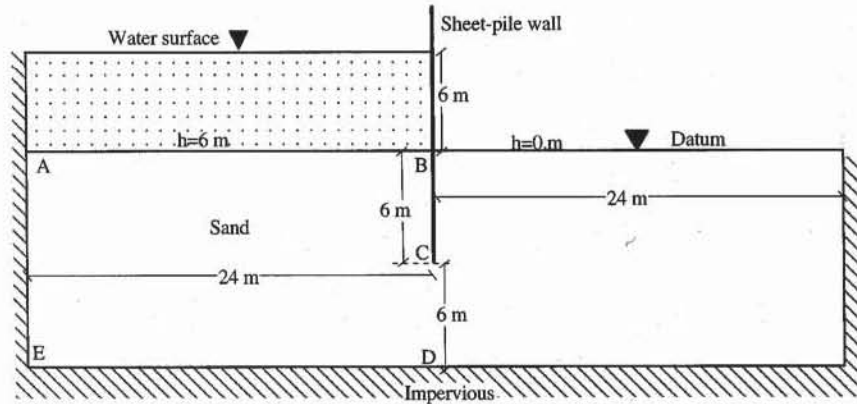


**Figure 4** Definition of the geometry for the original seepage problem with a sheet-pile wall.

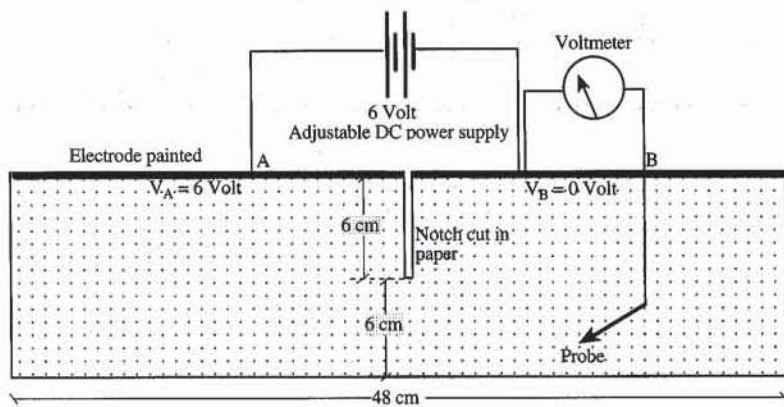


**Figure 5** Electrical analogy of the problem in Fig. 4.

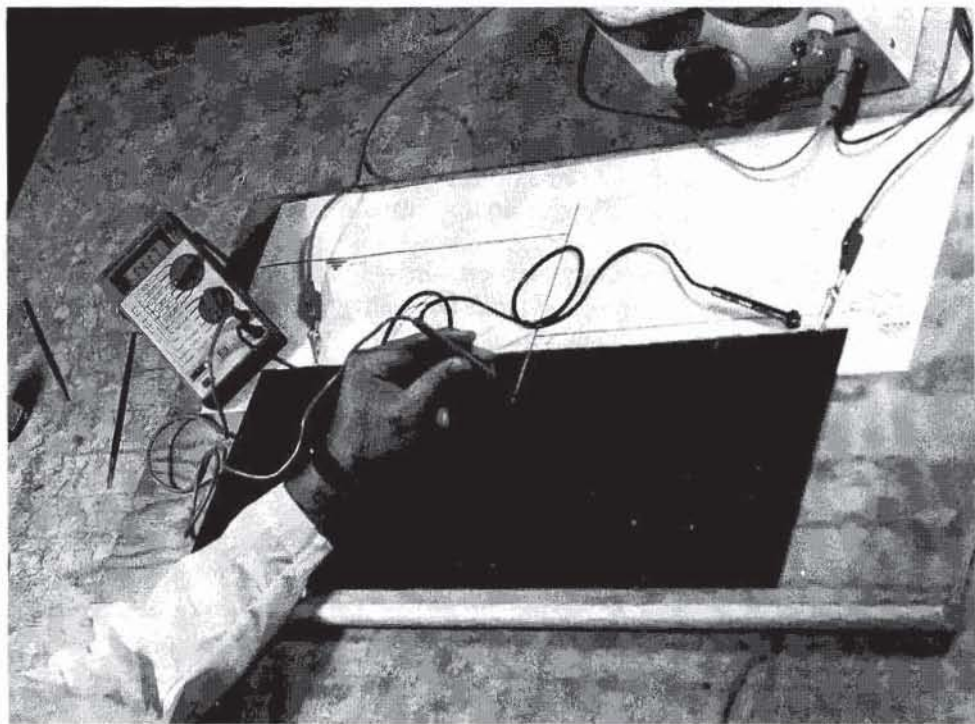


**Figure 6** Electrical analogy setup. The resistive paper is cut as shown in Fig. 5. The notch in the paper represents the sheet-pile wall.

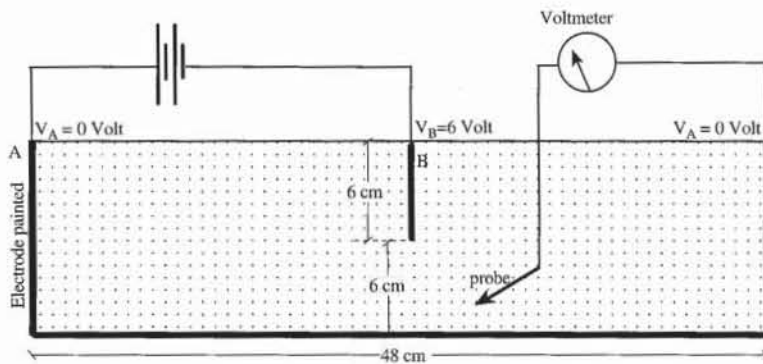


**Figure 7** Complementary seepage problem to obtain flow lines and flow net.

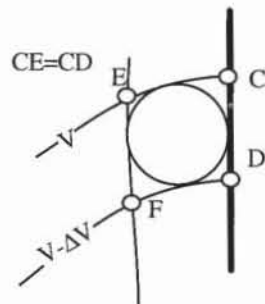


**Figure 8** Determination of the differential voltage between two complementary flow lines for the construction of flow nets.

equipotential boundaries become flow lines. As shown in Fig. 7, the complementary analog has the same size as the original model but has complementary boundaries. The differential voltage between electrodes  $A$  and  $B$  is set arbitrarily to the same value as in Fig. 5. The differential voltage  $\Delta V$  between two consecutive flow lines is determined as illustrated in Fig. 8. The distance  $CD$  between two consecutive equipotential lines is measured with a compass in the region of Fig. 5 where the equipotential lines are almost parallel. Point  $E$  is then drawn in Fig. 7 on the same equipotential line as  $C$  so that  $CD = CE$ . The differential voltage  $\Delta V = V_C - V_E$  is measured. The flow lines are then traced for the differential volt-

ages that are multiples of  $\Delta V$ . The flow net is finally obtained by superimposing equipotential and flow lines on the same piece of paper.

## EQUIPMENT

The following equipment is needed:

- Voltmeter with high input impedance. The high input impedance prevents the voltage measurements from interfering with the flow of electricity in the analog model.
- DC voltage supply with an adjustable voltage between 0 and 15 V.
- Resistive paper. This graphite-coated paper is an excellent material for use as an electrical-analogy cutout. Although its conductivity may vary slightly between the  $x$  and  $y$  directions, these differences in conductivity are of negligible importance for the solution of most seepage problems. The resistive paper should be handled and stored carefully because its conducting qualities become erratic when it is perforated or crumpled.
- Silver- or nickel-based paint to make electrodes. The electrodes should be much more conductive than the resistive paper. These metallic paints are available from electronic supply stores. These paints are used to mend heat-sensitive printed circuit boards that cannot be soldered.
- Scissors and rulers.

## TEST PROCEDURE

1. Identify the flow lines (impervious boundaries) and equipotential lines (prescribed total head) that form the boundaries of the confined seepage problem. Make a scaled cutout of the seepage problem with the resistive paper. Before cutting the paper, add a 3- to 5-mm-wide strip along the equipotential boundaries of the analog model. This strip will be reserved for painting electrodes.

2. Carefully paint the electrodes on the cutout with the conductive paint. The electrodes simulate the boundaries with a constant total head but are not part of the soil itself. The electrodes should be painted as straight as possible to form a continuous 3- to 5-mm-wide strip. The electrodes should be highly conductive with respect to the resistive paper. Their conductivity may be checked by measuring the voltage at several locations. The voltage should be almost constant along a highly conductive electrode. You may apply several coats of conductive paint to increase the electrode conductivity.

3. Apply a voltage across the upstream and downstream electrodes of the cutout. The voltage should be chosen to have a basic correspondence between voltage and total head. Trace at least 10 equipotential lines on the model by using the voltmeter probe. Lightly mark the points where the voltage is constant with a soft lead pencil. Do not perforate the paper since holes will change the model conductivity.

4. Make a tracing of the cutout and equipotential line locations and complete the flow net either by freehand sketching of the flow paths or by solving the complementary problem.

## LIMITATIONS OF ELECTRICAL ANALOGY

### Unconfined Seepage

In contrast to water, electrons are not affected by gravity. Hence the electrical analogy is limited to confined seepage problems and cannot be applied directly to unconfined seepage problems such as those found in earth dams. For instance, the earth dam of Fig. 9 must be represented by the cutout of Fig. 10, the upper boundary of which is constructed by the Casagrande method. Casagrande (1940) represents the top flow line with the following parabola:

$$= -\frac{y^2}{2S} + \frac{S}{2} \quad \text{and} \quad S = \sqrt{d^2 + H^2} - \epsilon \quad (10)$$

where  $d$  is the horizontal distance between points  $A$  and  $G$  of Fig. 11. Point  $G$  is defined so that

$$EG = 0.3EF \quad (11)$$

For the seepage problem of Fig. 9, the calculation results are listed in Table 1. The toe drain correction corresponding to  $\beta = 30^\circ$  is  $\Delta a/a = 0.36$  (Fig. 12). The distance  $a = AH$  is found by drawing the parabola of Eq. 10 in Fig. 10. The top flow line is corrected as shown in Fig. 10, and cut out as shown in Fig. 12.

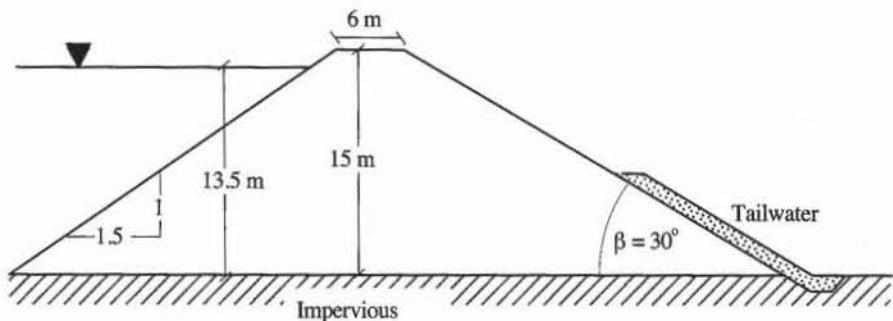
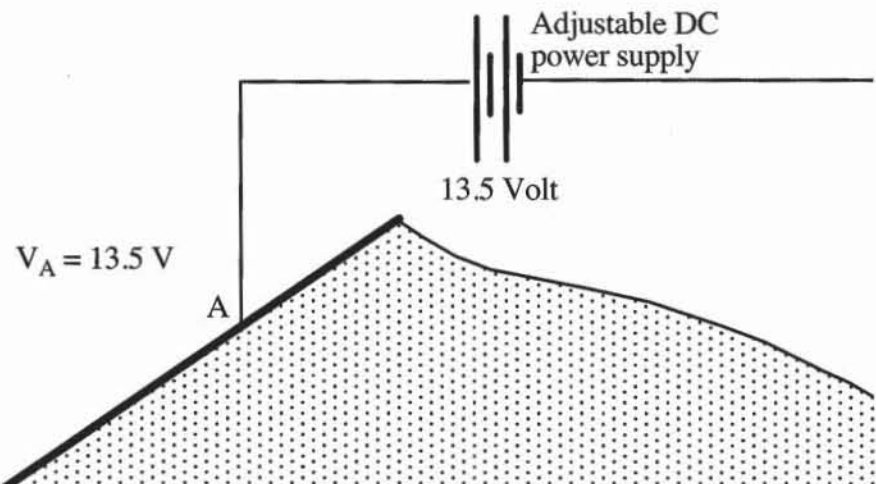
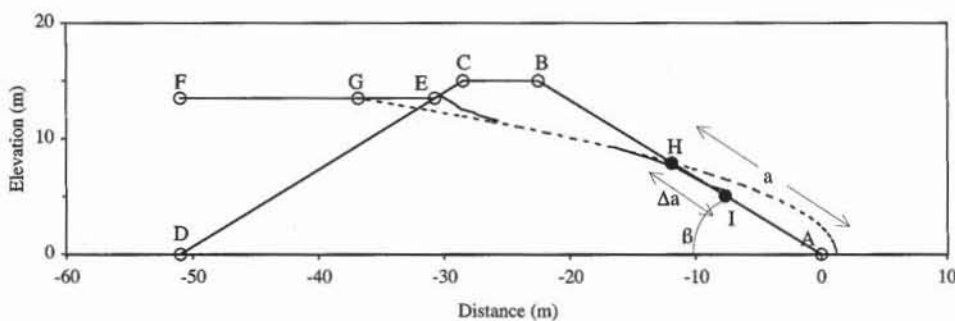
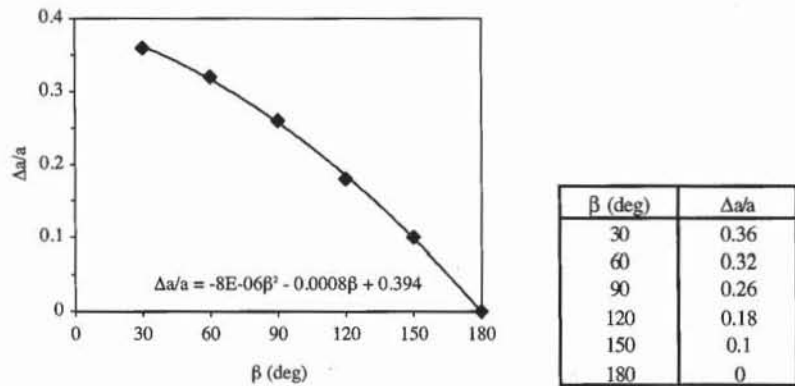


Figure 9 Seepage problem for an earth dam on an impervious base.





**Figure 11** Construction of the top flow line by the Terzaghi–Casagrande method.



**Figure 12** Toe-drain correction proposed by Casagrande (1937).

**TABLE 2**  
Calculation for seepage problem of Fig. 9

Inclination of upstream slope = 1.5	x (m)	y (m)
Inclination of downstream slope = 1.5		
Dam height = 15 m	A	0.00
Water level = 13.5 m	B	-22.50
Crest width = 6 m	C	-28.50
Inclination of drain = 33.69°	D	-51.00
$d = 36.83$ m	E	-30.75
$S = 2.40$	F	-36.83
$a = 14.27$ m	G	-51.00
$\Delta a = 5.11$ m	H	-11.87
	I	-7.62
		13.50
		13.50
		13.50
		5.08

### Seepage with Infinite Dimension and Anisotropic Permeability

The seepage problems with soil layers of infinite extent are difficult to model with an electrical analog of finite size. The effects of infinite size can be approximated by selecting a model three to six times longer than its height. It is recommended that this length be varied to assess its effects on the solution of the seepage problem.

The electrical paper has an isotropic resistivity. When the electrical analog is to be used to model seepage problems with an anisotropic permeability (i.e.,  $k_x \neq k_y$ ), the electrical model must be defined after scaling either the  $x$  or  $y$  coordinates as follows:

$$x_t = x \sqrt{\frac{k_x}{k_y}} \quad \text{or} \quad y_t = y \sqrt{\frac{k_y}{k_x}} \quad (12)$$

## REFERENCE

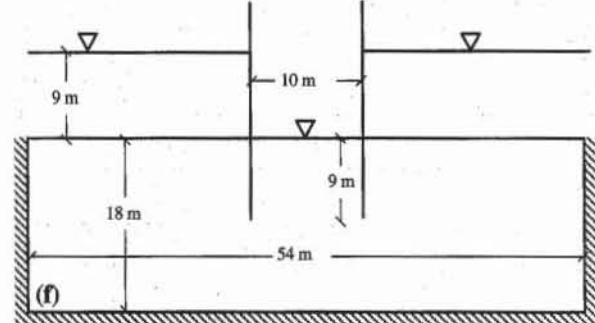
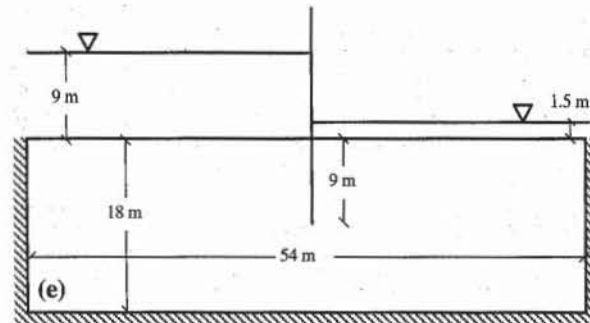
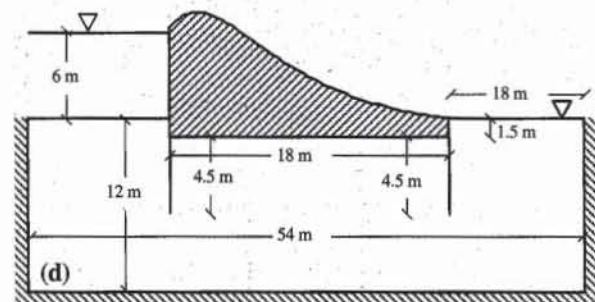
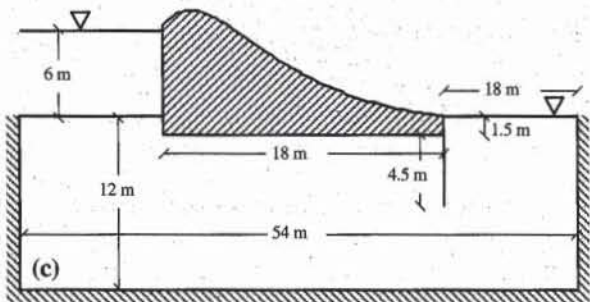
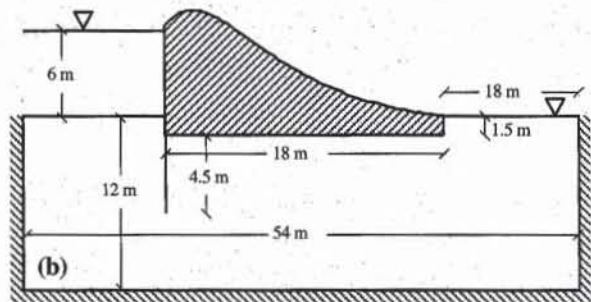
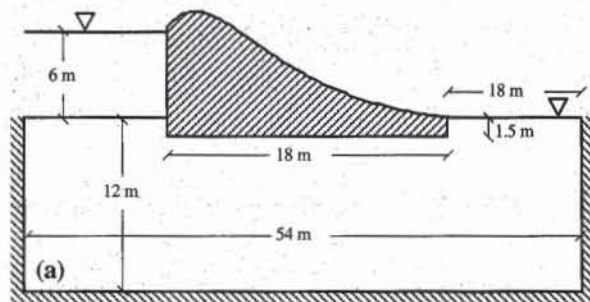
CASAGRANDE, A., 1937, "Seepage through dams," Contribution to Soil Mechanics, BSCE, 1925-1940 (Paper first published in J. New England Water Works Association, June 1937).

## REVIEW QUESTIONS

1. What is the purpose of the electrical analogy test? On what analogy is this test based?
2. What quantities correspond to water head and permeability in the flow of electrical current? What physical law corresponds to Darcy's law?
3. Do painted electrodes represent flow lines or equipotential lines?
4. How can you check the high conductivity of painted electrodes?
5. Write down the partial differential equation that governs the steady-state flow of water in two-dimensional problems with isotropic permeability. What is the name of this partial differential equation? Can you name some other fields of physics and engineering where this equation is found?
6. Why is it important not to fold, perforate, or kink the resistive paper?
7. Does perforation increase or decrease the conductivity of resistive paper? Can you suggest an application for carefully perforated holes?
8. Should the nickel-based paint have low or high conductivity?
9. Are painted electrodes strictly parts of the soil where water flows?
10. Is it possible to obtain the top flow lines from the electrical analogy? How?
11. Is it possible to obtain the top flow lines of unconfined seepage problems by using the electrical analogy directly? How do you define the electrical analog of an unconfined seepage problem?
12. What technique do you use to model an anisotropic seepage problem with an electrical analog model?

## EXERCISES

1. Determine the distribution of total head and flow net for one of the seepage problems [(a) to (f)] shown below using the electrical analogy method.
2. Determine the distribution of water pressure on the structure (cofferdam and/or sheet-pile wall) of one of the seepage problems shown below by using the electrical analogy method.



# 4-5 Finite Difference Solutions of Seepage Problems

## DEFINITION

The finite difference method is a numerical approach to solving partial differential equations such as those governing the two-dimensional steady-state flow of a fluid through a porous medium. In the case of confined problems with simple geometry and boundary conditions, the finite difference method can easily be implemented in spreadsheet programs. The method can be applied to multiple layers and anisotropic cases.

## FINITE DIFFERENCE SOLUTION OF SEEPAGE PROBLEMS

### Seepage Theory

When water flows steadily through a two-dimensional porous soil with an anisotropic permeability ( $k_x \neq k_y$ ), the distribution of total head  $h(x,y)$  within the saturated soil obeys the following partial differential equation:

$$k_x \frac{\partial^2 h}{\partial x^2} + k_y \frac{\partial^2 h}{\partial y^2} = 0 \quad (1)$$

Equation 1. becomes Laplace's equation in the case of isotropic permeability ( $k_x = k_y$ ):

$$\frac{\partial^2 h}{\partial x^2} + \frac{\partial^2 h}{\partial y^2} = 0 \quad (2)$$

In the case of confined seepage problems, the total head or the fluid velocity is prescribed on the boundaries. In mathematical terms, the boundary conditions are prescribed in either total head or gradients of total head.

### Principles of Finite Differences

**Discretization of function derivatives.** As shown in Fig. 1, a continuous function  $f(x)$  may be defined in terms of discrete values  $f_i$  corresponding to values  $x_i$  spaced along the  $x$  axis. Assuming that the function  $f$  is differentiable, the function may be expanded by using a Taylor expansion about  $x$ :

$$f(x + \Delta x) = f(x) + \frac{df}{dx}(x)\Delta x + \frac{1}{2!} \frac{d^2f}{dx^2}(x)\Delta x^2 + \frac{1}{3!} \frac{d^3f}{dx^3}(x)\Delta x^3 + \dots \quad (3)$$

Equation 3 may be written for  $x = x_i$ :

$$f_{i+1} = f_i + \frac{df}{dx}\Big|_i \Delta x + \frac{1}{2!} \frac{d^2f}{dx^2}\Big|_i \Delta x^2 + \frac{1}{3!} \frac{d^3f}{dx^3}\Big|_i \Delta x^3 + \dots \quad (4)$$

$$f_{i-1} = f_i - \frac{df}{dx}\Big|_i \Delta x + \frac{1}{2!} \frac{d^2f}{dx^2}\Big|_i \Delta x^2 - \frac{1}{3!} \frac{d^3f}{dx^3}\Big|_i \Delta x^3 + \dots \quad (5)$$

The first-order differential may be approximated from discrete values by subtracting Eq. 4 from Eq. 5:

$$\frac{df}{dx}\Big|_i \approx \frac{f_{i+1} - f_{i-1}}{2\Delta x} \quad (6)$$

The second-order derivative may be approximated by adding Eqs. 4 and 5:

$$\frac{d^2f}{dx^2}\Big|_i \approx \frac{f_{i+1} + f_{i-1} - 2f_i}{\Delta x^2} \quad (7)$$

Equations 6 and 7 are second-order approximations of the first- and second-order derivatives. The errors between the exact and approximate differentials are proportional to  $\Delta x^2$ . When  $\Delta x$  tends toward zero, the approximated differential converges quadratically toward its exact values.

**Discretization of two-dimensional problems.** Equations 6 and 7 also apply to functions of two variables  $x$  and  $y$ , such as the two-dimensional distribution of total head over a spatial region. As shown in Fig. 2, the two-dimensional space is discretized with a grid of points, the coordinates of which are

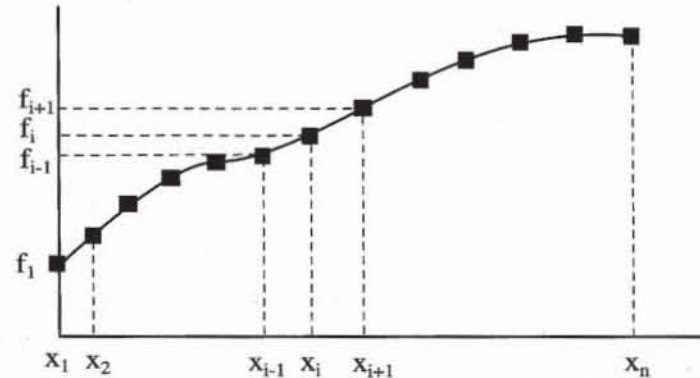
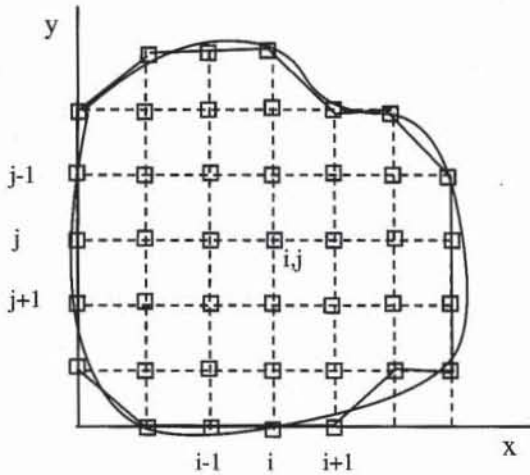
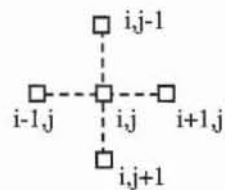


Figure 1 Discrete representation of a continuous function  $f$ .



**Figure 2** Discrete representation of a two-dimensional region.



**Figure 3** Nodes contributing to Eq. 8.

denoted by  $i$  and  $j$ . Curved boundaries have to be approximated with straight segments in order to be described with points.

If  $\Delta x$  and  $\Delta y$  are the nodes spacing in the  $x$  and  $y$  directions, respectively, the discretized form of Eq. 1 at point  $i, j$  is

$$\frac{k_x}{\Delta x^2} (h_{i+1,j} + h_{i-1,j} - 2h_{i,j}) + \frac{k_y}{\Delta y^2} (h_{i,j+1} + h_{i,j-1} - 2h_{i,j}) = 0 \quad (8)$$

As shown in Fig. 3, only the values of  $h$  at the nodes surrounding the node  $i, j$  contribute to Eq. 8. When  $\Delta x = \Delta y$ , Eq. 8 becomes

$$h_{i,j} = \frac{1}{2(1+\alpha)} (\alpha h_{i+1,j} + \alpha h_{i-1,j} + h_{i,j+1} + h_{i,j-1}) \quad (9)$$

where  $\alpha = k_x/k_y$ . When  $\Delta x = \Delta y$  and  $k_x = k_y$  ( $\alpha = 1$ ), Eq. 8 becomes

$$h_{i,j} = \frac{1}{4} (h_{i+1,j} + h_{i-1,j} + h_{i,j+1} + h_{i,j-1}) \quad (10)$$

**Boundary conditions.** In confined seepage, either the total head or the total flow is prescribed on the boundaries. For prescribed flow boundaries, we consider only impervious boundaries and exclude prescribed flux boundaries. For an impervious boundary, the seepage velocity is tangential to the boundary: that is,

$$\frac{\partial h}{\partial n} = 0 \quad (11)$$

where  $n$  is the coordinate normal to the boundary as shown in Fig. 4. In the case of a horizontal surface,  $n = y$  and Eq. 11 becomes

$$\frac{\partial h}{\partial y} = 0 \quad (12)$$

The first-order differential is approximated by introducing a fictitious node, outside the seepage domain (see Fig. 4). Using Eq. 6, at node  $i, j$ ; we obtain

$$\frac{\partial h}{\partial y} \approx h_{i,j+1} - h_{i,j-1} = 0 \quad (13)$$

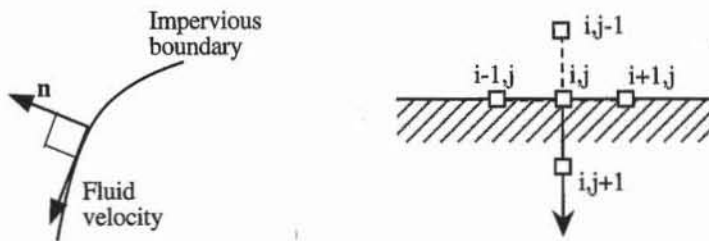


Figure 4 Impervious boundary conditions.

Therefore,  $h_{i,j+1} = h_{i,j-1}$ . The value of total head at the fictitious node  $i, j + 1$  is eliminated by combining Eqs. 10 and 13:

$$h_{i,j} = \frac{1}{4} (h_{i+1,j} + h_{i-1,j} + 2h_{i,j-1}) \quad (14)$$

In summary, for a horizontal impervious boundary, it is not necessary to define fictitious nodes; however, it is necessary to replace Eq. 10 by Eq. 14. The coefficient 2 in Eq. 14 applies to the internal nodes, not to the nodes on the boundary. Thus Eq. 14 may easily be generalized to a vertical boundary. Figure 5 gives additional relations for the total head at grid points on inclined boundaries and at various types of corner boundaries. In all these cases, the sum of the coefficients is equal to 1.

**Interfaces.** The partial differential equations (Eqs. 1 or 2) do not hold on an interface between soils of different permeability because the permeability and the hydraulic gradient are not continuous there. In the case of the horizontal in-

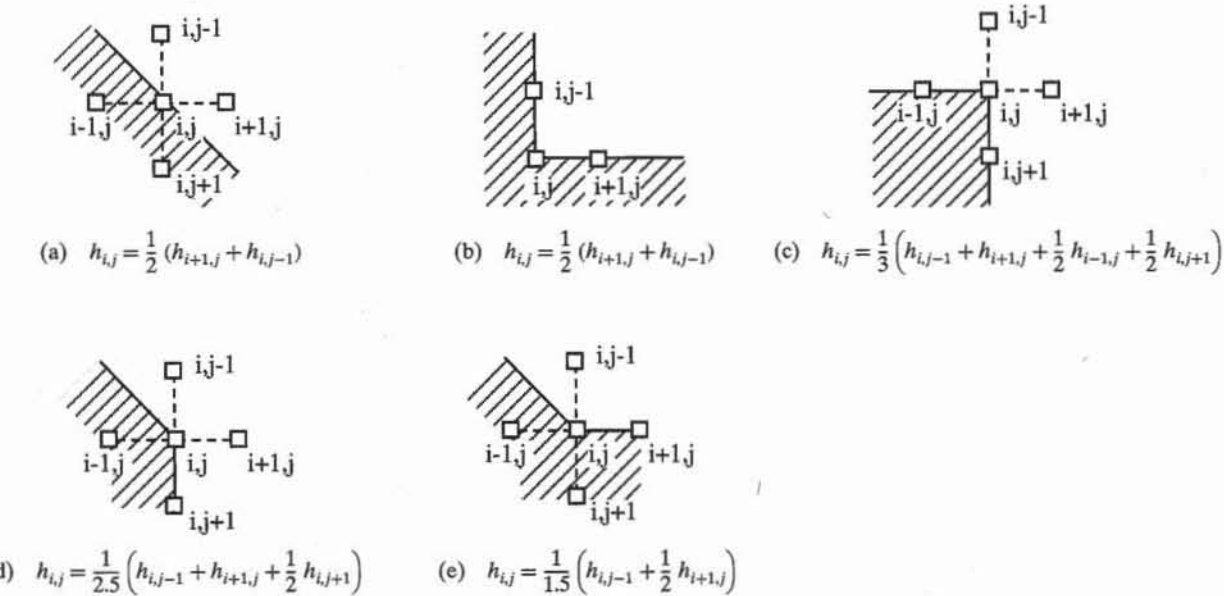


Figure 5 Relations for corners and 45° inclined surfaces of impervious boundaries.

terface shown in Fig. 6, the discharge velocity can only be defined on each side of the interface:

$$v_y^1 = k_1 \frac{h_{i,j} - h_{i,j-1}}{\Delta y} \quad \text{and} \quad v_y^2 = k_2 \frac{h_{i,j+1} - h_{i,j}}{\Delta y} \quad (15)$$

where  $v_y^1$  and  $v_y^2$  are the  $y$ -component of the discharge velocity in medium of permeability  $k_1$  and  $k_2$ , respectively. Due to the conservation of flux of water across the interface (i.e.,  $v_y^1 = v_y^2$ ), Eq. 15 becomes:

$$h_{i,j} = \frac{k_1}{k_1 + k_2} h_{i,j-1} + \frac{k_2}{k_1 + k_2} h_{i,j+1} \quad (16)$$

In the case of a vertical interface, Eq. 16 becomes:

$$h_{i,j} = \frac{k_1}{k_1 + k_2} h_{i-1,j} + \frac{k_2}{k_1 + k_2} h_{i+1,j} \quad (17)$$

It can be shown that the discharge velocity changes direction abruptly at the interface, and that its angle  $\alpha_1$  of incidence and angle  $\alpha_2$  of emergence are related through:

$$\frac{\tan \alpha_1}{\tan \alpha_2} = \frac{k_1}{k_2} \quad (18)$$

**Seepage flow.** The total quantity  $q$  of flow per unit of time may be calculated from the discrete values of total head, without drawing a flow net.  $q$  is obtained for any area  $A$  that cuts the flow completely:

$$q = \int_A (v_x n_x + v_y n_y) dA \quad (19)$$

where  $n_x$  and  $n_y = x$  and  $y$  components of a unit vector normal to surface  $A$ , and  $v_x$  and  $v_y = x$  and  $y$  components of seepage velocity (Fig. 7). If the surface  $A$  is vertical, then

$$q = \int_A v_x dA = \int_A k_x \frac{\partial h}{\partial x} dA \quad (20)$$

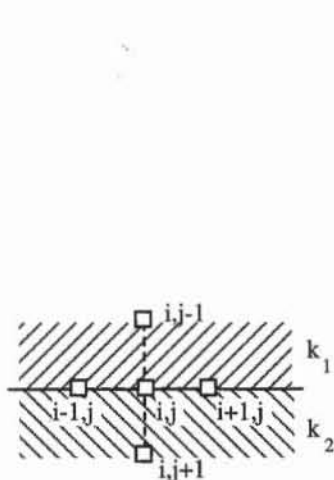


Figure 6 Interface between soils of different permeability.

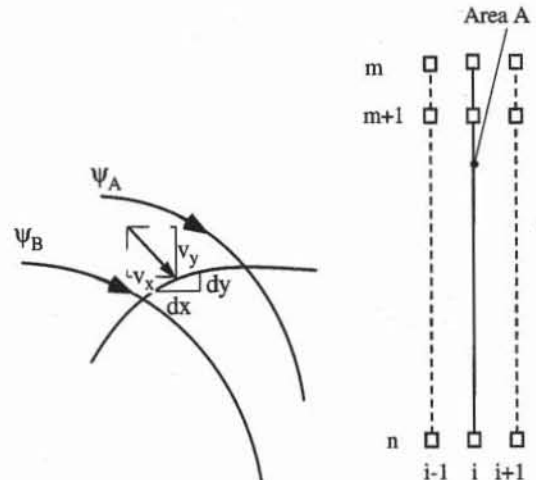


Figure 7 Flow lines and calculation of total quantity of seepage from discrete values of total head.

The area  $A$  of Eq. 20 may be selected arbitrarily, provided that it blocks the flow completely. In the case of the vertical section shown in Fig. 7 ( $m < n$ ), Eq. 20 may be integrated by using a trapezoidal rule:

$$q = \frac{\Delta x}{2} v_{i,m} + \Delta x \sum_{j=m+1}^{n-1} v_{i,j} + \frac{\Delta x}{2} v_{i,n} \quad (21)$$

where

$$v_{i,j} = \frac{k_x}{2\Delta x} (h_{i+1,j} - h_{i-1,j}) \quad (22)$$

Finally, the total quantity of seepage is

$$q = \frac{k_x}{4} \left[ h_{i+1,m} - h_{i-1,m} + 2 \sum_{j=m+1}^{n-1} (h_{i+1,j} - h_{i-1,j}) + h_{i+1,n} - h_{i-1,n} \right] \quad (23)$$

**Stream function and flow lines.** By definition, the stream function  $\psi(x, y)$  is

$$v_x = \frac{\partial \psi}{\partial y} \quad \text{and} \quad v_y = -\frac{\partial \psi}{\partial x} \quad (24)$$

The quantity of seepage  $dq$  through the small element with sides  $dx$  and  $dy$  in Fig. 7 is

$$dq = v_x dy - v_y dx = \frac{\partial \psi}{\partial y} dy + \frac{\partial \psi}{\partial x} dx = d\psi \quad (25)$$

Using Eq. 23, the quantity of seepage  $\Delta q$  between two nodes  $(i, j)$  and  $(i, j + 1)$  is

$$\begin{aligned} \Delta q &= \int_{i,j+1}^{i,j} v_x dy = \frac{k_x}{4} (h_{i+1,j} - h_{i-1,j} + h_{i+1,j+1} - h_{i-1,j+1}) \\ &= \Delta \psi = \psi_{i,j} - \psi_{i,j+1} \end{aligned} \quad (26)$$

The values of  $\psi_{i,j}$  are usually set equal to zero along one of the flow lines on the external boundary. After the calculation of total head  $h_{i,j}$ , the values of  $\psi_{i,j}$  in the interior are calculated with Eq. 26 by moving away from the flow line where  $\psi_{i,j} = 0$ . The stream function is constant on flow lines. To draw a flow net with equipotential and flow lines, it is useful to introduce the modified stream function  $\psi'_{i,j} = \psi_{i,j}/k$ . The flow net can be obtained by superimposing the contour lines of  $h_{i,j}$  and  $\psi'_{i,j}$  for identical value of contour interval.

### Solutions of Finite Difference Problems

The values of the total head at the grid points may be found by using either a direct method or an iterative method. These methods will be illustrated by considering the example in Fig. 8, which has no direct relation to a seepage problem. The Laplace equation holds inside the square region  $[0,1]$  by  $[0,1]$ . The function  $h(x,y)$  is prescribed on the boundary. It is equal to zero on the left, bottom, and

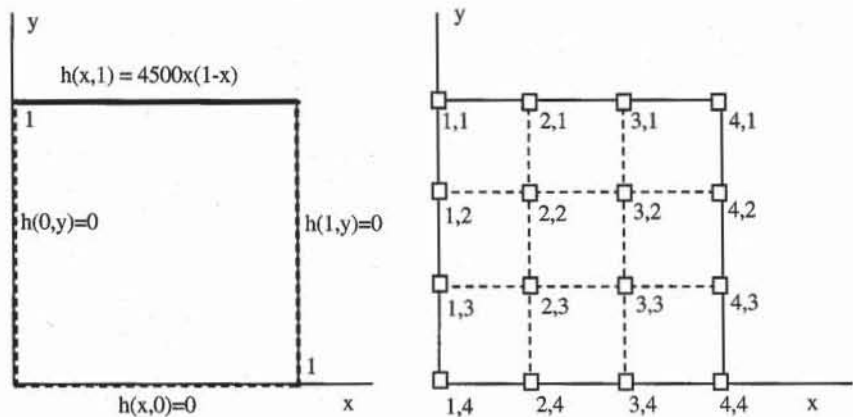


Figure 8 Example of boundary value problem.

right boundaries. It is equal to  $h(x) = 4500(1 - x)$  on the top boundary. The problem is to find the distribution of  $h$  inside the square region.

As shown in Fig. 8, the region is coarsely discretized with a grid with 16 nodes. The value of  $h$  is known at the 12 nodes at the boundaries. There are only four unknown values:  $h_{2,2}$ ,  $h_{2,3}$ ,  $h_{3,2}$ , and  $h_{3,3}$ .

**Direct method.** There are only two unknowns,  $h_{2,2}$  and  $h_{2,3}$ , owing to the symmetry about the line  $x = \frac{1}{2}$ , which implies that

$$h_{2,2} = h_{3,2} \quad \text{and} \quad h_{2,3} = h_{3,3} \quad (27)$$

These two unknowns  $h_{2,2}$  and  $h_{2,3}$  are found by solving the two linear equations

$$h_{2,2} = \frac{1}{4}(1000 + 0 + h_{2,3} + h_{2,2}) \quad \text{and} \quad h_{2,3} = \frac{1}{4}(0 + 0 + h_{2,2} + h_{2,3}) \quad (28)$$

The matrix equation corresponding to Eq. 28 is

$$\begin{pmatrix} 3 & -1 \\ -1 & 3 \end{pmatrix} \begin{pmatrix} h_{2,2} \\ h_{2,3} \end{pmatrix} = \begin{pmatrix} 1000 \\ 0 \end{pmatrix} \quad (29)$$

Its solutions are  $h_{2,2} = 375$  and  $h_{2,3} = 125$ . They are found by forming and solving a matrix equation, which is a lengthy operation for more complicated grids.

**Relaxation method.** The relaxation method is one of the solution methods for finite difference equations which is the most suited to spreadsheet calculations. In the relaxation method, the unknowns are initially assigned an arbitrary value. Then new values are calculated from old ones by iteratively using Eq. 28 until their final values satisfy Eq. 28 within a specified error tolerance.

For instance, the problem of Fig. 8 can be solved by relaxation as shown in Figs. 9 and 10. Nodes (1,1), (1,2), ... are represented by cells A1, A2, ..., respectively. The specified values of  $h$  are entered in cells A1, B1, C1, D1, A2, A3, A4, B4, C4, D4, D3, and D2. Equations 27 and 28 are defined in cells B2, B3, C2, and C3, where the function  $h$  is unknown.

As shown in Fig. 10, the relaxation solution gradually converges toward the exact solution within 100 iterations. The iterative calculations are activated by Options Calculation and by clicking on the iteration box. The number of itera-

	A	B	C	D
1	0	1000	1000	0
2	0	= $(B1+B3+A2+C2)/4$	= $B2$	0
3	0	= $(B2+B4+A3+C3)/4$	= $B3$	0
4	0	0	0	0

Figure 9 Formulas used for solving Eqs. 27 and 28 by relaxation.

	A	B	C	D
1	0	1000	1000	0
2	0	250	250	0
3	0	250	250	0
4	0	0	0	0

	A	B	C	D
1	0	1000	1000	0
2	0	375.2	375.1	0
3	0	125.1	125.1	0
4	0	0	0	0

A	B	C	D	
1	0	1000	1000	0
2	0	375	375	0
3	0	125	125	0
4	0	0	0	0

Figure 10 Results of relaxation calculation after 1, 5, and 100 iterations.

tions and the error tolerance can also be defined in the Calculation dialog box. When the iteration option is not activated, the error message "Cannot resolve circular references" should be displayed, indicating that the formulas of Fig. 9 are referring to each other's values.

### APPLICATION TO SEEPAGE PROBLEMS

Figure 11 defines a seepage problem with a sheet-pile wall. As shown in Fig. 12a, only the left half of the problem will be analyzed owing to the symmetry about the sheet-pile wall. The total head is  $h = 6$  m on AB. Owing to the problem symmetry,  $h = 3$  m on CD. In Fig. 12a the equipotential lines AB and CD, where the total head is constant, are dashed. The flow lines AED and BC which are followed by the water are solid. Figure 13 shows the spreadsheet representation of the seepage problem of Fig. 12a. The finite difference nodes are evenly spaced every 2 m in the  $x$  and  $y$  directions. There is a total of 91 nodes, 13 and 7 nodes in the  $x$  and  $y$  directions, respectively.

Figure 14 shows the formulas used in Fig. 12. The prescribed total head  $h = 6$  m is copied into cell range A2:M2, while  $h = 3$  m is copied into range M5:M8. The formulas for vertical impervious boundaries are entered in cell A3 and copied into range A4:A7. Those for right vertical boundaries are entered in cells M3 and M4. Equation 14 for horizontal impervious boundaries is entered in cell B8 and copied to C8:L8, Eq. 15 for a corner boundary is entered in cell A8 and Eq. 10 is entered in B3 and copied into range B3:L7.

The iterative calculations are turned on by using Options Calculations. The

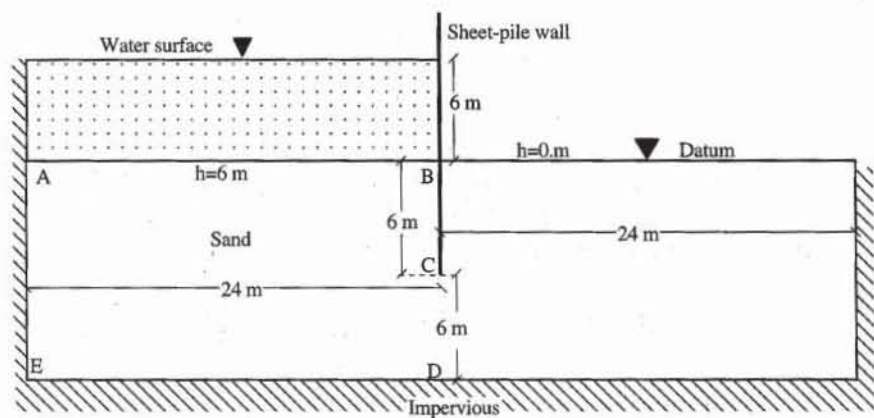


Figure 11 Definition of seepage problem with a sheet-pile wall.

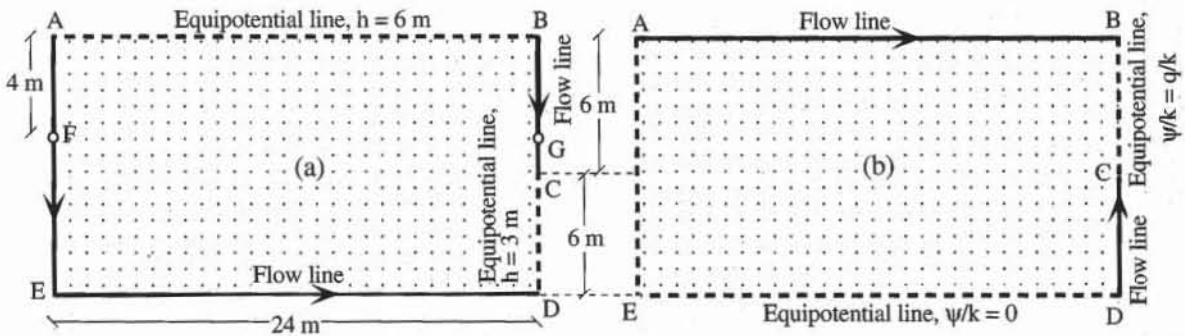


Figure 12 Boundary conditions for (a) original seepage problem and (b) complementary seepage problem.

	A	B	C	D	E	F	G	H	I	J	K	L	M
1	Total head (m)	Upstream head (m) = 6					Downstream head (m) = 3						
2	6.00	6.00	6.00	6.00	6.00	6.00	6.00	6.00	6.00	6.00	6.00	6.00	6.00
3	5.92	5.92	5.91	5.90	5.88	5.85	5.81	5.75	5.68	5.59	5.48	5.36	5.28
4	5.85	5.85	5.83	5.80	5.76	5.71	5.63	5.53	5.39	5.21	4.97	4.68	4.41
5	5.79	5.78	5.76	5.72	5.67	5.59	5.48	5.33	5.14	4.88	4.52	3.97	3.00
6	5.74	5.74	5.71	5.66	5.59	5.49	5.36	5.19	4.95	4.65	4.24	3.70	3.00
7	5.71	5.70	5.68	5.62	5.55	5.44	5.29	5.10	4.84	4.52	4.10	3.59	3.00
8	5.70	5.69	5.66	5.61	5.53	5.42	5.27	5.07	4.81	4.48	4.06	3.56	3.00
9	Quantity of flow per unit of time and unit of permeability = 3.2543												

Figure 13 Value of total head after 100 iterations.

results of the calculations after 100 iterations are shown in Fig. 13. The error after 100 iterations is less than 0.001 m. As shown in Figs. 13 and 14, the total quantity of seepage  $q$  (divided by permeability  $k$ ) is calculated in cell E9 by adapting Eq. 23 for the horizontal line FG passing at 4 m depth. Line FG cuts and blocks the flow completely.

Excel has several two- and three-dimensional capabilities to represent the distribution of total head. Figure 15 shows a two-dimensional contour plot, and Fig. 16 shows a three-dimensional surface plot. To get those plots, select the range

	A	B	C	D	J	K	L	M
1	Total head (m)				3			
2	$=\$F\$1$	$=\$F\$1$	$=\$F\$1$	$=\$F\$1$	$=\$F\$1$	$=\$F\$1$	$=\$F\$1$	$=\$F\$1$
3	$=(A2+A4+2*B3)/4$	$=(B2+A3+B4+C3)/4$	$=(C2+B3+C4+D3)/4$	$=(D2+C3+D4+E3)/4$	$=(J2+I3+J4+K3)/4$	$=(K2+J3+K4+L3)/4$	$=(L2+K3+L4+M3)/4$	$=(M2+M4+2*L3)/4$
4	$=(A3+A5+2*B4)/4$	$=(B3+A4+B5+C4)/4$	$=(C3+B4+C5+D4)/4$	$=(D3+C4+D5+E4)/4$	$=(J3+I4+J5+K4)/4$	$=(K3+J4+K5+L4)/4$	$=(L3+K4+L5+M4)/4$	$=(M3+M5+2*L4)/4$
5	$=(A4+A6+2*B5)/4$	$=(B4+A5+B6+C5)/4$	$=(C4+B5+C6+D5)/4$	$=(D4+C5+D6+E5)/4$	$=(J4+I5+J6+K5)/4$	$=(K4+J5+K6+L5)/4$	$=(L4+K5+L6+M5)/4$	$=\$J\$1$
6	$=(A5+A7+2*B6)/4$	$=(B5+A6+B7+C6)/4$	$=(C5+B6+C7+D6)/4$	$=(D5+C6+D7+E6)/4$	$=(J5+I6+J7+K6)/4$	$=(K5+J6+K7+L6)/4$	$=(L5+K6+L7+M6)/4$	$=\$J\$1$
7	$=(A6+A8+2*B7)/4$	$=(B6+A7+B8+C7)/4$	$=(C6+B7+C8+D7)/4$	$=(D6+C7+D8+E7)/4$	$=(J6+I7+J8+K7)/4$	$=(K6+J7+K8+L7)/4$	$=(L6+K7+L8+M7)/4$	$=\$J\$1$
8	$=(A7+B8)/2$	$=(A8+C8+2*B7)/4$	$=(B8+D8+2*C7)/4$	$=(C8+E8+2*D7)/4$	$=(I8+K8+2*J7)/4$	$=(J8+L8+2*K7)/4$	$=(K8+M8+2*L7)/4$	$=\$J\$1$

	H	I
9	Quantity of flow per unit of time and unit of permeability = $=(A3-A5+M3-M5+2*SUM(B3:L3)-2*SUM(B5:L5))/4$	

Figure 14 Formulas used in Fig. 13.

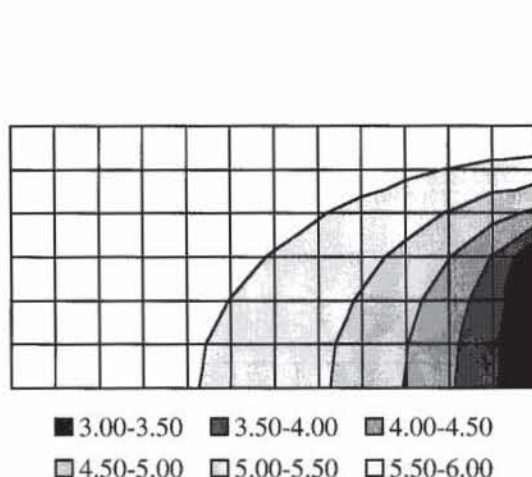


**Figure 15** Two-dimensional contour representation of total head for seepage problem of Fig. 11.

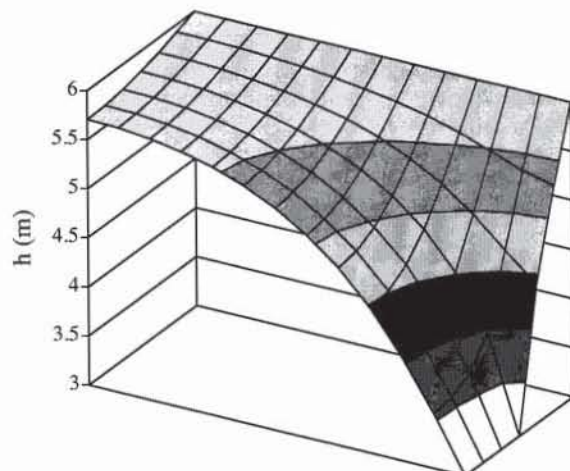


**Figure 16** Three-dimensional surface representation of total head for seepage problem of Fig. 11.

A2:M2 with the mouse, and select the appropriate three-dimensional chart type by using the Chart Wizard. Change the scale of the third axis to select the contour values. Inverse the second axis to display the contour in the right upward direction. Add the contour values by using the Insert Legend option. As shown in Fig. 17, the equipotential lines, which are the lines along which the total head is a constant, can be drawn using the three-dimensional chart type without the filling option.

The water pressure  $u$  is related to the total head  $h$  through

$$u = \gamma_w(h - y) \quad (30)$$

where  $\gamma_w$  is the water unit weight and  $y$  is the elevation with respect to the datum. The distribution of water pressure which corresponds to the total head in Fig. 15 is shown in Fig. 17. Figure 18 shows the formulas that are used to calculate the water pressure from the total head and the vertical mesh spacing. As shown in Fig. 17, the water pressure, which is hydrostatic away from the pile, becomes lower in the vicinity of the pile, owing to the water flow.

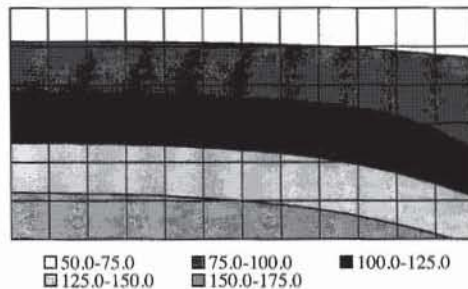


**Figure 17** Distribution of water pressure (kPa) in seepage problem of Fig. 11.

	A	F	G
1 0	Water pressure (kPa)	Vertical mesh spacing (m)= 2	
1 1	=9.8*(A2+(ROW(A11)-ROW(\$A\$11))*\$G\$10)	=9.8*(F2+(ROW(F11)-ROW(\$A\$11))*\$G\$10)	=9.8*(G2+(ROW(G11)-ROW(\$A\$11))*\$G\$10)
1 2	=9.8*(A3+(ROW(A12)-ROW(\$A\$11))*\$G\$10)	=9.8*(F3+(ROW(F12)-ROW(\$A\$11))*\$G\$10)	=9.8*(G3+(ROW(G12)-ROW(\$A\$11))*\$G\$10)
1 3	=9.8*(A4+(ROW(A13)-ROW(\$A\$11))*\$G\$10)	=9.8*(F4+(ROW(F13)-ROW(\$A\$11))*\$G\$10)	=9.8*(G4+(ROW(G13)-ROW(\$A\$11))*\$G\$10)
1 4	=9.8*(A5+(ROW(A14)-ROW(\$A\$11))*\$G\$10)	=9.8*(F5+(ROW(F14)-ROW(\$A\$11))*\$G\$10)	=9.8*(G5+(ROW(G14)-ROW(\$A\$11))*\$G\$10)
1 5	=9.8*(A6+(ROW(A15)-ROW(\$A\$11))*\$G\$10)	=9.8*(F6+(ROW(F15)-ROW(\$A\$11))*\$G\$10)	=9.8*(G6+(ROW(G15)-ROW(\$A\$11))*\$G\$10)
1 6	=9.8*(A7+(ROW(A16)-ROW(\$A\$11))*\$G\$10)	=9.8*(F7+(ROW(F16)-ROW(\$A\$11))*\$G\$10)	=9.8*(G7+(ROW(G16)-ROW(\$A\$11))*\$G\$10)
1 7	=9.8*(A8+(ROW(A17)-ROW(\$A\$11))*\$G\$10)	=9.8*(F8+(ROW(F17)-ROW(\$A\$11))*\$G\$10)	=9.8*(G8+(ROW(G17)-ROW(\$A\$11))*\$G\$10)

Figure 18 Formulas used to calculate the water pressure (kPa) of Fig. 17 from the total head of Fig. 13.

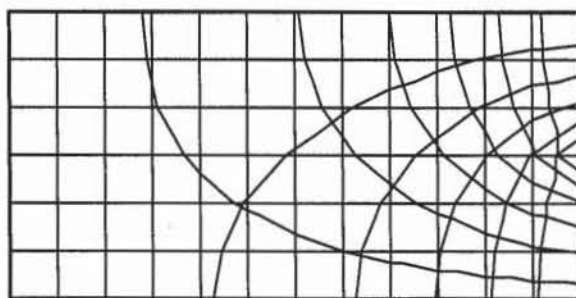


Figure 19 Flow net for seepage problem of Fig. 11.

As shown in Fig. 19, the flow lines, which represent the water trajectory, can be obtained by Eq. 26. They can also be obtained by using the same method as for the equipotential lines, but by solving the complementary seepage problem (Fig. 20). In the complementary seepage problem, boundary flow lines become equipotential boundaries, while equipotential boundaries become flow lines. The total head  $h(x,y)$  is also replaced by the modified flow function  $\psi' = \psi(x, y)/k$ , which must also obey the Laplace equation (i.e., Eq. 2). Therefore, the flow lines of the initial problem are transformed into prescribed  $\psi'$ -value lines. It is convenient to set  $\psi'$  equal to zero on one of those lines and  $q/k$  on the other line, where  $q$  is the total seepage flow, calculated using Eq. 23.

Figure 20 shows the value of  $\psi'$  as calculated by the formulas of Fig. 21. As shown in Fig. 19, the flow lines, where  $\psi'$  is constant, can be plotted by using two-dimensional contours. The flow net is obtained by manually superimposing the two-dimensional contours of  $h$  and  $\psi'$  with identical interval values along the third axis. One can verify that the flow lines intersect the equipotential lines at right angles and that these lines form curvilinear squares. The ratio between the number  $N_f$  of flow channels and the number  $N_d$  of equipotential drops should also be equal to  $q/(k \Delta h)$ , where  $q$  is the seepage flow calculated from Eq. 23 and  $\Delta h$  is the total head drop.

The finite difference technique described earlier can be applied to solve many practical seepage problems. Some examples of seepage problems are given in the exercises. In the case of thin sheet piles as shown in Fig. 22, an extra column of nodes must be inserted at the location of the sheet pile. As shown in Fig. 23, this additional column is required to have different total head on the front and back of the sheet pile. Beneath the sheet pile, the nodes are set to have the same total head. As shown in Fig. 24, this additional row unfortunately distorts the flow net in the vicinity of the sheet pile. This distortion was removed in

	A	B	C	D	E	F	G	H	I	J	K	L	M
<b>19</b>	Flow lines (complementary problem)				Upstream value (m) = 3.2543				Downstream value (m) = 0				
<b>20</b>	3.25	3.17	3.08	2.98	2.86	2.71	2.52	2.29	2.00	1.63	1.17	0.62	0.00
<b>21</b>	3.25	3.17	3.09	2.99	2.87	2.73	2.55	2.32	2.04	1.67	1.21	0.65	0.00
<b>22</b>	3.25	3.18	3.10	3.01	2.91	2.78	2.62	2.41	2.15	1.81	1.36	0.77	0.00
<b>23</b>	3.25	3.19	3.13	3.06	2.97	2.87	2.73	2.56	2.34	2.05	1.66	1.06	0.00
<b>24</b>	3.25	3.21	3.17	3.12	3.05	2.98	2.89	2.77	2.61	2.41	2.15	1.83	1.53
<b>25</b>	3.25	3.23	3.21	3.18	3.15	3.11	3.06	3.00	2.92	2.82	2.70	2.56	2.48
<b>26</b>	3.25	3.25	3.25	3.25	3.25	3.25	3.25	3.25	3.25	3.25	3.25	3.25	3.25

Figure 20 Values of  $\psi'$  after 100 iterations.

	A	B	C	D	K	L	M
<b>20</b>	$=\$H\$19$	$=(A20+C20+2*B21)/4$	$=(B20+D20+2*C21)/4$	$=(C20+E20+2*D21)/4$	$=(J20+L20+2*K21)/4$	$=(K20+M20+2*L21)/4$	$=\$L\$19$
<b>21</b>	$=\$H\$19$	$=(B20+A21+B22+C21)/4$	$=(C20+B21+C22+D21)/4$	$=(D20+C21+D22+E21)/4$	$=(K20+J21+K22+L21)/4$	$=(L20+K21+L22+M21)/4$	$=\$L\$19$
<b>22</b>	$=\$H\$19$	$=(B21+A22+B23+C22)/4$	$=(C21+B22+C23+D22)/4$	$=(D21+C22+D23+E22)/4$	$=(K21+J22+K23+L22)/4$	$=(L21+K22+L23+M22)/4$	$=\$L\$19$
<b>23</b>	$=\$H\$19$	$=(B22+A23+B24+C23)/4$	$=(C22+B23+C24+D23)/4$	$=(D22+C23+D24+E23)/4$	$=(K22+J23+K24+L23)/4$	$=(L22+K23+L24+M23)/4$	$=\$L\$19$
<b>24</b>	$=\$H\$19$	$=(B23+A24+B25+C24)/4$	$=(C23+B24+C25+D24)/4$	$=(D23+C24+D25+E24)/4$	$=(K23+J24+K25+L24)/4$	$=(L23+K24+L25+M24)/4$	$=(M23+M25+2*L24)/4$
<b>25</b>	$=\$H\$19$	$=(B24+A25+B26+C25)/4$	$=(C24+B25+C26+D25)/4$	$=(D24+C25+D26+E25)/4$	$=(K24+J25+K26+L25)/4$	$=(L24+K25+L26+M25)/4$	$=(M24+M26+2*L25)/4$
<b>26</b>	$=\$H\$19$	$=\$H\$19$	$=\$H\$19$	$=\$H\$19$	$=\$H\$19$	$=\$H\$19$	$=\$H\$19$

Figure 21 Formulas used in Fig. 20.

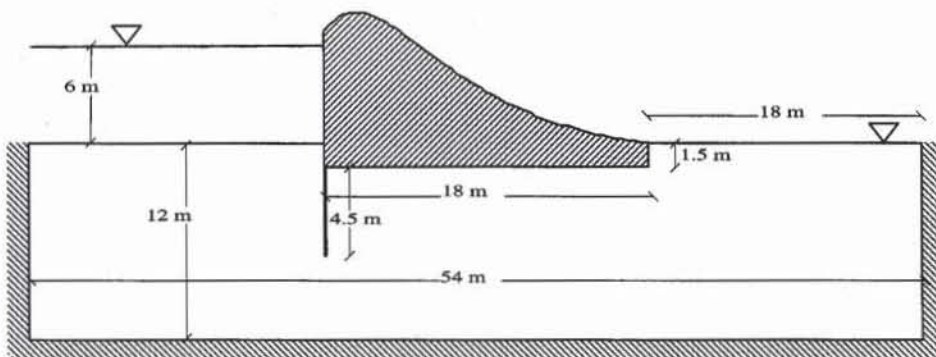


**Figure 22** Seepage problem with a cofferdam and a sheet-pile wall.

Fig. 25 after replotted the numerical results of Fig. 24 with a more advanced contouring program. Figures 26 and 27 show the distributions of water pressure on the bottom surface of the cofferdam and on the front and back of the sheet pile wall.

## LIMITATIONS

The present method is limited to confined seepage problems for which the boundary conditions have known positions. In its present form it does not apply to unconfined seepage problems such as those in earth dams, where the free surface is undefined. The determination of the position of unknown boundaries with finite difference is possible but requires that additional equations be solved.

One of the major limitations of the finite difference method is the difficulty encountered in describing curved boundary conditions and complicated layer geometries. For this reason, another numerical technique, referred to as the finite element method, is often preferred. Seepage problems of infinite size, such as cofferdams on soil strata extending to infinity, are also difficult to analyze by using a grid of finite size. In this case the infinite size can be approximated by taking a length equal to three to six times the stratum thickness. It is recommended this length be varied in order to assess its effects on the solution of the seepage problem.

## REVIEW QUESTIONS

1. What is the purpose of the finite difference method? How is it applied to confined seepage problems?
2. What is the partial differential equation that controls the distribution of total head for anisotropic and isotropic permeability?
3. What is the principal numerical technique used to solve the equations of finite difference methods?
4. Why does the grid spacing control the accuracy of the solution of a seepage problem with finite difference?
5. How do you represent curved boundaries in finite difference methods?
6. What is the main limitation of finite difference when dealing with seepage problems?

	A	L	M	N	O	Z	AA	AL
2	=\$G\$1	=\$G\$1	=\$G\$1				=\$L\$1	=\$L\$1
3	=(A2+A4+2*B3)/4	=(L2+K3+L4+M3)/4	=(M2+M4+2*L3)/4	=(O3+N4)/2	=(N3+P3+2*O4)/4	=(Y3+AA3+2*Z4)/4	=(AA4+AB3+AA2/2+Z3/2)/3	=(AL2+AL4+2*AK3)/4
4	=(A3+A5+2*B4)/4	=(L3+K4+L5+M4)/4	=(M3+M5+2*L4)/4	=(N3+N5+2*O4)/4	=(O3+N4+O5+P4)/4	=(Z3+Y4+Z5+AA4)/4	=(AA3+Z4+AA5+AB4)/4	=(AL3+AL5+2*AK4)/4
5	=(A4+A6+2*B5)/4	=(L4+K5+L6+M5)/4	=(M4+M6+2*L5)/4	=(N4+N6+2*O5)/4	=(O4+N5+O6+P5)/4	=(Z4+Y5+Z6+AA5)/4	=(AA4+Z5+AA6+AB5)/4	=(AL4+AL6+2*AK5)/4
6	=(A5+A9+2*B6)/4	=(L5+K6+L7+M6)/4	=(M5+M7+2*L6)/4	=(N5+N7+2*O6)/4	=(O5+N6+O7+P6)/4	=(Z5+Y6+Z7+AA6)/4	=(AA5+Z6+AA7+AB6)/4	=(AL5+AL7+2*AK6)/4
7	=(A6+A10+2*B7)/4	=(L6+K7+L8+M7)/4	=(N7+L7+M8+O7)/4	=M7	=(O6+N7+O8+P7)/4	=(Z6+Y7+Z8+AA7)/4	=(AA6+Z7+AA8+AB7)/4	=(AL6+AL8+2*AK7)/4
8	=(A5+A9+2*B8)/4	=(L7+K8+L9+M8)/4	=(M7+L8+M9+O8)/4	=M8	=(O7+N8+O9+P8)/4	=(Z7+Y8+Z9+AA8)/4	=(AA7+Z8+AA9+AB8)/4	=(AL7+AL9+2*AK8)/4
9	=(A6+A10+2*B9)/4	=(L8+K9+L10+M9)/4	=(M8+L9+M10+O9)/4	=M9	=(O8+N9+O10+P9)/4	=(Z8+Y9+Z10+AA9)/4	=(AA8+Z9+AA10+AB9)/4	=(AL8+AL10+2*AK9)/4
10	=(A9+B10)/2	=(K10+M10+2*L9)/4	=(L10+O10+2*M9)/4	=M10	=(N10+P10+2*O9)/4	=(Y10+AA10+2*Z9)/4	=(Z10+AB10+2*AA9)/4	=(AL9+AK10)/2

Figure 23 Formulas used in solving the seepage problem of Fig. 22.

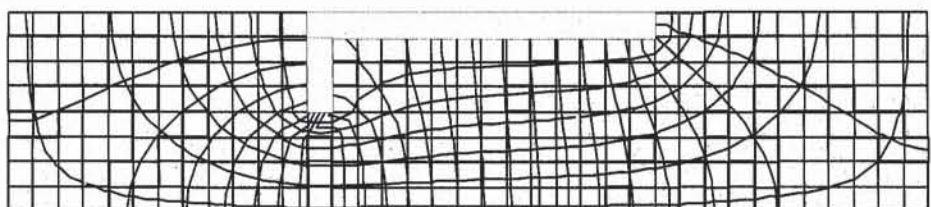


**Figure 24** Flow net of the seepage problem in Fig. 22.

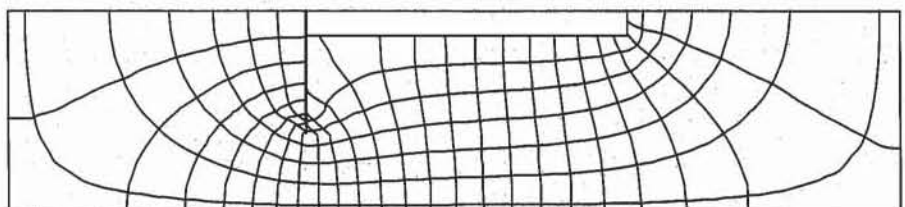


**Figure 25** Flow net of Fig. 24 redrawn with a more sophisticated contouring package.

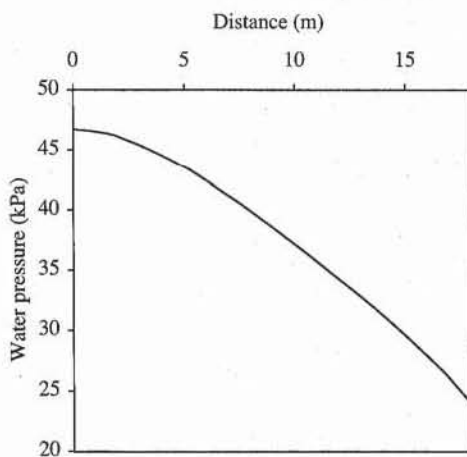


**Figure 26** Distribution of water pressure along the horizontal surface of the cofferdam of Fig. 22.

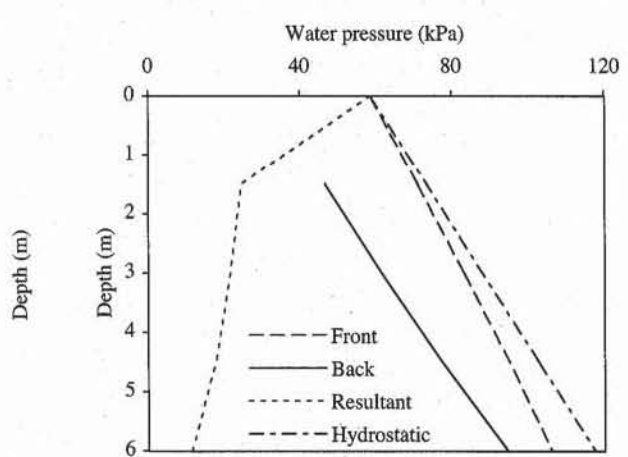
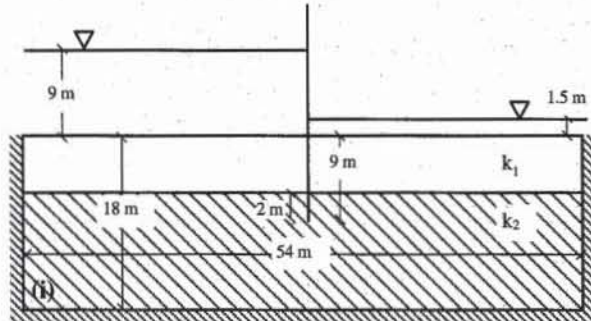
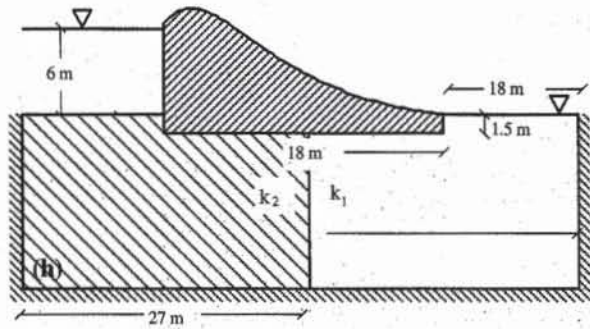
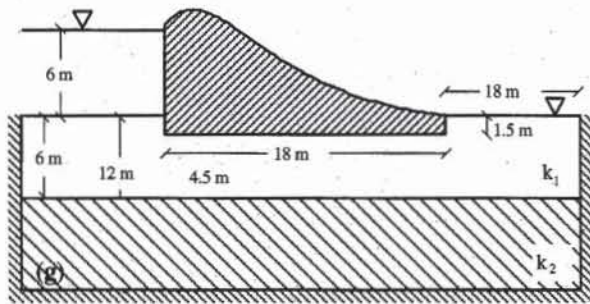


**Figure 27** Distribution of water pressure on the front and back of the sheet pile of Fig. 22.

## EXERCISES

1. Generalize Eq. 9 in the case of non-evenly spaced nodes.
2. Calculate the hydraulic gradient vector in terms of discrete head values.
3. Find the distribution of total head and flow net for one of the problems (a) to (f) in Exercise 2 of Chapter 4-4.
4. Find the distribution of total head and flow net for one of the problems (g), to (i) shown below.
5. Find the distribution of pressures on one of the structures (sheet-pile wall and/or cofferdam) defined in Exercises 3 and 4.
6. Plot the water pressure applied to the structure for one of the problems of Exercises 3 and 4.



7. Calculate the maximum hydraulic gradient and its location for one of the problems of Exercises 3 and 4.
  8. Compare the distributions of total head obtained by using two different grid spacings for one of the problems of Exercises 3 and 4.
  9. Compare the distribution of total head obtained by the electrical analogy methods and the finite difference method for one of the problems in Exercise 3.

# 5

# Stress-Strain-Strength Properties

- 5-1** Stress in soils
- 5-2** Strain in soils
- 5-3** Stress-strain relations
- 5-4** Laboratory tests for determination of stress-strain-strength of soils
- 5-5** Elastic properties of soils

# 5-1 Stress in Soils

Departing from solid mechanics, soil mechanics defines the concept of stress in a slightly different way to consider the particulate structure of soils. Here we review the concepts of Cauchy and Mohr stresses for describing the stress-strain response of soils in laboratory experiments.

## BODY FORCES AND CONTACT FORCES

As illustrated in Fig. 1a, a soil mass  $B$  is made of soil particles of various sizes. The voids between the grains may be partially or fully saturated with water. This solid–water–air system is considered to be homogeneous. The forces acting on element  $A$  of Fig. 1b are divided into two categories:

- The body forces acting on the volume of  $A$
- The surface forces acting on the surface of  $A$

### Body Forces

In soils, body forces are created by earth gravity, buoyancy, and water seepage. Their intensity is proportional to the volume on which they act. The resultant body force  $\mathbf{F}$  acting on volume  $V$  is the volume integral of the body force  $\mathbf{X}$  per unit volume:

$$\mathbf{F} = \int_V \mathbf{X} dv \quad (1)$$

The  $X$  and  $Y$  components of  $\mathbf{X}$  have the dimension of force per unit volume.  $[X] = [Y] = ML^{-2}T^{-2}$ , where  $M$ ,  $L$ , and  $T$  indicate the dimension of mass, length, and time, respectively. The body force of the earth gravity is

$$X = 0, \quad Y = -\rho g \quad (2)$$

where  $g$  is the earth gravitational acceleration (i.e.,  $g = 9.81 \text{ m/s}^2$ ) and  $\rho$  is the mass per unit volume. If the body is immersed in water,  $X$  for buoyancy is

$$X = 0, \quad Y = \rho_w g \quad (3)$$

where  $\rho_w$  is the unit mass of water. If water seeps through the soil interstices,  $X$  for seepage is

$$X = \rho_w g i_x, \quad Y = \rho_w g i_y \quad (4)$$

where  $i_x$  and  $i_y$  are the  $x$  and  $y$  components of hydraulic gradient  $i$ .

### Contact Forces

The small element  $A$  of Fig. 1b is not only subjected to body forces, but also interacts with its exterior through its surface. Consider the surface  $\Delta S_n$  of Fig. 1b with unit normal vector  $\mathbf{n}$  pointing inside the element. The exterior of  $A$  exerts the force  $\Delta \mathbf{F}$  and moment  $\Delta \mathbf{m}$  on surface  $\Delta S_n$ . Both  $\Delta \mathbf{F}$  and  $\Delta \mathbf{m}$  are functions of  $\Delta S_n$  and  $\mathbf{n}$ . As  $\Delta S_n$  tends toward zero,  $\Delta \mathbf{F}/\Delta S_n$  is assumed to tend toward the vector  $\mathbf{T}_n$ , whereas  $\Delta \mathbf{m}/\Delta S_n$  is assumed to become negligible. The subscript  $n$  of  $\Delta S_n$  and  $\mathbf{T}_n$  denotes the normal vector  $\mathbf{n}$ .  $\mathbf{T}_n$ , called the *stress (or traction) vector*, represents the force per unit area acting on surface  $\Delta S_n$ .

As shown in Fig. 2, on the vertical surface  $\Delta S_x$  with  $(n_x, n_y) = (1, 0)$ , the components of the stress vector  $\mathbf{T}_x$  are  $\sigma_{xx}$  and  $\tau_{xy}$ . On the horizontal surface  $\Delta S_y$  with  $(n_x, n_y) = (0, 1)$ , the components of the stress vector  $\mathbf{T}_y$  are  $\tau_{yx}$  and  $\sigma_{yy}$ . These stress components are tabulated in the following matrix:

	Component of stress	
	$x$	$y$
Surface normal to $x$	$\sigma_{xx}$	$\tau_{xy}$
Surface normal to $y$	$\tau_{yx}$	$\sigma_{yy}$

The components  $\sigma_{xx}$  and  $\sigma_{yy}$  are called *normal stresses*, whereas  $\tau_{xy}$  and  $\tau_{yx}$  are called *shear stresses*. The dimension of  $\sigma_{xx}$ ,  $\sigma_{yy}$ ,  $\tau_{xy}$ , and  $\tau_{yx}$  is force per unit area (i.e.,  $[\sigma_{xx}] = [\sigma_{yy}] = [\tau_{xy}] = [\tau_{yx}] = ML^{-1}T^{-2}$ ).  $\sigma_{xx}$  and  $\sigma_{yy}$  are also denoted as  $\sigma_x$  and  $\sigma_y$ . The physical origins of contact forces in soils are discussed later.

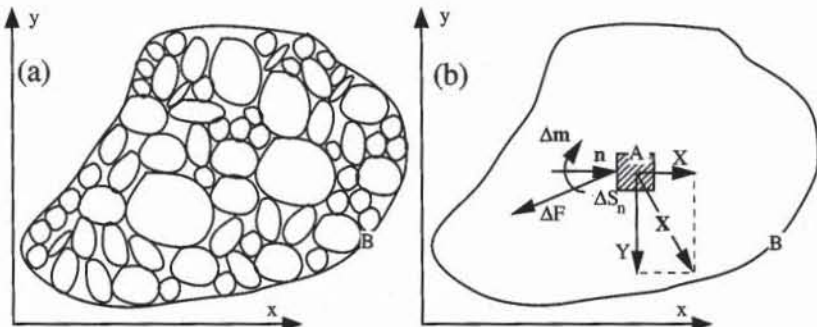
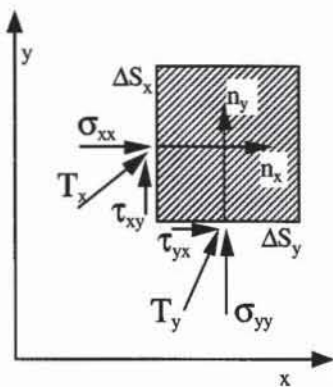


Figure 1 (a) Two-dimensional representation of a soil mass and (b) its idealization.



**Figure 2** Stress vectors and their components on horizontal and vertical surfaces.

### Equilibrium of Forces and Moments

If the soil mass  $B$  of Fig. 1b is in a static equilibrium, the total force that results from body forces on volume  $V$  and contact forces on the surface  $S$  enclosing volume  $V$  is equal to zero:

$$\int_S \mathbf{T}_n dS + \int_V \mathbf{X} dV = 0 \quad (5)$$

where  $\mathbf{T}_n$  is the stress vector acting on surface  $dS$  with normal vector  $\mathbf{n}$ . The total torque about the space origin resulting from body and surface forces is also equal to zero:

$$\int_S \mathbf{r} \otimes \mathbf{T}_n dS + \int_V \mathbf{r} \otimes \mathbf{X} dV = 0 \quad (6)$$

where  $\mathbf{r}$  is a position vector and  $\otimes$  is the cross product between two vectors.

### Equations of Stress Equilibrium

In general,  $\sigma_x$ ,  $\sigma_y$ ,  $\tau_{yx}$ , and  $\tau_{xy}$  are not constant throughout the soil mass but vary with the  $x$  and  $y$  coordinates. By applying the equilibrium of forces (i.e., Eq. 5) and moments (i.e., Eq. 6) to the small element of Fig. 3, it can be shown that  $\sigma_x$ ,  $\sigma_y$ ,  $\tau_{yx}$ , and  $\tau_{xy}$  obey the following equations:

$$\frac{\partial \sigma_x}{\partial x} + \frac{\partial \tau_{xy}}{\partial y} = X \quad (7)$$

$$\frac{\partial \tau_{yx}}{\partial x} + \frac{\partial \sigma_y}{\partial y} = Y \quad (8)$$

$$\tau_{xy} = \tau_{yx} \quad (9)$$

Equations 7 to 9 are called the *stress-equilibrium equations*. Equation 9 implies that there are only three independent stress components:  $\sigma_x$ ,  $\sigma_y$ , and  $\tau_{xy}$ . The stress-equilibrium equations are widely used in soil mechanics.

## CAUCHY REPRESENTATION OF STRESS

In the Cauchy representation, the stress vector is defined in a fixed  $x$ - and  $y$ -coordinate system. The stress vector has the same sign convention as the coordinates. In contrast to solid mechanics, soil mechanics imposes that the unit vector  $\mathbf{n}$  normal to the surface points inward to the material surface (see Fig. 4).

### Stress Acting on an Inclined Surface

Consider the uniform stress state within the material element of Fig. 4. By definition, the uniform stress state implies that  $\sigma_x$ ,  $\sigma_y$ , and  $\tau_{xy}$  are independent of  $x$  and  $y$ . There are no body forces (i.e.,  $X = Y = 0$ ) in Eqs. 7 and 8. As shown in Fig. 4, the stresses  $\sigma_{nx}$  and  $\sigma_{ny}$  acting on surface  $AB$  inclined at angle  $\theta$  with respect to the  $x$  axis can be calculated from  $\sigma_x$ ,  $\sigma_y$ , and  $\tau_{xy}$  by writing the equilibrium of forces acting on element  $AOB$  in the  $x$  and  $y$  directions:

$$\sigma_x AB \sin \theta + \tau_{xy} AB \cos \theta + AB \sigma_{nx} = 0 \quad (10)$$

$$\sigma_y AB \cos \theta + \tau_{xy} AB \sin \theta + AB \sigma_{ny} = 0 \quad (11)$$

Because the unit vector pointing inside the surface  $AB$  is  $\mathbf{n} = (n_x, n_y) = (-\sin \theta, -\cos \theta)$ , the stresses  $\sigma_{nx}$  and  $\sigma_{ny}$  acting on the surface with unit vector  $\mathbf{n}$  can be obtained by multiplying the stress matrix by  $\mathbf{n}$ :

$$\begin{pmatrix} \sigma_{nx} \\ \sigma_{ny} \end{pmatrix} = \begin{pmatrix} \sigma_x & \tau_{xy} \\ \tau_{xy} & \sigma_y \end{pmatrix} \begin{pmatrix} n_x \\ n_y \end{pmatrix} \quad (12)$$

Note that the orientation of  $\mathbf{n}$  with respect to the surface implies that  $\sigma_x$  and  $\sigma_y$  are positive for compression and negative for tension. This sign convention eliminates a lot of negative signs in soils, which, in contrast to metals, undergo mostly compressive stress.

### Principal Stress

By definition, the principal surfaces are free of shear stress. The stress vector acting on principal surfaces is thus collinear to their normal unit vector  $(n_x, n_y)$ .

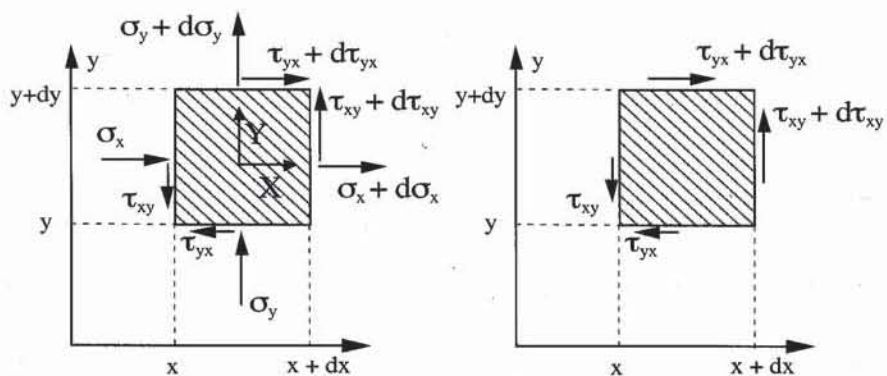


**Figure 3** Small element used for the calculation of equilibrium of (a) forces and (b) moment.

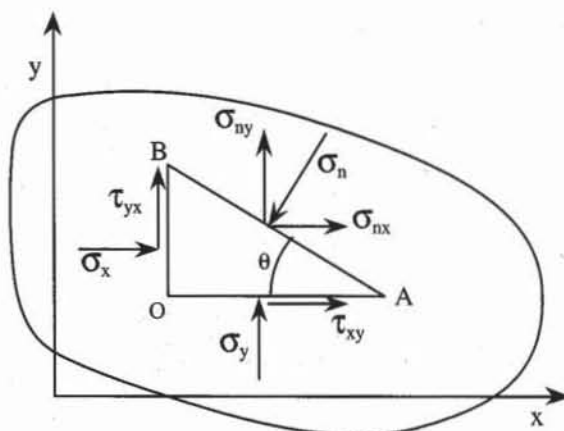


**Figure 4** Determination of stress acting on segment AB.

Their direction is found by solving the following eigenvalue problem:

$$\begin{pmatrix} \sigma_x & \tau_{xy} \\ \tau_{xy} & \sigma_y \end{pmatrix} \begin{pmatrix} n_x \\ n_y \end{pmatrix} = \sigma \begin{pmatrix} n_x \\ n_y \end{pmatrix} \quad (13)$$

where  $\sigma$  is the principal stress value.  $\sigma$  is obtained by solving the following quadratic equation:

$$\sigma^2 - \sigma(\sigma_x + \sigma_y) + \sigma_x\sigma_y - \tau_{xy}^2 = 0 \quad (14)$$

There are always two principal stresses: the major and minor principal stresses:

$$\sigma_1 = \frac{1}{2}(\sigma_x + \sigma_y) + \sqrt{\frac{1}{4}(\sigma_x - \sigma_y)^2 + \tau_{xy}^2} \quad (15)$$

$$\sigma_2 = \frac{1}{2}(\sigma_x + \sigma_y) - \sqrt{\frac{1}{4}(\sigma_x - \sigma_y)^2 + \tau_{xy}^2}$$

The principal stresses are equal when  $\sigma_x = \sigma_y$  and  $\tau_{xy} = 0$ , which is the hydrostatic pressure case. The orientation of the principal surfaces is found by setting  $\sigma$  equal to  $\sigma_1$  or  $\sigma_2$  in Eq. 13 and by solving for  $n_x$  and  $n_y$ :

$$\frac{n_y}{n_x} = \tan \theta = \frac{\sigma_x - \sigma}{\tau_{xy}} \quad (16)$$

where  $\theta$  is the inclination of  $\mathbf{n}$  with respect to the horizontal direction. Equation 16 does not apply to hydrostatic pressure, for which any direction is principal.

## MOHR REPRESENTATION OF STRESS

Mohr and Cauchy represent stresses in different ways. The Mohr representation, which is the most commonly used in geotechnical engineering, provides us with a graphical determination of stresses. In contrast to Cauchy, who uses fixed axes, Mohr defines the stresses in reference to the surface on which they act.

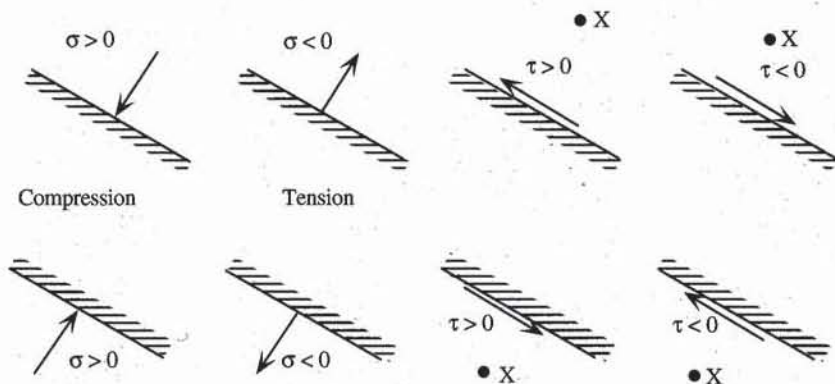


**Figure 5** Sign convention for Mohr representation of stresses in soil mechanics.

### Sign Convention for Stress

Figure 5 defines the sign convention of Mohr in soil mechanics. This sign convention is different from that of solid mechanics. Because normal stresses are usually compressive in soils, they are assigned a positive sign to avoid the profusion of negative signs. As shown in Fig. 5, compressive normal stresses are positive and tensile normal stresses are negative. The sign convention for shear stress  $\tau$  is more arbitrary than for normal stress. As shown in Fig. 5, if  $\tau$  acting on the surface produces a clockwise moment about a point  $X$  located at the exterior of the material surface,  $\tau$  is positive. If the moment about the point  $X$  is counterclockwise,  $\tau$  is negative. As shown in Fig. 5, the Mohr stresses on surfaces facing each other are identical, although the corresponding stress vectors have opposite direction.

### Stress Acting on an Inclined Surface

Consider the uniform state of stress within the element of Fig. 6. The stresses  $\sigma$  and  $\tau$  acting on  $AB$  can be calculated from  $\sigma_x$ ,  $\sigma_y$ , and  $\tau_{xy}$ , by writing the equilib-

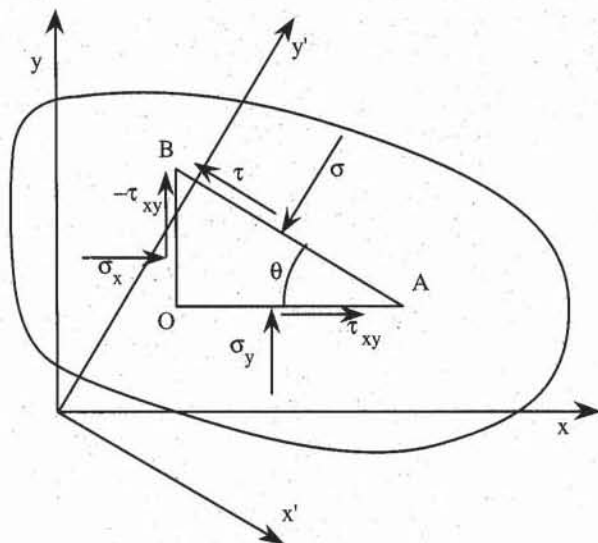


**Figure 6** Determination of stress acting on segment  $AB$ .

rium of forces in the  $x'$  and  $y'$  directions, which are parallel and normal to segment  $AB$ , respectively. As shown in Fig. 6, in the Mohr representation, the shear stresses acting on surfaces  $OA$  and  $OB$  must have opposite signs. The equilibrium of forces acting on element  $AOB$  in the  $y'$  direction is

$$\sigma_x OB \sin \theta + \tau_{xy} OB \cos \theta + \sigma_y OA \cos \theta + \tau_{xy} OA \sin \theta - AB\sigma = 0 \quad (17)$$

Note that the shear stress acting on the vertical surface is negative in the Mohr representation but produces a positive force in the  $y'$  direction. The equilibrium of forces in the  $x'$  direction implies that

$$\sigma_x OB \cos \theta - \tau_{xy} OB \sin \theta - \sigma_y OA \sin \theta + \tau_{xy} OA \cos \theta - AB\tau = 0 \quad (18)$$

From Fig. 6 we have

$$AO = AB \cos \theta \quad \text{and} \quad BO = AB \sin \theta \quad (19)$$

Using Eq. 19, Eqs. 17 and 18 become

$$\sigma = \sigma_x \sin^2 \theta + \sigma_y \cos^2 \theta + 2\tau_{xy} \sin \theta \cos \theta \quad (20)$$

$$\tau = \sigma_x \sin \theta \cos \theta - \sigma_y \sin \theta \cos \theta + \tau_{xy} (\cos^2 \theta - \sin^2 \theta)$$

Using the relations:

$$\sigma_x = \frac{1}{2}(\sigma_x + \sigma_y) + \frac{1}{2}(\sigma_x - \sigma_y) \quad \text{and} \quad \sigma_y = \frac{1}{2}(\sigma_x + \sigma_y) - \frac{1}{2}(\sigma_x - \sigma_y) \quad (21)$$

Eq. 20 becomes

$$\sigma = \frac{1}{2}(\sigma_x + \sigma_y) + \frac{1}{2}(\sigma_x - \sigma_y) \cos 2\theta + \tau_{xy} \sin 2\theta \quad (22)$$

$$\tau = \frac{1}{2}(\sigma_x - \sigma_y) \sin 2\theta + \tau_{xy} \cos 2\theta$$

### Mohr Circle

When  $\theta$  varies from  $-90^\circ$  to  $90^\circ$ ,  $\sigma$  and  $\tau$  of Eq. 22 describe a circle in the space  $(\sigma, \tau)$ , which has the equation

$$[\sigma - \frac{1}{2}(\sigma_x + \sigma_y)]^2 + \tau^2 = \frac{1}{4}(\sigma_x - \sigma_y)^2 + \tau_{xy}^2 \quad (23)$$

The  $(\sigma, \tau)$  space is called the *Mohr stress space*. As shown in Fig. 7, the circle of Eq. 23 is called the *Mohr circle*. It is centered at position  $(\sigma_m, 0)$  on the  $\sigma$  axis and has radius  $R$ :

$$\sigma_m = \frac{1}{2}(\sigma_x + \sigma_y) \quad \text{and} \quad R = \sqrt{\frac{1}{4}(\sigma_x - \sigma_y)^2 + \tau_{xy}^2} \quad (24)$$

The stress states  $(\sigma_x, -\tau_{xy})$  and  $(\sigma_y, \tau_{xy})$  are represented by points  $B$  and  $A$  in the Mohr space of Fig. 7, respectively. Points  $A$  and  $B$  are diametrically opposite on the Mohr circle and are used to construct the Mohr circle. The circle diameter is  $AB$ , and its center is the intersection between the  $\sigma$  axis and the segment  $AB$ . In conclusion, given a uniform stress state, the stresses acting on inclined surfaces are located on the circle of radius  $R$  centered at position  $(0, \sigma_m)$ .

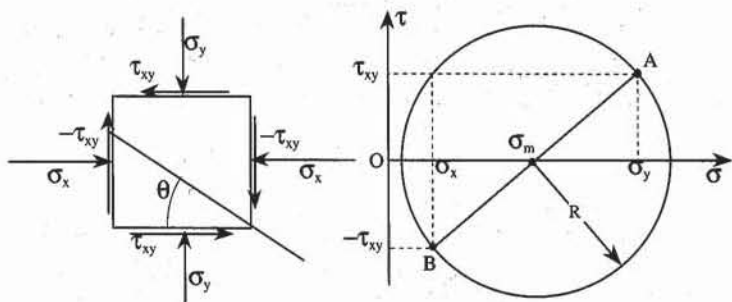


Figure 7 Construction of the Mohr circle in the Mohr space.

### Principal Stress

Using Eq. 22, the shear stress becomes zero for the following surface inclination  $\theta$ :

$$\tan 2\theta = \frac{2\tau_{xy}}{\sigma_x - \sigma_y} \quad (25)$$

For every set of  $\sigma_x$ ,  $\sigma_y$ , and  $\tau_{xy}$ , there are two values of  $\theta$  that satisfy Eq. 25. These two angles characterize the principal directions. By substituting Eq. 25 into Eq. 22, the principal stresses are

$$\sigma_1 = \frac{1}{2}(\sigma_x + \sigma_y) + \sqrt{\frac{1}{4}(\sigma_x - \sigma_y)^2 + \tau_{xy}^2} \quad (26)$$

$$\sigma_2 = \frac{1}{2}(\sigma_x + \sigma_y) - \sqrt{\frac{1}{4}(\sigma_x - \sigma_y)^2 + \tau_{xy}^2}$$

where  $\sigma_1$  is the major principal stress and  $\sigma_2$  is the minor principal stress, as for the Cauchy representation. In the Mohr space, the principal stresses are the intersections of the Mohr circle with the  $\sigma$  axis.

### Relation between Stress and Surface Orientation

Equation 22, which gives the stresses  $\sigma$  and  $\tau$  acting on an inclined surface, may be rewritten

$$\sigma - \sigma_m = R \left( -\frac{\sigma_x - \sigma_y}{2R} \cos 2\theta + \frac{\tau_{xy}}{2R} \sin 2\theta \right) \quad (27)$$

$$\tau = R \left( \frac{\sigma_x - \sigma_y}{2R} \sin 2\theta + \frac{\tau_{xy}}{2R} \cos 2\theta \right)$$

After introducing the angle  $\alpha$  shown in Fig. 8, Eq. 27 becomes

$$\sigma - \sigma_m = R(\cos \alpha \cos 2\theta + \sin \alpha \sin 2\theta) = R \cos(\alpha - 2\theta) \quad (28)$$

$$\tau = R(-\cos \alpha \sin 2\theta + \sin \alpha \cos 2\theta) = R \sin(\alpha - 2\theta) \quad (29)$$

By using Eqs. 28 and 29,  $\sigma$  and  $\tau$  on any inclined surface can be calculated from  $R$  and  $\alpha$ , provided that the surface inclination  $\theta$  is known.

### Pole of the Mohr Circle

In contrast to the physical stress states, which have three independent components— $\sigma_x$ ,  $\sigma_y$ , and  $\tau_{xy}$ —the Mohr circle has only two variables— $R$  and  $\sigma_m$ . Therefore, there is no unique correspondence between the Mohr circle and physical stresses. In fact, a particular Mohr circle corresponds to an infinite number of stress states. This problem is solved by adding a third variable, the pole.

The pole is constructed as shown in Fig. 8. (1) Draw points  $B$  and  $A$  with coordinates  $(\sigma_x, -\tau_{xy})$  and  $(\sigma_y, \tau_{xy})$ , respectively. (2) Draw the Mohr circle centered on the  $\sigma$  axis and passing through  $A$  and  $B$ . (3) Through  $A$ , draw the line parallel to the surface on which  $(\sigma_y, \tau_{xy})$  acts. This horizontal line intersects the circle at points  $A$  and  $P$ . (4) Through  $B$ , draw the line parallel to the surface on which  $(\sigma_x, -\tau_{xy})$  acts. This vertical line intersects the circle at points  $B$  and  $P$ . Lines  $AP$  and  $BP$  intersect at point  $P$  on the Mohr circle. Point  $P$  is the pole.

The pole is used to determine stresses on inclined surfaces graphically. Draw a straight line passing through the pole and parallel to the surface on which stresses need to be defined. This line intersects the Mohr circle at the desired normal and shear stresses. The pole can also be used to find the orientation of a surface on which is acting a given stress state  $\sigma$  and  $\tau$ . Draw the line through the pole and point  $(\sigma, \tau)$  on the Mohr circle. That line is parallel to the surface on which  $\sigma$  and  $\tau$  are acting.

The pole property derives from Eqs. 28 and 29. The graphical pole construction uses  $\theta$  instead of  $2\theta$  as in Eq. 27. As shown in Fig. 8, both angles  $AQM$  and  $APM$  intersect chord  $AM$ , and therefore  $AQM = 2\theta = 2APM$ .

The pole may be used to calculate the principal stress directions as shown in Fig. 9. The Mohr circle and its pole are first constructed from points  $A$  and  $B$ , as explained in Fig. 8. The line passing through  $P$  and  $(\sigma_1, 0)$  gives the orientation  $\theta_1$  of the surface on which  $\sigma_1$  is acting. The line passing through  $P$  and  $(\sigma_2, 0)$  gives the orientation  $\theta_2$  of the surface on which  $\sigma_2$  is acting. The orientation of surfaces where the shear stress is maximum (i.e.,  $\tau = \tau_{max}$ ) is found by drawing the two lines passing through the pole and points  $(\sigma_m, \pm \tau_{max})$  on the Mohr circle.

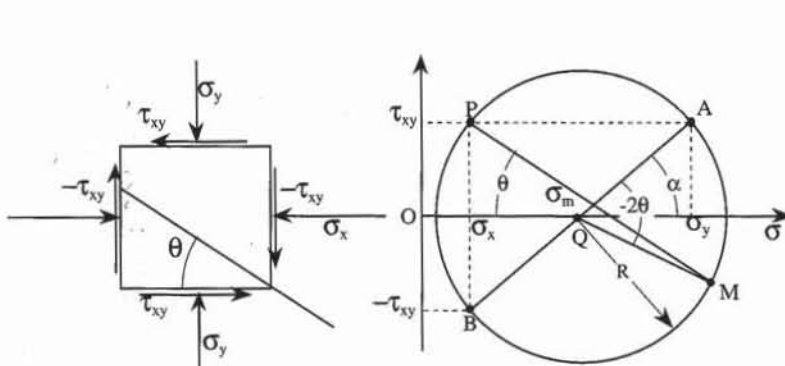


**Figure 8** Construction of the Mohr circle and its pole in the Mohr space.

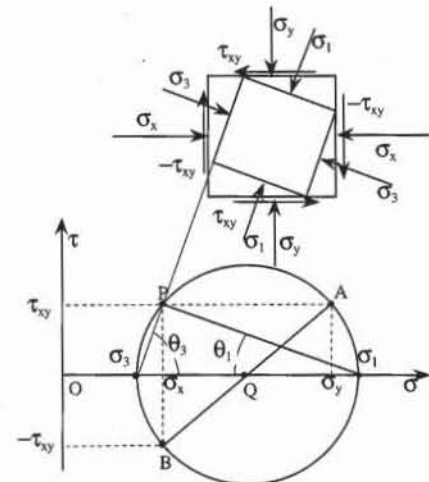


**Figure 9** Determination of principal stress direction by using the pole.

## TOTAL AND EFFECTIVE STRESSES

Stresses in soils are more difficult to describe than in other materials because soils are a mixture of solid, water, and air. We restrict our presentation of stresses to two-phase (i.e., fully saturated) soils. Three-phase (i.e., unsaturated) soils are beyond the scope of this book.

### Fillunger-Terzaghi Postulate

In saturated soils, the contact forces are distributed on soil grains and interstitial water. Fillunger (1915) and Terzaghi (1943) introduced the concept of effective stress to distinguish the contact forces acting on the soil grains from those acting on water. They postulated that the total stress vector  $\mathbf{T}_n$  acting on a surface with unit normal vector  $\mathbf{n}$  is the sum of the *effective stress*  $\mathbf{T}'_n$  and *porewater pressure*  $u$ :

$$\mathbf{T}_n = \mathbf{T}'_n + u\mathbf{n} \quad (30)$$

In the Mohr representation, Eq. 30 is written as

$$\sigma = \sigma' + u \quad \text{and} \quad \tau = \tau' \quad (31)$$

where  $\sigma$  and  $\tau$  are the normal and shear components of  $\mathbf{T}_n$  and  $\sigma'$  and  $\tau'$  are normal and shear components of  $\mathbf{T}'_n$ . The physical meaning of  $\mathbf{T}'_n$  and  $\sigma'$  is explained as follows. As shown in Fig. 10, the total normal stress acting on surface  $A$  is

$$\sigma = \frac{A_s}{A_w + A_s} \sigma_s + \frac{A_w}{A_w + A_s} u \quad (32)$$

where  $A_s$  is the solid-solid contact area,  $A_w$  the water-water contact area,  $\sigma_s$  the average normal stress on  $A_s$  (i.e., *granular stress*), and  $u$  the average pore pressure on  $A_w$ .  $A = A_s + A_w$  because the material has only two phases. The tangential total force acting on surface  $A$  is transmitted only through the solid-solid contact because water does not transmit any shear:

$$\tau = \frac{A_s}{A_w + A_s} \tau_s \quad (33)$$

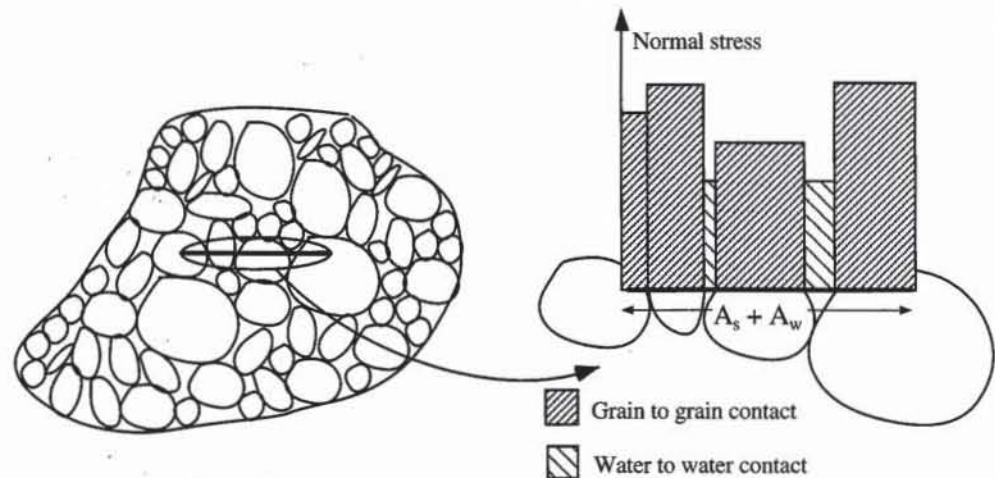


Figure 10 Grain-grain and water-water contacts in soils.

where  $\tau_s$  is the average shear stress on  $A_s$ . If surfaces  $A_w$  and  $A_s$  are the same for all cross sections, then

$$\frac{A_w}{A} = 1 - \frac{A_s}{A} = \frac{V_w}{V} = n \quad (34)$$

where  $n$  is the porosity. Therefore,

$$\sigma = (1 - n) \sigma_s + nu \quad \text{and} \quad \tau = (1 - n) \tau_s \quad (35)$$

Using Eqs. 31 and 35,

$$\sigma = \sigma' + u = (1 - n) \sigma_s + nu \quad (36)$$

Therefore, the effective stress is related to  $\sigma_s$  and  $u$  through

$$\sigma' = (1 - n) (\sigma_s - u) \quad \text{and} \quad \tau' = \tau = (1 - n) \tau_s \quad (37)$$

As shown in Eq. 37, the effective stress  $\sigma'$  depends on  $\sigma_s$  and  $u$ . In the case when  $\sigma_s \gg u$ ,  $\sigma'$  becomes equal to the *distributed granular stress*  $(1 - n)\sigma_s$ .

### Cauchy Representation of Total and Effective Stresses

In the Cauchy representation, Eq. 30 becomes

$$\begin{pmatrix} \sigma_x & \tau_{xy} \\ \tau_{xy} & \sigma_y \end{pmatrix} = \begin{pmatrix} \sigma'_x & \tau'_{xy} \\ \tau'_{xy} & \sigma'_y \end{pmatrix} + \begin{pmatrix} u & 0 \\ 0 & u \end{pmatrix} \quad (38)$$

where the first matrix represents the *total stress*, and the second matrix, the *effective stress*.

### Mohr Representation of Total and Effective Stresses

Like total stresses, effective stresses have a Mohr circle. As shown in Fig. 11, the Mohr circles of effective and total stresses have the same diameter because of Eq. 31. The center and pole of the Mohr circle of effective stress are obtained from those of total stress by a translation in the amount  $-u$  along the  $\sigma$  axis.

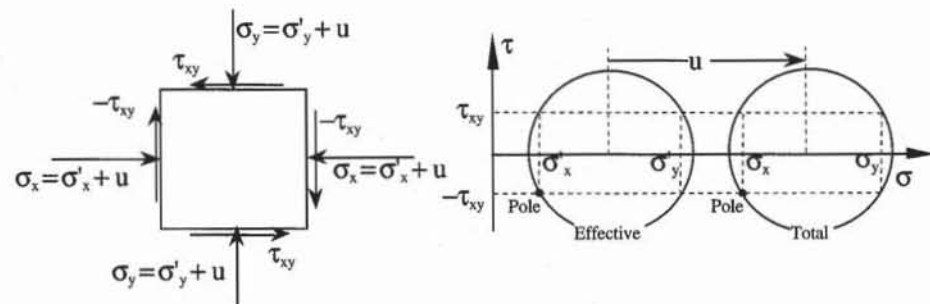


Figure 11 Mohr circles and poles of effective and total stresses.

## S-T REPRESENTATION

The evolution of the Mohr circle during a loading process can be defined in terms of  $s$  and  $t$ , where  $s$  is the  $\sigma$ -coordinate of the Mohr circle center and  $t$  is the Mohr circle radius:

$$s = \frac{1}{2}(\sigma_1 + \sigma_3) \quad \text{and} \quad t = \frac{1}{2}(\sigma_1 - \sigma_3) \quad (39)$$

where  $\sigma_1$  is the major principal stress and  $\sigma_3$  is the minor principal stress. The effective coordinates  $s'$  and  $t'$  are:

$$s' = \frac{1}{2}(\sigma'_1 + \sigma'_3) \quad \text{and} \quad t' = \frac{1}{2}(\sigma'_1 - \sigma'_3) \quad (40)$$

The  $s$ - $t$  and  $s'$ - $t'$  components are referred to as the *MIT stress system*. Using Eq. 31,  $s$ ,  $t$ ,  $s'$ , and  $t'$  are related through

$$s = s' + u \quad \text{and} \quad t = t' \quad (41)$$

Figure 12 schematizes the evolution of the effective and total Mohr circles during an arbitrary loading process. The Mohr circles of total and effective stress and their corresponding points in the  $s$ - $t$  and  $s'$ - $t'$  spaces are shown in Fig. 12. The Mohr circles  $A$  and  $A'$  have the same radius, but their centers are separated by pore pressure  $u_A$ . Points  $A'$  and  $A$  have identical  $t$  (i.e.,  $t_A = t'_A$ ), but different  $s$  (i.e.,  $s_A = s'_A + u_A$ ).

## THREE-DIMENSIONAL STRESS

Stresses are three-dimensional in the field and in the laboratory. We discuss briefly the three-dimensional representations of Cauchy and Mohr. Additional information can be found in Chen and Saleeb (1982).

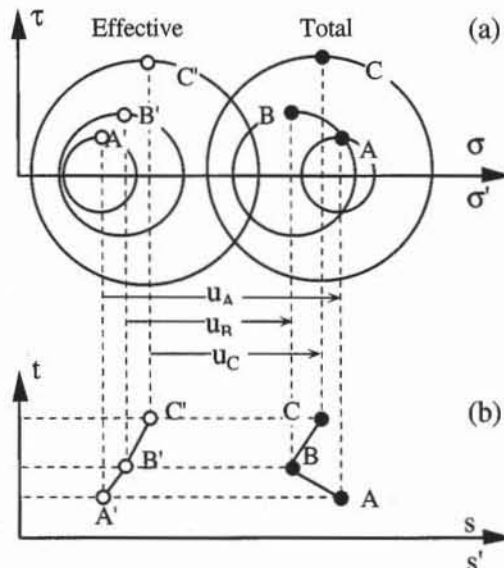


**Figure 12** Evolution of the Mohr circle of effective and total stresses, and their representation in the  $s$ - $t$  and  $s'$ - $t'$  spaces.

### Cauchy Representation

In three dimensions, the stress vector  $(\sigma_{nx}, \sigma_{ny}, \sigma_{nz})$  acting on the surface with normal unit vector  $(n_x, n_y, n_z)$  is given by the Cauchy stress tensor

$$\begin{pmatrix} \sigma_{nx} \\ \sigma_{ny} \\ \sigma_{nz} \end{pmatrix} = \begin{pmatrix} \sigma_x & \tau_{xy} & \tau_{xz} \\ \tau_{xy} & \sigma_y & \tau_{yz} \\ \tau_{xz} & \tau_{yz} & \sigma_z \end{pmatrix} \begin{pmatrix} n_x \\ n_y \\ n_z \end{pmatrix} \quad (42)$$

The principal stresses  $\sigma_1$ ,  $\sigma_2$ , and  $\sigma_3$  are found by solving the following eigenvalue problem:

$$\begin{pmatrix} \sigma_x & \tau_{xy} & \tau_{xz} \\ \tau_{xy} & \sigma_y & \tau_{yz} \\ \tau_{xz} & \tau_{yz} & \sigma_z \end{pmatrix} \begin{pmatrix} n_x \\ n_y \\ n_z \end{pmatrix} = \sigma \begin{pmatrix} n_x \\ n_y \\ n_z \end{pmatrix} \quad (43)$$

which is equivalent to solving the following cubic equation:

$$\sigma^3 - I_1\sigma^2 + I_2\sigma - I_3 = 0 \quad (44)$$

where  $I_1$ ,  $I_2$ , and  $I_3$  are the stress invariants

$$I_1 = \sigma_x + \sigma_y + \sigma_z$$

$$I_2 = \sigma_x\sigma_y + \sigma_y\sigma_z + \sigma_z\sigma_x - \tau_{xy}^2 - \tau_{yz}^2 - \tau_{zx}^2 \quad (45)$$

$$I_3 = \sigma_x\sigma_y\sigma_z - \sigma_x\tau_{yz}^2 - \sigma_y\tau_{zx}^2 - \sigma_z\tau_{xy}^2 + 2\tau_{xy}\tau_{yz}\tau_{zx}$$

Equation 44 can be solved analytically as follows:

$$\begin{aligned} \sigma_1 &= \frac{I_1}{3} + \frac{2}{3} \sqrt{I_1^2 - 3I_2} \cos \theta \\ \sigma_2 &= \frac{I_1}{3} + \frac{2}{3} \sqrt{I_1^2 - 3I_2} \cos \left( \frac{2\pi}{3} - \theta \right) \\ \sigma_3 &= \frac{I_1}{3} + \frac{2}{3} \sqrt{I_1^2 - 3I_2} \cos \left( \frac{2\pi}{3} + \theta \right) \end{aligned} \quad (46)$$

where  $\theta$  is given by

$$\cos 3\theta = \frac{2I_1^3 - 9I_1I_2 + 27I_3}{2(I_1^2 - 3I_2)^{3/2}} \quad (47)$$

The stress invariants of Eq. 45 can also be expressed in terms of principal stresses:

$$I_1 = \sigma_1 + \sigma_2 + \sigma_3, \quad I_2 = \sigma_1\sigma_2 + \sigma_2\sigma_3 + \sigma_1\sigma_3, \quad \text{and} \quad I_3 = \sigma_1\sigma_2\sigma_3 \quad (48)$$

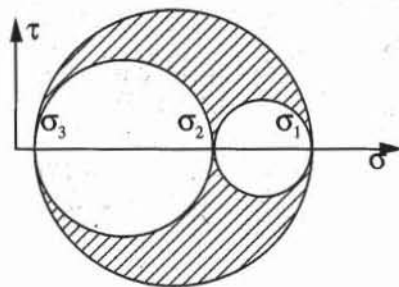


**Figure 13** Mohr representation of three-dimensional stresses.

The principal stress directions are found by setting  $\sigma$  equal to  $\sigma_1$ ,  $\sigma_2$ , or  $\sigma_3$  in Eq. 43.

### Mohr Representation

As shown in Fig. 13, in three dimensions, the stress point  $(\sigma, \tau)$  describes the shaded area between the three circles passing through points  $(\sigma_1, 0)$ ,  $(\sigma_2, 0)$ , and  $(\sigma_3, 0)$  where  $\sigma_1$ ,  $\sigma_2$ , and  $\sigma_3$  are the principal stresses. The geometrical determination of point  $(\sigma, \tau)$  in this area is impractical because it is much more complicated than in two dimensions. When the intermediate principal stress  $\sigma_2$  is equal to the major or minor principal stress (i.e.,  $\sigma_2 = \sigma_1$ , or  $\sigma_2 = \sigma_3$ ), the shaded area becomes a circle, and the three-dimensional Mohr representation coincides with the two-dimensional representation. This is the case of axisymmetric stresses, for which

$$\sigma_x = \sigma_y \quad \text{and} \quad \tau_{xy} = \tau_{yz} = \tau_{zx} = 0 \quad (49)$$

Therefore, axisymmetric stresses can be described by using the Mohr representation.

### P-Q REPRESENTATION

In the case of axisymmetric stress states (Eq. 49), it is convenient to introduce the mean effective pressure  $p'$  and the deviator stress  $q$

$$p' = \frac{1}{3}(\sigma'_1 + 2\sigma'_3) \quad \text{and} \quad q = \sigma_1 - \sigma_3 = \sigma'_1 - \sigma'_3 \quad (50)$$

where  $\sigma'_1$  and  $\sigma'_3$  are the axial and radial effective stress, respectively, and  $\sigma_1$  and  $\sigma_3$  are their total stress counterparts. The total mean pressure  $p$  corresponding to  $p'$  is  $p = \frac{1}{3}(\sigma_1 + 2\sigma_3) = p' + u$ . The  $p$ - $q$  and  $p'$ - $q$  components are referred to as the *Cambridge stress system*. Using Eq. 39,

$$s' = p' + \frac{q}{6} \quad \text{and} \quad t = \frac{q}{2} \quad (51)$$

Note that  $s' = p'$  and  $t = q = 0$  when  $\sigma'_1 = \sigma'_3$ , and that  $s' \neq p'$  and  $t \neq q$  otherwise. Table 1 summarizes the definitions of the MIT and Cambridge stress systems.  $p$  and  $q$  are also related to the stress invariants through

$$p = \frac{1}{3} I_1 \quad \text{and} \quad q = \sqrt{I_1^2 - 3I_2} \quad (52)$$

**TABLE 1**  
The MIT and Cambridge stress notations

Principal stresses	MIT notation $s-t$ and $s'-t$ stresses	Cambridge notation $p-q$ and $p'-q$ stresses
$\sigma_1 = \sigma'_1 + u$	$s = \frac{1}{2}(\sigma_1 + \sigma_3) = s' + u$	$p = \frac{1}{3}(\sigma_1 + 2\sigma_3) = p' + u$
$\sigma'_1 = \sigma_1 - u$	$s' = \frac{1}{2}(\sigma'_1 + \sigma'_3) = s - u$	$p' = \frac{1}{3}(\sigma'_1 + 2\sigma'_3) = p - u$
$\sigma_3 = \sigma'_3 + u$	$t = \frac{1}{2}(\sigma_1 - \sigma_3)$	$q = \sigma_1 - \sigma_3$
$\sigma'_3 = \sigma_3 - u$	$t' = t = \frac{1}{2}(\sigma'_1 - \sigma'_3)$	$q' = q = \sigma'_1 - \sigma'_3$
$\sigma'_1$	$\sigma'_1 = s' + t$	$\sigma'_1 = p' + \frac{2}{3}q$
$\sigma'_3$	$\sigma'_3 = s' - t$	$\sigma'_3 = p' - \frac{1}{3}q$

## REFERENCES

- CHEN, W. F., and A. F. SALEEB, 1982, *Constitutive Equations for Engineering Materials*, Vol. 1, John Wiley & Sons, New York, pp. 48–108.  
 FILLUNGER, P., 1915, Versuche über die Zugfestigkeit bei Allseitigem Wasserdruck, *Österr. Wochenschr. Öffentl. Baudienst*, Vol. H.29, pp. 443–448.  
 TERZAGHI, K., 1943, *Theoretical Soil Mechanics*, John Wiley & Sons, New York.

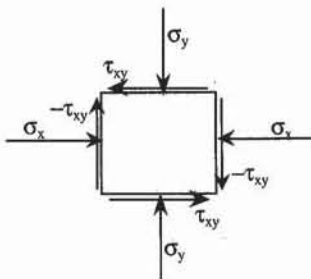
## REVIEW QUESTIONS

- What are the main types of force acting on a soil element?
- Define three different types of body forces acting in soils.
- What is the physical dimension of stress?
- Define the Cauchy representation of stresses. How does it relate stress matrix and stress vector on an inclined surface?
- Define *principal stresses*.
- Define the sign convention for the Cauchy and Mohr representations of stress.
- What does the Mohr circle represent?
- Define the radius and center position of the Mohr circle from arbitrary stresses acting on a square element.
- Define the pole of the Mohr circle. Why do we introduce the pole of the Mohr circle?
- What is the principle of the pole of the Mohr circle?
- What are the effective stress and total stress?
- What is the difference between effective stress and distributed granular stress? Under what conditions are these stresses equal?
- Define the  $s$  and  $t$  coordinates. Why are they useful?
- Why does the Mohr circle have a limited use in three dimensions?
- What are the stress invariants?

## EXERCISES

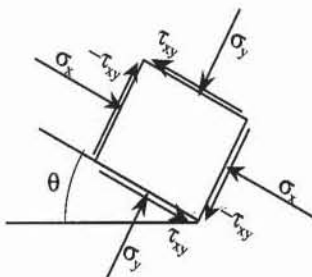
- Derive the stress equilibrium equations (Eqs. 7 to 9) by using Fig. 3.
- (a) Draw the Mohr circle and its pole for the following stress state.

- (b) Find the stresses acting on a surface inclined at  $30^\circ$  with respect to the horizontal direction.



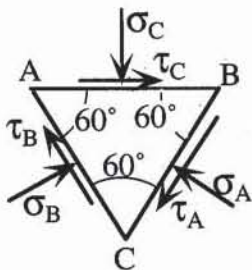
$$\sigma_x = 20 \text{ kPa}, \quad \sigma_y = 100 \text{ kPa}, \quad \tau_{xy} = 10 \text{ kPa}$$

3. (a) Draw the Mohr circle and its pole for the following stress state.  
 (b) Find the stresses acting on a surface inclined at  $30^\circ$  with respect to the horizontal direction.  
 (c) Find the values and inclinations of the principal stresses by using the pole.



$$\sigma_x = 20 \text{ kPa}, \quad \sigma_y = 100 \text{ kPa}, \quad \tau_{xy} = 10 \text{ kPa}, \quad \theta = 30^\circ$$

4. (a) Find stress  $\sigma_C$ ,  $\sigma_A$ , and  $\tau_A$  on the triangular element in order to have an equilibrium.  
 (b) Plot the Mohr circle and its pole.  
 (c) Verify that the stress points  $(\sigma_A, \tau_A)$ ,  $(\sigma_B, \tau_B)$ , and  $(\sigma_C, \tau_C)$  are on the Mohr circle and are obtained by using the pole.



$$\tau_B = 20 \text{ kPa}, \quad \sigma_B = 100 \text{ kPa}, \quad \tau_C = 10 \text{ kPa}$$

5. In a triaxial test at constant confining pressure, only the major principal stress  $\sigma_1$  varies from 50 to 100 kPa, whereas stresses  $\sigma_2$  and  $\sigma_3$  remain equal to 50 kPa. Draw the corresponding  $s-t$  stress path.

# 5-2 Strain in Soils

## INTRODUCTION

In the following section we review the concepts of strain for describing the stress-strain response of soils in laboratory experiments. Strains are first presented in two dimensions, using the tensor and Mohr representations, and then in three dimensions.

## TWO-DIMENSIONAL DISPLACEMENT AND STRAIN IN SOILS

As shown in Fig. 1, the soil mass  $H$  deforms from its initial to final positions when it is subjected to external loads (e.g., weight of a building) or internal forces (e.g., the soil's own weight). The small element  $OACB$  located within soil mass  $H$  deforms as shown in Fig. 2. Like stresses, strains are defined by assuming that soils are continuous materials. Figure 2 shows the initial position of element  $OACB$  and its final position  $O''A''C''B''$ .

The displacement of point  $O$  from its initial position  $(x, y)$  is characterized by the displacement vector  $(u, v)$ . The components  $u$  and  $v$  are assumed to be continuous functions of  $x$  and  $y$ . Therefore, in the close proximity of point  $O$ ,  $u$  and  $v$  may be approximated by using Taylor expansions:

$$u(x + dx, y + dy) = u(x, y) + \frac{\partial u}{\partial x}(x, y)dx + \frac{\partial u}{\partial y}(x, y)dy + \dots \quad (1)$$

$$v(x + dx, y + dy) = v(x, y) + \frac{\partial v}{\partial x}(x, y)dx + \frac{\partial v}{\partial y}(x, y)dy + \dots \quad (2)$$

As listed in Table 1, the coordinates of the displacement vectors of points  $A$ ,  $B$ , and  $C$  may be calculated by using Eqs. 1 and 2 and their position relative to point  $O$ . The displacements of  $O$ ,  $A$ ,  $B$ , and  $C$  are represented in Fig. 3. The element  $O''A''C''B''$  is obtained by translating  $OACB$  purely, without deforming or rotating it.

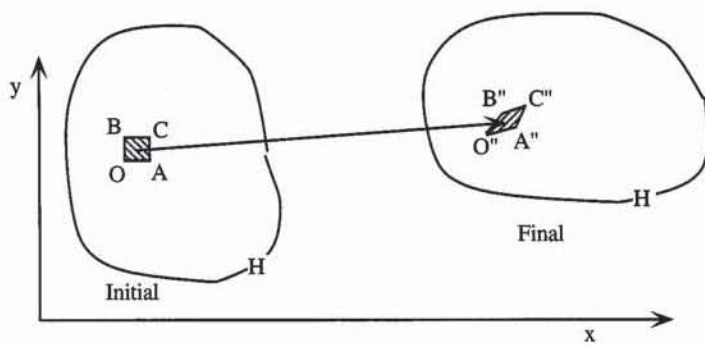


**Figure 1** Initial and final positions of a soil mass during a deformation process.

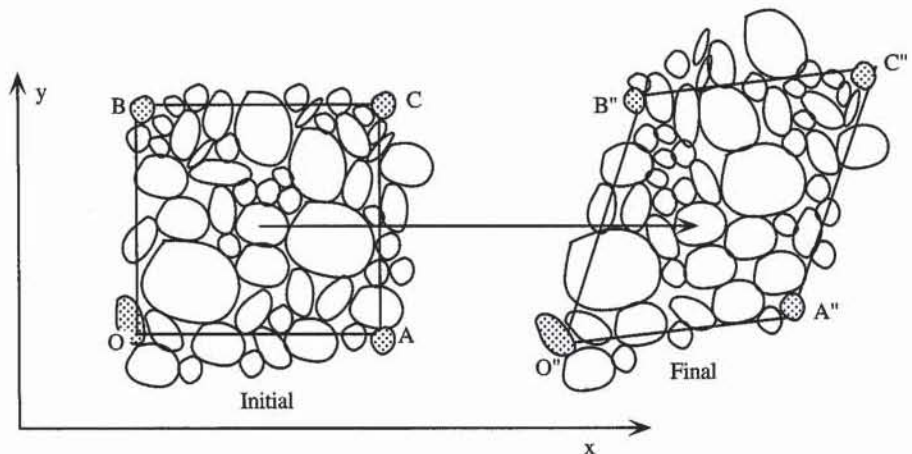


**Figure 2** Deformation of the small element of Fig. 1 from initial to final positions.

**TABLE 1**

Coordinates of initial positions of points  $O$ ,  $A$ ,  $B$ , and  $C$  and coordinates of their displacement

Point	Initial position		Point	Final position		Displacement	
	$x$	$y$		$x$	$y$		
$O$	$x$	$y$	$O''$	$u$	$v$		
$A$	$x + dx$	$y$	$A''$	$u + \frac{\partial u}{\partial x} dx$	$v + \frac{\partial v}{\partial x} dx$		
$B$	$x$	$y + dy$	$B''$	$u + \frac{\partial u}{\partial y} dy$	$v + \frac{\partial v}{\partial y} dy$		
$C$	$x + dx$	$y + dy$	$C''$	$u + \frac{\partial u}{\partial x} dx + \frac{\partial u}{\partial y} dy$	$v + \frac{\partial v}{\partial x} dx + \frac{\partial v}{\partial y} dy$		

### Axial Strain

The material fiber  $OA$ , which is made of the soil particles between  $O$  and  $A$ , becomes  $O''A''$  after the deformation process. The elongation of  $OA$  in the  $x$  direction is

$$O''D - OA = u + \frac{\partial u}{\partial x} dx - u = \frac{\partial u}{\partial x} dx \quad (3)$$

Because  $OA$  is equal to  $dx$ , the elongation of  $OA$  per unit length in the  $x$  direction is

$$\frac{O''D - OA}{OA} = \frac{\partial u}{\partial x} = -\varepsilon_x \quad (4)$$

where  $\varepsilon_x$  is the axial strain in the  $x$  direction, by definition. Owing to the sign convention of soil mechanics,  $\varepsilon_x$  is positive in compression, which justifies the negative sign in Eq. 4. Similarly, the elongation of fiber  $OB$  per unit length in the  $y$  direction per unit length is

$$\frac{O''E - OB}{OB} = \frac{\partial v}{\partial y} = -\varepsilon_y \quad (5)$$

where  $\varepsilon_y$  is the axial strain in the  $y$  direction, by definition.

### Shear Strain

As shown in Fig. 3, the rotations of fibers  $OA$  and  $OB$  are equal to the angles  $\overline{A'O''A''}$  and  $\overline{B'O''B''}$ , respectively.  $\overline{A'O''A''}$  can be approximated by using Fig. 3:

$$\overline{A'O''A''} \approx \tan(\overline{A'O''A''}) = \frac{\frac{\partial v}{\partial x} dx}{dx + \frac{\partial u}{\partial x} dx} \approx \frac{\frac{\partial v}{\partial x}}{1 + \frac{\partial u}{\partial x}} \quad (6)$$

where  $|\partial u/\partial x|$  is assumed much smaller than 1.  $\overline{B'O''B''}$  is

$$\overline{B'O''B''} \approx \tan(\overline{B'O''B''}) = \frac{\frac{\partial u}{\partial y} dy}{dy + \frac{\partial v}{\partial y} dy} \approx \frac{\frac{\partial u}{\partial y}}{1 + \frac{\partial v}{\partial y}} \quad (7)$$

where  $|\partial v/\partial y|$  is also assumed much smaller than 1. The angular distortion of  $\overline{AOB}$  is

$$\overline{AOB} - \overline{A''O''B''} \approx \frac{\partial u}{\partial y} + \frac{\partial v}{\partial x} = -\gamma_{xy} = -2\varepsilon_{xy} \quad (8)$$

where  $\varepsilon_{xy}$  is the shear strain and  $\gamma_{xy}$  is the engineering shear strain, by definition. From a physical point of view, the shear strain  $\gamma_{xy}$  is the angular distortion of two fibers that are initially perpendicular.

### Volumetric Strain

As shown in Fig. 3, the area  $OABC = S = dx dy$  becomes the area  $O''A''B''C'' = S''$ . It can be shown that the area change per unit area is

$$\frac{S - S''}{S} = \varepsilon_x + \varepsilon_y = \varepsilon_v \quad (9)$$

where  $\varepsilon_v$  is the volumetric strain. Eq. 9 assumes that the absolute values of  $\partial u/\partial x$  and  $\partial v/\partial y$  are much smaller than 1. The volumetric strain  $\varepsilon_v$  is positive when  $S$  decreases, and negative when  $S$  increases.

### Rigid-Body Rotation

As shown in Fig. 3,  $OC$  transforms into  $O''C''$  and rotates by the angle  $\overline{C'O''C''}$ , where

$$\overline{C'O''C''} = \frac{1}{2} \overline{A'O''A''} - \frac{1}{2} \overline{B'O''B''} \quad (10)$$

Therefore,

$$\overline{C'O''C''} \approx \frac{1}{2} \left( \frac{\partial u}{\partial y} - \frac{\partial v}{\partial x} \right) = -\omega \quad (11)$$

where  $\omega$  is the angle of rigid-body rotation about point  $O''$ , by definition. In general, a rigid rotation  $\omega$  about the origin creates the following displacement:

$$\begin{pmatrix} u \\ v \end{pmatrix} = \begin{pmatrix} \cos\omega - 1 & -\sin\omega \\ \sin\omega & \cos\omega - 1 \end{pmatrix} \begin{pmatrix} x \\ y \end{pmatrix} \quad (12)$$

In the case of infinitesimal rotations (i.e.,  $|\omega| \ll 1$ ), Eq. 12 becomes

$$\begin{pmatrix} u \\ v \end{pmatrix} = \begin{pmatrix} 0 & -\omega \\ \omega & 0 \end{pmatrix} \begin{pmatrix} x \\ y \end{pmatrix} \quad (13)$$

which implies that points  $A$ ,  $B$ , and  $C$  are subjected to rigid-body rotation of angle  $\omega$  about point  $O''$ . As the translation for  $O$  to  $O''$ , the rigid-body rotation creates no axial and shear strain in the element  $OACB$ .

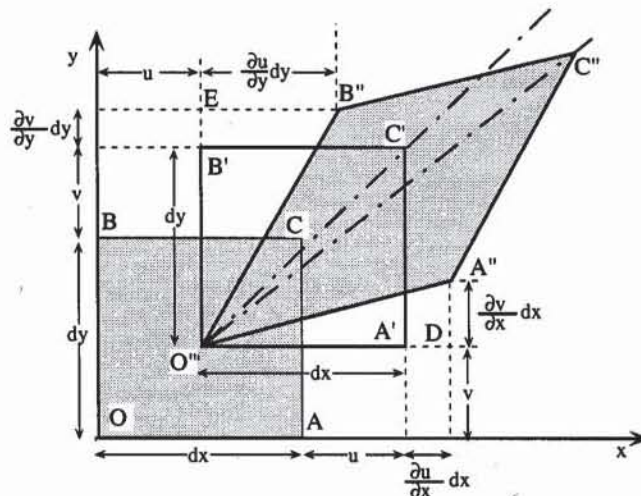


**Figure 3** Infinitesimal displacement of points  $A$ ,  $B$ , and  $C$ , neighbors of  $O$ .

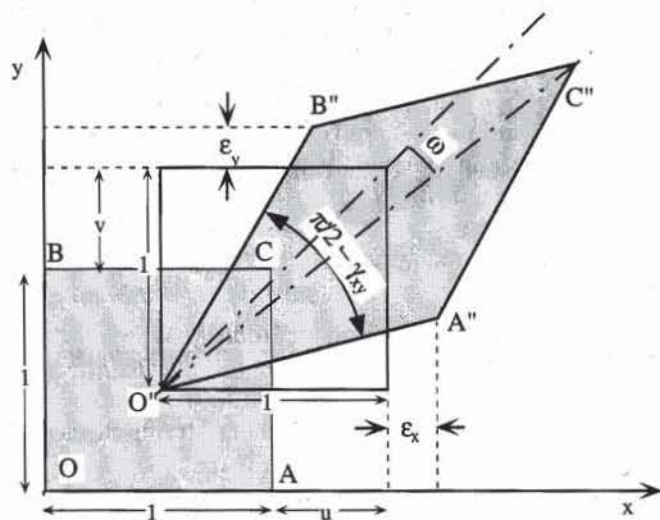


**Figure 4** Physical interpretation of strains  $\epsilon_x$ ,  $\epsilon_y$ ,  $\gamma_{xy}$ , and rotation  $\omega$ .

### Summary

As shown in Fig. 4,  $\epsilon_x$  and  $\epsilon_y$  represent the length change per unit length in the horizontal and vertical directions, respectively, whereas  $\gamma_{xy}$  represents the angular distortion of two segments that are initially perpendicular. The angle  $\omega$  of rigid-body rotation represents the rotation of the diagonals about  $O''$ . Note that the foregoing relations between strain and displacement are valid only for infinitesimal deformation (i.e.,  $|\partial u/\partial x|$ ,  $|\partial v/\partial y|$ ,  $|\partial u/\partial y|$ , and  $|\partial v/\partial x| \ll 1$ ). The description of large strain is beyond the scope of this book.

## VARIATION OF STRAIN WITH DIRECTION

Axial and shear strains may be calculated for elements oriented in any direction. As shown in Fig. 5, when the  $x'$  and  $y'$  axes are obtained from the  $x$  and  $y$  axes by a  $-\theta$  rotation, the  $x-y$  and  $x'-y'$  coordinates are related through

$$\begin{pmatrix} x' \\ y' \end{pmatrix} = \begin{pmatrix} \cos \theta & -\sin \theta \\ \sin \theta & \cos \theta \end{pmatrix} \begin{pmatrix} x \\ y \end{pmatrix} \quad \text{or} \quad \begin{pmatrix} x \\ y \end{pmatrix} = \begin{pmatrix} \cos \theta & \sin \theta \\ -\sin \theta & \cos \theta \end{pmatrix} \begin{pmatrix} x' \\ y' \end{pmatrix} \quad (14)$$

Equation 14 applies also to the displacement vectors:

$$\begin{pmatrix} u' \\ v' \end{pmatrix} = \begin{pmatrix} \cos \theta & -\sin \theta \\ \sin \theta & \cos \theta \end{pmatrix} \begin{pmatrix} u \\ v \end{pmatrix} \quad (15)$$

The small element  $oacb$  within  $OACB$  is aligned along the  $x'$  and  $y'$  axes. The deformed element is  $o''a''c''b''$ . By using the previous definitions, the axial strain in the  $x'$  and  $y'$  directions and the shear strain are

$$\epsilon_{x'} = -\frac{\partial u'}{\partial x'}, \quad \epsilon_{y'} = -\frac{\partial v'}{\partial y'}, \quad \text{and} \quad \gamma_{x'y'} = -\frac{\partial u'}{\partial y'} - \frac{\partial v'}{\partial x'} \quad (16)$$

Using Eqs. 14 and 15, the following relations are obtained:

$$\frac{\partial x}{\partial x'} = \frac{\partial y}{\partial y'} = \frac{\partial u}{\partial u'} = \frac{\partial v}{\partial v'} = \cos \theta \quad \text{and} \quad \frac{\partial x}{\partial y'} = -\frac{\partial y}{\partial x'} = -\frac{\partial u'}{\partial v} = \frac{\partial v'}{\partial u} = \sin \theta \quad (17)$$

Using Eq. 17 and the chain rule of differentiation yields

$$\begin{aligned}\epsilon_{x'} &= -\frac{\partial u'}{\partial x} \frac{\partial x}{\partial x'} - \frac{\partial u'}{\partial y} \frac{\partial y}{\partial x'} = -\frac{\partial u'}{\partial x} \cos \theta + \frac{\partial u'}{\partial y} \sin \theta \\ &= -\left(\frac{\partial u' \partial u}{\partial x \partial x} + \frac{\partial u' \partial v}{\partial v \partial x}\right) \cos \theta + \left(\frac{\partial u' \partial u}{\partial u \partial y} + \frac{\partial u' \partial v}{\partial v \partial y}\right) \sin \theta\end{aligned}\quad (18)$$

Finally, the axial and shear strains of element oabc are

$$\epsilon_{x'} = \epsilon_x \cos^2 \theta + \epsilon_y \sin^2 \theta - \gamma_{xy} \sin \theta \cos \theta$$

$$\epsilon_{y'} = \epsilon_x \sin^2 \theta + \epsilon_y \cos^2 \theta + \gamma_{xy} \sin \theta \cos \theta$$

$$\gamma_{x'y'} = 2\epsilon_x \sin \theta \cos \theta - 2\epsilon_y \sin \theta \cos \theta + \gamma_{xy} (\cos^2 \theta - \sin^2 \theta) \quad (19)$$

Equation 19 is similar to Eq. 20.5-1 defining the stresses on an inclined surface. The variation of strain with direction may be described by using two different approaches: strain tensor and Mohr circle.

## TENSOR REPRESENTATION OF STRAIN

The strain tensor is defined as the stress tensor. It gives the projections  $\epsilon_{nx}$  and  $\epsilon_{ny}$  of the strains  $\epsilon_x$ ,  $\epsilon_y$ , and  $\epsilon_{x'y'}$  on the  $x$  and  $y$  axes.

### Strain Tensor

As shown in Fig. 6, the unit vector normal to the surface bc is  $\mathbf{n} = (n_x, n_y)$ , and the unit vector tangent to bc is  $\mathbf{t} = (n_y, -n_x)$ . The strains  $\epsilon_{nx}$  and  $\epsilon_{ny}$  along the direction  $\mathbf{n}$  are obtained from the strain matrix:

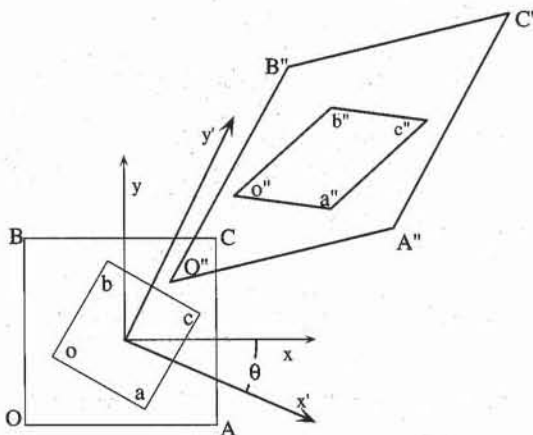


Figure 5 Initial and deformed elements.

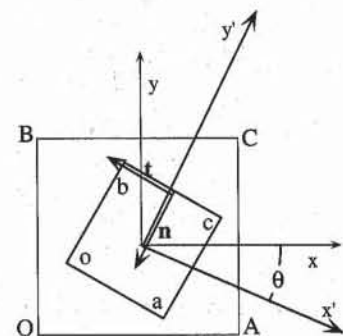


Figure 6 Strain on an inclined element.

$$\begin{pmatrix} \epsilon_{nx} \\ \epsilon_{ny} \end{pmatrix} = \begin{pmatrix} \epsilon_x & \epsilon_{xy} \\ \epsilon_{xy} & \epsilon_y \end{pmatrix} \begin{pmatrix} n_x \\ n_y \end{pmatrix} \quad (20)$$

The unit vector  $\mathbf{n}$  points inside the surface  $bc$  to obtain positive axial strain in compression and negative axial strain in tension. The normal strain  $\epsilon_n$  along the  $\mathbf{n}$  direction is obtained by projecting  $(\epsilon_{nx}, \epsilon_{ny})$  onto the  $\mathbf{n}$  direction:

$$\epsilon_n = \epsilon_{nx}n_x + \epsilon_{ny}n_y = \epsilon_x n_x^2 + \epsilon_y n_y^2 + 2\epsilon_{xy}n_x n_y = \epsilon_x n_x^2 + \epsilon_y n_y^2 + \gamma_{xy}n_x n_y \quad (21)$$

and the corresponding shear strain  $\gamma_t$  by projecting  $(\epsilon_{nx}, \epsilon_{ny})$  onto the  $\mathbf{t}$  direction:

$$\gamma_t = 2\epsilon_t = 2(\epsilon_{nx}n_y - \epsilon_{ny}n_x) = 2\epsilon_x n_x n_y - 2\epsilon_y n_x n_y + \gamma_{xy}(n_y^2 - n_x^2) \quad (22)$$

When  $\mathbf{n}$  is normal to surface  $ac$  [i.e.,  $(n_x, n_y) = (-\cos \theta, \sin \theta)$ ], Eqs. 21 and 22 become

$$\epsilon_n = \epsilon_x \cos^2 \theta + \epsilon_y \sin^2 \theta - \gamma_{xy} \sin \theta \cos \theta = \epsilon_x'$$

$$\gamma_t = -2\epsilon_x \sin \theta \cos \theta + 2\epsilon_y \sin \theta \cos \theta - \gamma_{xy}(\cos^2 \theta - \sin^2 \theta) = -\gamma_{x'y'} \quad (23)$$

and when  $\mathbf{n}$  is normal to surface  $bc$  [i.e.,  $(n_x, n_y) = (-\sin \theta, -\cos \theta)$ ]:

$$\epsilon_n = \epsilon_x \sin^2 \theta + \epsilon_y \cos^2 \theta + \gamma_{xy} \sin \theta \cos \theta = \epsilon_y'$$

$$\gamma_t = 2\epsilon_x \sin \theta \cos \theta - 2\epsilon_y \sin \theta \cos \theta + \gamma_{xy}(\cos^2 \theta - \sin^2 \theta) = \gamma_{x'y'} \quad (24)$$

Equations 23 and 24 give the same strains as Eq. 19. The strain tensor therefore represents strain along various directions.

### Principal Strain

By definition, the principal surfaces remain perpendicular to each other during a deformation process. Therefore, their normals  $(n_x, n_y)$  are found by solving the following eigenvalue problem:

$$\begin{pmatrix} \epsilon_x & \epsilon_{xy} \\ \epsilon_{xy} & \epsilon_y \end{pmatrix} \begin{pmatrix} n_x \\ n_y \end{pmatrix} = \epsilon \begin{pmatrix} n_x \\ n_y \end{pmatrix} \quad (25)$$

where  $\epsilon$  is the principal strain values.  $\epsilon$  is obtained by solving the following quadratic equation:

$$\epsilon^2 - \epsilon(\epsilon_x + \epsilon_y) + \epsilon_x \epsilon_y - \epsilon_{xy}^2 = 0 \quad (26)$$

The major and minor principal strains are

$$\begin{aligned} \epsilon_1 &= \frac{1}{2} (\epsilon_x + \epsilon_y) + \sqrt{\frac{1}{4} (\epsilon_x - \epsilon_y)^2 + \epsilon_{xy}^2} \\ \epsilon_3 &= \frac{1}{2} (\epsilon_x + \epsilon_y) - \sqrt{\frac{1}{4} (\epsilon_x - \epsilon_y)^2 + \epsilon_{xy}^2} \end{aligned} \quad (27)$$

The principal strains are equal when  $\epsilon_x = \epsilon_y$  and  $\epsilon_{xy} = 0$ , which is the case of

purely volumetric deformation. The principal surface directions are found as for the principal stress directions.

## MOHR REPRESENTATION OF STRAIN

Like stresses, strains can be represented by using the Mohr circle.

### Sign Conventions for Strain

Figure 7 defines the sign convention of strains for Mohr representation. As shown in Fig. 7, compressive strains are positive and tensile strains are negative. The sign of angular distortion is defined as that of shear stress.

### Mohr Circle

Because strain components obey Eq. 23, when  $\theta$  varies from  $-90^\circ$  to  $90^\circ$ , the point  $(\epsilon, \gamma/2)$  describes the following circle in the space  $(\epsilon, \gamma/2)$ :

$$[\epsilon - \frac{1}{2}(\epsilon_x + \epsilon_y)]^2 + \frac{1}{4}\gamma^2 = \frac{1}{4}(\epsilon_x - \epsilon_y)^2 + \epsilon_{xy}^2 \quad (28)$$

The  $(\epsilon, \gamma/2)$  space is called the *Mohr strain space*. As shown in Fig. 8, the Mohr circle of Eq. 28 is centered on the  $\epsilon$  axis at position  $\epsilon_m$  and has radius  $R$ :

$$\epsilon_m = \frac{1}{2}(\epsilon_x + \epsilon_y) \quad \text{and} \quad R = \sqrt{\frac{1}{4}(\epsilon_x - \epsilon_y)^2 + \epsilon_{xy}^2} \quad (29)$$

The strains  $(\epsilon_x, -\epsilon_{xy})$  and  $(\epsilon_y, \epsilon_{xy})$  are represented by points *B* and *A* in the Mohr plane of Fig. 8, respectively. Given a uniform strain state, the normal and shear strains along any direction are located on the circle with center position  $(0, \epsilon_m)$  and radius  $R$ . The principal strains are the intersections of the Mohr circle with the  $\epsilon$  axis (Eq. 27).

The definition and properties of the pole of strain are identical to that of stress (see Fig. 8). The pole can be used to calculate the principal strain directions and to find the orientation of the element undergoing the maximum angular distortion.

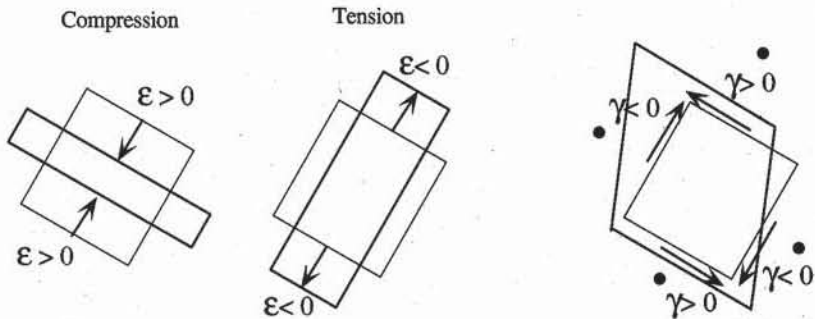


**Figure 7** Sign conventions for Mohr representations of strains in soil mechanics.

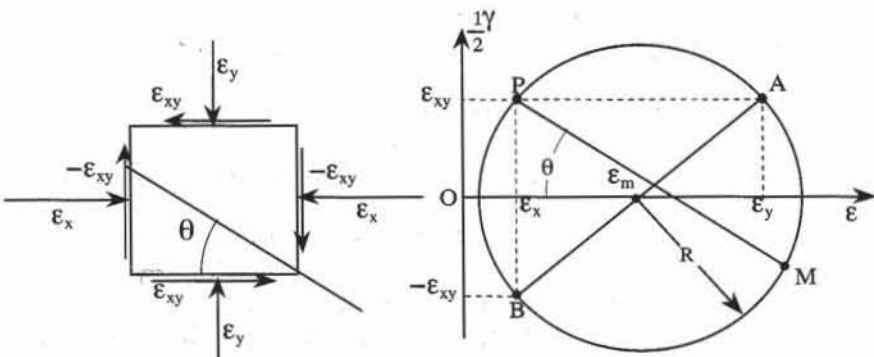


Figure 8 Construction of Mohr circle of strain in Mohr space.

### THREE-DIMENSIONAL STRAIN

As mentioned previously, soils undergo three-dimensional strains in the field and the laboratory. We discuss briefly the three-dimensional representations. In three dimensions, the strain tensor gives the  $x$ ,  $y$ , and  $z$  projections ( $\epsilon_{nx}$ ,  $\epsilon_{ny}$ ,  $\epsilon_{nz}$ ) of strain along the unit vector ( $n_x$ ,  $n_y$ ,  $n_z$ ):

$$\begin{pmatrix} \epsilon_{nx} \\ \epsilon_{ny} \\ \epsilon_{nz} \end{pmatrix} = \begin{pmatrix} \epsilon_x & \epsilon_{xy} & \epsilon_{xz} \\ \epsilon_{xy} & \epsilon_y & \epsilon_{yz} \\ \epsilon_{xz} & \epsilon_{yz} & \epsilon_z \end{pmatrix} = \begin{pmatrix} n_x \\ n_y \\ n_z \end{pmatrix} \quad (30)$$

The strain components are defined from the derivatives of the displacement components  $u$ ,  $v$ , and  $w$ , in the  $x$ ,  $y$ , and  $z$  directions:

$$\epsilon_x = -\frac{\partial u}{\partial x}, \quad \epsilon_y = -\frac{\partial v}{\partial y}, \quad \epsilon_z = -\frac{\partial w}{\partial z} \quad (31)$$

$$\gamma_{xy} = 2\epsilon_{xy} = -\frac{\partial u}{\partial y} - \frac{\partial v}{\partial x}, \quad \gamma_{yz} = 2\epsilon_{yz} = -\frac{\partial v}{\partial z} - \frac{\partial w}{\partial y}, \quad \gamma_{xy} = 2\epsilon_{xz} = -\frac{\partial w}{\partial x} - \frac{\partial u}{\partial z}$$

The principal strains  $\epsilon_1$ ,  $\epsilon_2$ , and  $\epsilon_3$  are found by solving the following eigenvalue problem:

$$\begin{pmatrix} \epsilon_x & \epsilon_{xy} & \epsilon_{xz} \\ \epsilon_{xy} & \epsilon_y & \epsilon_{yz} \\ \epsilon_{xz} & \epsilon_{yz} & \epsilon_z \end{pmatrix} \begin{pmatrix} n_x \\ n_y \\ n_z \end{pmatrix} = \epsilon \begin{pmatrix} n_x \\ n_y \\ n_z \end{pmatrix} \quad (32)$$

which leads to the same cubic equation and invariants as for stress.

As in the case of stress, the three-dimensional Mohr representation of strain is complicated. When two principal strains coincide, it becomes identical to the two-dimensional Mohr representation.

The volumetric strain which is equal to  $(V_0 - V)/V_0$ , where  $V_0$  is the initial volume and  $V$  the deformed volume, can be related to the strain components as follows

$$\epsilon_v = \frac{V_0 - V}{V_0} = \epsilon_x + \epsilon_y + \epsilon_z \quad (33)$$

**REVIEW QUESTIONS**

1. What is the sign convention for strain in soil mechanics?
2. What are the relations between strain and displacement? In what range do these equations apply?
3. What are the physical meanings of axial strain and shear strain?
4. What is the relation between volumetric strain and normal strain in two and three dimensions?
5. Do rigid-body rotation and translation create strain?
6. What is the physical meaning of principal strains?
7. What are the two representations that are used for strains?
8. Calculate the center and radius of the Mohr circle of two-dimensional strain in terms of  $\epsilon_x$ ,  $\epsilon_y$ , and  $\epsilon_{xy}$ .
9. Define the pole of the Mohr circle of strain. What is the use of the pole?
10. Under which condition is the Mohr representation useful in three dimensions?

**EXERCISE**

1. Show that the area change  $\epsilon_v$  of a unit area is equal to  $\epsilon_x + \epsilon_y$ , where  $\epsilon_x$  and  $\epsilon_y$  are axial strains in the  $x$  and  $y$  directions.

## 5-3 Stress-strain Relations

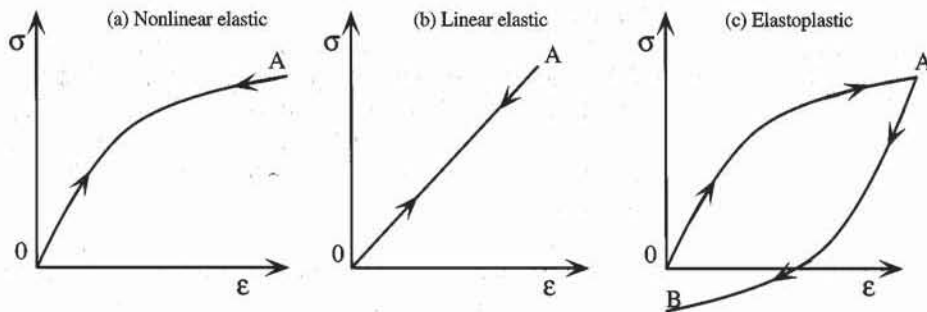
### INTRODUCTION

When soils are subjected to stress changes in the laboratory and in the field, they deform in complicated ways which can be represented in terms of stress-strain relationships. To describe the stress-strain relations of soils, we first survey some basic models.

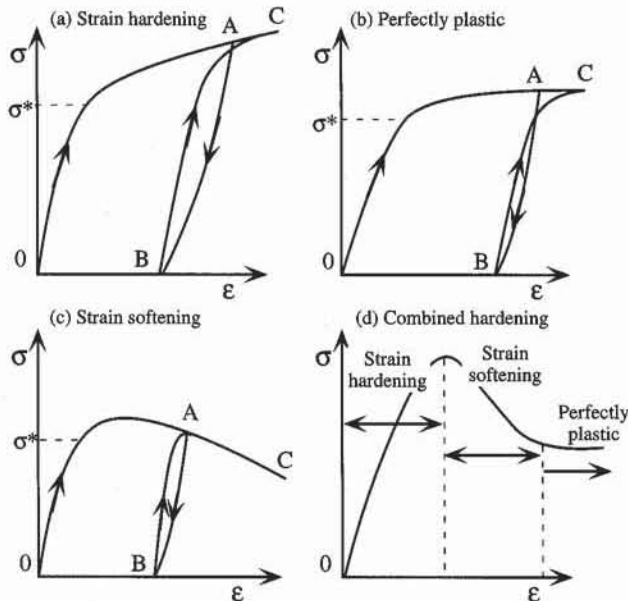
### FUNDAMENTALS OF STRESS-STRAIN RELATIONS

Figure 1 shows three major types of idealized stress-strain curves for materials subjected to loading and unloading. In the one-dimensional case, loading corresponds to an increase in applied strain or stress, while unloading is associated with a removal of strain or stress. Figure 1a shows identical responses during loading *OA* and unloading *AO*. The strain is fully recovered when the stress is removed. This reversibility characterizes *elastic* materials. The elastic material is *linear* when the stress-strain curve is straight (Fig. 1b), and *nonlinear* when it is curved (Fig. 1a). As shown in Fig. 1c, when a significant amount of strain is not recovered upon unloading, the material behavior is *irreversible* (or *elastoplastic*). The responses of nonlinear-elastic and elastoplastic models are different during unloading, but may be identical during loading. In one-dimension, the elastic and irreversible behaviors are distinguishable only after an unloading.

Figure 2 shows several types of irreversible behavior that are observed for soils. In all cases, the behavior is considered elastic below the yield stress  $\sigma^*$  and irreversible beyond  $\sigma^*$ . The yield stress  $\sigma^*$  marks the transition between reversible and irreversible behaviors. The determination of  $\sigma^*$  is not always trivial and may be subject to interpretations. In Fig. 2a, the material is *strain hardening*—it is stronger during the reloading *BC* than during the previous loading *OA*. The loading *OA* has hardened the material, thus the term *strain hardening*. In Fig. 2c, the material is *strain softening*—it is softer during the reloading *BC* than during loading *OA*. The previous loading *OA* has weakened the material of Fig. 2c. In Fig.



**Figure 1** Idealized types of stress-strain behaviors: (a) nonlinear elastic model, (b) linearly elastic model, and (c) elastoplastic model.



**Figure 2** Various types of elastoplastic behaviors: (a) strain hardening, (b) perfectly plastic, (c) strain softening, and (d) combination of a to c.

2b, the material does not harden or soften—it is *perfectly plastic*. The stress remains constant as the strain becomes very large. The curves  $OA$  and  $BC$  are similar, and are not influenced by previous loadings. As shown in Fig. 2d, soils may be strain hardening, strain softening, then perfectly plastic. This behavior, which is complicated to describe and to measure in the laboratory, is generally simplified for engineering purposes.

Figure 3 shows three simplified models used in soil mechanics: (a) rigid-perfectly plastic, (b) elastic-perfectly plastic, and (c) elastic-strain hardening. The *rigid-perfectly plastic* model of Fig. 3a is useful in stability analysis, to calculate the maximum load sustainable by a soil mass. However, this model provides only the failure stress, and cannot be used to calculate strain or displacement. The failure stress of soils, also referred to as *shear strength*, is described in Chapter 7-1. As shown in Fig. 3b, the *elastic-perfectly plastic* model first behaves elastically for stress  $\sigma$  smaller than  $\sigma^*$ , then becomes perfectly plastic when  $\sigma$  reaches  $\sigma^*$  (i.e.,

$\sigma$  remains constant with strain). The rigid-perfectly plastic model is a particular case of elastic-perfectly plastic model with a very stiff elastic response. As shown in Fig. 3c, in contrast to perfectly-plastic models, the *elastic-strain hardening* model has a yield stress that depends on the loading history. Initially, the yield stress is equal to  $\sigma_0^*$ , and becomes  $\sigma_A^*$  after the loading OA. Strain hardening is used in Chapter 6-1 to describe the irreversible behavior of clays during consolidation tests.

The behaviors in Figs. 1 to 3 are *rate independent* (or *inviscid*): they do not depend on the rate of loading or unloading. Rate dependency is generally neglected in most practical applications, except for the long-term settlement of fine-grained soils. In contrast to inviscid materials, *rate-dependent* (or *viscous*) materials depend on the rate of loading. As shown in Fig. 4, when the applied stress is constant, the strain increases with time (creep) for a viscous material but remains constant for an inviscid material. As shown in Fig. 5, when the applied strain is constant, the stress decreases with time (relaxation) for a viscous material but re-

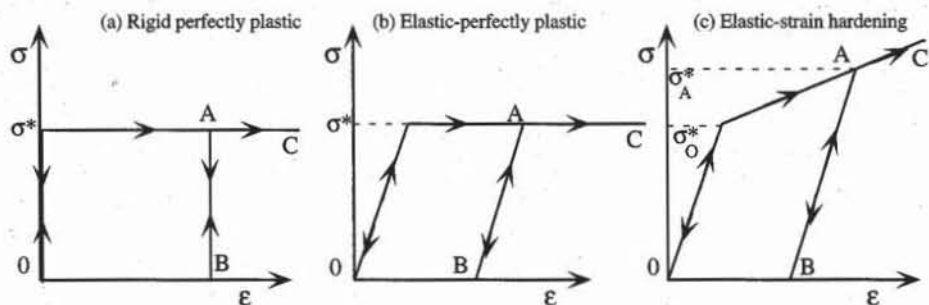


Figure 3 Idealized behaviors commonly used in soil mechanics.

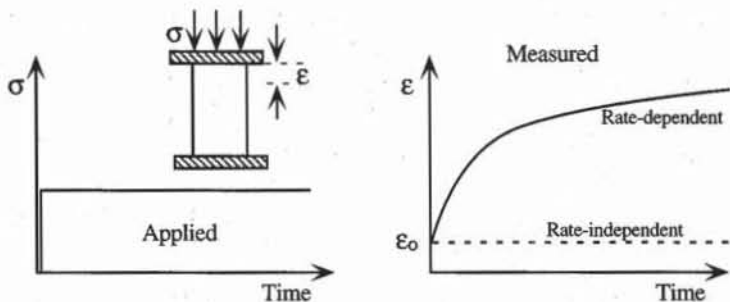


Figure 4 Creep effect in rate-dependent materials.

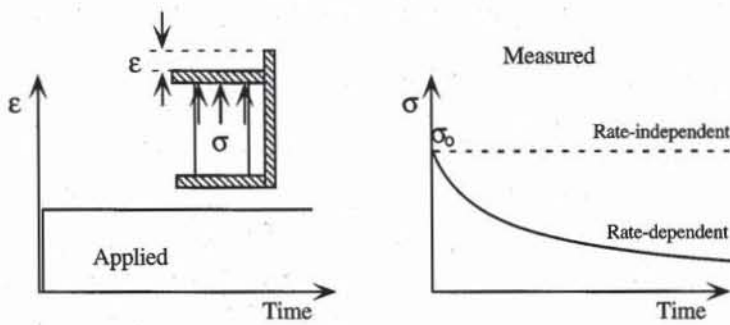


Figure 5 Stress-relaxation effect in rate-dependent materials.

mains constant for an inviscid material. Some features of the rate dependent behavior of soils are presented in Chapter 6-1.

## CONSTITUTIVE EQUATIONS FOR SOILS

The most accurate and general representation of soil behavior is based on constitutive equations. These advanced methods are capable of describing the nonlinear, irreversible, and rate-dependent stress-strain response of soils under various loadings including cyclic and dynamic conditions. Various types of constitutive equations have been proposed for soils (e.g., Bardet, 1986; Dafalias and Herrmann, 1985; Lade, 1977; and Schofield and Wroth, 1968). Refer to Chen and Saleeb (1982) for more information. When these constitutive equations are implemented in finite element programs, they can be used to solve geotechnical engineering problems such as boundary value problems. Examples of finite element applications to geotechnical engineering can be found in Zienkiewicz and Taylor (1991).

## REFERENCES

- BARDET, J. P., 1986, Bounding surface plasticity model for sands, *J. Eng. Mechanics*, ASCE, Vol. 112, No. 11, pp. 1198–1217.
- CHEN, W. F., and A. F. SALEEB, 1982, *Constitutive Equations for Engineering Materials*, John Wiley & Sons, New York, pp. 441–559.
- DAFALIAS, Y. F., and L.R. HERRMANN, 1985, Bounding surface plasticity: II. Applications to isotropic cohesive soils, *J. Eng. Mechanics*, ASCE, Vol. 111, No. 12, pp. 1263–1291.
- LADE, P. V., 1977, Elasto-plastic stress-strain theory for cohesionless soil with curved yield surfaces, *Int. J. Solids Structures*, Vol. 113, pp. 1019–1035.
- SCHOFIELD, A. N., and C. P. WROTH, 1968, *Critical State Soil Mechanics*, McGraw-Hill, London, U.K.
- ZIENKIEWICZ, O. C., and R. L TAYLOR, 1991, *The Finite Element Method*, McGraw-Hill, London, U.K.

# 5-4 Laboratory Tests for Determination of Stress–Strain–Strength of Soils

## STRESSES IN THE FIELD

Most geotechnical engineering analyses have to determine: (1) the initial stress state and stress history of the soil prior to any construction activity, and (2) the deformation and stability of soils resulting from the changes in stresses imposed by construction.

### Initial Stresses

The initial stresses in the field, also referred to as *in-situ* stresses, must first be defined due to their effects on nonlinear soil behavior. As shown in Fig. 1, for horizontal ground conditions, the *in-situ* stresses are expressed in terms of the effective vertical stress  $\sigma'_{z0}$  and effective horizontal stresses  $\sigma'_{x0}$  and  $\sigma'_{y0}$ :

$$\sigma'_{z0} = \gamma z - u_0 \quad \text{and} \quad \sigma'_{x0} = \sigma'_{y0} = K_0 \sigma'_{z0} \quad (1)$$

where  $\gamma$  is the average total unit weight of soil above depth  $z$ ,  $u_0$  the water pressure at depth  $z$ , and  $K_0$  the coefficient of lateral earth pressure at rest. The value of  $K_0$  depends on soil properties and loading history. The stress caused by the weight of soils above a given depth is called *overburden* stress. As shown in Fig. 1, the initial stress state can be represented in terms  $\sigma' - \tau$  and  $s' - t$ . Point A is on the line passing through the origin and having for slope  $(1 - K_0)/(1 + K_0)$ . The total vertical stress  $\sigma_{z0}$  and total horizontal stresses  $\sigma_{x0}$  and  $\sigma_{y0}$  corresponding to  $\sigma'_{z0}$ ,  $\sigma'_{x0}$  and  $\sigma'_{y0}$  are

$$\sigma_{z0} = \gamma z = \sigma'_{z0} + u_0 \quad \text{and} \quad \sigma_{x0} = \sigma_{y0} = K_0 \sigma'_{z0} + u_0 \quad (2)$$

### Stress Changes Applied by Engineered Constructions

As illustrated in Fig. 1, various types of constructions impose different stress changes to soils in the field. For all these loadings, the approximate changes in total and effective stresses are represented in  $\sigma' - \tau$  and  $s' - t$  spaces. In  $s' - t$

space, point  $A$  represents the initial effective stress state before construction. Segments  $AB$  and  $AB'$  represent the change in total stress and effective stress due to construction, respectively. Points  $B$  and  $B'$  have the same  $t$  component, but their  $s$  components are related through  $s_B = s_{B'} + u_B$  where  $u_B$  is the excess pore pressure induced by external loading. Points  $B$  and  $B'$  coincide when  $u_B = 0$ , but differ otherwise. Figure 1 shows the effective stress Mohr circles corresponding to points  $A$  and  $B$ , assuming that  $u_B = 0$ . Point  $B$  indicates a change in total stress, and not an absolute value of total stress; it does not account for the initial water pressure  $u_0$ .

The position of points  $B$  and  $B'$  varies depending on the type of construction and the location of the soil element. As shown in Fig. 1b, the soil element beneath the tank is subjected to an increase in vertical stress  $\Delta\sigma_z$ , which is represented by  $AB$  in  $s - t$  space. If the loading generates an excess pore pressure, the effective stress change is represented by  $AB'$  instead of  $AB$ . When the stress increment  $\Delta\sigma_z$  remains constant, point  $B'$  will move toward point  $B$  as the excess pore pressure dissipates with time. Behind the retaining wall of Fig. 1c (active case), the soil element is subjected to an increase in lateral stress  $\Delta\sigma_x$  while the vertical stress  $\sigma'_z$  remains constant. In front of the anchor of Fig. 1d (passive case), the soil element endures an increase in lateral stress  $\Delta\sigma_x$ . Beneath the center of the excavation of Fig. 1e, the soil is subjected to a decrease in vertical stress  $\Delta\sigma_z$ . As shown in Fig. 1f, the change in stress on a soil element depends on its position. Element C is subjected to an increase in vertical stress  $\Delta\sigma_z$ , element D to an increase in shear stress  $\Delta\tau_{xz}$ , and element E to a decrease in vertical stress  $\Delta\sigma_z$ .

## LABORATORY TESTING OF SOILS

Figure 1 illustrates the variety of loadings which constructions apply to soils. The objective of laboratory soil testing is to determine the stress-strain response and shear strength of soil samples by subjecting them to stress paths with direction and initial state similar to those in the field. The initial state of soil samples is generally altered after they have been removed from the field, transported to the laboratory, and cut into laboratory specimens. Reliable laboratory tests attempt first to reproduce the initial state, especially density, then to recreate the initial stresses and loading history by performing an isotropic or  $K_o$  consolidation.

We now briefly introduce the laboratory tests for determining the stress-strain-strength properties of soils, and describe the loading they apply to soil samples in terms of stress paths.

### Isotropic Test

The *isotropic test* simulates approximately the effects of overburden pressure on soils in the field by assuming  $K_0 = 1$ . As shown in Fig. 2, the isotropic test applies pressure  $\sigma_c$  to soil samples, generally in the triaxial cell (Fig. 8). The effective stresses are

$$\sigma'_x = \sigma'_y = \sigma'_z = \sigma_c \quad \text{and} \quad \tau_{xy} = \tau_{yz} = \tau_{zx} = 0 \quad (3)$$

Figure 2 shows the stress path of the isotropic loading in  $\sigma' - \tau$  and  $s' - t$  spaces. In  $\sigma' - \tau$  space, the Mohr circle is reduced to a point. In  $s' - t$  space,  $s' = \sigma_c$  and  $t = 0$ . In both spaces, the stress path is horizontal and the stress point moves with  $\sigma_c$ .

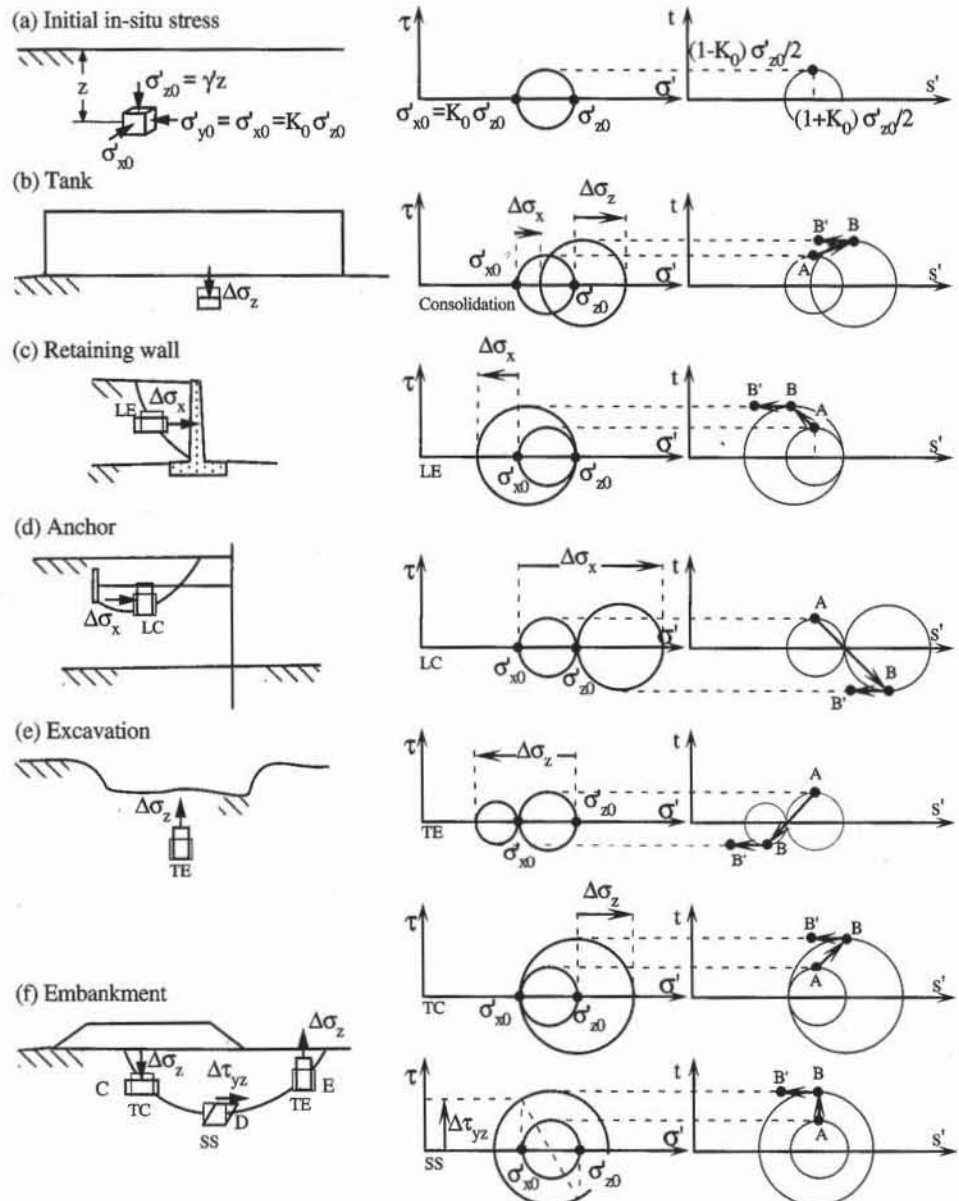


**Figure 1** Initial in-situ stresses, and stress changes resulting from some typical constructions in geotechnical engineering.

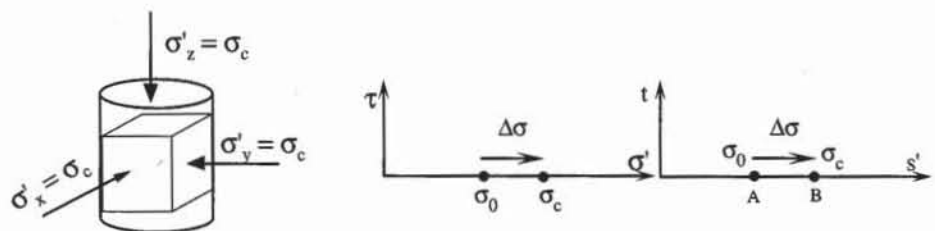


**Figure 2** Stresses acting on samples, and stress paths in  $\sigma' - \tau$  and  $s' - t$  spaces during an isotropic test.

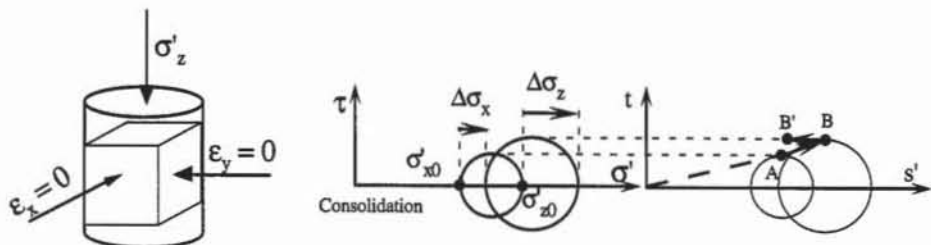


**Figure 3** Stresses and strains applied to sample, and stress paths in  $\sigma' - \tau$  and  $s'$  and  $t$  spaces during a  $K_0$  test.

### **$K_0$ Test**

The  $K_0$  test simulates an increase of overburden, and recreates the loading history and initial stress states of soils in the field. The loading conditions are

$$\sigma'_x = \sigma'_y, \tau_{xy} = \tau_{yz} = \tau_{zx} = 0, \text{ and } \varepsilon_x = \varepsilon_y = 0 \quad (4)$$

In contrast to the isotropic test, the  $K_0$  test applies different lateral and vertical stresses (i.e.,  $\sigma'_z \neq \sigma'_x$ ). This anisotropic loading can be performed in the triaxial test (Fig. 8) by controlling simultaneously the variation of axial stress  $\sigma_z$  and confining pressure  $\sigma_x$  so that the soil sample does not deform laterally.

### **Confined Compression Test**

The *confined compression test*, also referred to as *oedometer* and *consolidation test* (see Chapter 6-1), is used to calculate the settlement of footings, tanks and embankments. It simulates the vertical loading applied to soils in the field, including the overburden and changes in vertical stress due to constructions. As shown in Fig. 4, the soil sample, which is confined in a stiff ring, is loaded axially. The stiff ring prevents the sample from expanding radially, a condition which prevails for the soil element under the tank of Fig. 1b. Except for the axial strain  $\varepsilon_z$ , all strain components are assumed to be equal to zero:

$$\varepsilon_x = \varepsilon_y = \gamma_{xy} = \gamma_{yz} = \gamma_{zx} = 0 \quad (5)$$

During the consolidation test, the axial stress  $\sigma_z$  is varied in abrupt steps, and the resulting variation of  $\varepsilon_z$  is measured with time. The excess pore pressure generated by these abrupt loads dissipates gradually with time. The effective stress path, which cannot be represented exactly because the effective lateral stress is not measured, is assumed to be similar to the  $K_0$  stress path.



**Figure 4** Consolidation cell, and strains and stresses applied to samples during the confined compression test.

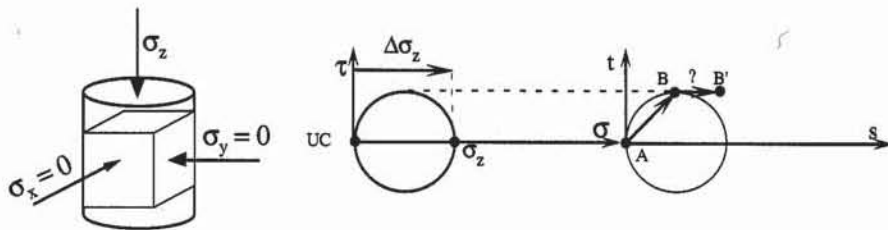


**Figure 5** Stresses acting on sample, and stress paths in  $\sigma - \tau$  and  $s - t$  spaces during unconfined compression tests.

### Unconfined Compression Test

The *unconfined compression test* (see Chapters 7-2 and 7-3) is a rapid means to obtain approximate values of the shear strength of fine-grained soils. As shown in Fig. 11, the total axial stress  $\sigma_z$  is applied to the sample which has no radial confinement. The total stresses are all equal to zero, except for axial stress  $\sigma_z$ :

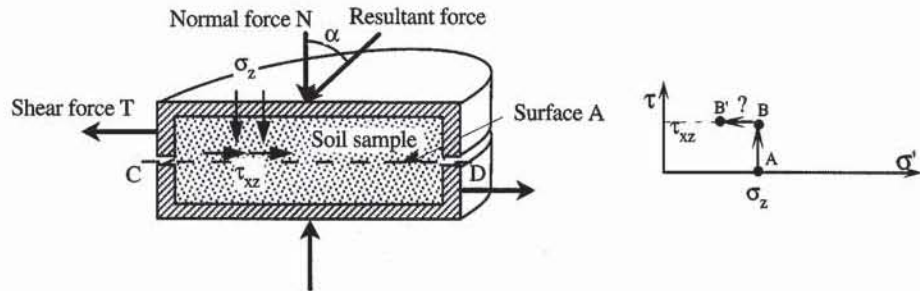
$$\sigma_x = \sigma_y = \tau_{xy} = \tau_{yz} = \tau_{zx} = 0 \quad (6)$$

Figure 5 shows the stress paths in  $\sigma - \tau$  and  $s - t$  spaces. The Mohr circle expands about A with  $\sigma_z$ . The effective stress path cannot be represented because the initial and excess pore pressures are undefined.

### Direct Shear Test

The *direct shear test* (see Chapters 7-4 and 7-5) simulates the effects of shear loads acting on a predetermined failure surface (e.g., the circular failure surface under the embankment of Fig. 1f). As shown in Fig. 6, the soil sample which is confined by two rigid boxes is subjected to the normal load  $N$ , and is sheared by the shear force  $T$ . If  $A$  is the area of surface CD, the shear stress acting on CD is  $\tau_{xz} = T/A$ , and the normal stress is  $\sigma_z = N/A$ . The stress path or Mohr circle cannot be drawn because  $\sigma_x$  is not defined. The strains are not uniform, and cannot be measured. The direct shear test is useful to determine the shear strength of soils, but not their stress-strain response.

As shown in Fig. 7a, the predecessor of the direct shear device—the double direct shear apparatus—was initially devised by Collin in 1846. The soil is placed in a split box, the central part of which is sheared by hanging weights. In the torsional direct shear test of Fig. 7b, the soil sample fills an annulus confined between two hollow annular caps. The torsional direct shear device allows us to apply larger shear displacement than the direct shear apparatus because the area of the shear surface remains constant.



**Figure 6** Direct shear cell and variation of stress on surface CD.

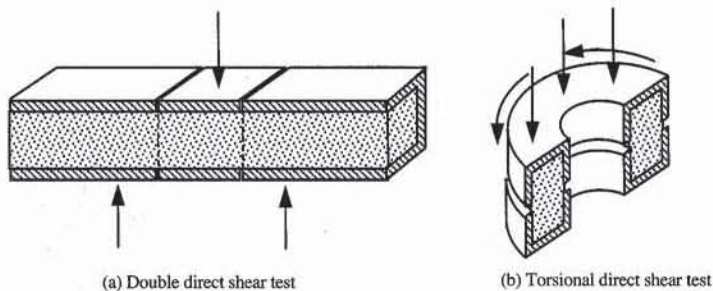


Figure 7 Double and torsional direct shear devices.

### Triaxial Test

The *triaxial test* (see Chapters 7-6 and 7-8) is one of the most reliable and useful laboratory tests for determining the stress-strain-strength characteristics of soils. It is more reliable than the unconfined compression test and direct shear test.

As shown in Fig. 8, the cylindrical soil specimen is encased within a rubber sleeve. The lower and upper caps are equipped with porous disks, and are connected to the drainage system. The lateral stress  $\sigma_3$  is applied by adjusting the confining pressure inside the triaxial chamber, and the axial stress  $\sigma_1$  is applied by pushing the piston.

The triaxial test is *unconsolidated* or *consolidated*, depending on whether the soil sample is consolidated or not before being sheared. During the consolidation phase, the stresses are increased gradually to recreate the initial stresses of specimens in the field. The samples can be isotropically or  $K_0$  consolidated.

During the shear phase following the consolidation phase, the stresses are varied to simulate the loadings applied to soils by constructions. The shear phase may be either drained or undrained. The test is *drained* when the drainage valves (*A* and *B* in Fig. 8) are open, so that water can drain without change in pore pressure. The test is *undrained* when the drainage valves are closed, so no water is allowed to drain from the sample. During undrained tests, there is excess pore pressure, and the total and effective stresses do not coincide. During drained tests, there is no pore pressure, and effective and total stresses are equal.

To summarize the consolidation and shear phases, the triaxial tests are labeled by using several letters including C or U for the consolidation phase (*Consolidated* or *Unconsolidated*), and D or U for drainage conditions during the shear phase (*Drained* or *Undrained*). Table 1 identifies additional tests, which combine several possible types of consolidation (none, isotropic, or  $K_0$ ), drainage conditions (drained or undrained), and variation of axial and lateral stresses (constant, increasing or decreasing). Drained tests are always consolidated.

The axial stress  $\sigma_1$  and lateral stress  $\sigma_3$  acting on the triaxial sample can be decreased, increased, or kept constant separately. This produces the  $s - t$  stress paths of Fig. 9 which are referred to as *Triaxial Compression* (TC), *Lateral Extension* (LE), *Triaxial Extension* (TE), and *Lateral Compression* (LC). Hereafter we describe only the stress paths during triaxial tests with isotropic consolidation. Those with  $K_0$  consolidated triaxial tests have already been shown in Fig. 1.

During the isotropically consolidated triaxial compression (TC), the axial stress  $\sigma_z$  is increased while the radial stress  $\sigma_x = \sigma_y$  is kept constant:

$$\sigma_x = \sigma_y = \sigma_c, \quad \text{and} \quad \tau_{xy} = \tau_{yz} = \tau_{zx} = 0 \quad (7)$$

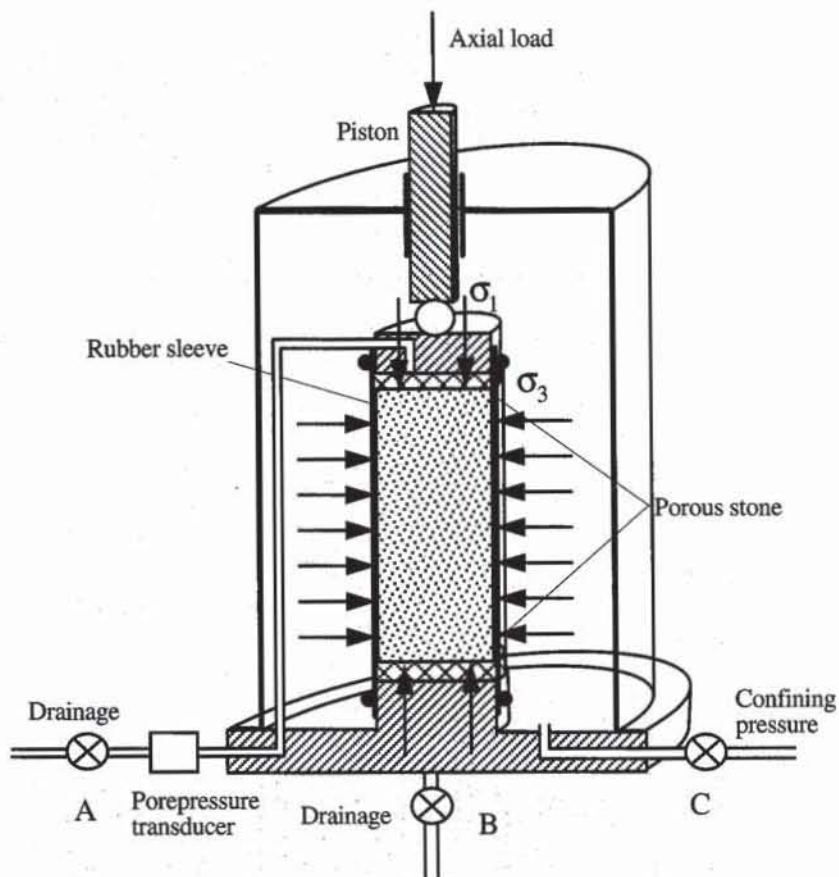


Figure 8 Experimental setup of triaxial test.

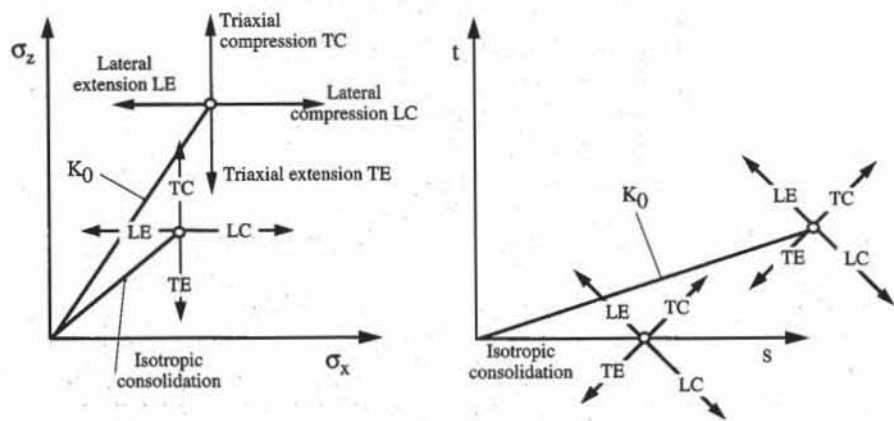
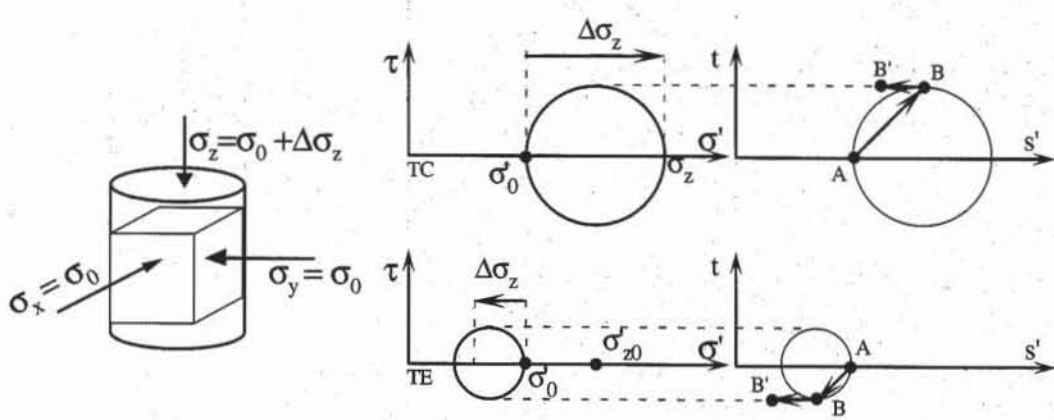


Figure 9 Stress paths in  $\sigma_x - \sigma_z$  and  $s - t$  spaces during isotropically and  $K_0$  consolidated triaxial compression (TC), triaxial extension (TE), lateral triaxial compression (LC), and lateral triaxial extension (LE).

**TABLE 1**

Various types of triaxial test

Appellations	Type of consolidation	Drainage conditions	Axial stress	Lateral stress	Full name
CD, CID, or CIDC	Isotropic	Drained	Increasing	Constant	Consolidated drained triaxial compression
CDE, or CIDE	Isotropic	—	Decreasing	—	Consolidated drained triaxial extension
CK <sub>0</sub> DC	K <sub>0</sub>	—	Increasing	—	K <sub>0</sub> consolidated drained triaxial compression
CK <sub>0</sub> DE	K <sub>0</sub>	—	Decreasing	—	K <sub>0</sub> consolidated drained triaxial extension
CDLC or CIDLC	Isotropic	—	Constant	Increasing	Consolidated drained lateral triaxial compression
CDLE or CIDLE	Isotropic	—	—	Decreasing	Consolidated drained lateral triaxial extension
CK <sub>0</sub> DLC	K <sub>0</sub>	—	—	Increasing	K <sub>0</sub> consolidated drained lateral triaxial compression
CK <sub>0</sub> DLE	K <sub>0</sub>	—	—	Decreasing	K <sub>0</sub> consolidated drained lateral triaxial extension
CU, CIU, or CIUC	Isotropic	Undrained	Increasing	Constant	Consolidated undrained triaxial compression
CK <sub>0</sub> U or CK <sub>0</sub> UC	K <sub>0</sub>	—	Increasing	Constant	K <sub>0</sub> consolidated undrained triaxial compression
CUE or CIUE	Isotropic	—	Decreasing	Constant	Consolidated undrained triaxial extension
CK <sub>0</sub> UE	K <sub>0</sub>	—	Decreasing	Constant	K <sub>0</sub> consolidated undrained triaxial extension
CULC or CIULC	Isotropic	—	Constant	Increasing	Consolidated undrained lateral triaxial compression
CULE or CIULE	Isotropic	—	—	Decreasing	Consolidated undrained lateral triaxial extension
CK <sub>0</sub> ULC	K <sub>0</sub>	—	—	Increasing	K <sub>0</sub> consolidated undrained lateral triaxial compression
CK <sub>0</sub> ULE	K <sub>0</sub>	—	—	Decreasing	K <sub>0</sub> consolidated undrained lateral triaxial extension
UU or UUC	None	—	Increasing	Constant	Unconsolidated undrained triaxial compression
UUE	None	—	Decreasing	Constant	Unconsolidated undrained triaxial extension



**Figure 10** Stress changes applied to samples and stress paths in  $\sigma' - \tau$  and  $s' - t$  spaces during isotropically consolidated drained and undrained triaxial compression (TC) and extension (TE) tests.

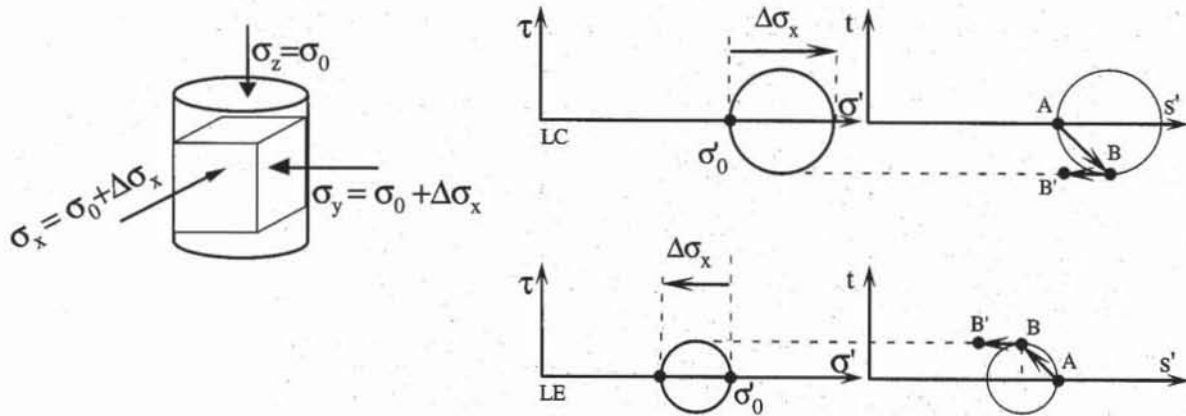


**Figure 11** Stress changes applied to samples and stress paths in  $\sigma' - \tau$  and  $s' - t$  spaces during isotropically consolidated drained and undrained lateral triaxial compression (LC) and extension (LE) tests.

Equation 7 also holds during triaxial extension (TE), in which the axial stress  $\sigma_z$  is decreased. Figure 10 shows the TC and TE stress paths in  $\sigma' - \tau$  and  $s' - t$  spaces. Point A represents the initial stress state, segment AB the change in total stress, and segment AB' the change in effective stress. B and B' coincide for drained tests, but differ for undrained tests due to excess pore pressure. For both loadings, the Mohr circle varies with  $\sigma'_z$  but keeps a fixed point (i.e.,  $\sigma'_x = \sigma'_y = \sigma_0$ ). The  $s' - t$  stress paths follow a straight line inclined at  $45^\circ$ .

Equation 7 applies also to lateral triaxial extension (LE) and lateral triaxial compression (LC), in which the axial stress  $\sigma_z$  is kept constant while the radial stress  $\sigma_x = \sigma_y$  varies. Figure 11 shows the LC and LE stress paths in  $\sigma' - \tau$  and  $s' - t$  spaces. The  $s' - t$  stress paths follow a straight line inclined at  $-45^\circ$ .

### Simple Shear Test

The *simple shear test* is an improved version of the direct shear test, which generates uniform stress and strain and is suitable for determining the stress-strain re-

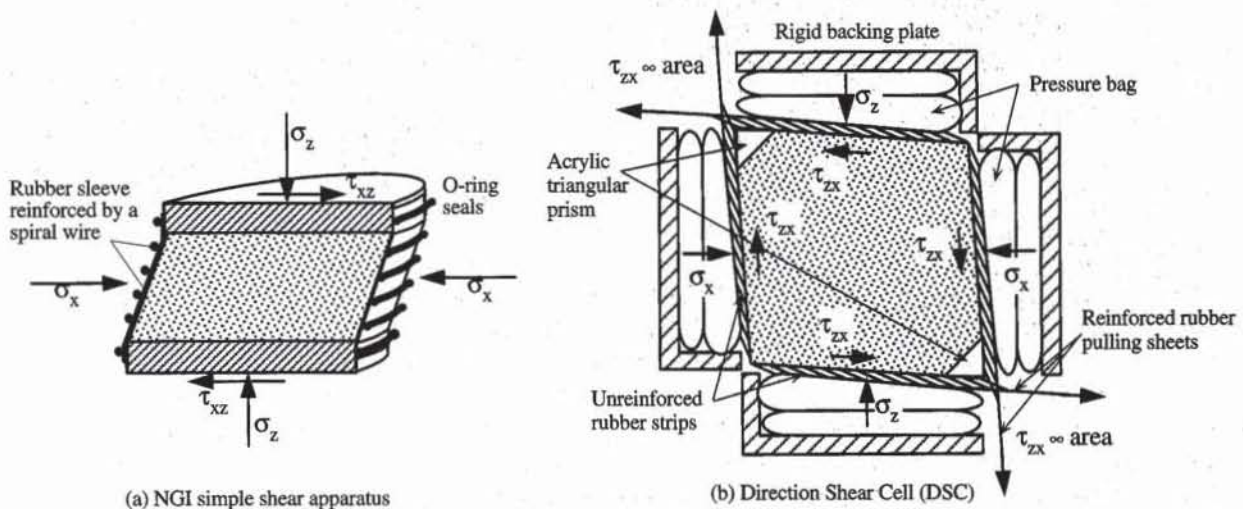


Figure 12 Simple shear devices.

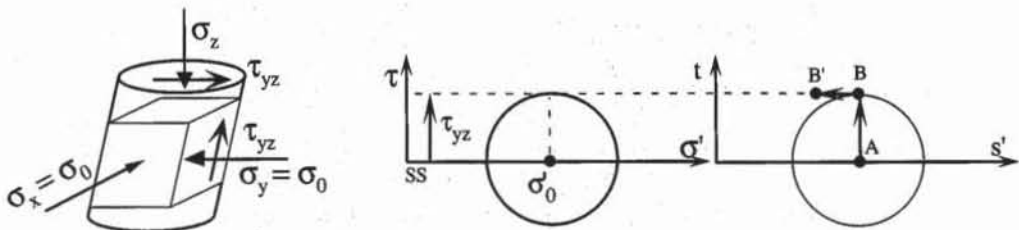
sponse of soils. In the simple shear apparatus of Fig. 12a, the cylindrical sample is confined in a rubber sleeve reinforced by a spiral wire. The confining pressure is transmitted to the soil sample through the rubber sleeve. The spiral wire prevents the sample from expanding radially, but not from being sheared.

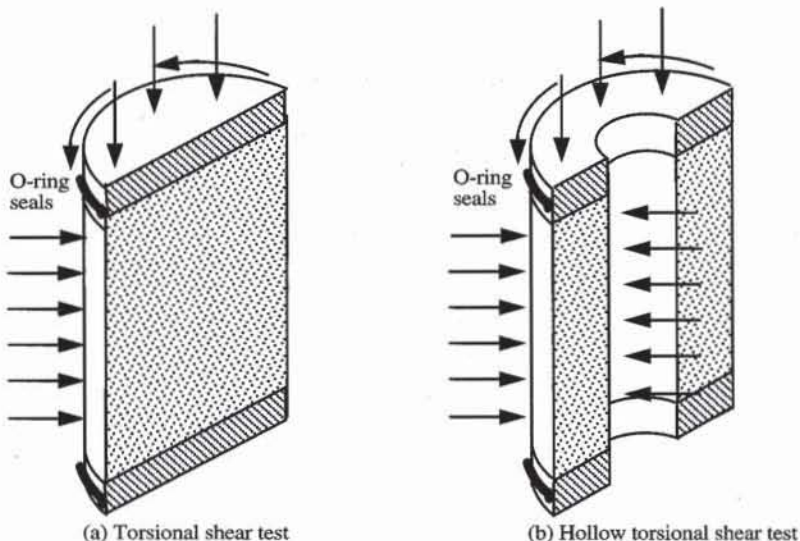
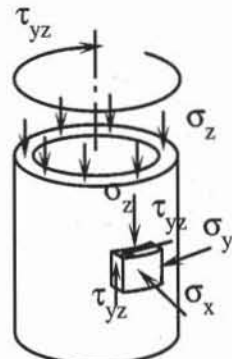
Like the triaxial test, the simple shear test has a consolidation and shear phase. During the shear phase,  $\sigma_x$ ,  $\sigma_y$ , and  $\sigma_z$  are kept equal to  $\sigma_o$  and the shear stress  $\tau_{yz}$  is increased:

$$\sigma_x = \sigma_y = \sigma_z = \sigma_o, \text{ and } \tau_{xy} = \tau_{xz} = 0 \quad (8)$$

Figure 13 shows the corresponding stress path in  $\sigma - \tau$  and  $s - t$  spaces.

In the simple shear device of Fig. 12b, also referred to as direct simple shear (Arthur et al., 1981), the rectangular sample is confined between two rigid boundaries, and four flexible boundaries. The normal stresses  $\sigma_x$  and  $\sigma_z$  are applied by pressure bags. The shear stress  $\tau_{zx}$  is applied by rubber strips attached to pulling sheets. There is no deformation in the  $y$  direction (i.e.,  $\epsilon_y = 0$ ), a condition which is known as plane strain. As shown in Fig. 12b, the controlled variation of lateral and shear stresses allows one to vary the orientation of the principal stresses.

Figure 13 Strains applied to samples, and stress paths in  $\sigma - \tau$  and  $s' - t$  spaces during the simple shear test of Fig. 12a.

**Figure 14** Torsional shear devices.**Figure 15** State of stress in hollow torsional apparatus (after Saada and Townsend, 1981).

### Torsional Test

In the *torsional shear test* of Fig. 14a, the soil cylinder is subjected to a twisting moment, which is applied through the ribbed top and bottom caps. The lateral confining pressure is applied to the specimen through the flexible rubber sleeve. The *hollow torsional device* of Fig. 14b is an improved version of the torsional device which maintains uniform strain across the specimen. There are inner and outer rubber sleeves that transmit the lateral pressure to both sides of the hollow soil specimen. As shown in Fig. 15, the axial and lateral stress and shear stress can be controlled in the hollow cylinder, which allows one to incline the orientation of the principal stresses. (Saada and Townsend, 1981).

### Plane Strain Compression Test

Plane strain experiments (e.g., Fig. 12b) are used to determine the properties of soils under plane-strain conditions (i.e.,  $\epsilon_y = 0$ ), which are found in the analysis of very long structures. Figure 16 shows another example of a plane strain apparatus where the soil sample which is encased in a flexible membrane is confined between two parallel glass plates and two loading platens.

### True Triaxial Apparatus

The *true triaxial apparatus* allows one to control independently the *three* normal stresses applied to cubical samples of soils. The term "true" is used to avoid confusion with the triaxial test which controls only stresses along two axes. Figure 17 shows the principle of a true triaxial apparatus with rigid platens. The cubical soil sample is encased in a rubber membrane. The six platens are activated by mechanical means so that they generate a rectangular shape. There is also an apparatus with a flexible membrane and a combination of both (e.g., Lade and Duncan, 1973). The true triaxial apparatus is a research tool which has been used to investigate three-dimensional soil behavior. It is rarely used in the practice of geotechnical engineering.

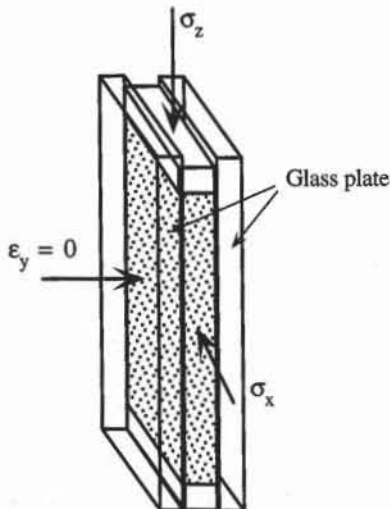


**Figure 16** Plane strain compression apparatus.

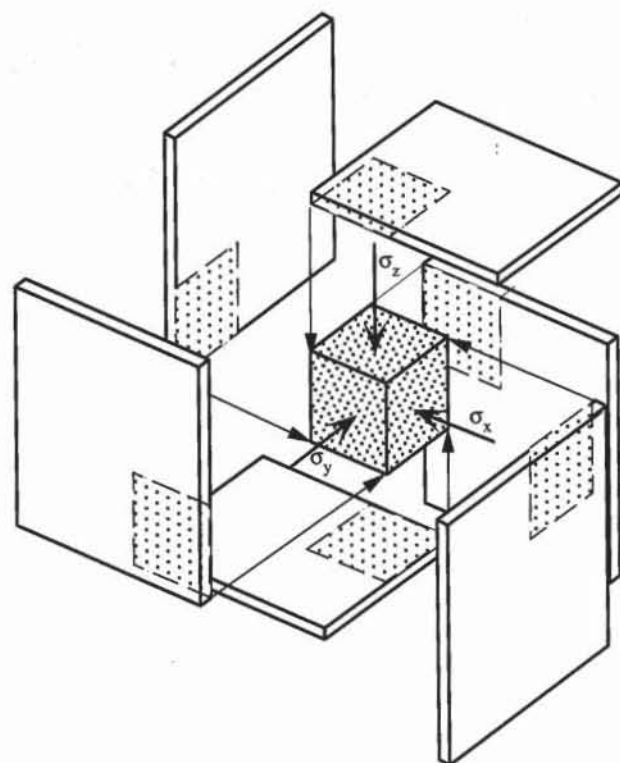


**Figure 17** True triaxial apparatus with rigid platens.

## REFERENCES

- ARTHUR, J. R. F., S. BEKENSTEIN, J. T. GERMAINE, and C. C. LADD, 1981, Stress path with controlled rotation of principal stress directions, in *Laboratory Shear Strength of Soils, ASTM Special Technical Publication 740*, R. N. Yong and F. C. Townsend, eds., American Society for Testing and Materials, Philadelphia, PA.
- COLLIN, A., 1856, *Experimental Investigation on Sliding in Clay Slopes*, Translated from French by W. R. Schriever, University of Toronto Press, 1956, Toronto, Canada.
- LADE, P. V., and J. M. DUNCAN, 1973, Cubical triaxial tests on cohesionless soils, *J. Soil Mech. Found. Eng. Div.*, ASCE, Vol. 99, No. 10, pp. 793–812.
- SAADA, A. S., and F. C. TOWNSEND, 1981, State-of-the-Art: Laboratory strength testing of soils, in *Laboratory Shear Strength of Soils, ASTM Special Technical Publication 740*, R. N. Yong and F. C. Townsend, eds., American Society for Testing and Materials, Philadelphia, PA, pp. 7–77.

# 5-5 Elastic Properties of Soils

Many constitutive models have been proposed to describe the behavior of soils observed in the laboratory. Linear isotropic elasticity is certainly the most elementary and convenient stress-strain relationship to use for describing the deformation of soils before they fail.

## ELASTICITY AND ELASTIC PROPERTIES

The isotropic linearly-elastic stress-strain relationship (or generalized Hooke's law) is defined as follows:

$$\begin{aligned}\varepsilon_x &= \frac{1}{E}(\sigma_x - v(\sigma_y + \sigma_z)) & \varepsilon_{xy} &= \frac{\tau_{xy}}{2G} \\ \varepsilon_y &= \frac{1}{E}(\sigma_y - v(\sigma_z + \sigma_x)) \quad \text{and} \quad \varepsilon_{yz} &= \frac{\tau_{yz}}{2G} \\ \varepsilon_z &= \frac{1}{E}(\sigma_z - v(\sigma_x + \sigma_y)) & \varepsilon_{xz} &= \frac{\tau_{xz}}{2G}\end{aligned}\quad (1)$$

where  $E$  is Young's modulus,  $v$  the Poisson ratio, and  $G$  the shear modulus  $= \frac{E}{2(1+v)}$ . Equation 1 can be inverted so that the stresses are functions of strains:

$$\begin{aligned}\sigma_x &= \lambda \varepsilon_v + 2G\varepsilon_x & \tau_{xy} &= 2G\varepsilon_{xy} \\ \sigma_y &= \lambda \varepsilon_v + 2G\varepsilon_y & \tau_{yz} &= 2G\varepsilon_{yz} \\ \sigma_z &= \lambda \varepsilon_v + 2G\varepsilon_z & \tau_{xz} &= 2G\varepsilon_{xz}\end{aligned}\quad (2)$$

where  $\varepsilon_v$  is the volumetric strain ( $\varepsilon_v = \varepsilon_x + \varepsilon_y + \varepsilon_z$ ), and  $\lambda$  is Lame's modulus ( $\lambda = \frac{vE}{(1+v)(1-2v)}$ ). Using Eq. 1, the mean pressure  $p$  is proportional to  $\varepsilon_v$ :

$$p = \frac{1}{3}(\sigma_x + \sigma_y + \sigma_z) = Be_v \quad (3)$$

where  $B$  is the bulk modulus ( $B = \frac{E}{3(1-2v)}$ ). An additional elastic constant—the constrained modulus  $M$ —relates axial strain and stress during a confined compression test where  $\epsilon_x = \epsilon_y = 0$ :

$$\sigma_z = M\epsilon_z \quad \text{and} \quad M = \frac{E(1-v)}{(1+v)(1-2v)} \quad (4)$$

For isotropic linearly elastic materials, there are six material constants:  $E$ ,  $v$ ,  $G$ ,  $\lambda$ ,  $B$ , and  $M$ . However, there are only two independent constants. The moduli  $E$ ,  $v$ ,  $G$ ,  $\lambda$ ,  $B$  and  $M$  can be expressed in terms of two other moduli as given in Table 1.

**TABLE 1**Relations among elastic moduli  $E$ ,  $G$ ,  $B$ ,  $v$ ,  $\lambda$ , and  $M$ 

	Shear modulus $G$	Young's modulus $E$	Constrained modulus $M$	Bulk modulus $B$	Lame modulus $\lambda$	Poisson ratio $v$
$G, E$	$G$	$E$	$\frac{G(4G-E)}{3G-E}$	$\frac{GE}{9G-3E}$	$\frac{G(E-2G)}{3G-E}$	$\frac{E-2G}{2G}$
$G, M$	$G$	$\frac{G(3M-4G)}{M-G}$	$M$	$M - \frac{4}{3}G$	$M - 2G$	$\frac{M-2G}{2(M-G)}$
$G, B$	$G$	$\frac{9GB}{3B+G}$	$B + \frac{4}{3}G$	$B$	$B - \frac{2}{3}G$	$\frac{3B-2G}{2(3B+G)}$
$G, \lambda$	$G$	$\frac{G(3\lambda+2G)}{\lambda+G}$	$\lambda + 2G$	$\lambda + \frac{2}{3}G$	$\lambda$	$\frac{\lambda}{2(\lambda+G)}$
$G, v$	$G$	$2G(1+v)$	$\frac{2G(1-v)}{1-2v}$	$\frac{2G(1+v)}{3(1-2v)}$	$\frac{2Gv}{1-2v}$	$v$
$E, B$	$\frac{3BE}{9B-E}$	$E$	$\frac{B(9B+3E)}{9B-E}$	$B$	$\frac{B(9B-3E)}{9B-E}$	$\frac{3B-E}{6B}$
$E, v$	$\frac{E}{2(1+v)}$	$E$	$\frac{E(1-v)}{(1+v)(1-2v)}$	$\frac{E}{3(1-2v)}$	$\frac{vE}{(1+v)(1-2v)}$	$v$
$B, \lambda$	$\frac{3}{2}(B-\lambda)$	$\frac{9B(B-\lambda)}{3B-\lambda}$	$3B-2\lambda$	$B$	$\lambda$	$\frac{\lambda}{3B-\lambda}$
$B, M$	$\frac{3}{4}(M-B)$	$\frac{9B(M-B)}{3B+M}$	$M$	$B$	$\frac{3B-M}{2}$	$\frac{3B(2M-1)+M}{3B(2M+1)-M}$
$B, v$	$\frac{3B(1-2v)}{2(1+v)}$	$3B(1-2v)$	$\frac{3B(1-v)}{1+v}$	$B$	$\frac{3Bv}{1+v}$	$v$

### Homogeneity and Isotropy

Equation 1 assumes that the samples are homogeneous and isotropic. *Homogeneity* specifies that the elastic properties are the same everywhere in the laboratory samples. This assumption holds for uniform samples with particles relatively small compared to the whole sample, but not for those with heterogeneous composition containing a few large particles. *Isotropy* postulates that the elastic properties are the same in all directions. This assumption applies to remolded laboratory samples constructed under isotropic conditions, but not to the soil samples which acquired directional, laminated and varved structures during their natural

deposition and stress history in the field. In this case, it may be preferable to use anisotropic, instead of isotropic, elasticity (see Chen and Seeb, 1982) to describe their directional behavior, at the cost of determining additional soil properties. Hereafter, we only use the isotropic linearly-elastic model and assume homogeneous samples. Homogeneity and isotropy are convenient assumptions to characterize the deformation properties of soils with a minimum number of parameters.

## ELASTIC RESPONSES IN CONVENTIONAL LABORATORY TESTS

The relations of elasticity can be simplified in the case of soil laboratory tests introduced in Chapter 5-3, namely, the isotropic, consolidation, triaxial, unconfined compression, and simple shear tests.

### Isotropic Test

For the isotropic test (Eq. 3.5-4), Eq. 1 gives the following elastic strains:

$$\varepsilon_x = \varepsilon_y = \varepsilon_z = \frac{1 - 2\nu}{E} \sigma_c \quad (5)$$

where  $\sigma_c$  is the applied pressure. Equation 5 implies that  $\varepsilon_v$  and  $\sigma_c$  are linearly related through

$$\varepsilon_v = \varepsilon_x + \varepsilon_y + \varepsilon_z = \frac{3(1 - 2\nu)}{E} \sigma_c = \frac{1}{B} \sigma_c \quad (6)$$

where  $B$  is the bulk modulus. As shown in Fig. 1, Eq. 6 predicts a linear relation between  $\sigma_c$  and  $\varepsilon_v$ , while experiments generally produce nonlinear relations. The experimental response can be fitted with straight lines, either tangent at the origin, which produces the initial bulk modulus  $B_i$ , or over a larger range of pressure, which gives the secant bulk modulus  $B_s$ . Only  $B$  can be measured in the isotropic test.  $E$  and  $\nu$  cannot be defined individually.

Figure 2 shows the experimental response of the dense Sacramento River sand during an isotropic loading ABD, and two cycles of unloading - reloading BCB and DED. The response during loading is softer than that during the cycles of unloading and reloading. The straight lines defined by  $B_i$  and  $B_s$  crudely approximate the nonlinear stress-strain response. As shown in Fig. 3,  $B_s$  is calculated at points A, C and E of Fig. 2 for the loading and unloading - reloading cycles.  $B_s$  approximately increases with the square root of pressure.

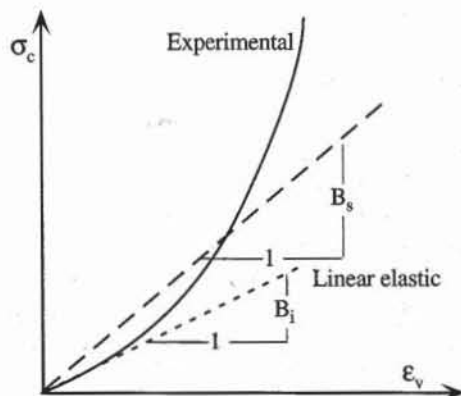


**Figure 1** Experimental response, and initial and secant bulk moduli during an isotropic test.

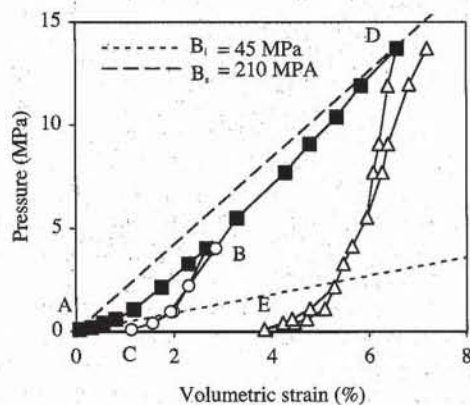


**Figure 2** Experimental stress-strain response, initial and secant bulk moduli during isotropic loading (solid points) and two cycles of unloading – reloading (hollow points) on dense Sacramento River sand (data after Lee and Seed, 1967).

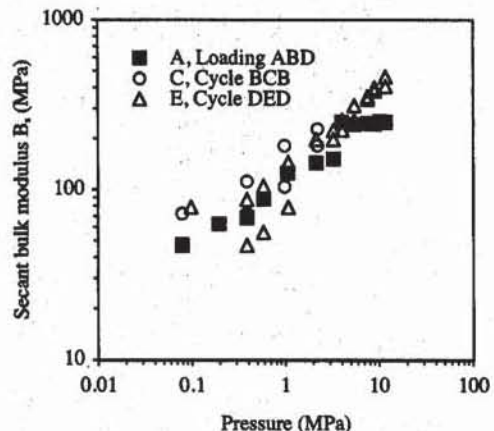


**Figure 3** Variation of secant bulk modulus \$B\_s\$ with pressure at points A, C, and E for the test of Fig. 2.

### Unconfined Compression Test

For the unconfined compression test (Eq. 6.5-4), Eq. 1 implies that \$\sigma\_z\$ and \$\varepsilon\_z\$ are linearly related and gives the following elastic strains,

$$\varepsilon_z = \frac{1}{E} \sigma_z, \quad \varepsilon_x = \varepsilon_y = -\frac{\nu}{E} \sigma_z = -\nu \varepsilon_z \quad (7)$$

As shown in Fig. 4, the experimental response may be approximated by drawing a straight line through the origin to obtain the initial Young's modulus \$E\_i\$, or over a larger strain range to get a secant Young's modulus \$E\_s\$. Figure 5 shows the measured response of a remolded clay during the unconfined compression test (\$E\_i = 4 \text{ MPa}\$, and \$E\_s = 0.5 \text{ MPa}\$ at \$\varepsilon\_z = 16\%\$). As shown in Fig. 6, \$E\_s\$ decreases gradually from \$E\_i\$ to zero with \$\varepsilon\_z\$. The Poisson ratio \$\nu\$ cannot be calculated from the unconfined compression test.

### Drained Triaxial Compression Test

It is convenient to reset the stresses and strains to zero at the beginning of shear, and to introduce the stress changes \$\Delta\sigma\_x\$, \$\Delta\sigma\_y\$, and \$\Delta\sigma\_z\$:

$$\Delta\sigma_x = \sigma'_x - \sigma_0, \quad \Delta\sigma_y = \sigma'_y - \sigma_0, \quad \text{and} \quad \Delta\sigma'_z = \sigma'_z - \sigma_0 \quad (8)$$

where \$\sigma\_0\$ is the confining pressure. Equation 9.5-4 implies that \$\Delta\sigma\_x = \Delta\sigma\_y = 0\$. Using Eq. 8, the triaxial test gives the same elastic strain and linear relations as the unconfined compression:

$$\varepsilon_z = \frac{1}{E} \Delta\sigma_z, \quad \varepsilon_x = \varepsilon_y = -\frac{\nu}{E} \Delta\sigma_z = -\nu \varepsilon_z \quad (9)$$

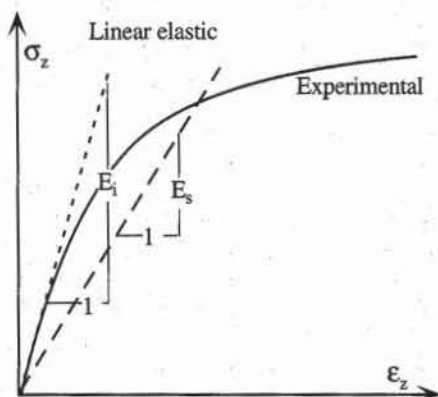


**Figure 4** Experimental stress-strain response, and initial and secant Young's moduli during an unconfined compression test.

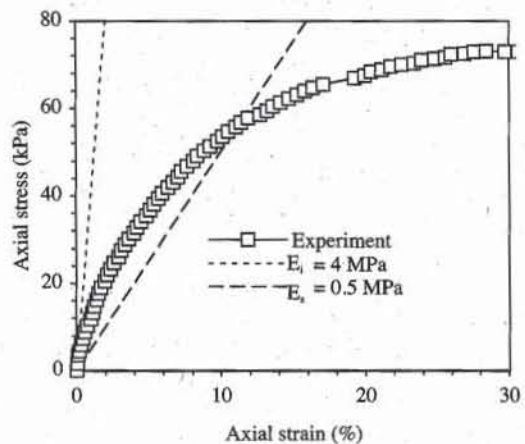


**Figure 5** Measured stress-strain response, initial and secant Young's moduli during unconfined compression of remolded Aardvack clay.

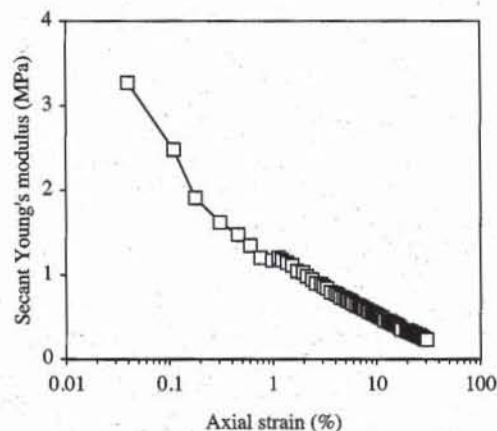


**Figure 6** Variation of secant Young's modulus  $E_s$  versus axial strain in the test of Fig. 5.

and  $\epsilon_v = \epsilon_x + \epsilon_y + \epsilon_z = (1 - 2\nu) \epsilon_z$ . As shown in Fig. 7, the slope of the theoretical straight line is  $E$  for the stress-strain response and  $1 - 2\nu$  for the volumetric response. The experimental response may be approximated with straight lines either tangent at the origin, which produces the initial moduli  $E_i$  and  $v_i$ , or over a larger strain range, which gives the secant moduli  $E_s$  and  $v_s$ . The volume change of the soil sample is measured directly in the drained triaxial test. For theoretical and practical reasons, the values of  $\nu$  must be kept between 0 and 0.5.

Figures 8 and 9 show the stress-strain and volumetric responses of dense Sacramento River sand during a drained triaxial compression test at constant confining pressure  $\sigma'_3$ . As shown in Fig. 9, the axial stress  $\sigma'_1$  is divided by  $\sigma'_3$ . The initial moduli are  $E_i = 375$  MPa and  $v_i = 0.25$ ; and the secant moduli are  $E_s = 50$  MPa and  $v_s = 0.6$  for axial strain  $\epsilon_z = 5\%$ . As shown in Figs. 10 and 11,  $E_s$  decreases from its maximum value  $E_i$  with  $\epsilon_z$ , while  $v_s$  increases from  $v_i$  and exceeds 0.5 when  $\epsilon_z > 2\%$ . The fact that  $v_i > 0.5$  is caused by the dilatation of the soil specimen during shear. Due to theoretical considerations, the values of  $v_s$  larger than 0.5 cannot be used in engineering analysis; they would produce negative values for the secant bulk modulus, constrained modulus, and Lame's modulus (see Table 1).

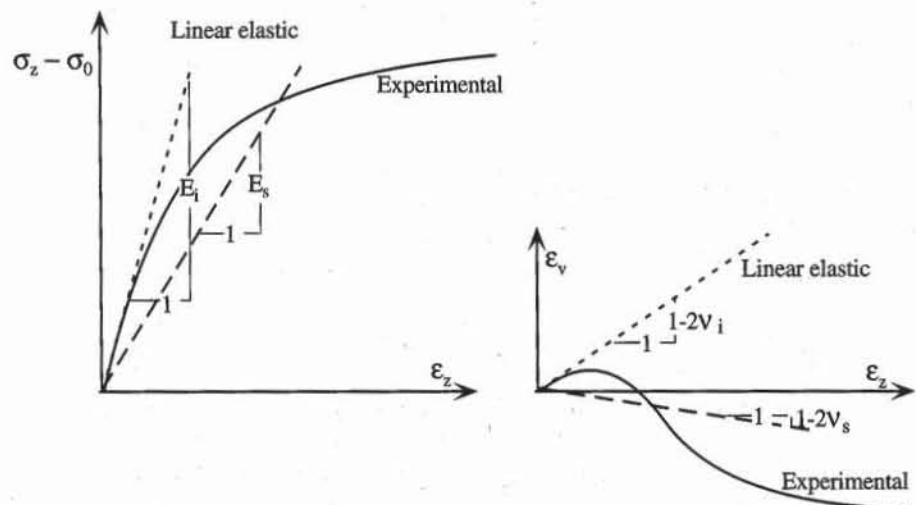


**Figure 7** Experimental responses, and initial and secant Young's modulus and Poisson ratio during a drained triaxial compression test.

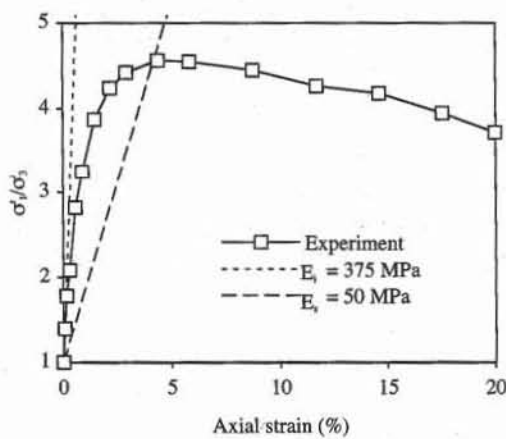


**Figure 8** Measured stress-strain response of dense Sacramento River sand, initial and secant Young's moduli during drained triaxial compression at 588 kPa confining pressure (data after Lee and Seed, 1967).

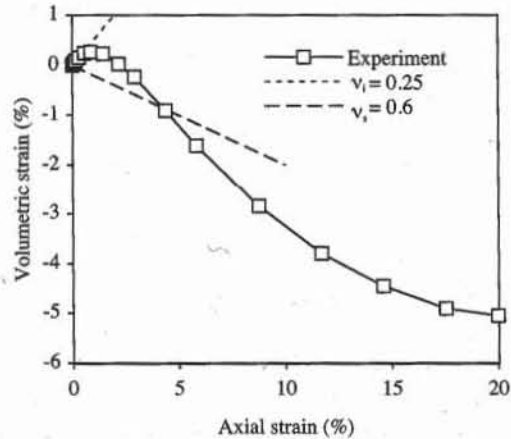


**Figure 9** Measured volumetric response of dense Sacramento River sand, initial and secant Poisson ratios during the test of Fig. 8.

### Confined Compression Test

For the confined compression test (Eq. 5.5-4), Eq. 1 gives the following elastic strain and linear relations:

$$\varepsilon_v = \varepsilon_z = \frac{1}{M} \sigma'_z \quad \text{and} \quad M = \frac{E(1-\nu)}{(1+\nu)(1-2\nu)} \quad (10)$$

$$\sigma'_x = \sigma'_y = K_0^e \sigma'_z \quad \text{and} \quad K_0^e = \frac{\nu}{1-\nu}$$

where  $K_0^e$  is the elastic coefficient of lateral earth pressure at rest, and  $M$  is the constrained modulus.

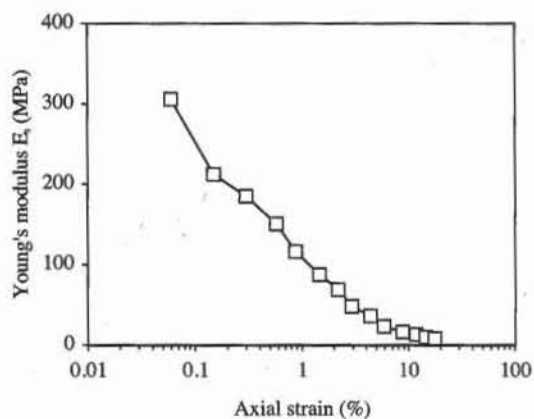


**Figure 10** Variation of secant Young's modulus with axial strain in the test of Fig. 8.

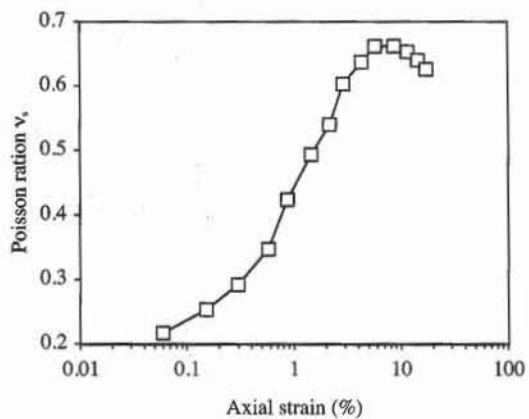


**Figure 11** Variation of secant Poisson ratio with axial strain in the test of Fig. 8.

As shown in Fig. 12, the initial constrained modulus  $M_i$  and secant modulus  $M_s$  approximate the experimental response at the origin, and over a larger strain range, respectively. Figure 13a shows the measured stress-strain response of San Francisco Bay mud subjected to confined compression test.  $M_i = 0.14$  MPa, and  $M_s = 0.09$  MPa at  $\epsilon_z = 25\%$ . As shown in Fig. 13b,  $M_s$  first decreases then increases with axial strain, due to an increase in radial stress.

### Simple Shear Test

For the simple shear test (Eq. 8.5-4), Eq. 1 gives the following elastic strain and linear relations:

$$\gamma_{yz} = \frac{1}{G} \tau_{yz}, \quad \text{and} \quad \epsilon_x = \epsilon_y = \epsilon_z = \gamma_{xz} = \gamma_{xy} = 0 \quad (11)$$

where  $G$  is the elastic shear modulus.

As shown in Fig. 14, the initial shear modulus  $G_i$  and secant shear modulus  $G_s$  approximate the experimental response at the origin, and over a larger strain range, respectively.

### TYPICAL VALUES OF ELASTIC CONSTANTS

Tables 2 to 4 list typical ranges of values of Young's modulus  $E$  and Poisson ratio  $\nu$  for various soils, rocks, and other materials.

The values of  $E$  for rocks in Table 2 are computed at confining pressures between 300 and 500 MPa.  $E$  varies from 7 GPa for partially decomposed granite to 200 GPa for steel. In contrast to rocks and metals, soils have a much broader range of  $E$  values. In Table 3, the lowest values for  $E$  (0.4 MPa) are observed for soft clay and peat; the largest (1.4 GPa) for dense gravels and glacial till. Loose sands, silts and clays have generally smaller values of  $E$  than rocks. However, dense gravels and hard clays may have values of  $E$  similar to those of weathered and decomposed sedimentary rocks. The values of elastic properties listed in Tables 2 and 3 should be considered as estimates that may vary widely from actual values. The elastic properties of soils are influenced by a number of factors, which

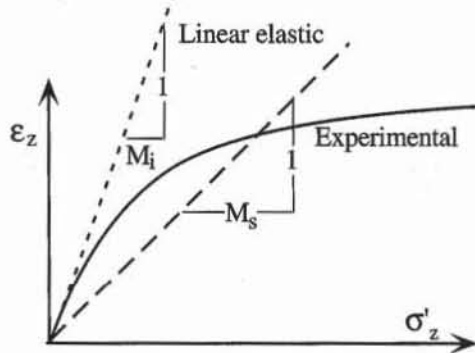


**Figure 12** Experimental responses, initial and secant constrained moduli during a confined compression test.

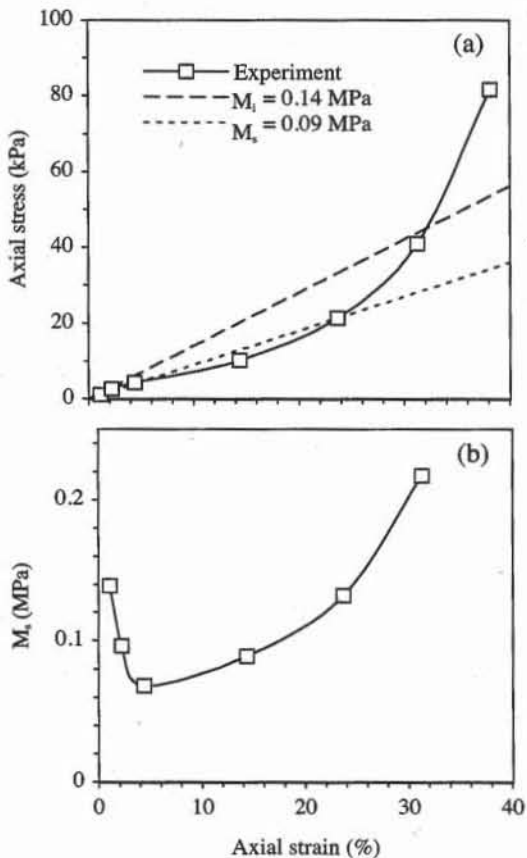


**Figure 13** Results of confined compression of San Francisco Bay mud: (a) measured stress-strain response, initial and secant constrained moduli, and (b) variation of secant constrained modulus  $M_s$  with axial strain (data after Holtz and Kovacs, 1981).

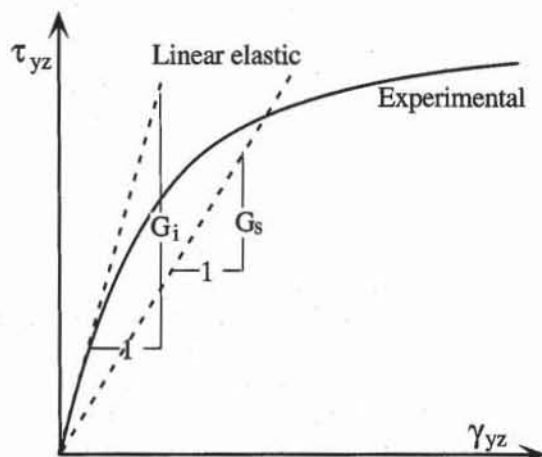


**Figure 14** Experimental responses, initial and secant shear moduli during a simple shear test.

**TABLE 2**

Values of Young's modulus and Poisson ratio for various materials.

Material	Young's modulus (GPa)	Poisson ratio	References
Amphibolite	93-121	0.28-0.30	Lambe and Whitman (1979)
Anhydrite	68	0.30	—
Diabase	87-117	0.27-0.30	—
Diorite	75-108	0.26-0.29	—
Dolomite	110-121	0.30	—
Dunite	149-183	0.26-0.28	—
Feldspathic Gneiss	83-118	0.15-0.20	—
Gabbro	89-127	0.27-0.31	—
Granite	73-86	0.23-0.27	—
Limestone	87-108	0.27-0.30	—
Marble	87-108	0.27-0.30	—
Mica Schist	79-101	0.15-0.20	—
Obsidian	65-80	0.12-0.18	—
Oligoclase	80-85	0.29	—
Quartzite	82-97	0.12-0.15	—
Rock salt	35	0.25	—
Slate	79-112	0.15-0.20	—
Ice	7.1	0.36	—
Aluminium	55-76	0.34-0.36	—
Steel	200	0.28-0.29	—
Granite sound	31-57	0.15-0.24	Converse (1962)
Granite partially decomposed	7-14	0.15-0.24	—
Limestone	21-48	0.16-0.23	—
Sound, intact igneous and metamorphics	57-96	0.25-0.33	Hunt (1986)
Sound, intact sandstone and limestone	38-76	0.25-0.33	—
Sound intact shale	10-40	0.25-0.33	—
Coal	10-20	—	—

include type of soil, water content, density, void ratio, fabric anisotropy, temperature, time, stress history, consolidation stress, applied shear stress, initial stress state, rate of strain, degree of sample disturbance, testing conditions, amplitude, and direction of stress changes.

As shown in Table 3, the Poisson ratio  $\nu$  has a small range of variation (i.e., 0 to 0.45). When  $\nu = 0.5$ , the material is incompressible,  $G = E/3$  and  $B \rightarrow \infty$ .

#### Variation of Initial Shear Modulus with Pressure, Overconsolidation Ratio and Void Ratio

Figure 15 shows the variation of secant shear modulus  $G_s$  with shear strain amplitude  $\gamma$  which was obtained from resonant column tests on Nevada sand. Resonant column tests are dynamic tests which are described in Kramer (1996). During these dynamic tests,  $G_s$  is first equal to the initial modulus  $G_i$ , which is also referred to as  $G_{\max}$ , then decreases when  $\gamma$  exceeds 0.001%.

As shown in Fig. 16,  $G_{\max}$  varies with the mean effective pressure  $p'$  [ $p' = (\sigma'_1 + \sigma'_2 + \sigma'_3)/3$ ]. Several empirical models have been proposed for the initial shear modulus  $G_{\max}$ . Hardin and Drnevich (1972) and Hardin (1978) proposed that

$$G_{\max} = \frac{198}{0.3 + 0.7e^2} OCR^k \sqrt{p'} \text{ (MPa)} \quad (11)$$

**TABLE 3**

Approximate values of Young's modulus in MPa for various soils

Soil group	Soil type	Bowles (1988)	Cernica (1995)	Converse (1962)	Hallam et al. (1978)	Hunt (1986)
Organic soil	Muck	—	—	0.5–3.5	—	—
	Peat	—	—	—	0.4–1	—
		—	—	—	0.8–2	—
Clay	Very soft	2–15	—	—	—	—
	Soft	2–25	3	—	1–3	2–4
	Medium	15–50	7	—	—	—
	Stiff	—	—	—	2.5–5	8–19
	Weak plastic	—	—	1.4–4	—	—
	Stiff plastic	—	—	4.2–8	—	—
	Semi-firm	—	—	—	5–10	—
	Semi-solid	—	—	6.9–14	—	—
	Hard	50–100	14	—	—	8–19
	Sandy	25–250	36	—	—	—
	Boulder clay, solid	—	—	—	30–100	—
Silt	Silt	2–20	—	—	3–10	2–19
	Soft, slightly clayey sea silt	—	—	—	2–5	—
	Soft, very strongly clayey silt	—	—	—	0.5–3	—
	Soft	—	—	—	4–8	—
	Semi-firm	—	—	—	5–20	—
Sand	Loose	10–25	15	10–21	20–80	10–29
	Medium	—	—	—	50–150	29–48
	Dense	50–81	80	52–83	49–78	48–77
	Silty	5–20	—	—	—	—
Gravel	Loose	50–150	100	—	—	29–77
	Dense	100–200	150	102–204	—	96–192
Gravel	Gravel without sand	—	—	—	100–200	—
	Coarse gravel, sharp edged	—	—	—	150–300	—
Loess		14–60	—	—	—	14–58
Glacial till	Loose	10–150	—	—	—	—
	Dense	150–720	—	—	—	—
	Very dense	500–1440	—	—	—	—

Note: Actual values may vary widely from those shown.

**TABLE 4**

Approximate values of Poisson ratio for various soils

Soil group	Soil type	Bowles (1988)	Cernica (1995)	Converse (1962)	Hunt (1986)	Poulos (1975)
Clay	Soft	—	0.4	—	—	—
	Medium	—	0.3	—	—	0.3–0.35
	Hard	—	0.25	—	—	—
	Stiff plastic	—	—	0.4–0.45	—	—
	Saturated	0.4–0.5	—	—	—	—
	Unsaturated	0.1–0.3	—	—	—	—
	Soft normally consolidated	—	—	—	—	0.35–0.45
	Stiff overconsolidated	—	—	—	—	0.1–0.3
	Sandy	0.2–0.3	0.25	—	—	—
Silt		0.3–0.35	—	—	0.3–0.35	—
Loess		0.1–0.3	—	—	0.1–0.3	—
Sand	Loose	—	0.2	—	0.2–0.35	0.35–0.4
	Medium	—	—	—	—	0.3–0.35
	Dense	0.3–0.4	0.3	0.3–0.36	0.3–0.4	0.25–0.3
Gravel	Loose	—	0.2	—	—	—
	Dense	—	0.3	—	—	—

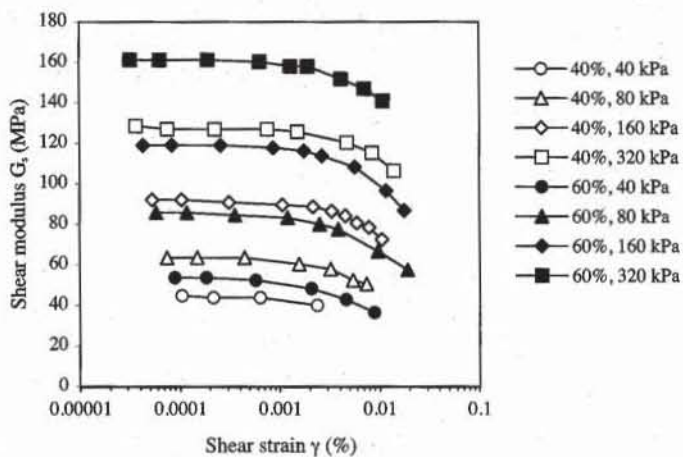


**Figure 15** Variation of secant shear modulus  $G_s$  with shear strain amplitude during resonant column tests at various confining pressures for Nevada sand at 40 and 60% relative density (data after Arulmoli et al., 1992).

where  $e$  is the void ratio,  $OCR$  the overconsolidation ratio,  $k$  an overconsolidation ratio exponent given in Table 5, and  $p'$  the mean effective pressure in MPa.  $OCR = p'_{\max}/p'$  where  $p'_{\max}$  is the largest value of  $p'$  that the soil underwent in its past.  $OCR = 1$  for normally consolidated clay and  $OCR > 1$  for overconsolidated soils (see Chapter 6-1). Jamiolkowski et al (1991) suggested that

$$G_{\max} = \frac{198}{e^{1.3}} OCR^k \sqrt{p'} \text{ (MPa)} \quad (12)$$

Seed and Idriss (1970) proposed that

$$G_{\max} = K \sqrt{p'} \text{ (MPa)} \quad (13)$$

where  $K$  is given in Table 6. As shown in Fig. 16, Eqs. 11 to 13 are equally capable of describing the variation of  $G_{\max}$  for Nevada sand at relative density  $D_r = 40$  and 60% ( $e = 0.736$  and 0.661), respectively.

**TABLE 5**  
Overconsolidation ratio  
exponent  $k$  (after Hardin and Drnevich, 1972).

Plasticity index (%)	$k$
0	0.00
20	0.18
40	0.30
60	0.41
80	0.48
$\geq 100$	0.50

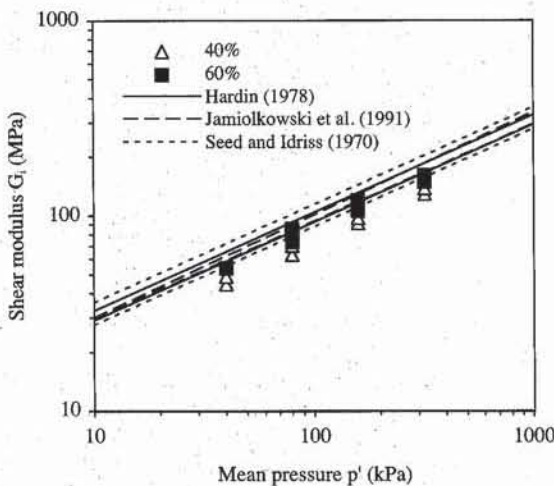


**Figure 16** Variation of initial shear modulus  $G_i$  with mean effective pressure  $p'$  measured in the tests of Fig. 15.

**TABLE 6**  
Estimation of  $K$  (adapted  
from Seed and Idriss, 1970).

e	K	$D_f(\%)$	K
0.4	484	30	235
0.5	415	40	277
0.6	353	45	298
0.7	304	60	360
0.8	270	75	408
0.9	235	90	484

#### Variation of Elastic Properties with Strain

The variation of shear modulus  $G$  with shear strain can also be represented in the static triaxial test conditions by introducing the equivalent shear strain  $\varepsilon_z - \varepsilon_x$ . During the triaxial test, Eq. 1 becomes:

$$\frac{1}{2}(\sigma_z - \sigma_x) = G(\varepsilon_z - \varepsilon_x), \quad \varepsilon_x = \varepsilon_y, \quad \text{and} \quad \gamma_{xy} = \gamma_{yz} = \gamma_{zx} = 0 \quad (14)$$

where  $\varepsilon_x$  is related to volumetric strain  $\varepsilon_v$  through

$$\varepsilon_x = \varepsilon_y = \frac{1}{2}(\varepsilon_v - \varepsilon_z) \quad (15)$$

Based on this definition of equivalent shear strain, the stress-strain relations of Figs. 17a and b have identical slope  $G$  and maximum stress. Figure 18 shows the variation of  $G_s/G_i$  with axial strain during drained triaxial tests at constant mean pressure  $p'$  where  $G_i$  is obtained from Fig. 16. The static values of  $G_s/G_i$  are not represented for  $\varepsilon_z - \varepsilon_x < 0.02\%$  due to the scatter in data caused by inaccurate measurement of small strain, but are replaced by the dynamic values of  $G_s/G_i$  measured during the resonant column test of Fig. 15. The results of Fig. 18 fall within the range of typical values obtained by Seed and Idriss (1970).

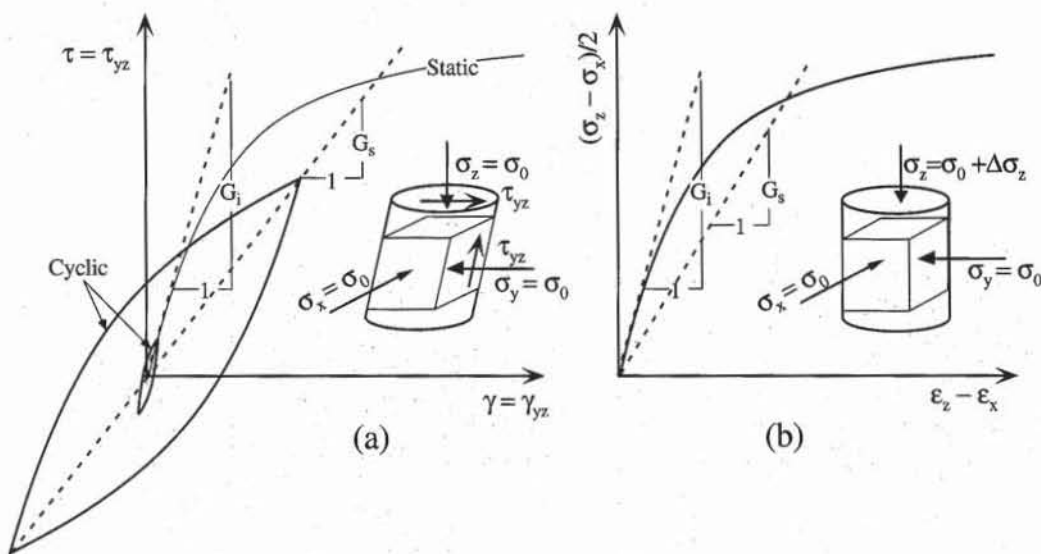


**Figure 17** Determination of initial shear modulus  $G_i$  and secant shear modulus  $G_s$  during (a) cyclic or dynamic simple shear tests, and (b) static triaxial tests.

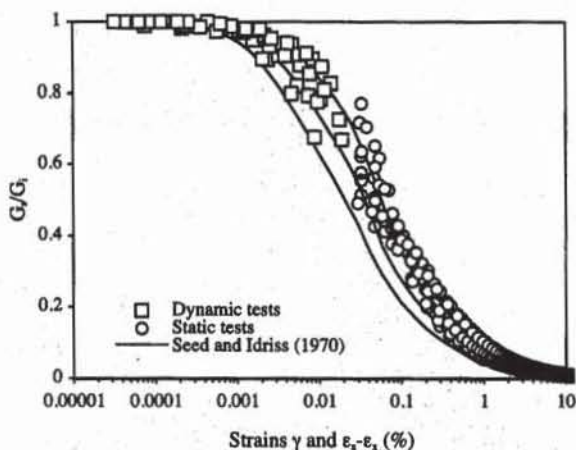


**Figure 18** Variation of  $G_s/G_i$  versus shear strain calculated from dynamic resonant column test, and static drained triaxial test at constant mean pressures on Nevada sand at 40 and 60% relative density (data after Arulmoli et al., 1992).

The determination of the elastic properties of soils and soft rocks during static tests requires measuring strain smaller than 0.001%, which can only be accomplished by using local strain measurement, away from the loading platens where displacement transducers are usually located (e.g., Jardine et al., 1984; Kim et al., 1994; LoPresti et al., 1993; Tatsuoka et al., 1994; and Tatsuoka and Kohata, 1996). As shown in Fig. 19, the axial strain  $\varepsilon_z$  during the triaxial test is usually equal to  $\Delta H/H_0$  where  $\Delta H$  is the displacement measured by the external displacement transducer, and  $H_0$  is the initial sample height. In contrast to  $\varepsilon_z$ , the local strain  $\varepsilon'_z$ , is taken equal to  $\Delta H'/H'_0$  where  $\Delta H'$  is the local displacement

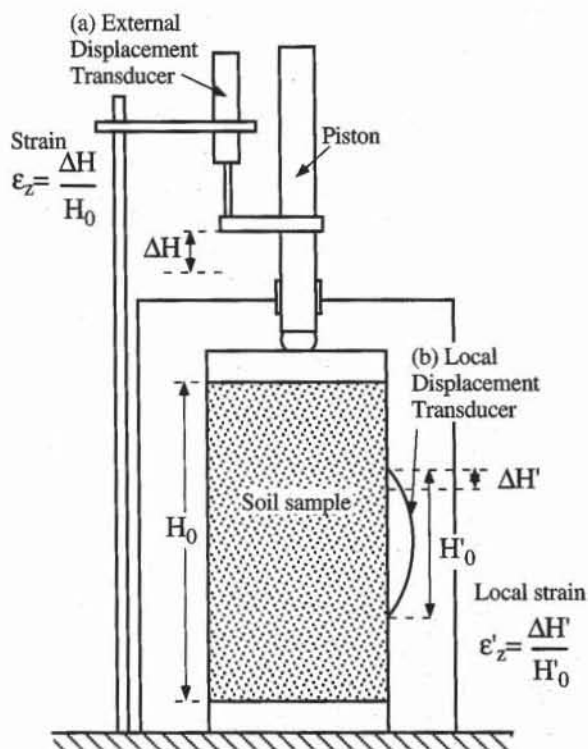


**Figure 19** Measurement of axial strain of soil samples (a) with external displacement transducer, and (b) local displacement transducer (after Tatsuoka and Kohata, 1995)

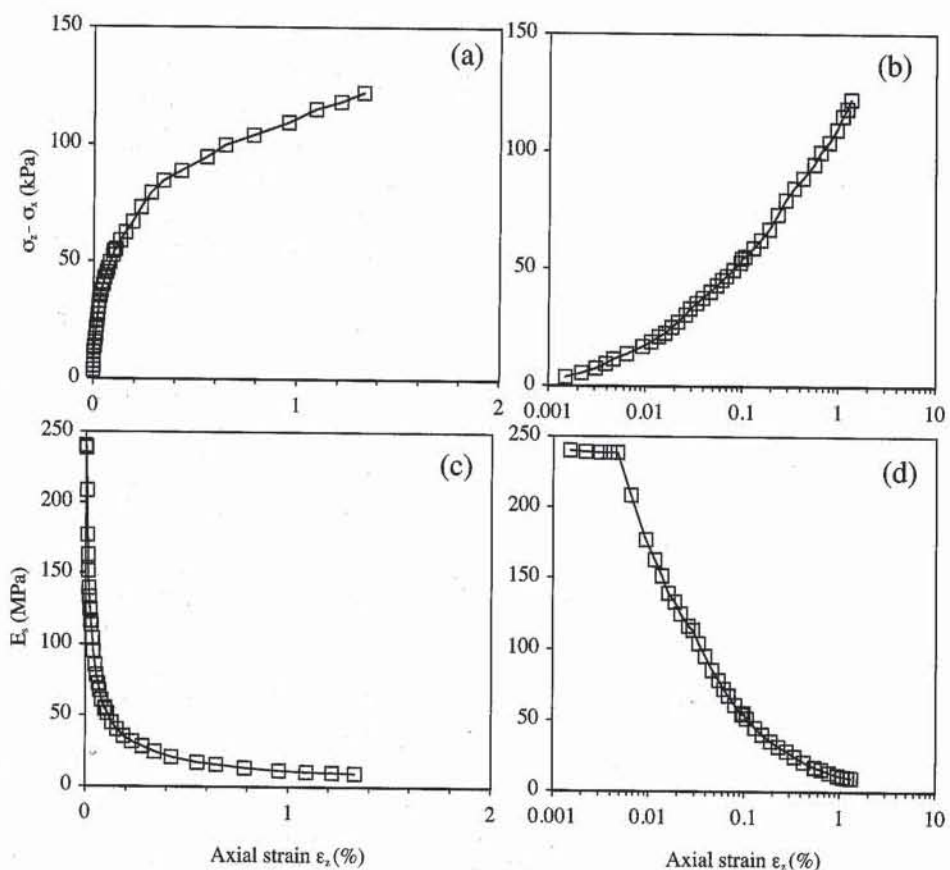
measured by the flexible bending element of initial length  $H'_0$  which is attached to the soil specimen.

Figure 20 shows an example of local strain measurement during a drained triaxial test at 300 kPa confining pressure on normally consolidated white clay. The strain-strain response and secant Young's modulus  $E_s$  were represented by using linear and logarithmic scales to emphasize the small strain behavior. As shown in Fig. 20d, when  $\epsilon_z < 0.003\%$ ,  $E_s$  is constant and equal to  $E_i$ , and the material is linear elastic. As shown in Fig. 21, in fine-grained soils, the typical variation of  $G_s/G_i$  with shear strain depends on plasticity index  $PI$ , and is bounded by the variation of  $G_s/G_i$  for sands for which  $PI = 0$ .

Local strain measurements in static tests reveal that soils are much stiffer at small strains than previously obtained from conventional strain measurement. Such a finding closes the gap between the dynamic and static measurement of ground stiffness. In the past, dynamic measurement of Young's modulus, or shear modulus, have given results so much higher than static values determined in the laboratory that the dynamic values have been discounted. However in a number of recent cases, the accurately determined static small-strain values of stiffness have been found to be very close to the values measured by dynamic methods (Burland, 1989).

## REFERENCES

- ARULMOLI, K., K. K. MURALEETHARAN, M. M. HOSSAIN, and L. S. FRUTH, 1992, VELACS: Verification of Liquefaction Analyses by Centrifuge Studies. Labora-



**Figure 20** Example of local strain measurement during drained triaxial test at 300 kPa confining pressure on normally consolidated white clay,  $w = 61\%$  and  $PI = 30\%$  (after Biarez and Hicher, 1994).

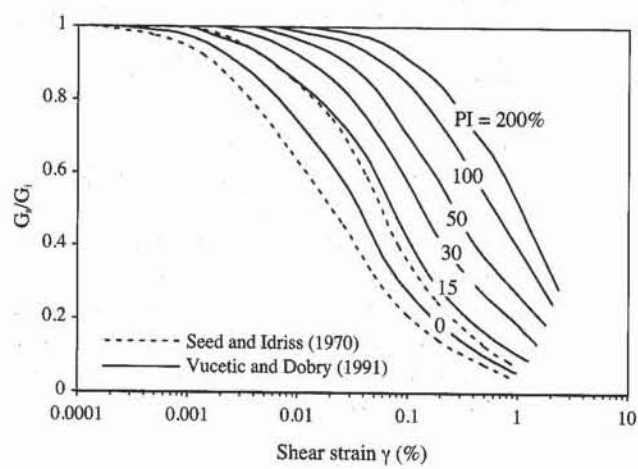


**Figure 21** Variation of shear modulus ratio  $G_s/G_i$  with shear strain amplitude for sands (after Seed and Idriss, 1970) and fine grained soils of different plasticity index PI (after Vucetic and Dobry, 1991).

- tory testing program. Soil data report, *The Earth Technology Corporation*, Project No. 90-0562, Irvine, CA.
- BIAREZ, J., and P.-Y. HICHER, 1994, *Elementary Mechanics of Soil Behavior, Saturated Remoulded Soils*, A. A. Balkema, Rotterdam, Netherlands, pp. 30-32.
- BOWLES, J. E., 1988, *Foundation Analysis and Design*, 4th ed., McGraw-Hill, New York, pp. 99-100.
- BURLAND, J. B., 1989, Ninth Laurits Bjerrum Memorial Lecture, Small is beautiful - The stiffness of soils at small strains, *Canadian Geotech. J.*, Vol. 26, pp. 499-516.
- CERNICA, J. N., 1995, *Geotechnical Engineering, Soil Mechanics*, John Wiley & Sons, New York, p. 241.
- CONVERSE, F. J., 1962, Foundations subjected to dynamic forces, Chapter 8 of *Foundation Engineering*, G.A. Leonards ed., McGraw-Hill, New York, pp. 769-825.
- DJOENAIDI, W. J., 1985, A compendium of soil properties and correlations, *Master of Engineering Science in Geotechnical Engineering*, University of Sydney, Sydney, Australia.
- HALLAM, M. G., N. J. HEAF, and L. R. WOOTTON, 1978, Dynamic of marine structures, *Report UR 8, 2nd edition*, CIRIA Underwater Engineering Group.
- HARDIN, B. O., 1978, The nature of stress-strain behavior of soils, *Proceedings of the ASCE Geotechnical Engineering Division, Specialty Conference, Earthquake Engineering and Soil Dynamics*, Pasadena, CA, Vol. 1, pp. 3-89.
- HARDIN, B. O., and V. P. DRNEVICH, 1972, Shear modulus and damping in soils: design equations and curves, *J. Soil Mech. Found. Div.*, ASCE, Vol. 98, No. SM7, pp. 667-692.
- HOLTZ, R. D., and W. D. KOVACZ, 1981, *An Introduction to Geotechnical Engineering*, Prentice-Hall, Englewood Cliffs, NJ.
- HUNT, R. E., 1986, *Geotechnical Engineering Techniques and Practices*, McGraw-Hill, New York, p. 134.
- JAMIOLKOWSKI, M., S. LEROUEIL, and D. C. F. LoPRESTI, 1991, Theme lecture: Design parameters from theory to practice, *Proceedings of Geo-Coast 1991*, Yokohama, Japan, pp. 1-41.
- JARDINE, R. J., M. J. SYMES, and J. B. BURLAND, 1984, The measurement of soil stiffness in the triaxial apparatus, *Geotechnique*, Vol. 34, pp. 323-340.
- KIM, D.-S., F. TATSUOKA, and K. OCHI, 1994, Deformation characteristics at small strains of sedimentary soft rocks by triaxial compression tests, *Geotechnique*, Vol. 44, No. 3, pp. 461-478.
- KRAMER, S. L., 1996, *Geotechnical Earthquake Engineering*, Prentice Hall, Upper Saddle River, NJ, pp. 184-253.
- LAMBE, T. W. and R. V. WHITMAN, 1979, *Soil Mechanics, SI Version*, John Wiley & Sons, New York, p. 161.
- LEE, K. L., and H. B. SEED, 1967, Drained Strength Characteristics of Cohesionless Soils, *J. Soil Mech. Found. Div.*, ASCE, Vol. 93, No. SM6, pp. 117-141.
- LOPRESTI, D. C. F., O. PALLARA, R. LANCELOTTA, M. ARMANDI, and R. MANISCALCO, 1993, Monotonic and cyclic loading behaviour of two sands at small strains, *Geotech. Testing J.*, ASTM, Vol. 16, No. 4, pp. 409-424.
- POULOS, H. G., 1975, Settlement of isolated foundations, *Proceedings of the Symposium on Soil Mechanics - Recent Developments*, Sydney, Australia, pp. 181-212.
- SEED, H. B. and K. L. LEE, 1967, Undrained Strength Characteristics of Cohesionless Soils, *J. Soil Mech. Found. Div.*, ASCE, Vol. 93, No. SM6, pp. 333-360.

- SEED, H. B., and I. M. IDRISI, 1970, Soil moduli and damping factors for dynamic response analyses, *Report EERC 70-10*, Earthquake Engineering Research Center, University of California, Berkeley, CA.
- TATSUOKA, F., and Y. KOHATA, 1995, Stiffness of hard soils and soft rocks in engineering applications, *Report of the Institute of Industrial Science, The University of Tokyo*, Vol. 38, No. 5, Serial No. 242, 140 p.
- TATSUOKA, F., T. SATO, C. S. PARK, Y. S. KIM, J. N. MUKABI, and J. KOHATA, 1994, Measurements of elastic properties of geomaterials in laboratory compression tests, *Geotech. Testing J.*, ASTM, Vol. 17, No. 1, pp. 80–94.
- VUCETIC, M. and R. DOBRY, 1991, Effects of soil plasticity on cyclic response, *J. Geotech. Eng.*, ASCE, Vol. 117, No. 1, pp. 89–107.

## REVIEW QUESTIONS

1. Define nonlinear-elastic, linear-elastic, and elastoplastic materials by using stress-strain curves.
2. Define strain hardening, perfectly plastic, and strain softening materials by using stress-strain curves.
3. Define rigid-perfectly plastic, and elastic-perfectly plastic materials by using stress-strain curves.
4. What is the yield stress for an elastoplastic material?
5. What is a viscous material?
6. Define *creep* and *relaxation*.
7. What is the number of independent material constants in the isotropic linear theory of elasticity?
8. What is the relation between the bulk modulus, Young's modulus, and the Poisson ratio?
9. What is the relation between the shear modulus, Young's modulus, and the Poisson ratio?
10. What is the constrained modulus?
11. What are the theoretical constraints on Young's modulus and the Poisson ratio?
12. What is the state of stress during the isotropic test? What is the elastic relation between volumetric strain and pressure?
13. What is the state of stress during the unconfined compression test? What is the elastic relation between axial strain and axial stress?
14. What is the state of stress during the drained triaxial test? What are the elastic relations between axial strain and axial stress, and between volumetric stress and axial strain?
15. What is the state of stress during the confined compression test?

## EXERCISES

1. From the results of the isotropic test on dense Sacramento River sand in Table E1, plot the volumetric strain versus pressure. Calculate the initial bulk modulus at 78 kPa, and plot the variation of secant bulk modulus versus pressure.

TABLE E1

1			2		
Pressure (kPa)	Void ratio	Volumetric strain (%)	Pressure (kPa)	Void ratio	Volumetric strain (%)
78	0.608	0.06	11925	0.506	6.40
196	0.604	0.31	9081	0.509	6.22
392	0.600	0.56	7708	0.511	6.09
588	0.596	0.81	5531	0.513	5.97
1069	0.590	1.18	4119	0.518	5.66
2167	0.581	1.74	3285	0.521	5.47
3285	0.572	2.30	2157	0.524	5.28
4021	0.566	2.67	1079	0.527	5.10
2216	0.572	2.30	588	0.533	4.72
981	0.577	1.99	392	0.537	4.47
392	0.584	1.55	98	0.547	3.85
78	0.591	1.12	392	0.541	4.23
392	0.584	1.55	588	0.538	4.41
981	0.578	1.93	1079	0.532	4.79
2216	0.572	2.30	2157	0.524	5.28
4021	0.563	2.86	3285	0.521	5.47
5492	0.556	3.29	4119	0.518	5.66
7708	0.540	4.29	5531	0.513	5.97
9081	0.532	4.79	7708	0.508	6.28
10395	0.523	5.34	9081	0.506	6.40
11925	0.515	5.84	11964	0.499	6.84
13729	0.503	6.59	13729	0.493	7.21

Initial void ratio = 0.609

2. From the results of the unconfined compression of a remolded clay in Table E2, calculate the initial Young's modulus. Plot the variation of secant Young's modulus versus axial strain.

TABLE E2

Axial strain (%)	Axial stress (kPa)
0.0	0.0
1.0	8.7
1.9	13.8
2.9	20.2
5.0	31.6
5.8	35.2
6.9	40.6
7.8	45.5
8.8	50.2
9.9	56.1
11.0	58.3
12.0	60.8
13.4	63.0
14.1	64.7
15.0	65.3
16.0	66.7
18.0	67.3
20.1	69.7
21.1	70.1

3. From the results of the confined compression test on San Francisco Bay mud in Table E3, calculate the initial constrained modulus. Plot the variation of secant constrained modulus versus axial strain.

**TABLE E3**

Axial stress (kPa)	Axial strain (%)
1	1.1
3	2.2
4	4.4
10	14.3
21	23.7
41	31.3
82	38.2
22	37.0
6	34.2

4. From the results of the drained triaxial compression test of a sand in Table E4, calculate the initial Young's modulus and Poisson ratio. Plot the variation of secant Young's modulus and Poisson ratio versus axial strain.

**TABLE E4**

$\sigma'_1 / \sigma'_3$	$\sigma_1 - \sigma_3$ (kPa)	Axial strain (%)	Volumetric strain (%)
1.00	0.0	0.00	0.00
1.39	229.5	0.06	0.03
1.78	459.0	0.15	0.09
2.08	635.5	0.30	0.15
2.82	1070.9	0.58	0.24
3.25	1323.9	0.88	0.27
3.87	1688.7	1.46	0.22
4.24	1906.4	2.19	0.03
4.42	2012.3	2.92	-0.24
4.56	2094.7	4.38	-0.91
4.55	2088.8	5.85	-1.61
4.45	2030.0	8.77	-2.85
4.26	1918.2	11.70	-3.80
4.18	1871.1	14.60	-4.46
3.94	1729.9	17.55	-4.91
3.72	1600.5	20.00	-5.05

Confining Pressure = 588 kPa

Initial void Ratio = 0.596

# 6

# Consolidation

**6-1** Principles of consolidation

**6-2** Consolidation test

# 6-1 Principles of Consolidation

## INTRODUCTION

When fine-grained soils are subjected to changes in load due to construction, they deform in a way different from that of coarse-grained materials. Their deformation takes place not only at the time of the load application, but also continues for very long time periods which may last several years. The long-term settlement of fine-grained soil layers is primarily controlled by *consolidation*, a physical process in which the interstitial water that is under excess pressure slowly diffuses through the compressible matrix of soil particles. After the excess pore pressure has completely dissipated, fine-grained soils can also deform due to their viscous nature. The properties that characterize the amplitude and rate of deformation for fine-grained soils are determined in the consolidation test.

## NONLINEAR AND IRREVERSIBLE COMPRESSIBILITY

### One-Dimensional Tests

The basic setup of the consolidation test is shown in Fig. 1. The soil sample is inside a stiff ring which blocks its lateral expansion, and between two porous disks, which drains its porewater. The sample is completely immersed in water and remains fully saturated during the test. When the axial stress  $\sigma$  is applied, the sample of initial height  $h_0$  deforms vertically with time. It ultimately settles the amount  $\Delta h$  when the excess porewater pressure is completely dissipated (i.e., when the internal effective stress  $\sigma'$  becomes equal to the externally applied stress  $\sigma$ ). The corresponding axial strain  $\epsilon_z$  is

$$\epsilon_z = \frac{\Delta h}{h_0} \quad (1)$$

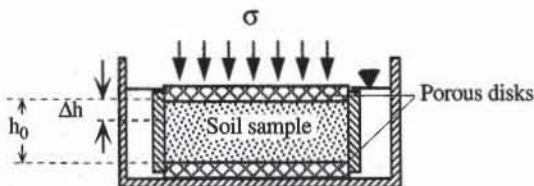


**Figure 1** Basic experimental setup of consolidation cell.

Because the stiff ring prohibits lateral strain (i.e.,  $\varepsilon_x = \varepsilon_y = 0$ ), the volumetric strain  $\varepsilon_v$  is equal to the axial strain:

$$\varepsilon_v = \varepsilon_x + \varepsilon_y + \varepsilon_z = \varepsilon_z = \frac{\Delta h}{h_0} \quad (2)$$

The volumetric strain is also

$$\varepsilon_v = \frac{V_0 - V}{V_0} = \frac{V_0/V_s - V/V_s}{V_0/V_s} = \frac{e_0 - e}{1 + e} \quad (3)$$

where  $e$  is the present void ratio,  $e_0$  the initial void ratio,  $V$  the present volume,  $V_0$  the initial volume, and  $V_s$  the total volume of soil particles alone. Therefore,  $e$  is related to  $\Delta h$  through

$$e = e_0 - \varepsilon_v(1 + e_0) = e_0 - \frac{\Delta h}{h_0}(1 + e_0) \quad (4)$$

Figure 2 shows an experimental result that is representative of the response of fine-grained soils subjected to a loading-unloading cycle in the consolidation test. The same experimental results are plotted in two different ways: vertical strain  $\varepsilon_z$  versus effective stress  $\sigma'$  and void ratio  $e$  versus  $\sigma'$ . The  $\sigma'$  axis has a linear scale in Fig. 2a but a logarithmic scale in Fig. 2b. As shown in Fig. 2b,  $e$  decreases from the initial state A as  $\sigma'$  is increased. From point A to B, the relation between  $e$  and  $\sigma'$  is nonlinear. The material behaves differently during loading (from A to B) and unloading (from B to C), which indicates that the nonlinear  $e-\sigma'$  relation is also irreversible.

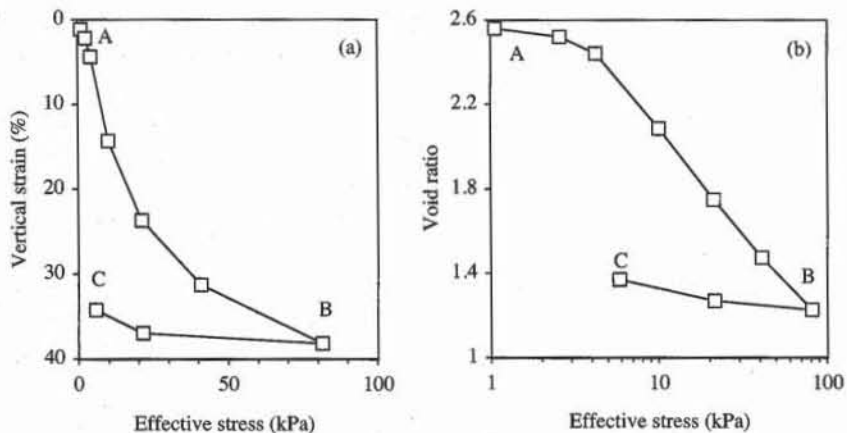


**Figure 2** Consolidation test results on San Francisco bay mud: (a) vertical strain versus effective stress in linear scale, and (b) void ratio versus effective stress in semilogarithmic scale (after Holtz and Kovacs, 1981).

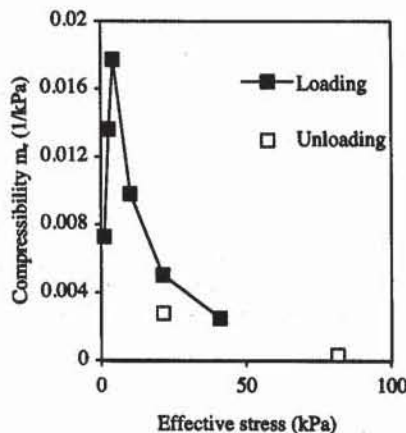


**Figure 3** Variation of the compressibility of Fig. 2 with stress level and loading direction.

### Coefficient of Compressibility

Within the small stress interval from  $\sigma'_1$  to  $\sigma'_2$ , the  $\varepsilon_z - \sigma'$  curve is characterized by the coefficient of compressibility  $m_v$ :

$$m_v = \frac{\varepsilon_{v1} - \varepsilon_{v2}}{\sigma'_2 - \sigma'_1} \quad (5)$$

where  $\varepsilon_{v1}$  is the volumetric strain at effective stress  $\sigma'_1$  and  $\varepsilon_{v2}$  is the volumetric strain at  $\sigma'_2$ . Since  $\varepsilon_z = \varepsilon_v$ ,  $m_v = 1/M$ , where  $M$  is the constrained modulus of elasticity (see Chapter 5-5).  $m_v$  is inversely proportional to stress [ $m_v = F^{-1}L^2$ , where  $L$  and  $F$  represent the dimension of length and force, respectively].  $m_v$  is also computed from the  $e - \sigma'$  curve using Eq. 4:

$$m_v = \frac{e_1 - e_2}{1 + e_1} \frac{1}{\sigma'_2 - \sigma'_1} \quad (6)$$

where  $e_1$  is the void ratio at  $\sigma'_1$  and  $e_2$  is the void ratio at  $\sigma'_2$ . As shown in Fig. 3,  $m_v$  varies with the stress level and the loading direction.  $m_v$  is generally used to calculate the vertical settlement  $s$  of a layer of initial thickness  $h_0$  subjected to the increased  $\Delta\sigma'$  in vertical effective stress:

$$s = m_v h_0 \Delta\sigma' \quad (7)$$

Caution should be exercised in the calculation and use of  $m_v$ . The value of  $m_v$  depends not only on the stress level but also on the loading direction (i.e., loading or unloading). Equation 7 applies provided that the soils in the laboratory and the field undergo a similar stress level, stress increment, and loading direction.

### $e - \sigma'$ Curves for Clays

Figure 2b shows that  $e$  varies linearly with  $\log \sigma'$  in some parts, whereas Fig. 2a displays a complicated nonlinear relation between  $\varepsilon_z$  and  $\sigma'$ . The void ratio  $e$  is therefore more convenient than  $\varepsilon_z$  to represent consolidation results.

Figures 4 to 6 show a few examples of consolidation results covering a wide variety of soils. Figure 4 shows the consolidation curves for glacial lake silty clays (Rutledge, 1944). Sample CP1 is an undisturbed sample taken from the field, sample CP2 is artificially remolded from sample CP1, and sample CP3 is in turn remolded from sample CP2. As shown in Fig. 4, the consolidation curves of samples CP1, CP2, and CP3, although they retained a similar shape, are influenced by remolding.

Figure 5 shows the consolidation curves that are typical of soils from the lower Mississippi River Valley near Baton Rouge, Louisiana (Kaufman and Sherman, 1964). These soils are made of silts and sandy silts with clay strata and are classified as CH and CL-clay of high and low plasticity, respectively. During the deposition process in the Mississippi River Valley, they have been subjected to wetting and drying cycles. The consolidation curves of these clays are also compared to that of a poorly graded sand. As shown in Fig. 5, sand is much less compressible than clay and undergoes smaller changes in void ratio.

Figure 6 shows the consolidation curves of Mexico City clay (Rutledge, 1944). This soil was previously thought to be a volcanic ash that had been weathered and had become an allophane clay mineral. Indeed, Mexico City clay is not really a clay mineral, but is composed primarily of porous microfossils and diatoms, which are responsible for very high void ratio, water content, and compressibility (Holtz and Kovacs, 1981). As shown in Fig. 6, the solid and dashed lines represent the response of undisturbed and remolded samples taken from different locations. The difference in undisturbed responses illustrates the difficulty in obtaining reproducible results on clays having such a large void ratio. As expected, remolding almost completely destroys the preconsolidation effects.

### Elastoplastic Modeling of $e-\sigma'$ Responses

Figure 7 shows the consolidation curve of clay tills (MacDonald and Sauer, 1970), a typical response for fine-grained soils. The relation between  $e$  and  $\sigma'$  is nonlinear and irreversible. The material behaves differently during loading (*A* to *C*, or

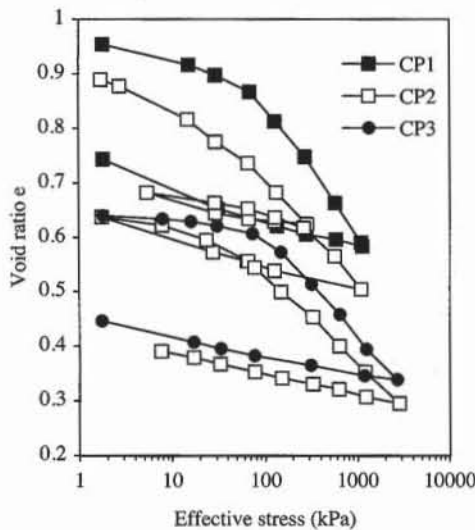


Figure 4 Consolidation test results on Chicago and Indiana clays (after Rutledge, 1944).

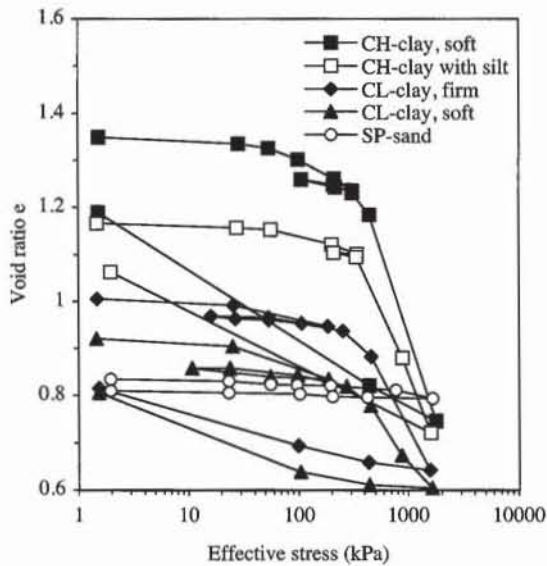
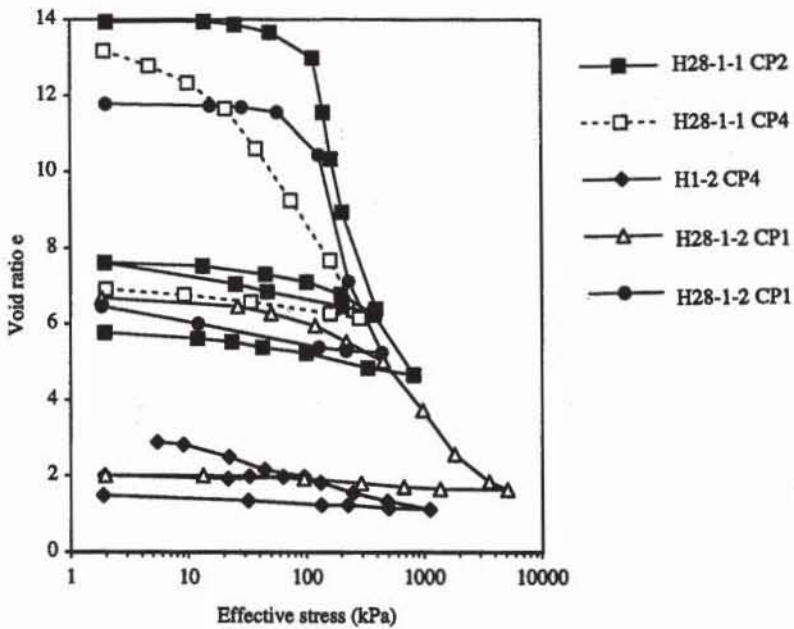


Figure 5 Consolidation test results on nearly normally consolidated clays and silts (after Kaufman and Sherman, 1964).



**Figure 6** Consolidation test results on Mexico City clay (after Rutledge, 1944).

$D$  to  $E$ ) and unloading ( $C$  to  $D$ , or  $E$  to  $F$ ). The material response of Fig. 7 is not elastic but is elastoplastic.

Figure 8 illustrates the elastoplastic modeling of the response  $e$ - $\log \sigma'$  of Fig. 7. Starting from point  $A$ ,  $e$  varies linearly with  $\log \sigma'$  when  $\sigma'$  is increased from  $\sigma'_A$  to  $\sigma'_B$ :

$$e = e_A - C_s \log \frac{\sigma'}{\sigma'_A} \quad (8)$$

where  $C_s$  is the swelling index,  $e_A$  the void ratio at point  $A$ , and  $\sigma'_A$  the effective stress at point  $A$ . Equation 8 is valid until  $\sigma'$  reaches stress  $\sigma'_B$ , at which point the  $e$ - $\sigma'$  curve abruptly becomes steeper than the branch  $AB$ . When  $\sigma' > \sigma'_B$ ,  $e$  varies again linearly with  $\log \sigma'$  but with a steeper slope:

$$e = e_B - C_c \log \frac{\sigma'}{\sigma'_B} \quad (9)$$

where  $C_c$  is the compression index,  $e_B$  the void ratio at point  $B$  and  $\sigma'_B$  the effective stress at point  $B$ . When  $\sigma'$  is decreased from  $\sigma'_C$  to  $\sigma'_D$ , the point  $(e$ - $\log \sigma')$  follows the unloading branch  $CD$ , which is parallel to  $AB$  and has the same swelling index. But Eq. 8 is now referenced about  $C$  instead of  $A$ :

$$e = e_C - C_s \log \frac{\sigma'}{\sigma'_C} \quad (10)$$

When  $\sigma'$  is increased again, the point  $(e$ - $\log \sigma')$  follows the branch  $CD$  in the opposite direction and moves toward  $E$  on the branch that extends  $BC$ . When  $\sigma'$  is finally decreased from  $E$  to  $F$ , the point  $(e$ - $\log \sigma')$  follows the branch  $EF$  parallel to  $AB$  and  $CD$ . The branch  $BCE$  is called the *virgin compression line* (VCL). The

branches *AB*, *CD*, and *EF* are *swelling lines*. A particular clay has only one virgin consolidation curve but an indefinite number of swelling branches. The swelling branches are always to the left of VCL. The point (*e*–log  $\sigma'$ ) cannot go to the right of VCL.

The stress-strain relations specified by Eqs. 8 to 10 are nonlinear because *e* is a logarithmic function of  $\sigma'$ . They are also irreversible because it is not possible to return to point *A* once  $\sigma'$  has exceeded  $\sigma'_B$ . The threshold of irreversibility is defined by the largest effective stress applied, which is also referred to as the *preconsolidation pressure*  $\sigma'_p$ . When the stress state is smaller than  $\sigma'_p$ , the response is described by a swelling branch. When the stress state is equal to  $\sigma'_p$ , the response follows the VCL for loading and a swelling line for unloading. The preconsolidation pressure  $\sigma'_p$  either increases or remains constant but never decreases. During the loading *ABC* of Fig. 8,  $\sigma'_p$  moves from  $\sigma'_B$  to  $\sigma'_C$ .  $\sigma'_p$  is constant during the unloading *CD* and reloading *DC* but increases again during the loading *CE*.

### Compression and Swelling Indices and Compressibility

The compression index  $C_c$  is the slope of the virgin consolidation line (VCL) in the *e*–log  $\sigma'$  axes, whereas the swelling index  $C_s$  is the slope of a swelling curve. These indices are

$$C_c = \frac{e_B - e_C}{\log(\sigma'_C / \sigma'_B)} \quad \text{and} \quad C_s = \frac{e_D - e_C}{\log(\sigma'_C / \sigma'_D)} \quad (11)$$

where *B* and *C* are two points on the VCL, and *C* and *D* are two points on a swelling line as shown in Fig. 8. Both  $C_c$  and  $C_s$  are positive dimensionless numbers, and  $C_s$  is always smaller than  $C_c$ . In contrast to  $m_v$ ,  $C_c$  and  $C_s$  are constant for a soil. As mentioned previously,  $m_v$  depends on the loading direction and the position relative to the VCL. For very small loading steps, the compressibility coefficient  $m_v$  is related to  $C_c$  and  $C_s$  through

$$m_v = -\frac{1}{(1+e)\ln(10)} \frac{de}{d\sigma'} = \begin{cases} \frac{0.435}{1+e} \frac{C_c}{\sigma'} & \text{for loading on VCL} \\ \frac{0.435}{1+e} \frac{C_s}{\sigma'} & \text{otherwise} \end{cases} \quad (12)$$

### Overconsolidation Ratio, Normally Consolidated and Overconsolidated Clays

The overconsolidation ratio OCR characterizes the position of the present state (*e*,  $\sigma'$ ) relative to the preconsolidation pressure  $\sigma'_p$ :

$$OCR = \frac{\sigma'_p}{\sigma'} \quad (13)$$

When the excess pore pressure is dissipated completely, OCR is always larger or equal than 1. Based on the overconsolidation ratio, clays are divided into normally consolidated and overconsolidated.

Normally consolidated clays have never been subjected to an effective stress greater than the present effective stress (OCR = 1). Examples of normally con-

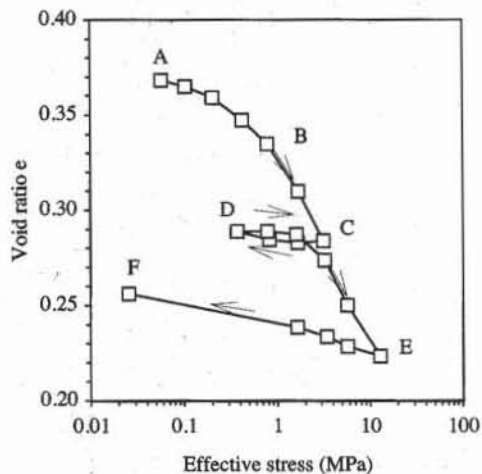


**Figure 7** Typical experimental results during one-dimensional compression tests on clay tills (data after MacDonald and Sauer, 1970).

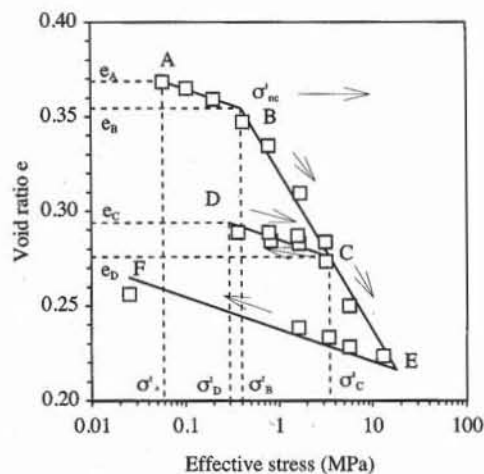


**Figure 8** Idealized representation of stress-strain response of Fig. 7.

Solidated clays are geologically recent alluvial deposits which have never been eroded. Normally consolidated clays are sensitive to the effects of disturbances, which influence the  $e-\sigma'$  relationship.

Overconsolidated clays have been subjected to an effective stress greater than the present effective stress ( $OCR > 1$ ). This past loading could have been the result of deposits of soils and rocks, perhaps 2 to 3 km thick, which were subsequently eroded away in the course of geological time or by a great thickness of ice during periods of glaciation. Other factors such as aging, dessication, and fluctuation in water level, may also contribute to modify the mechanical behavior of clays.

### Determination of Preconsolidation Pressure

There are primarily two ways to determine the preconsolidation pressure  $\sigma'_p$ , which is the largest effective stress undergone by the soil. Both methods detect  $\sigma'_p$  from the  $e$ -log  $\sigma'$  curve.

#### Method a (Casagrande, 1936; and ASTM 2435)

- Choose the point of minimum curvature on the consolidation curve (point A in Fig. 9).
- Draw the horizontal line AB from point A.
- Draw the line AC tangent to the curve at point A.
- Draw the line AD so that the angles BAD and DAC are equal.
- Extend the straight portion EF of the virgin compression curve as shown in Fig. 9.
- The preconsolidation stress  $\sigma'_p$  is the intersection point M between EF and AD.

#### Method b

- Extend the straight portion EF of the virgin compression curve as shown in Fig. 9.

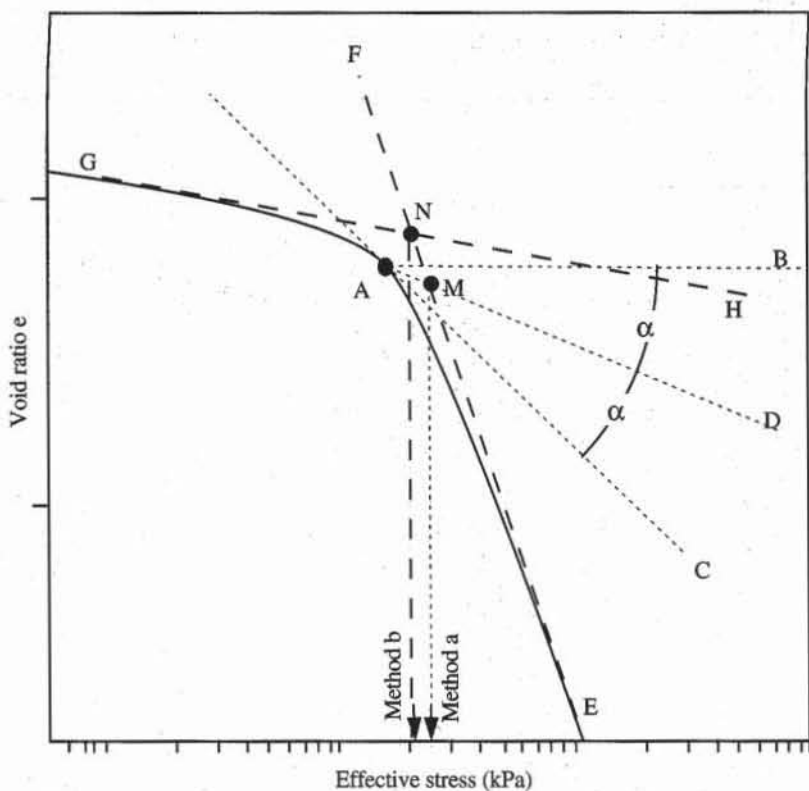


**Figure 9** Determination of preconsolidation pressure with methods a and b.

- Extend the straight portion  $GH$  of the compression curve as shown in Fig. 9.
- The preconsolidation stress  $\sigma'_p$  is the intersection point  $N$  between  $EF$  and  $GH$ .

As shown in Fig. 9, methods a and b predict only slightly different preconsolidation pressure. They give similar results for practical purposes.

#### Typical Values and Correlations for Compressibility Indices

Table 1 lists the values of compression index  $C_c$ , swelling index  $C_s$ , and Atterberg limits for various clays. The values of  $C_c$  vary from 2.6 for montmorillonite ( $Na^-$ ) to 0.08 for clay till, whereas those of  $C_s$  range from 0.01 to 0.51.

Many different correlations have been published for correlating  $C_c$  and  $C_s$  to the index properties of soils (Djoenaidi, 1985). Figure 10 shows three types of correlations between  $C_c$  and the liquid limit, initial void ratio, and natural water content. The correlations between  $C_c$  and the natural water content appear to be more consistent than the others. One of these correlations still in use today is due to Terzaghi and Peck (1967):

$$C_c = 0.009 (LL - 10) \quad (14)$$

where  $LL$  is the liquid limit in percent. As shown in Fig. 11, Eq. 14 describes the measured values of  $C_c$  for some, but not all clays. Based on the critical state model (see Chapter 7-1), Wroth and Wood (1978) showed that:

$$C_c = G_s \frac{PI}{200} \quad \text{and} \quad C_s = C_c(1 - \Lambda) \quad (15)$$

TABLE 1

Values of compression and swelling indices and Atterberg limit for various clay minerals and natural soils.

Type of clays	Undisturbed $C_c$	Remolded $C_c$	Swelling $C_s$	Liquid limit (%)	Plastic limit (%)	Plasticity index (%)	References
Boston blue clay	0.32	0.21	0.07	41	20	21	1
Chicago clay	0.42	0.22	—	58	21	37	1,2
Louisiana clay	0.33	0.29	0.05	74	26	48	1,2
New Orleans clay	0.29	0.26	0.04	79	26	53	1,2
Fort Union clay	0.26	—	0.04	89	20	69	1
Delaware organic silty clay	0.95	—	—	84	46	38	1
Indiana silty clay	0.21	0.12	—	36	20	16	1
Fore River clay	0.36	0.25	0.09	49	21	28	1
Beauharnois clay	0.55	—	0.01	56	22	34	1
Cincinnati clay	0.17	—	0.02	30	12	18	1
St Lawrence clay	0.84	—	0.04	55	22	33	1
Siburua clay	0.21	—	0.08	70	26	44	1
CL-clay, soft	0.34	—	—	41	24	17	4
CL-clay, firm	0.44	—	—	50	23	27	4
ML-sandy silt	0.16	—	—	31	25	6	4
CH-clay, soft	0.84	—	—	81	25	56	4
CH-clay with silt strata	0.52	—	—	71	28	43	4
Montmorillonite, $\text{Na}^+$	2.6	—	—	710	54	656	3
Montmorillonite, $\text{K}^+$	1	—	—	660	98	562	3
Montmorillonite, $\text{Ca}^{+2}$	2.2	—	0.51	510	81	429	3
Montmorillonite, $\text{H}^+$	1.9	—	0.34	440	55	385	3
Montmorillonite, $\text{Mg}^{+2}$	1.9	—	0.44	410	60	350	3
Montmorillonite, $\text{Fe}^{+3}$	1.6	—	0.03	290	75	215	3
Illite, $\text{Na}^+$	1.1	—	0.15	120	53	67	3
Illite, $\text{K}^+$	0.62	—	0.27	120	60	60	3
Illite, $\text{Ca}^{+2}$	0.86	—	0.21	100	45	55	3
Illite, $\text{H}^+$	0.61	—	0.10	100	51	49	3
Illite, $\text{Mg}^{+2}$	0.56	—	0.18	94	46	48	3
Illite, $\text{Fe}^{+3}$	—	—	0.15	110	49	61	3
Kaolinite, $\text{Na}^+$	0.26	—	—	53	32	21	3
Kaolinite, $\text{K}^+$	—	—	0.06	49	29	20	3
Kaolinite, $\text{Ca}^{+2}$	0.21	—	0.06	38	27	11	3
Kaolinite, $\text{H}^+$	0.23	—	0.05	53	25	28	3
Kaolinite, $\text{Mg}^{+2}$	0.24	—	0.08	54	31	23	3
Kaolinite, $\text{Fe}^{+3}$	0.24	—	0.06	59	37	22	3
Attapulgite, $\text{Mg}^{+2}$	0.77	—	0.24	270	150	120	3
Clay till	0.08	—	—	24	12	12	5

## References

<sup>1</sup>Winterkorn and Wang, 1975<sup>2</sup>Mitchell, 1976<sup>3</sup>Lambe and Whitman, 1979<sup>4</sup>Kaufman and Sherman, 1964<sup>5</sup>MacDonald and Sauer, 1970

where  $G_s$  is the soil specific density and  $\Lambda$  a critical state material constant. For  $G_s = 2.7$  and  $\Lambda = 0.8$ , Eq. 15 becomes

$$C_c = \frac{PI}{74} \quad \text{and} \quad C_s = \frac{PI}{370} \quad (16)$$

As shown in Fig. 12, there is a general agreement between the measured values of  $C_c$  and  $C_s$  and those calculated from Eq. 16. The measured values of the swelling index  $C_s$  are generally about 5 times smaller than  $C_c$ , as predicted by Eq. 16. As shown in Fig. 13, Lambe and Whitman (1979) suggest that the representa-

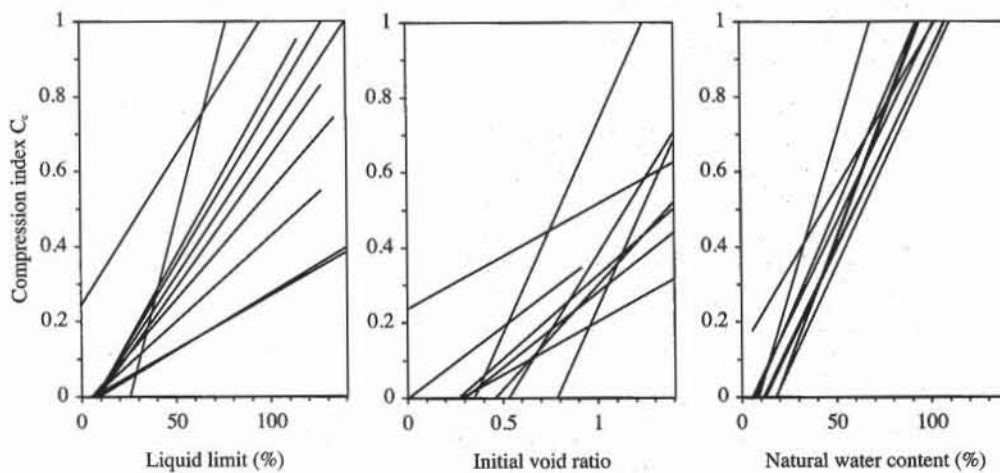


**Figure 10** Empirical relations between compression index  $C_c$ , liquid limit, initial void ratio, and natural water content (after Djoenaidi, 1985).

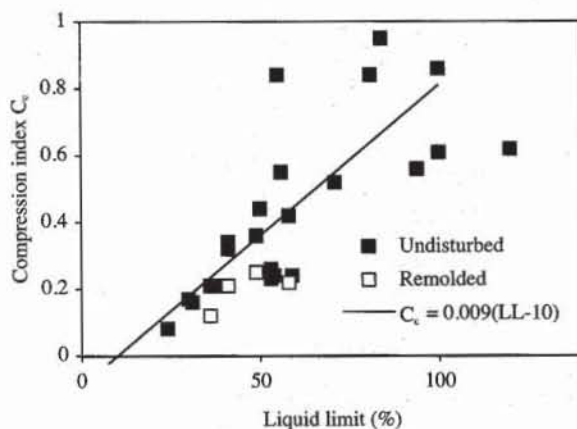


**Figure 11** Relation between compression index  $C_c$  and liquid limit for clays (experimental data of Table 1).

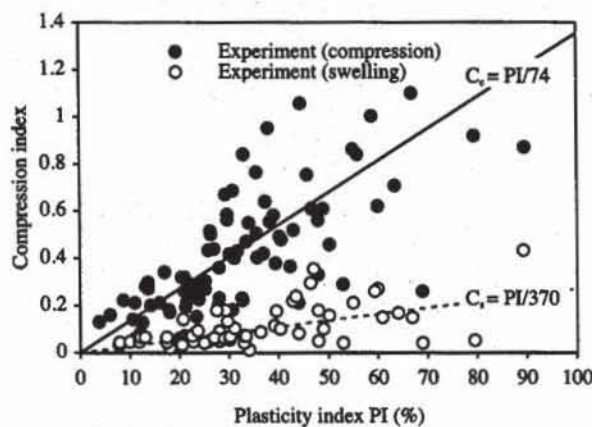


**Figure 12** Variation of compression index  $C_c$  and swelling index  $C_s$  with plasticity index (experimental data from Table 1 and Kulhawy and Mayne, 1990).

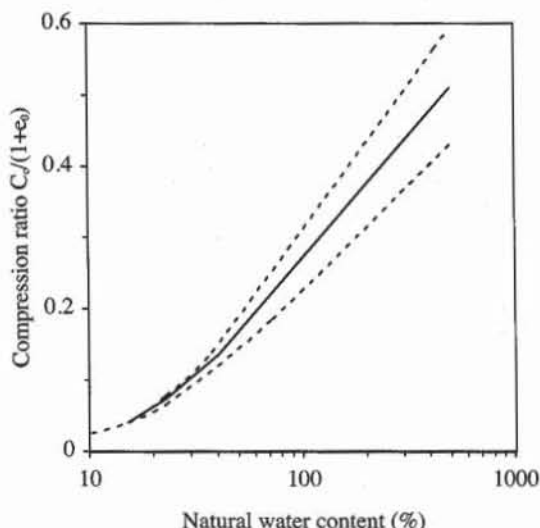


**Figure 13** Range of variation of  $C_c/(1 + e_0)$  with natural water content (Lambe and Whitman, 1979).

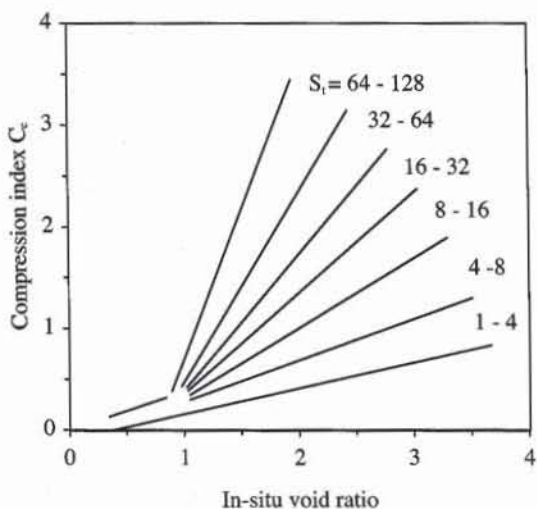


**Figure 14** Influence of sensitivity  $S_t$  on compression index (Leroueil et al., 1983).

tion of  $C_c/(1 + e_0)$  versus the natural water content reduces the data scatter, where  $e_0$  is the initial void ratio.

As shown in Fig. 14, the sensitivity  $S_t$  of clays, which is the ratio between their undrained shear strengths in undisturbed and remolded states (see Chapter 7-1), influences strongly the compressibility index of clays, especially marine clays (Leroueil et al., 1983). An example of the effect of disturbance on the compressibility of sensitive soils can also be found in Fig. 6.

## RATE OF CONSOLIDATION

### Definition

When a load is applied to a specimen of saturated soil in the consolidation test, it is initially carried by the porewater, which is much less compressible than the assembly of soil particles. The resulting porewater pressure, in excess of the hydrostatic water pressure, is termed *excess porewater pressure*. When water drains from the soil pores, the load is gradually shifted from water to soil particles. For fully saturated soils, the load transfer is accompanied by a volume change equal to the volume of drained water. This process is known as *consolidation*.

The consolidation process is illustrated with the spring analogy of Fig. 15. As shown in Fig. 15a, the assembly of soil grains is modeled with a spring. If the weight  $W$  is placed on the model with the valve closed,  $W$  is carried entirely by the water, which is stiffer than the spring. If the valve is opened and the water is allowed to escape, the load will eventually be carried entirely by the spring (Fig. 15c). The time required to transfer  $W$  from water to spring depends on how rapidly the water escapes through the valve. In soils, the rate of volume change and porewater diffusion is related to the soil permeability. In most sands the permeability is so large that the consolidation time is negligible, whereas in

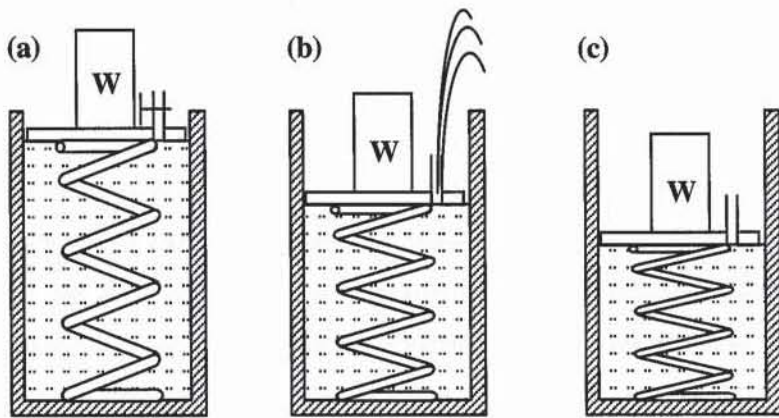


**Figure 15** Spring analogy to soil consolidation.

clays, the permeability is small and slows down the rate of consolidation considerably.

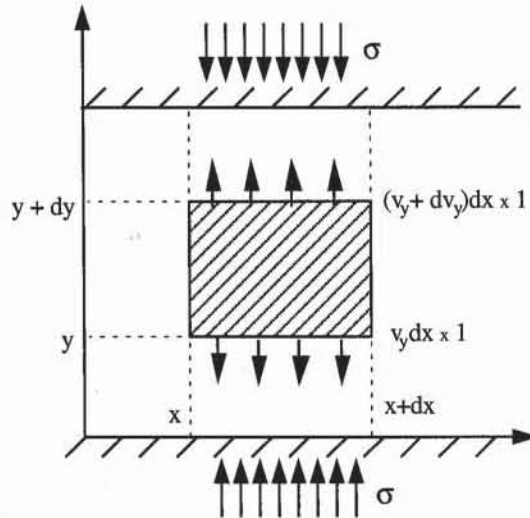
### Consolidation Theory

Figure 16 shows a layer of soil which is consolidating. The soil layer of thickness  $H$  is loaded by two porous boundaries which allow water to drain. The soil layer is infinitely wide so that the soil deformation and flow of water can be assumed one-dimensional and in the vertical  $y$  direction.

When the water flows only in the  $y$  direction, there is no discharge velocity in the  $x$  and  $z$  directions (i.e.,  $v_x = v_z = 0$ ). If the flow obeys Darcy's law, the discharge velocity  $v_y$  in the  $y$  direction is

$$v_y = -k \frac{\partial h}{\partial y} \quad (17)$$

where  $k$  is the permeability coefficient,  $h = \frac{u}{\gamma_w} + y$  the total head,  $u$  the water



**Figure 16** Small element of a soil layer undergoing consolidation.

pressure, and  $\gamma_w$  the unit weight of water. For the small element shown in Fig. 16, the incoming and outgoing volume of water during a unit time interval is  $v_y dx \times 1$ , and  $(v_y + \frac{\partial v_y}{\partial y} dy)dx \times 1$ , respectively. Therefore the volume of water  $V_w$  stored or lost by the element per unit of time is

$$\frac{dV_w}{dt} = \left( v_y + \frac{\partial v_y}{\partial y} dy \right) dx \times 1 - v_y dx \times 1 = \frac{\partial v_y}{\partial y} dy dx = -k \frac{\partial^2 h}{\partial y^2} dx dy \quad (18)$$

The water pressure  $u$  can be defined as the sum of static pore pressure  $u_s$  and excess pore pressure  $u_e$  (i.e.,  $u = u_s + u_e$ ). The second-order derivative of  $u_s$  is equal to 0 (i.e.,  $\frac{\partial^2 u_s}{\partial y^2} = 0$ ) because  $u_s$  varies linearly with respect to  $y$ . Eq. 18 becomes

$$\frac{dV_w}{dt} = \frac{k}{\gamma_w} \left( \frac{\partial^2 u_s}{\partial y^2} + \frac{\partial^2 u_e}{\partial y^2} \right) dx dy = -\frac{k}{\gamma_w} \frac{\partial^2 u_e}{\partial y^2} dx dy \quad (19)$$

If the soil behaves elastically, the change in void ratio resulting from the change in effective stress  $d\sigma'$  is

$$\frac{de}{1+e_0} = m_v d\sigma' \quad (20)$$

where  $e_0$  is the initial void ratio and  $m_v$  the soil compressibility. The change in void ratio is related to the initial volume  $V_0$ , solid volume  $V_s$  and void volume  $V_v$  through

$$\frac{de}{1+e_0} = \frac{d(V_v + V_s)}{V_0} = \frac{dV_v}{V_0} = \frac{dV_v}{dx \times dy \times 1} \quad (21)$$

where the soil particles are assumed incompressible (i.e.,  $dV_s = 0$ ). The change in the void volume  $dV_v$  per time  $dt$  is

$$\frac{dV_v}{dt} = m_v \frac{\partial \sigma'}{\partial t} dx dy \quad (22)$$

If the total stress  $\sigma$  is constant (i.e.,  $\frac{\partial \sigma}{\partial t} = \frac{\partial \sigma'}{\partial t} + \frac{\partial u}{\partial t} = 0$ ), the time derivative of effective stress is

$$\frac{\partial \sigma'}{\partial t} = -\frac{\partial u_e}{\partial t} \quad (23)$$

because  $u_s$  is time independent (i.e.,  $\frac{\partial u_s}{\partial t} = 0$ ). Equation 22 becomes:

$$\frac{dV_v}{dt} = -m_v \frac{\partial u_e}{\partial t} dx dy \quad (24)$$

When the soil element remains fully saturated, the volume of voids and interstitial water changes at the same rate:

$$\frac{dV_v}{dt} = \frac{dV_w}{dt} \quad (25)$$

Equations 19, 24 and 25 give the consolidation equation:

$$\frac{\partial u_e}{\partial t} = C_v \frac{\partial^2 u_e}{\partial y^2} \quad (26)$$

where  $C_v$  is the coefficient of consolidation:

$$C_v = \frac{k}{\gamma_w m_v} \quad (27)$$

$C_v$  has the dimension of  $L^2 T^{-1}$  and its units are generally  $m^2/yr$ . The assumptions of the consolidation theory are summarized as follows:

- The layer of soil is homogeneous and is laterally confined.
- The soil is fully saturated.
- Soil particles and water are incompressible.
- The flow of water is one-dimensional.
- Darcy's law describes the flow of water through soil.
- The permeability coefficient  $k$  remains constant.
- The relationship between  $e$  and  $\sigma'$  is linear during a stress increment.
- The soil's own weight has negligible effects.

### Consolidation of a Soil Layer under Constant Load

Equation 26 is a partial differential equation with two variables, time  $t$  and position  $y$ . The unknown function is the excess pore water pressure, noted hereafter as  $u(y, t)$ . Equation 26 can be solved for the particular boundary and initial conditions of Fig. 17, which represents the consolidation test. As shown in Fig. 17b, when the layer is drained at the top and bottom, the boundary conditions are

$$u(0, t) = u(H, t) = 0 \text{ for } t \geq 0 \quad (28)$$

When the initial excess pressure is uniform in the layer at time  $t = 0$ , the initial conditions are

$$u(y, 0) = u_i \text{ for } 0 < y < H \quad (29)$$

The analytical solution of Eqs. 26 to 29 is

$$u(y, t) = u_i \sum_{n=0}^{\infty} \frac{4}{(2n+1)\pi} \sin \left[ (2n+1)\pi \frac{y}{H} \right] e^{-(2n+1)^2 \pi^2 T_v / 4} \quad (30)$$

where  $T_v = \frac{C_v t}{d^2}$  is the dimensionless time factor, and  $d = H/2$  is the drainage distance. Equation 30 applies when the water drains at both top and bottom surfaces

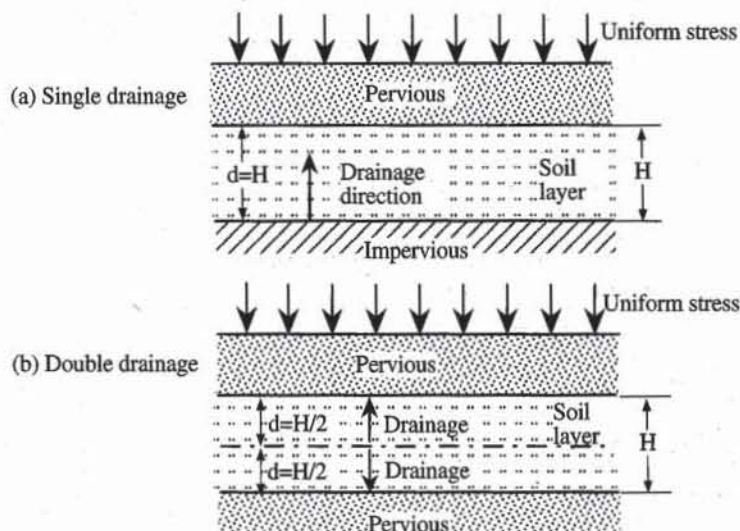


**Figure 17** Definition of (a) single- and (b) double-drainage consolidation problems.

(double drainage, Fig. 17a). When the water drains at only one surface (single drainage, Fig. 17b). Eq. 30 can also be applied by using  $d = H$ . In the standard consolidation test, the sample is between two porous disks (i.e.,  $d = H/2$ ).

When the change in total stress  $\Delta\sigma$  applied to the layer is kept constant, the change in effective stress  $\Delta\sigma'(y, t)$  and excess pore pressure  $u(y, t)$  in the layer are related through

$$\Delta\sigma = u_i = \Delta\sigma'(y, t) + u(y, t) \quad (31)$$

At the beginning of consolidation,  $\Delta\sigma'(y, t) = 0$  and  $u(y, t) = u_i$ . At the end of consolidation,  $\Delta\sigma'(y, t) = \Delta\sigma$  and  $u(y, t) = 0$ . The progress of consolidation at position  $y$  and time  $t$  is then characterized by introducing the degree  $U_y$  of consolidation

$$U_y = \frac{u_i - u(y, t)}{u_i} = \frac{\Delta\sigma'(y, t)}{\Delta\sigma} \quad (32)$$

where  $U_y = 0$  at the beginning of consolidation and  $U_y = 1$ , at the end of consolidation. The settlement of a small element of thickness  $dy$  is  $ds_f$  after consolidation, and  $ds(t)$  at time  $t$  during consolidation

$$ds_f = m_v \Delta\sigma dy \quad \text{and} \quad ds(t) = m_v \Delta\sigma'(y, t) dy = m_v \Delta\sigma U_y dy \quad (33)$$

Using Eq. 33, the total settlement of the layer of thickness  $H$  after and during consolidation are

$$s_f = \int_0^H ds_f = m_v H \Delta\sigma \quad \text{and} \quad s(t) = \int_0^H ds(t) = \frac{s_f}{H} \int_0^H U_y dy = s_f U \quad (34)$$

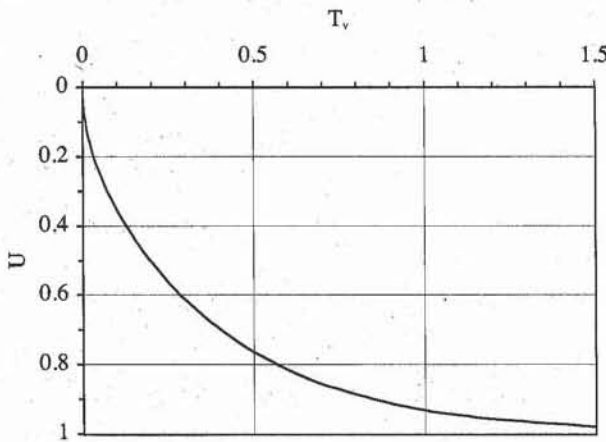


Figure 18 Relation between  $U$  and  $T_v$ .

where  $U$  is the average degree of consolidation of the entire layer,

$$U = \frac{1}{H} \int_0^H U_y dy \quad (35)$$

Using Eq. 30, Eq. 35 becomes:

$$U = 1 - \frac{8}{\pi^2} \sum_{\substack{m=1 \\ odd}}^{+\infty} \frac{e^{-m^2 \pi^2 T_v / 4}}{m^2} \quad (36)$$

Figure 18 shows the variation of  $U$  with  $T_v$  which is given by Eq. 36.  $U$  varies from 0 at the beginning of consolidation ( $T_v = 0$ ) and tends toward 1 at the end of consolidation ( $T_v \rightarrow \infty$ ). Eq. 36 can be approximated as follows:

$$U(T_v) = \begin{cases} U_1(T_v) = \sqrt{\frac{4}{\pi} T_v} & \text{for } T_v < 0.2827 \\ U_2(T_v) = 1 - \frac{8}{\pi^2} \exp\left(-\frac{\pi^2}{4} T_v\right) & \text{for } T_v \geq 0.2827 \end{cases} \quad (37)$$

or inversely,

$$T_v(U) = \begin{cases} T_1(U) = \frac{\pi}{4} U^2 & \text{for } U < 0.6 \\ T_2(U) = -0.085 - 0.933 \log(1-U) & \text{for } U \geq 0.6 \end{cases} \quad (38)$$

Several methods for determining the coefficient of consolidation from experimental results are based on Eqs. 34 to 38. These methods are described later in this chapter.

### Initial, Primary, and Secondary Compressions, and Compression Ratios

Equation 26 describes the time-dependent deformation of soils that results from the diffusion of water. However, this phenomenon, hereafter referred to as the *primary consolidation* or *primary compression*, is not the only phenomenon taking place during the consolidation test; it is accompanied by initial and secondary compressions. Figure 19 introduces these different compressions by using a typical variation of dial reading with time during consolidation test. The dial reading indicates the settlement of the soil sample.

As shown in Fig. 19, the dial reading  $d_0$  at the beginning of primary consolidation (i.e.,  $U = 0\%$ ) is different from the dial reading  $d_c$  at  $t = 0$ , due to the *initial compression*, which takes place before the primary consolidation, almost instantaneously with the load application. The initial compression corresponds to an abrupt settlement unexplained by the primary consolidation, and is due partly to the compression of small pockets of gas within the pore spaces, and partly to the elastic compression of soil grains.

As shown in Fig. 19, the *secondary compression*, also referred to as creep, continues after the primary consolidation is completed and the excess pore pressure is dissipated. The final dial reading  $d_f$  is larger than  $d_{100}$  corresponding to  $U = 100\%$ . The secondary compression is caused by the particle movements and readjustments without a change in effective stress. For most soils, it also takes place during primary compression to a negligible extent, and becomes only noticeable near the completion of the primary compression. The secondary compression phenomenon will be covered in more detail later.

The relative magnitude of initial, primary and secondary phases is expressed in terms of the *initial compression ratio*  $r_i$ , *primary compression ratio*  $r_p$ , and *secondary compression ratio*  $r_s$ :

$$r_i = \frac{d_c - d_0}{d_c - d_f}, \quad r_p = \frac{d_0 - d_{100}}{d_c - d_f}, \quad \text{and} \quad r_s = \frac{d_{100} - d_f}{d_c - d_f} \quad (39)$$

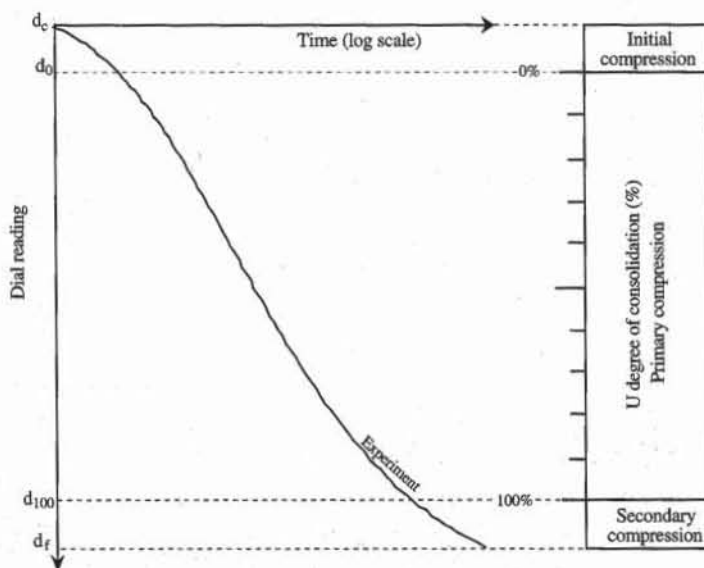


**Figure 19** Initial, primary, and secondary compressions during the consolidation test.

where  $d_c$  is the initial dial reading,  $d_f$  the final dial reading,  $d_0$  the dial reading at the beginning of primary consolidation, and  $d_{100}$  the dial reading at the end of primary consolidation. The compression ratios  $r_i$ ,  $r_p$ , and  $r_s$  are the proportions of initial (i.e.,  $d_c - d_0$ ), primary (i.e.,  $d_0 - d_{100}$ ), and secondary (i.e.,  $d_{100} - d_f$ ) compressions to the total compression (i.e.,  $d_c - d_f$ ).  $r_i$ ,  $r_p$ , and  $r_s$  are dimensionless, and  $r_i + r_p + r_s = 1$ . For most inorganic clays, the primary compression ratio  $r_p$  is larger than  $r_i$  and  $r_s$ . Several methods for determining the compression ratios are described later in this chapter.

### Typical Values and Correlations for Consolidation Coefficients

Table 2 lists the values of consolidation coefficients  $C_v$  for various soils and indicates their range of variation. The smallest value for  $C_v$  is equal to  $0.1 \text{ m}^2/\text{yr}$  in the case of sensitive Swedish clay, whereas the largest value is about  $30,000 \text{ m}^2/\text{yr}$  which implies a very rapid rate of consolidation. Sands and gravels may have even larger consolidation coefficients due to their large permeability coefficient. Figure 20 shows the approximate relation between the coefficient of consolidation with the liquid limit in cases of undisturbed and remolded samples of fine-grained soils.

**TABLE 2**

Values of consolidation coefficient for various soils.

Type of soil	Coefficient of consolidation ( $\text{m}^2/\text{yr}$ )	Coefficient of consolidation ( $10^{-4} \text{ cm}^2/\text{s}$ )	References
Mexico City clay (MH)	0.9–1.5	0.28–0.47	Leonards and Girault (1961)
Boston blue clay	6–18	1.89–5.68	Ladd and Luscher (1965)
(CL, marine deposit glacial clay, illite)			
Organic silt (OH)	0.6–3.0	0.19–0.95	Lowe et al. (1964)
Glacial lake clays (CL)	2.0–2.7	0.63–0.85	Wallace and Otto (1964)
Chicago silty clay (CL)	2.70	0.85	Terzaghi and Peck (1967)
Swedish medium-sensitive clays (CL-CH)	0.1–0.2	0.03–0.06	Holtz and Broms (1972)
San Francisco Bay mud (CL)	0.6–1.2	0.19–0.38	
Maine clay (silty, glacial clay, partially illite)	6.3–13	1.99–3.97	
Normally consolidated stuarine silty clay	3.17–32	1–10	Lee et al. (1983)
Stiff red clay	3.17	1	
Sandy clay	32–317	10–100	
Silt	317–31710	100–10000	
London clay	1.90–6.34	0.6–2.0	Skempton and Henkel (1957)
Shellhaven postglacial clay	1.27–3.81	0.4–1.2	Skempton and Henkel (1953)
Tilbury postglacial clay	2.85–3.49	0.9–1.1	
Calcareous silt (normally consolidated)	1015	320	Poulos (1980)
Carbonate silt	222	70	
Marine clay	634–6342	200–2000	Bishop and Henkel (1962)
Boulder clay	63–634	20–200	
Boulder clay and residual clay	3.17–630	1–20	

### ALTERNATE CONSOLIDATION TESTS

One of the major disadvantages of the consolidation test is the length of time required for completion. A typical test can take up to two weeks (see Chapter 6-2). To reduce the testing period, several alternate methods have been proposed.

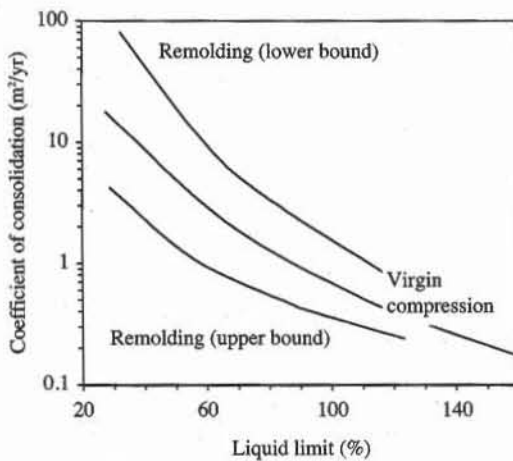


**Figure 20** Approximate correlation of the coefficient of consolidation with liquid limit (after NAVFAC, 1982).

### Summary of Alternate Tests

The principles of the alternate consolidation test can be explained by using the experimental setup of Fig. 21. The soil sample in the consolidation cell is subjected to the total stress  $\sigma$  which is applied by the piston moving at a control rate of either displacement or load. The water is allowed to drain through the upper face of the sample, and is kept at the back pressure  $u_B$ . On the lower side of the sample, there is no drainage and a pore pressure transducer records the pore pressure  $u_A$ . The settlement  $\Delta h$  of the sample is recorded by a displacement transducer.

Using Figs. 21 and 22, the various consolidation methods can be summarized as follows:

- (a) *Conventional incremental loading*: the total stress  $\sigma$  is kept constant during each loading segment.
- (b) *Constant rate of strain (CRS)*: the vertical deformation  $\Delta h$  is applied at a constant rate.
- (c) *Constant rate of loading*: the applied total stress  $\sigma$  is increased at a constant rate.
- (d) *Constant pore pressure gradient*: the difference in pore pressure  $u_A - u_B$  between the upper and lower faces of the sample is kept constant.
- (e) *Constant ratio of pore pressure to load*: the loading is applied such that the pore pressure  $u_A$  is always a fixed proportion of the total stress  $\sigma$ .
- (f) *Consolidation with back pressure control*: the back pressure  $u_B$  is initially equal to the pore pressure  $u_A$  in the sample and is steadily reduced to a constant final value.

We will only briefly summarize the constant rate of strain consolidation, which is covered by ASTM 4186. The description of other procedures can be found in Head (1986) and Lowe et al. (1969).

### Constant Rate of Strain Consolidation

During the *constant rate of strain (CRS)* consolidation tests, the vertical deformation  $\Delta h$  is applied at a constant rate, and the pore pressure  $u_A$  and total stress  $\sigma$

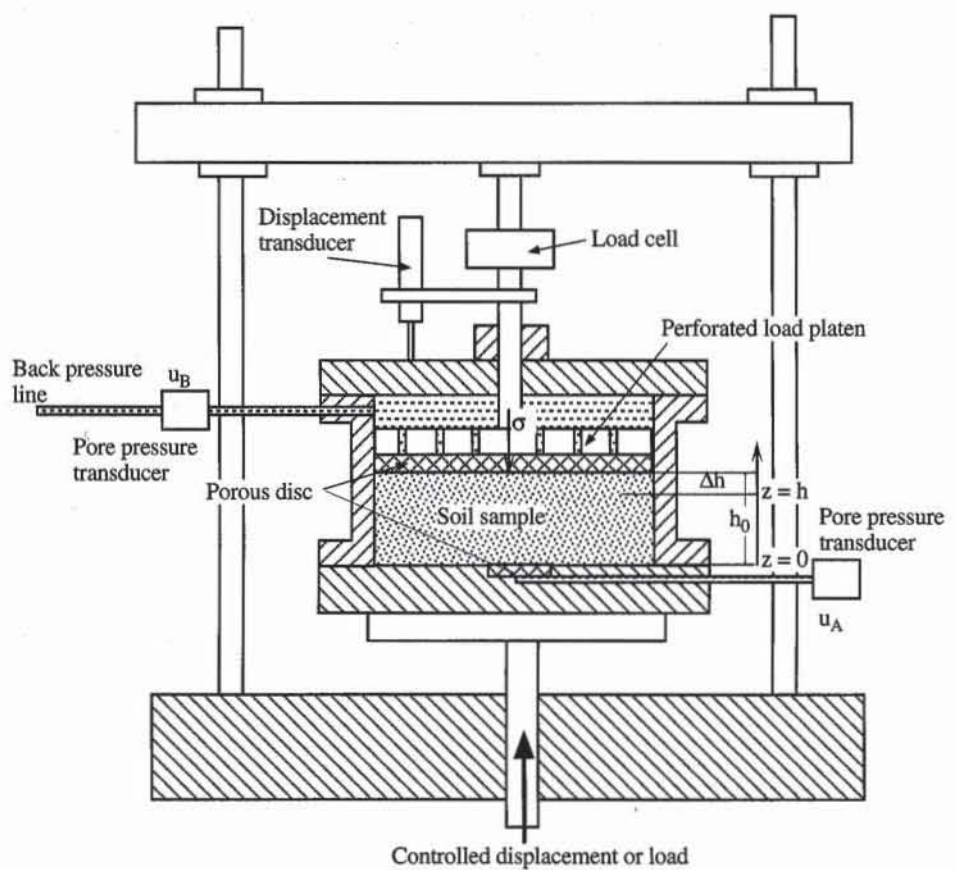


**Figure 21** Experimental setup for alternate consolidation test (after Head, 1986).

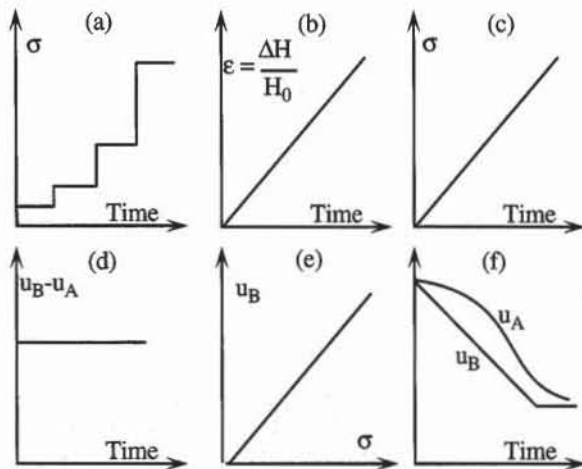


**Figure 22** Representation of loading patterns for consolidation tests: (a) conventional incremental loading, (b) constant rate of strain, (c) constant rate of loading, (d) constant pore pressure gradient, (e) constant pore pressure ratio, and (f) back pressure control.

are measured at specified time intervals. The back pressure  $u_B$  is set equal to zero. The spatial distribution of pore pressure within the layer of thickness  $h$  is assumed to be parabolic, that is

$$u(z, t) = u_A(t) \left(1 - \frac{z^2}{h^2}\right) \quad (40)$$

and obeys the following boundary conditions

$$u(0, t) = u_A(t), \quad u(h, t) = u_B = 0, \quad \text{and} \quad \frac{\partial u}{\partial z}(0, t) = 0 \quad (41)$$

The layer thickness is  $h_0$  at time  $t = 0$ , and decreases at the constant rate  $r$  specified during the test. The average pore pressure excess in the layer is

$$\bar{u}(t) = \frac{1}{h} \int_0^h u(z, t) dz = \frac{2}{3} u_A(t) \quad (42)$$

The rate of change in volume of water is

$$\frac{dV_w}{dt} = \frac{k}{\gamma_w} \frac{\partial^2 u}{\partial z^2} A = -\frac{2k}{\gamma_w} \frac{u_A(t)}{h^2} A = -rA \quad (43)$$

where  $A$  is the surface area of the soil sample. The average effective stress in the layer is:

$$\bar{\sigma}'(t) = \sigma(t) - \bar{u}(t) = \sigma(t) - \frac{2}{3} u_A(t) \quad (44)$$

The rate of change in volume of solid is

$$\frac{dV_v}{dt} = -m_v \frac{\partial \bar{\sigma}'}{\partial t} A = -m_v \left( \frac{d\sigma}{dt} - \frac{2}{3} \frac{du_A}{dt} \right) A = -rA \quad (45)$$

Therefore the consolidation coefficient is:

$$C_v(t) = \frac{k}{\gamma_w m_v} = \frac{1}{2} \left( \frac{d\sigma}{dt} - \frac{2}{3} \frac{du_A}{dt} \right) \frac{h^2}{u_A(t)} \quad (46)$$

Replacing the time derivative by small increment, Eq. 46 becomes

$$C_v \approx \frac{\bar{h}^2}{2\bar{u}_A \delta t} \left( \delta\sigma - \frac{2}{3} \delta u_A \right) \quad (47)$$

where  $\delta t$  is the time interval between two measurements,  $\bar{h}$  the average height during  $\delta t$ ,  $\bar{u}_A$  the average excess pore pressure during  $\delta t$ ,  $\delta\sigma$  the change in applied total stress during  $\delta t$ , and  $\delta u_A$  the change in excess pore pressure during  $\delta t$ . The average coefficient of consolidation in a time interval can also be calculated as follows (ASTM 4186)

$$C_v \approx -\frac{\bar{h}^2 \log \left( \frac{\sigma_2}{\sigma_1} \right)}{2(t_2 - t_1) \log \left( 1 - \frac{\bar{u}_A}{\bar{\sigma}} \right)} \quad (48)$$

where  $\sigma_1$  is the total stress at time  $t_1$ ,  $\sigma_2$  the total stress at time  $t_2 = t_1 + \delta t$ ,  $\bar{h}$  the average height during  $\delta t$ , and  $\bar{\sigma}$  the average total stress during  $\delta t$ . The average effective stress  $\bar{\sigma}'$  in the layer during  $\delta t$  is

$$\bar{\sigma}' = \bar{\sigma} - \frac{2}{3} \bar{u}_A \quad (49)$$

and the corresponding void ratio  $e$  is

$$e = e_0 - \frac{\Delta h}{h_0} (1 + e_0) \quad (50)$$

where  $e_0$  is the initial void ratio and  $h_0$  the initial sample height.

Like the conventional consolidation test, the CRS consolidation test gives the variation of effective stress and coefficient of consolidation with void ratio. However, the CRS consolidation does not last as long as the conventional test because it does not wait for the complete dissipation of pore pressure. The duration of the test is controlled by the strain rate. ASTM 4186 recommends to select a strain rate so that the excess pore pressure remains between 3 and 30% of the applied stress at any time during the test. One of the disadvantages of the CRS consolidation test is to require the measurement of pore pressure and force.

Figure 23 shows the results of a CRS consolidation test at constant strain rates of 0.024 and 0.06% per min on Masena clay (Smith and Wahls, 1969). The CRS consolidation results are in good agreement with those of conventional tests, especially at lower strain rate.

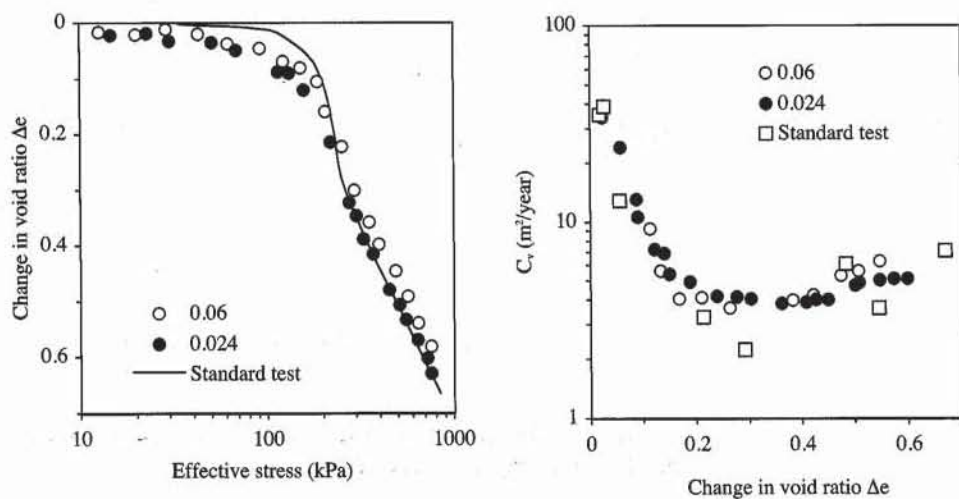


**Figure 23** Results of constant rate of strain consolidation tests at 0.024 and 0.06% per min on Masena clay and comparison with standard tests (after Smith and Wahls, 1969).

## SECONDARY COMPRESSION

As mentioned previously, the settlement of fine-grained soils in the consolidation test is caused not only by primary consolidation but also by secondary compression. In contrast to primary consolidation, secondary compression takes place at constant effective stress and without a diffusion of excess pore pressure.

### Theory

In general, while the excess pore pressure is still dissipating, both primary and secondary compressions take place simultaneously, which complicates interpretation of the consolidation test results. Hereafter, secondary compression is assumed to be negligible during primary compression, and is identified after primary consolidation is completed.

Secondary compression is reported by using expressions similar to those used for primary compression. The change in void ratio  $\Delta e_s$  resulting from secondary compression from time  $t_s$  to time  $t$  is described as follows (Mesri and Godlewski, 1977):

$$\Delta e_s = C_\alpha \log_{10} \left( \frac{t}{t_s} \right) \quad (51)$$

where  $C_\alpha$  is the secondary compression index. The secondary compression axial strain  $\epsilon_s$  corresponding to  $\Delta e_s$  is

$$\epsilon_s = C_{\alpha e} \log_{10} \left( \frac{t}{t_s} \right) \quad (52)$$

where  $C_{\alpha e}$  is the modified secondary compression index, which is related to  $C_\alpha$  using Eq. 4:

$$C_{\alpha e} = \frac{C_\alpha}{1 + e_s} \quad (53)$$

$e_s$  is the void at the beginning of the secondary compression.  $e_s$  may also be set equal to  $e_0$  without introducing substantial errors. Using Eq. 41, the secondary compression settlement is

$$s_s = h_s C_{\alpha e} \log_{10} \left( \frac{t}{t_s} \right) \quad (54)$$

where  $h_s$  is the sample height at the beginning of secondary compression.

### Typical Values and Correlations for Coefficient of Secondary Compression

Table 3 lists values of the ratio between the coefficient  $C_\alpha$  of secondary compression and the compression index  $C_c$ . Values of  $C_\alpha$  may be obtained by using the values of  $C_c$  listed in Table 1. As shown in Table 3, the ratio  $C_\alpha/C_c$  is almost constant for a given soil, and varies from 0.025 to 0.1 for all soils.

As shown in Fig. 24,  $C_{\alpha e}$  has been correlated to the natural water content

for a wide variety of clays. Based on Fig. 24, the following relation was suggested for normally consolidated clays

$$C_{\alpha e} = 0.0001 w_n \quad (55)$$

where  $w_n$  is the natural water content in percent.

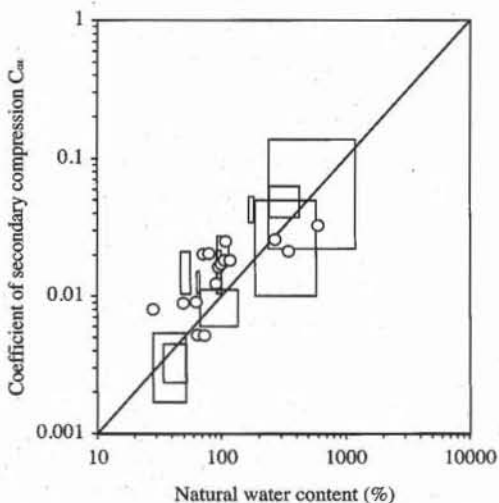


**Figure 24** Variation of coefficient of secondary compression  $C_{\alpha e}$  with natural water content (Mesri, 1973).

**TABLE 3**

Values of secondary consolidation coefficient for various soils (after Mesri and Godlewski, 1977).

Type of soil	$C_{\alpha}/C_c$
Whangamarino clay	0.03–0.04
Norfolk organic silts	0.03
Calcareous organic silt	0.035–0.06
Amorphous and fibrous peat	0.035–0.083
Canadian Muskeg	0.09–0.10
Leda clay (Canada)	0.03–0.06
Peat	0.075–0.085
Post glacial organic clay	0.05–0.07
Soft blue clay	0.026
Organic clays and silts	0.04–0.06
Sensitive clay, Portland	0.025–0.055
San Francisco Bay Mud	0.04–0.06
New Liskeard varved clay (Canada)	0.03–0.06
Mexico City clay	0.03–0.035
Hudson River silt	0.03–0.06
New Haven organic clay silt	0.04–0.075

## DETERMINATION OF CONSOLIDATION COEFFICIENTS

As derived in Eq. 34, during primary consolidation, the settlement  $s(t)$  of soil samples at time  $t$  is

$$s(t) = s_f U(T_v) \quad \text{and} \quad T_v = \frac{C_v t}{d_m^2} \quad (56)$$

where  $s_f$  is the final settlement,  $C_v$  the coefficient of consolidation,  $d_m$  the average drainage distance,  $T_v$  the dimensionless time factor, and  $U(T_v)$  the function of  $T_v$  given in Eqs. 36 to 38. During the consolidation test, the settlement  $s(t)$  is continuously monitored by the displacement dial reading  $d(t)$ . In this case, Eq. 56 becomes

$$s(t) = d(t) - d_0 = s_f U(T_v) = (d_{100} - d_0) U(T_v) \quad (57)$$

where  $d_0$  is the dial reading at the beginning of consolidation ( $U = 0\%$ ), and  $d_{100}$  is the dial reading after completion of consolidation ( $U = 100\%$ ). The dial reading  $d(t)$  at time  $t$  is therefore

$$d(t) = d_0 + (d_{100} - d_0) U\left(\frac{C_v t}{d_m^2}\right) \quad (58)$$

The average drainage distance  $d_m = h/2$  for samples between two porous disks (double drainage), and  $d_m = h$  for single drainage where  $h$  is the average sample height during consolidation. In the case of double drainage, the average drainage distance  $d_m$  is

$$d_m = \frac{1}{2} \left( h_0 + d_i - \frac{1}{2} (d_{100} + d_0) \right) \quad (59)$$

where  $h_0$  is the initial sample height corresponding to dial reading  $d_i$ .  $d_m$  also corresponds to  $U = 50\%$ .

The coefficient of consolidation  $C_v$  is determined by matching Eq. 58 with the data points that are relevant only to the primary consolidation. Four methods for determining  $C_v$  are presented, including two traditional procedures—the log-time and square-root-time methods—and two other methods based on regression analysis.

### Log-Time Method

In the log-time method, the theoretical curve  $U(T_v)$  is plotted by using a logarithmic scale for  $T_v$ , as shown in Fig. 25, and is matched with the experimental data points of primary consolidation by determining  $C_v$ ,  $d_0$ , and  $d_{100}$ . As shown in Fig. 26,  $d_0$  is determined by selecting two experimental data points  $A$  and  $B$  that are both on the theoretical curve  $T_v = T_1(U)$  for  $U < 0.6$ :

$$\frac{t_B}{t_A} = \frac{T_v^B}{T_v^A} = \frac{U_B^2}{U_A^2} = \frac{(d_B - d_0)^2}{(d_A - d_0)^2} \quad (60)$$

where  $d_A$  is the dial reading time at point  $A$ ,  $t_A$  the time at point  $A$ ,  $T_v^A$  the time factor at point  $A$ , and  $U_A$  the degree of consolidation at point  $A$ . Similar definitions apply for points  $B$ . By using Eq. 60,  $d_0$  is

$$d_0 = \frac{d_A \sqrt{t_B} - d_B \sqrt{t_A}}{\sqrt{t_B} - \sqrt{t_A}} \quad (61)$$

It is a common practice to choose  $t_A \approx 1$  min and  $t_B \approx 4 t_A$  so that Eq. 61 becomes  $d_0 = 2d_A - d_B$ .

$d_{100}$  is calculated by determining the end of primary consolidation (i.e.,  $U =$

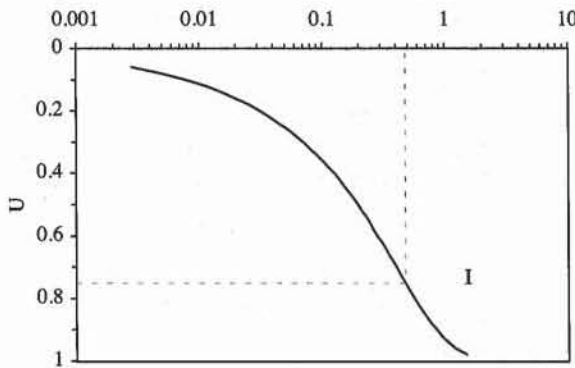


**Figure 25** Theoretical relation  $U(T_v)$  plotted with a logarithmic scale for  $T_v$ .

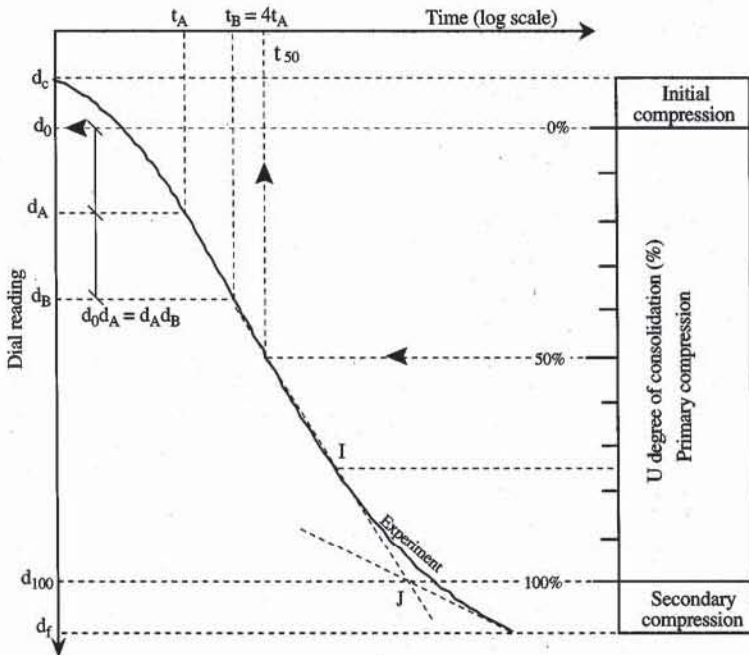


**Figure 26** Determination of  $C_v$  with-log-time method.

100%). As shown in Fig. 25, the theoretical curve has a point of inflection  $I$  at  $U \approx 75\%$ . At point  $I$ , the curve has a different curvature and the steepest slope. As shown in Fig. 26, the intersection point  $J$  of the tangent point  $I$  with the backward extension of the secondary compression line defines the point where  $U = 100\%$ . The middle  $d_{50}$  of segment  $d_0 d_{100}$  is

$$d_{50} = \frac{1}{2}(d_0 + d_{100}) \quad (62)$$

and corresponds to  $U = 50\%$  and time  $t_{50}$ , which is thus obtained from the experimental curve. By using Eq. 17 with  $U = 50\%$ ,  $T_v = 0.197$  and  $C_v$  is

$$C_v = 0.197 \frac{d_m^2}{t_{50}} \quad (63)$$

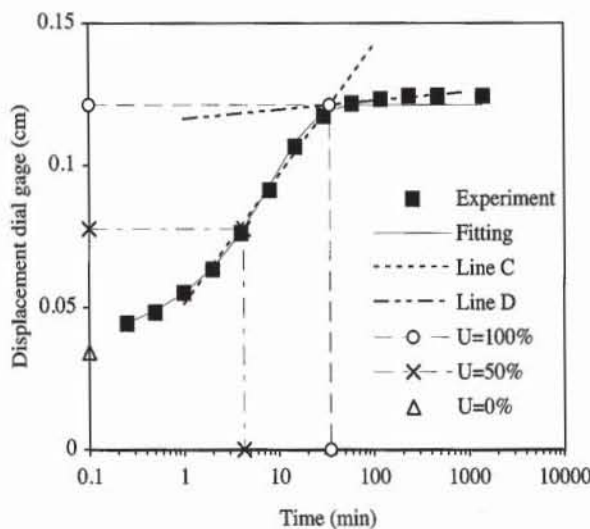


**Figure 27** Determination of  $C_v$  with log-time method.

### Example of $C_v$ Determination with Log-Time Method

Figure 27 to 30 show the experimental and fitted results, the calculation details, and the formulas used for the consolidation test. The straight lines  $C$  and  $D$  of Fig. 27 are tangent to the experimental curve on each side of the inflection point. They are determined by using a linear regression through selected data points and give the intersection point  $(t_{100}, d_{100})$ , which corresponds to  $U = 100\%$ . The time  $t_{50}$  corresponding to  $d_{50}$  is calculated by using the user-defined function INTER, which performs a linear interpolation on the points  $(\log_{10} t_i, d_i)$  (see Chapter 8-1). The fitted data points are determined by using Eq. 58.  $U(T_v)$  is implemented in the user-defined function  $U$  of Fig. 30. As shown in Fig. 27, there is a very good agreement between the experimental and fitted points, which implies that  $C_v$  is defined correctly.

### Square-Root-Time Method

The function  $U(T_v)$  is plotted in Fig. 31 versus the square root of  $T_v$ . The square-root-time method determines  $d_0$ ,  $d_{100}$ , and  $C_v$  so that the theoretical curve of Fig. 31 falls as closely as possible to the experimental data points relevant to the primary consolidation. The dial reading is plotted against the square root of time as shown in Fig. 32.  $d_0$  is given by the intercept  $D$  of line  $DB$  passing through the straight part of the experimental curve.

The next step is to find  $t_{90}$  and  $d_{90}$  corresponding to  $U = 90\%$ . Using Eq. 38 for  $U = U_s$ , we obtain

$$\sqrt{\frac{t_2(U_s)}{t_1(U_s)}} = \sqrt{\frac{T_2(U_s)}{T_1(U_s)}} = \frac{2}{U_s \sqrt{\pi}} \sqrt{-0.085 - 0.933 \log_{10}(1 - U_s)} = \alpha(U_s) \quad (64)$$

When  $U_s = 0.9$ , Eq. 64 becomes

$$\alpha(0.9) = 1.1545 \quad (65)$$

	A	B	C	D	E	F
1	<b>Log-time method</b>					
2	Time (min)	Displacement dial gage (cm)	Fitted displacement (cm)		line C	line D
3	t	d				
4	0.0	0.0000	0.0340		Slope $s_C$ or $s_D$ =	0.0454 0.0032
5	0.3	0.0445	0.0446		Intercept $i_C$ or $i_D$ =	0.0512 0.1163
6	0.5	0.0483	0.0490		Dial reading at time $t_A$ , $d_A$ =	0.0551 cm
7	1.0	0.0551	0.0552		Time $t_B$ =	4.0 min
8	2.0	0.0635	0.0639		Dial reading at time $t_B$ , $d_B$ =	0.0762 cm
9	4.0	0.0762	0.0763	Dial reading at beginning of primary consolidation $d_0$ =	0.0340 cm	
10	8.0	0.0912	0.0928		Initial height $h_0$ =	1.905 cm
11	15.0	0.1067	0.1084		Initial dial reading $d_i$ =	0 cm
12	30.0	0.1173	0.1189	Time at 100% of primary consolidation $t_{100}$ =	34.79 min	
13	60.0	0.1217	0.1212	Dial reading at 100% of primary consolidation $d_{100}$ =	0.1212 cm	
14	120.0	0.1232	0.1212	Dial reading at 50% of primary consolidation $d_{50}$ =	0.0776 cm	
15	240.0	0.1245	0.1212	Time at 50% of primary consolidation $t_{50}$ =	4.27 min	
16	480.0	0.1245	0.1212	Average drainage distance $d_m$ =	0.9137 cm	
17	1440.0	0.1245	0.1212	Coefficient of consolidation $C_v$ =	0.0385 $\text{cm}^2/\text{min}$	
18				Initial compression ratio $r_i$ =	27.3%	
19				Primary compression ratio $r_p$ =	70.1%	
20				Secondary compression ratio $r_s$ =	2.6%	

**Figure 28** Example of data set for determination of  $C_v$  with log-time method.

	D	E	F
3	Slope $s_C$ or $s_D = =SLOPE(B10:B12,LOG(A10:A12))$		$=SLOPE(B13:B16,LOG(A13:A16))$
4	Intercept $i_C$ or $i_D = =INTERCEPT(B10:B12,LOG(A10:A12))$		$=INTERCEPT(B13:B16,LOG(A13:A16))$
5	Time $t_A = =A7$		min
6	Dial reading at time $t_A$ $d_A = =B7$		cm
7	Time $t_B = =A9$		min
8	Dial reading at time $t_B$ $d_B = =B9$		cm
9	Dial reading at beginning of primary consolidation $d_0 = =(dA*SQRT(tB)-dB*SQRT(tA))/(SQRT(tB)-SQRT(tA))$		cm
10	Initial height $h_0 = 1.905$		cm
11	Initial dial reading $d_i = 0$		cm
12	Time at 100% of primary consolidation $t_{100} = =10^{(iD-iC)/(sC-sD)}$		min
13	Dial reading at 100% of primary consolidation $d_{100} = =sC*LOG(t_{100})+iC$		cm
14	Dial reading at 50% of primary consolidation $d_{50} = =(d0+d_{100})/2$		cm
15	Time at 50% of primary consolidation $t_{50} = =INTER(d_{50},d,t)$		min
16	Average drainage distance $d_m = =(h_0+d_i-(d0+d_{100})/2)/2$		cm
17	Coefficient of consolidation $C_v = =0.197*dm^2/t_{50}$		cm <sup>2</sup> /min
18	Initial compression ratio $r_i = =(B4-d0)/(B4-B17)$		
19	Primary compression ratio $r_p = =(d0-d_{100})/(B4-B17)$		
20	Secondary compression ratio $r_s = =1-r_i-r_p$		

C	
2	Fitted displacement (cm)
3	
4	$=d0+(d_{100}-d0)*U(Cv*t/dm^2)$
5	$=d0+(d_{100}-d0)*U(Cv*t/dm^2)$

Figure 29 Formulas used in Fig. 28.

	B	C
2	<b>U</b>	Degree of consolidation
3	=RESULT(1)	
4	=ARGUMENT("T",1)	Dimensionless time factor
5	=IF(T>0.2827,RETURN(1-8/PI()^2/EXP(PI()^2*T/4)),RETURN(SQRT(4*T/PI())))	

Figure 30 User-defined function  $U$  used in Fig. 29.

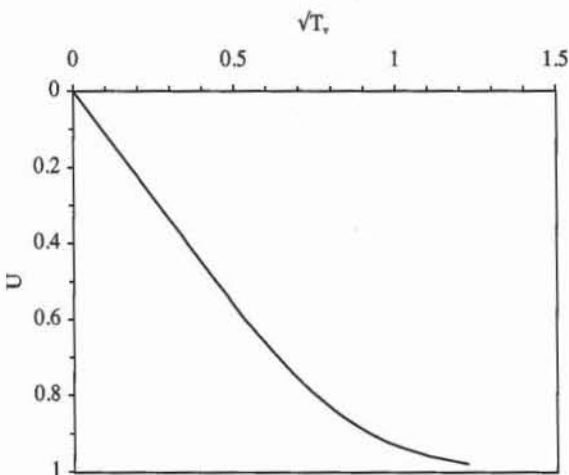


Figure 31 Theoretical relation  $U(T_v)$  plotted versus the square root of  $T_v$ .

The time  $t_{90}$  corresponding to  $U = 90\%$  is found by drawing the straight line  $DC$ , the slope of which is  $1/1.1545$  times the slope of line  $DB$ . The straight line  $DC$  cuts the experimental consolidation curve at point  $E$ , which corresponds to  $U = 90\%$  and has for coordinates  $d_{90}$  and  $\sqrt{t_{90}}$ . Using Eqs. 37 and 51,  $C_v$  and  $d_{100}$  are

$$C_v = 0.848 \frac{d^2}{t_{90}} \quad \text{and} \quad d_{100} = d_0 - \frac{10}{9}(d_0 - d_{90}) \quad (66)$$

### Generalized Square-Root-Time Method

The square-root method can be generalized to values of  $U_s$  between 0.6 and 1. The slope of line  $DC$  is now  $1/\alpha(U_s)$  times the slope of line  $DB$ . This generalized square-root method is implemented in the user-defined function CONSO. The first step is to select  $m$  data points and to fit them by linear regression with line  $DB$ :

$$d = d_0 + \beta \sqrt{t} \quad (67)$$

where  $d_0$  is the intercept and  $\beta$  is the slope. The second step is to find the intersection between the data points and line  $DC$ :

$$d = d_0 + \beta' \sqrt{t} \quad \text{with} \quad \beta' = \frac{\beta}{\alpha(U_s)} \quad (68)$$

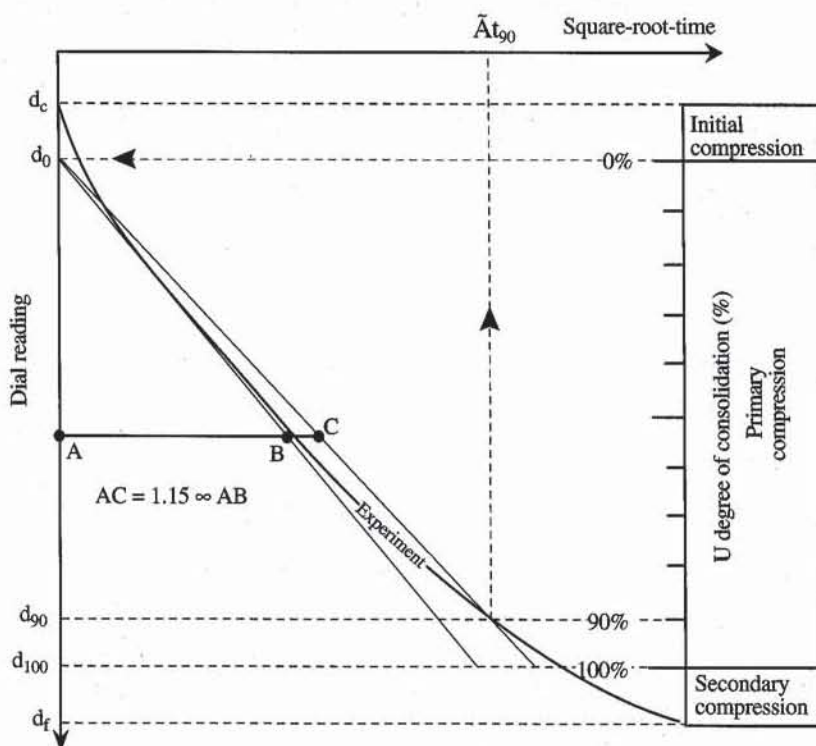


**Figure 32** Determination of  $C_v$  with square-root-time method.

The  $n$  data points  $(d_i, \sqrt{t}_i)$  form jointed segments, each having the equation

$$d = d_i + \frac{d_{i+1} - d_i}{\sqrt{t}_{i+1} - \sqrt{t}_i} (\sqrt{t} - \sqrt{t}_i) \quad (69)$$

The segment connecting points  $i$  and  $i + 1$  is intersected by line  $DC$  when

$$(d_i - d_0 - \beta' \sqrt{t}_i) (d_{i+1} - d_0 - \beta' \sqrt{t}_{i+1}) \leq 0 \quad (70)$$

The coordinates of the intersection point are

$$\sqrt{t}_s = \frac{(d_0 - d_i) (\sqrt{t}_{i+1} - \sqrt{t}_i) + (d_{i+1} - d_i) \sqrt{t}_i}{d_{i+1} - d_i - \beta' (\sqrt{t}_{i+1} - \sqrt{t}_i)} \quad \text{and} \quad d_s = d_0 + \beta' \sqrt{t}_s \quad (71)$$

Therefore, the consolidation coefficient  $C_v$  and  $d_{100}$  are

$$C_v = T_v(U_s) \frac{d^2}{t_s} \quad \text{and} \quad d_{100} = d_0 + \frac{1}{U_s} (d_s - d_0) \quad (72)$$

#### User-Defined Function CONSO

Figure 33 lists the user-defined function CONSO for the generalized square-root-time method. CONSO determines the following quantities:  $t_s$  is the time at  $U = U_s$ ,  $d_s$  the dial reading at  $U = U_s$ ,  $d_0$  the dial reading at  $U = 0\%$ ,  $d_{100}$  the dial

A	B	C
12	Conso	User-defined function
13	=RESULT(64)	Input
14	=ARGUMENT("T";64)	$t_i$ , time series
15	=ARGUMENT("D";64)	$d_i$ , dial reading series
16	=ARGUMENT("H0";1)	$h_0$ , height of sample at beginning of time series
17	=ARGUMENT("TB";1)	$t_b$ , time at beginning of square root time fitting
18	=ARGUMENT("TE";1)	$t_e$ , time at end of square root time method
19	=ARGUMENT("US";1)	$U_s$ , variable ( $0.6 < U_s < 1$ )
20	=IF(OR(ROWS(T)<>ROWS(D));RETURN(#VALUE!))	Arrays T and D must be in columns
21	n=ROWS(T)	Number of input data points
22	=SET.VALUE(D25:D29;{0,0,0,0,0})	Find slope b by using a
23	=FOR("I";1;n)	linear regression for square root time
24	= IF(AND(INDEX(T;I)>=TB;INDEX(T;I)<=TE))	with points such that $T \leq t_i \leq T_e$
25	m = SET.VALUE(m;m+1)	number of selected points
26	ax = SET.VALUE(ax;ax+SQRT(INDEX(T;I)))	sum of $\sqrt{t_i}$
27	ay = SET.VALUE/ay;ay+INDEX(D;I))	sum of $d_i$
28	axy = SET.VALUE(axy;axy+INDEX(D;I)*SQRT(INDEX(T;I)))	sum of $\sqrt{t_i}d_i$
29	axx = SET.VALUE(axx;axx+INDEX(T;I))	sum of $t_i$
30	= END.IF()	
31	=NEXT()	
32	aUs = 2*SQRT((-0.085-0.933*LOG(1-US))/PI())/US	$a(U_s)$
33	bp =(m*axy-ax*ay)/(m*axx-ax^2)/aUs	$b'$ slope of straight line
34	d0 =(ay*axx-ax*axy)/(m*axx-ax^2)	$d_0$ , intercept of straight line
35	=FOR("I";1;n-1)	Find the intersection of straight line
36	= IF(INDEX(T;I)>TE)	with data segments
37	= IF((INDEX(D;I+1)-d0-bp*SQRT(INDEX(T;I+1)))*(INDEX(D;I)-d0-bp*SQRT(INDEX(T;I)))<=0)	
38	Dt = SQRT(INDEX(T;I+1))-SQRT(INDEX(T;I))	
39	Dd = INDEX(D;I+1)-INDEX(D;I)	
40	ts = ((d0-INDEX(D;I))*Dt+Dd*SQRT(INDEX(T;I)))/2/(Dd-bp*Dl)^2	
41	ds = d0+bp*SQRT(ts)	
42	= d0	
43	d_100 = (ds-d0)/US+d0	
44	dm = (H0+INDEX(D;1)-(d0+d_100)/2)/2	
45	Cv = Tv(US)*dm^2/ls	
46	ri = (INDEX(D;1)-d0)/(INDEX(D;1)-INDEX(D;n))	
47	rp = (d0-d_100)/(INDEX(D;1)-INDEX(D;n))	
48	rs = 1-ri-rp	
49	= RETURN(B40:B48)	
50	= END.IF()	Note:
51	= END.IF()	$h_0$ is not the initial sample height, but
52	=NEXT()	the height at beginning of time series
53	=RETURN(#VALUE!)	

Figure 33 User-defined function CONSO for determination of consolidation coefficient and compression ratios.

reading at  $U = 100\%$ ,  $d_m$  the average drainage length,  $C_v$  the consolidation coefficient,  $r_i$  the initial compression ratio,  $r_p$  the primary compression ratio, and  $r_s$  the secondary compression ratio. The input data are:  $(t_i, i = 1, \dots, n)$  is the time series,  $(d_i, i = 1, \dots, n)$  the dial reading series,  $h_0$  the sample height at dial reading  $d_i$ ,  $t_b$  the starting time for fitting line DB,  $t_e$  the ending time for fitting line DB, and  $U_s$  the fitting degree of consolidation ( $0.6 < U_s < 1$ ). All input data with the same dimension should have the same unit. The time series should be increasing and starting at  $t_1 = 0$ . Times  $t_b$  and  $t_e$  select the data points for fitting line DB. In general,  $t_b$  is selected equal to 1 min to eliminate initial compression.  $t_e$  is selected large enough to have at least three data points between  $t_b$  and  $t_e$ .

### Example of $C_v$ Determination with Square-Root-Time Methods

Figures 34 and 36 show the experimental results of Fig. 27 which are fitted by using the square-root-time method for  $U_s = 90\%$  and  $99\%$ . Figures 35 to 38 compare the experimental and fitted curves, and list the formulas used in the calculation. The calculations are performed by the user-defined function CONSO. Times  $t_b$  and  $t_e$  select the data points for fitting line DB. Both square-root-time methods give similar results for  $C_v$ ,  $r_i$ ,  $r_p$ , and  $r_s$ . These values are also close to those found by the log-time method. The generalized method ( $U_s = 99\%$ ) fits the data points slightly better than the conventional method ( $U_s = 90\%$ ).

### Nonlinear Optimization with Constraints

Nonlinear optimization with constraints (see Chapter 8-1) can be applied to optimize the following three variables:  $d_0$ ,  $d_{100}$ , and  $C'_v = C_v/d_m^2$  with the following constraints:

$$d_0 \geq d_1, \quad d_{100} \leq d_n, \quad d_{100} \geq d_0, \quad \text{and } C'_v \geq 0 \quad (73)$$

where  $d_1$  is the first dial reading, and  $d_n$  is the last dial reading. The function to minimize is the error  $E$  between the experimental dial reading  $d_i$  and fitted dial reading  $d_i^p = d_0 + (d_{100} - d_0) U(C'_v t_i)$  at time  $t_i$ :

$$E = \sum_{i=1}^n (d_i - d_i^p)^2 \quad (74)$$

	A	B	C	D	E	F	G
1	Square root-time method						
2	Elapsed (min)	Displacement dial gage (cm)	$\sqrt{t}$ ( $\sqrt{\text{min}}$ )	Fitted displacement (cm)			
3	t	d					
4	0.0	0.0000	0.0	0.0336	Initial height $h_n =$	1.905 cm	
5	0.3	0.0445	0.5	0.0442	Starting time for fitting, $t_b =$	0.3 min	
6	0.5	0.0483	0.7	0.0486	Ending time for fitting, $t_e =$	4.0 min	
7	1.0	0.0551	1.0	0.0549	Degree of consolidation of method $U_s =$	99%	
8	2.0	0.0635	1.4	0.0637	Time corresponding to $U_s$ , $t_s =$	36.86 min	
9	4.0	0.0762	2.0	0.0761	Dial reading corresponding to $U_s$ , $d_s =$	0.1185 cm	
10	8.0	0.0912	2.8	0.0926	Dial reading at beginning of primary consolidation $d_0 =$	0.0336 cm	
11	15.0	0.1067	3.9	0.1077	Dial reading at 100% of primary consolidation $d_{100} =$	0.1193 cm	
12	30.0	0.1173	5.5	0.1174	Average drainage distance $d_m =$	0.9143 cm	
13	60.0	0.1217	7.7	0.1193	Coefficient of consolidation $C_v =$	0.0404 $\text{cm}^2/\text{min}$	
14	120.0	0.1232	11.0	0.1193	Initial compression ratio $r_i =$	27.0%	
15	240.0	0.1245	15.5	0.1193	Primary compression ratio $r_o =$	68.9%	
16	480.0	0.1245	21.9	0.1193	Secondary compression ratio $r_s =$	4.1%	
17	1440.0	0.1245	37.9	0.1193			
18	initial slope = 0.021  modified slope = 0.014  intersection point	0.00		0.0336			
19		10.00		0.2463			
20		0.00		0.0336			
21		10.00		0.1734			
22	intersection point	0.00		0.1185			
23		6.07		0.1185			

Figure 34 Data set for square-root-time method ( $U_s = 90\%$ ).

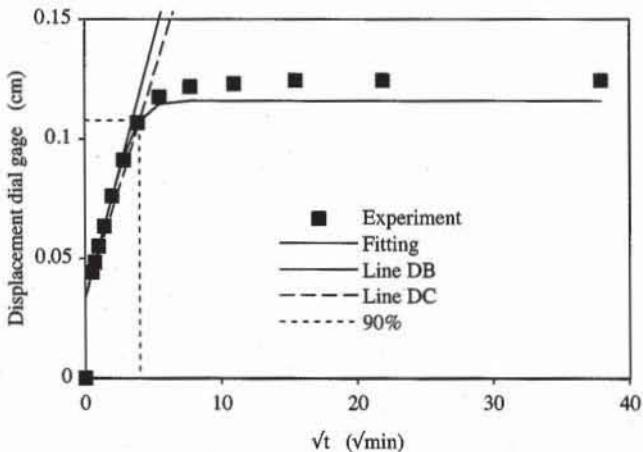


**Figure 35** Experimental and fitted data points for the square-root-time method ( $U_s = 90\%$ ).

	E	F	G
3			
4	Initial height $h_0 =$	1.905 cm	
5	Starting time for fitting, $t_b =$	0.3 min	
6	Ending time for fitting, $t_e =$	4.0 min	
7	Degree of consolidation of method $U_s =$	99%	
8	Time corresponding to $U_s$ , $t_s =$	36.86 min	
9	Dial reading corresponding to $U_s$ , $d_s =$	0.1185 cm	
10	Dial reading at beginning of primary consolidation $d_0 =$	0.0336 cm	
11	Dial reading at 100% of primary consolidation $d_{100} =$	0.1193 cm	
12	Average drainage distance $d_m =$	0.9143 cm	
13	Coefficient of consolidation $C_v =$	0.0404 $\text{cm}^2/\text{min}$	
14	Initial compression ratio $r_i =$	27.0%	
15	Primary compression ratio $r_p =$	68.9%	
16	Secondary compression ratio $r_s =$	4.1%	

**Figure 36** Data set for determination of consolidation coefficient and compression ratios with the generalized square-root-time method ( $U_s = 99\%$ ).

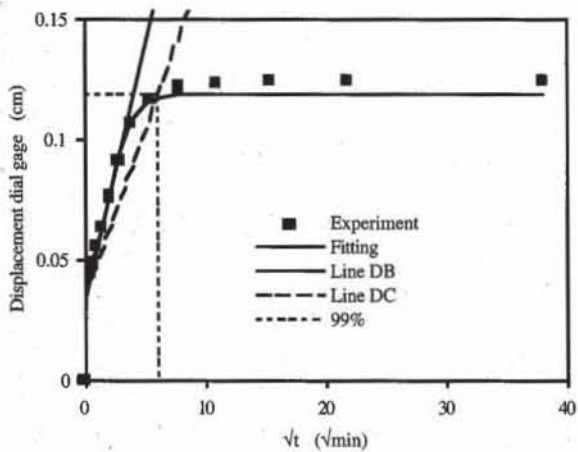


**Figure 37** Experimental and fitted data points for the generalized square-root-time method ( $U_s = 99\%$ ).

	C	D	
2	$\sqrt{t}$ ( $\sqrt{\text{min}}$ )	Fitted displacement (cm)	
3			
4	=SQRT(t)	=d0+(d_100-d0)*U(Cv*t/dm^2)	
5	=SQRT(t)	=d0+(d_100-d0)*U(Cv*t/dm^2)	

	E	F	G
8	Time corresponding to $U_s$ , $t_s = \text{Conso}(t,d,h0,tb,te,Us)$	min	
9	Dial reading corresponding to $U_s$ , $d_s = \text{Conso}(t,d,h0,tb,te,Us)$	cm	
10	Dial reading at beginning of primary consolidation $d_0 = \text{Conso}(t,d,h0,tb,te,Us)$	cm	
11	Dial reading at 100% of primary consolidation $d_{100} = \text{Conso}(t,d,h0,tb,te,Us)$	cm	
12	Average drainage distance $d_m = \text{Conso}(t,d,h0,tb,te,Us)$	cm	
13	Coefficient of consolidation $C_v = \text{Conso}(t,d,h0,tb,te,Us)$	$\text{cm}^2/\text{min}$	
14	Initial compression ratio $r_i = \text{Conso}(t,d,h0,tb,te,Us)$		
15	Primary compression ratio $r_p = \text{Conso}(t,d,h0,tb,te,Us)$		
16	Secondary compression ratio $r_s = \text{Conso}(t,d,h0,tb,te,Us)$		

Figure 38 Formulas used in Figs. 34 and 36.

Once the optimal values of  $d_0$ ,  $d_{100}$ , and  $C'_v$  are found,  $d_m$  is given by Eq. 59, and  $C_v = C'_v d_m^2$ . Equation 73 applies when the dial readings increase with time, and for a decreasing series becomes

$$d_0 \leq d_1, \quad d_{100} \geq d_n, \quad d_{100} \leq d_0, \quad \text{and} \quad C'_v \geq 0 \quad (75)$$

Figures 39 and 40 show the same data set as that used for the square-root-time and log-time methods, and Fig. 41 lists the formulas used in Fig. 39. In Excel, the nonlinear optimization with constraints is performed by using SOLVER (see Chapter 8-1). Note that the first point is omitted in calculating  $E$  in order to remove the initial compression. At the beginning of the calculations,  $C'_v$ ,  $d_0$ , and  $d_{100}$  were set equal to 0.01,  $d_1$ , and  $d_n$ . As shown in Fig. 39, SOLVER generally produces results that are more accurate than the log-time and square-root-time methods. In most cases the optimization converges without a problem when the variables  $C'_v$ ,  $d_0$ , and  $d_{100}$  are properly constrained and initialized.

### Comparison of Methods

As shown in Table 4, all methods for determining  $C_v$  work well and give similar results. Compared to the log-time method, the square-root-time method can detect the beginning and end of primary compression during the consolidation test. It can also be used to start the next loading step automatically as soon as the primary consolidation is almost completed.

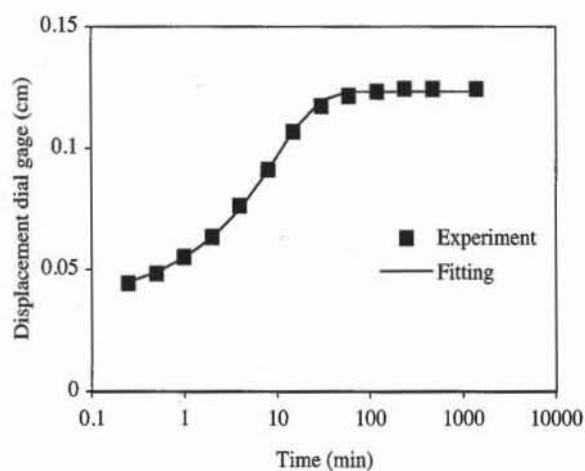


Figure 39 Experimental data points and fitting for nonlinear optimization with constraints.

	A	B	C	D	E	F
1	Solver method (only primary consolidation)					
2	Time (min)	Displacement dial gage (cm)	Fitted displacement d <sup>P</sup> (cm)			
3	t	d	d <sup>P</sup>	Dial reading at beginning of primary consolidation d <sub>0</sub> = 0.0350 cm		
4	0.0	0.0000	0.0350	Dial reading at 100% of primary consolidation d <sub>100</sub> = 0.1234 cm		
5	0.3	0.0445	0.0449	Coefficient C <sub>v</sub> /d <sup>2</sup> <sub>m</sub> = 0.0400 1/min		
6	0.5	0.0483	0.0491	Error E = 0.0012 cm <sup>2</sup>		
7	1.0	0.0551	0.0549	Initial height h <sub>0</sub> = 1.905 cm		
8	2.0	0.0635	0.0632	Coefficient of consolidation C <sub>v</sub> = 0.0333 cm <sup>2</sup> /min		
9	4.0	0.0762	0.0748	Average drainage distance d <sub>m</sub> = 0.9129 cm		
10	8.0	0.0912	0.0908	Initial compression ratio r <sub>i</sub> = 28.1%		
11	15.0	0.1067	0.1070	Primary compression ratio r <sub>p</sub> = 71.0%		
12	30.0	0.1173	0.1196	Secondary compression ratio r <sub>s</sub> = 0.9%		
13	60.0	0.1217	0.1232			
14	120.0	0.1232	0.1234			
15	240.0	0.1245	0.1234			
16	480.0	0.1245	0.1234			
17	1440.0	0.1245	0.1234			

Figure 40 Data set and results of nonlinear optimization with constraints.

TABLE 4

Comparison of results obtained by log-time, square-root-time ( $U_s=90\%$  and  $99\%$ ), and SOLVER methods

	Method			
	Log	$U_s=90\%$	$U_s=99\%$	SOLVER
Dial reading at beginning of primary consolidation (cm) d <sub>0</sub>	0.0340	0.0336	0.0336	0.0350
Dial reading at 100% of primary consolidation (cm) d <sub>100</sub>	0.1212	0.1159	0.1193	0.1234
Coefficient of consolidation (cm <sup>2</sup> /min) C <sub>v</sub>	0.038	0.044	0.040	0.033
Initial compression ratio r <sub>i</sub> (%)	27.3	27.0	27.0	28.1
Primary compression ratio r <sub>p</sub> (%)	70.1	66.1	68.9	71.0
Secondary compression ratio r <sub>s</sub> (%)	2.6	6.9	4.1	0.9

		C
2	Fitted displacement (cm)	
3	$d^p$	
4	$=d0+(d_{100}-d0)*U(Cv*t/dm^2)$	
5	$=d0+(d_{100}-d0)*U(Cv*t/dm^2)$	
D	E	F
6	Error $E = \text{SUMPRODUCT}(d-dp,d-dp)$	$\text{cm}^2$
7	Initial height $h_0 = 1.905$	$\text{cm}$
8	Coefficient of consolidation $C_v = E5*dm^2$	$\text{cm}^2/\text{min}$
9	Average drainage distance $d_m = (h_0+B4-(d_0+d_{100})/2)/2$	$\text{cm}$
10	Initial compression ratio $r_i = (B4-d0)/(B4-B17)$	
11	Primary compression ratio $r_p = -(d_0-d_{100})/(B4-B17)$	
12	Secondary compression ratio $r_s = 1-r_i-r_p$	

Figure 41 Formulas used in Fig. 40.

### Determination of Coefficient of Secondary Compression

Figures 42 and 43 show an example of consolidation test results obtained on a silt. Figure 44 lists the formulas used in Fig. 43. SOLVER is first used to define the primary compression parameters  $C_v$ ,  $d_0$ , and  $d_{100}$ . The first and last five data points are excluded from the SOLVER optimization, because they are attributed to the initial and secondary compressions. Using Eq. 54, the dial reading during the secondary compression is written as

$$d = d_s + h_s C_{ae} \log_{10} \frac{t}{t_s} = A \log_{10}(t) + B \quad (76)$$

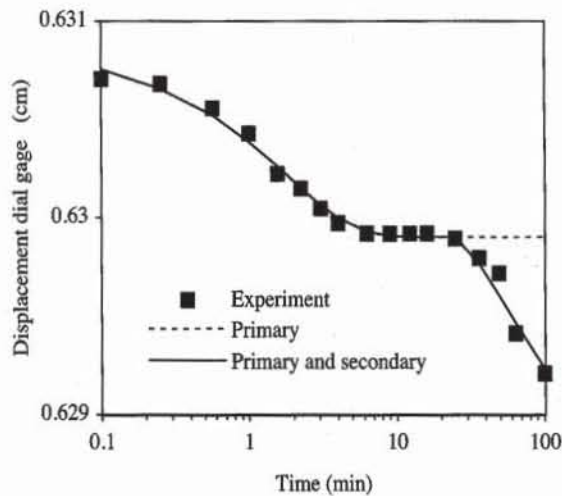


Figure 42 Experimental data and fittings for primary compression alone, and primary with secondary compressions.

	A	B	C	D	E	F	G
1	Solver method (primary and secondary consolidations)						
2	Measured		Fitted				
3	Time (min)	Displacement dial gage (cm)	Fitted displacement $d^p$ (cm)	Primary and secondary (cm)			
4	t	d	$d^p$				
5	0.00	0.6312	0.6309	0.6309	<b>Primary compression</b>		
6	0.10	0.6307	0.6308	0.6308	Dial reading at beginning of primary consolidation $d_0$ =	0.6309 cm	
7	0.25	0.6307	0.6307	0.6307	Dial reading at 100% of primary consolidation $d_{100}$ =	0.6299 cm	
8	0.57	0.6306	0.6305	0.6305	Coefficient $C_v = C_s/d_m^2$ =	0.2164 1/min	
9	1.00	0.6304	0.6304	0.6304	Error E =	0.8579	
10	1.57	0.6302	0.6303	0.6303	Initial compression ratio $r_i$ =	14.5%	
11	2.25	0.6301	0.6302	0.6302	Primary compression ratio $r_p$ =	51.0%	
12	3.07	0.6300	0.6301	0.6301	Secondary compression ratio $r_s$ =	34.5%	
13	4.00	0.6300	0.6300	0.6300	Initial height $h_0$ =	1.899 cm	
14	6.25	0.6299	0.6299	0.6299	Dial reading at sample height $h_0$ , $d_i$ =	0.635 cm	
15	9.00	0.6299	0.6299	0.6299	Average drainage distance $d_m$ =	0.9518 cm	
16	12.25	0.6299	0.6299	0.6299	Coefficient of consolidation $C_v$ =	0.1961 $\text{cm}^2/\text{min}$	
17	16.00	0.6299	0.6299	0.6299	<b>Secondary compression</b>		
18	25.00	0.6299	0.6299	0.6299	Slope s =	-0.0012	
19	36.00	0.6298	0.6299	0.6298	Intercept i =	0.6316	
20	49.00	0.6297	0.6299	0.6296	Sample height at beginning of secondary compression $h_s$ =	1.9041 cm	
21	64.00	0.6294	0.6299	0.6295	Starting time for secondary compression $t_s$ =	27.73 min	
22	100.00	0.6292	0.6299	0.6292	Modified secondary compression index $C_{os}$ =	0.063%	

Figure 43 Example of consolidation data set for determination of  $C_{os}$ .

	E	F	G
8		Error E = =SUMPRODUCT(d-dp,d-dp)*1000000	
9		- Initial compression ration r <sub>i</sub> = =(B5-d0)/(B5-B22)	
10		- Primary compression ratio r <sub>p</sub> = =(d0-d_100)/(B5-B22)	
11		- Secondary compression ratio r <sub>s</sub> = =1-r <sub>i</sub> -r <sub>p</sub>	
12		- Initial height h <sub>0</sub> = 1.899	cm
13		- Dial reading at sample height h <sub>0</sub> , d <sub>i</sub> = 0.635	cm
14		- Average drainage distance d <sub>m</sub> = =(h <sub>0</sub> +d <sub>i</sub> -(d <sub>0</sub> +d <sub>100</sub> )/2)/2	cm
15		- Coefficient of consolidation C <sub>v</sub> = =Cvp*d <sub>m</sub> <sup>2</sup>	cm <sup>2</sup> /min
16		<b>Secondary compression</b>	
17		Slope s = =SLOPE(B18:B22,LOG(A18:A22))	
18		Intercept i = =INTERCEPT(B18:B22,LOG(A18:A22))	
19		Sample height at beginning of secondary compression h <sub>s</sub> = =h0+di-d_100	cm
20		Starting time for secondary compression t <sub>s</sub> = =10 <sup>(d_100-i)</sup>	min
21		Modified secondary compression index C <sub>αε</sub> = =ABS(s/ha)	

	C	D
3	Fitted displacement (cm)	Primary and secondary (cm)
4	d <sup>p</sup>	
5	=d0+(d_100-d0)*U(Cv*t/dm^2) =IF(t>ta,dp-ha*Cae*LOG(t/ta),dp)	
6	=d0+(d_100-d0)*U(Cv*t/dm^2) =IF(t>ta,dp-ha*Cae*LOG(t/ta),dp)	

Figure 44. Formulas used in Fig. 43.

where  $d_s$  is the dial reading at time  $t_s$  when the secondary compression starts, and the coefficients  $A$  and  $B$  are

$$A = h_s C_{\alpha\varepsilon} \quad \text{and} \quad B = d_s - A \log_{10}(t_s) \quad (77)$$

In the formulas of Fig. 44, the secondary compression is assumed negligible when  $t < t_s$ . The slope  $A$  and intercept  $B$  were calculated by linear regression. The dial reading at the beginning of secondary compression was set equal to  $d_{100}$  and the time  $t_s$  was calculated as follows:

$$t_s = 10 \frac{d_s - B}{A} \quad (78)$$

As shown in Fig. 42, there is a good agreement between the experimental and fitted data points.

## REFERENCES

- See Introduction for references to ASTM procedures (pages 4 to 6).
- ARMOUR, D. W., Jr., and V. P. DRNEVITCH, 1986, Improved techniques for the constant-rate-of-strain consolidation for soils: Testing and evaluation, *ASTM Special Technical Publication No. 892*, Yong R. N. and F. C. Townsend, eds., American Society for Testing and Materials, Philadelphia, pp. 170–183.
- BISHOP, A. W., and D. J. HENKEL, 1962, *The Measurement of Soil Properties in the Triaxial Test*, 2nd ed., Edward Arnold, London, 228 p.
- CASAGRANDE, A., 1936, The determination of pre-consolidation load and its prac-

- tical significance, *Discussion D-34, Proceedings of the First International Conference on Soil Mechanics and Foundation Engineering*, Cambridge, Vol. III, pp. 60-64.
- DJOENAIDI, W. J., 1985, A Compendium of soil properties and correlations, *Master of Engineering Science Thesis*, School of Civil and Mineral Engineering, University of Sydney, Sydney, Australia.
- HEAD, K. H., 1986, *Manual of Soil Laboratory Testing, Vol. 3 Effective Stress Tests*, John Wiley & Sons, New York, pp. 1197-1225.
- HOLTZ, R. D., and B. B. BROMS, 1972, Long-term loading tests at Skå-Edeby, Sweden: relation of undisturbed sampling to laboratory testing, *Proceedings of the ASCE Specialty Conference on Performance of Earth and Earth-Supported Structures*, Purdue University, West Lafayette, IN, Vol. 1, Part 1, pp. 435-464.
- HOLTZ, R. D., and W. D. KOVACS, 1981, *An Introduction to Geotechnical Engineering*, Prentice Hall, Englewood Cliffs, NJ, pp. 283-423.
- KAUFMAN, R. I., and W. C. SHERMAN, Jr., 1964, Engineering measurements for Port Allen Lock, *J. Soil Mech. Found. Eng. Div.*, ASCE, Vol. 90, No. SM5, pp. 221-247.
- KULHAWY, F. H., and P. W. MAYNE, 1990, *Manual on Estimating Soil Properties for Foundations Design*, Report EL-9800 to Electric Power Research Institute, Cornell University, Ithaca, New York.
- LADD, C. C., and U. LUSCHER, 1965, Engineering properties of the soils underlying the M.I.T campus, *Research Report R65-68, Soil Publication 185*, Department of Civil Engineering, Massachusetts Institute of Technology, Cambridge, MA.
- LAMBE, T. W., and R. V. WHITMAN, 1979, *Soil Mechanics, SI Version*, John Wiley & Sons, New York, 553 p.
- LEE, I. K., W. WHITE, and O. G. INGLES, 1983, *Geotechnical Engineering*, Pitman Publishing, Marsfield, MA, 508 p.
- LEONARDS, G. A., and P. GIRAUT, 1961, A study of the one-dimensional consolidation test, *Proceedings of the Ninth International Conference on Soil Mechanics and Foundation Engineering*, Paris, Vol. 1, pp. 116-130.
- LEROUEIL, S., F. TAVENAS, and J. P. LEBIHAN, 1983, Propriétés caractéristiques des argiles de l'est du Canada, *Can. Geotech. J.*, Vol. 20, No. 4, pp. 681-705.
- LOWE, J. III., P. F. ZACHEO, and H. S. FELDMAN, 1964, Consolidation testing with back pressure, *J. Soil Mech. Found. Eng. Div.*, ASCE, Vol. 90, No. SM5, pp. 69-86.
- LOWE, J. III., E. JONA, and V. OBRICIAN, 1969, Controlled gradient consolidation test, *J. Soil Mech. Found. Eng. Div.*, ASCE, Vol. 95, No. SM1, pp. 77-98.
- MACDONALD, A. B., and E. K. SAUER, 1970, The engineering significance of Pleistocene stratigraphy in the Saskatoon area, Saskatchewan, Canada, *Can. Geotech. J.*, Vol. 7, No. 2., pp. 116-126.
- MESRI, G., and P. M. GODLEWSKI, 1977, Time- and stress-compressibility interrelationship, *J. Geotech. Eng.*, ASCE, Vol. 103, No. 5, pp. 417-430.
- MESRI, G., Coefficients of secondary compression, *J. Soil Mech. Found. Eng. Div.*, ASCE, Vol. 99, No. SM1, pp. 123-137.
- MITCHELL, J. K., 1976, *Fundamentals of Soil Behavior*, John Wiley & Sons, New York, 422 p.
- NAVFAC, 1982, *Soil Mechanics (Design Manual 7.1)*, Naval Facilities Engineering Command, Alexandria, 355 p.
- POULOS, H. G., 1980, A review of the behavior and engineering properties of car-

- bonate soils, *Research Report R381*, School of Civil Engineering, University of Sydney, Sydney, Australia, 46 p.
- RUTLEDGE, P. C., 1944, Relation of undisturbed sampling to laboratory testing, *Trans., ASCE*, Vol. 109, pp. 1162–1163.
- SKEMPTON, A. W., 1944, Notes on the compressibility of clays, *Q. J. Geol. Soc. London*, Vol. C, pp. 119–135.
- SKEMPTON, A. W., and D. J. HENKEL, 1953, The post-glacial clays of the Thames Estuary at Tilbury and Shellhaven, *Proceedings of the Third International Conference on Soil Mechanics and Foundation Engineering*, Zurich, Vol. 1, pp. 302–308.
- SKEMPTON, A. W., and D. J. HENKEL, 1957, Test on London clay from deep boring at Paddington, Victoria and the South Bank, *Proceedings of the Fourth International Conference on Soil Mechanics and Foundation Engineering*, London, Vol. 1, pp. 100–106.
- SMITH, R. E. and H. E. WAHL, 1969, Consolidation under constant rate of strain, *J. Soil Mech. Found. Eng. Div., ASCE*, Vol. 95, No. SM2, pp. 519–538.
- TERZAGHI, K., and R. B. PECK, 1967, *Soil Mechanics in Engineering Practice*, 2nd Ed., John Wiley & Sons, New York, 729 pp.
- WALLACE, G. B., and W. C. OTTO, 1964, Differential settlement at Selfridge Air Force base, *J. Soil Mech. Found. Eng. Div., ASCE*, Vol. 90, No. 5, pp. 197–220.
- WINTERKORN, H. F., and H. Y. FANG, 1975, Soil technology and engineering properties of soils, Chap. 2 of *Foundation Engineering Handbook*, H. F. Winterkorn and H. Y. Fang, eds., Van Nostrand Reinhold, New York, pp. 67–120.
- WISSA, A. E. Z., J. T. CHRISTIAN, E. H. DAVIS, and S. HEIBERG, 1971, Consolidation at constant rate of strain, *J. Soil Mech. Found. Eng. Div., ASCE*, Vol. 97, No. SM10, pp. 1393–1421.
- WROTH, C. P., and D. M. WOOD, 1978, The correlation of index properties with some basic engineering properties of soils, *Can. Geotech. J.*, Vol. 15, No. 2, pp. 137–145.

## REVIEW QUESTIONS

1. Which soil properties are measured during a consolidation test?
2. To what kinds of soils is the consolidation test applicable?
3. Which strain and stress components vary during a consolidation test?
4. What is the relation between volumetric strain and void ratio? Derive this relation.
5. Which is the most common system of coordinates to report the compressibility of soils?
6. Define *coefficient of compressibility* ( $m_v$ ).
7. Why does  $m_v$  depend on the size and direction of the load increment?
8. How does  $m_v$  relate to the calculation of settlement?
9. What are the preconsolidation pressure and overconsolidation ratio?
10. Define *virgin consolidation line*.
11. What is a swelling line?
12. Define *compression index* ( $C_c$ ) and *swelling index* ( $C_s$ ).
13. What are two ways to define the preconsolidation pressure?
14. What are normally and overconsolidated clays?
15. Are there approximate relations to calculate the compression index in terms of the liquid limit?
16. What are the minimum and maximum values for  $C_c$  and swelling index  $C_s$  in soils?

17. Write the consolidation equation. Which variables does it relate? Which material parameters control the porewater pressure diffusion?
18. What is the dimensionless time factor  $T_v$ ?
19. What is the average degree of consolidation  $U$ ?
20. Which basic relation relates  $T_v$  and  $U$  when  $U < 0.6$ ?
21. How many phases are distinguished during the consolidation tests? Which parameters characterize the relative importance of these phases?
22. What are primary and secondary compressions? What is their primary difference?
23. Define the initial, primary, and secondary compression ratios in terms of dial reading. What is the meaning of these ratios?
24. What methods are commonly used to determine the consolidation coefficient  $C_v$ ?
25. Briefly explain the log-time method.
26. Briefly explain the square-root-time method.
27. On which mathematical principle is the SOLVER method based?
28. How do you detect the secondary compression during the consolidation test?
29. What are log-time and square-root-time methods? What are the corrections introduced in these methods? Why do we need to introduce these corrections?
30. What are typical values for the coefficient of consolidation? In what units is it generally expressed?
31. Is there a relation between  $C_a$  and  $C_c$ ?
32. What is the relation between coefficients of consolidation and permeability? Does the coefficient of consolidation increase or decrease with permeability?

## EXERCISES

1. For the data of Table E1, plot the  $e-\sigma'$  curve and determine the preconsolidation pressure and compression and swelling indices. Plot the variation of compressibility  $m$ , versus effective stress.
2. Same as Exercise 1 but for the data of Table E2.

TABLE E1

Effective stress (kPa)	Vertical strain (%)	Void ratio
1	1.1	2.56
3	2.2	2.52
4	4.4	2.44
10	14.3	2.08
21	23.7	1.75
41	31.3	1.47
82	38.2	1.22
22	37.0	1.27
6	34.2	1.37

Initial void ratio, 2.6.

TABLE E2

Soil type	Liquid limit (%)	Effective stress (kPa)	Void ratio $\epsilon$
CH-clay with silt	71	1.5	1.167
		27.5	1.157
		56.0	1.153
		202.2	1.121
		344.5	1.100
		210.3	1.103
		337.7	1.095
		888.3	0.879
		1605.9	0.722
		2.0	1.062

3. Same as Exercise 1 but for the data of Table E3.
4. Same as Exercise 1 but for the data of Table E4.
5. Same as Exercise 1 but for the data of Table E5.
6. Same as Exercise 1 but for the data of Table E6.
7. Same as Exercise 1 but for the data of Table E7.

TABLE E3

Soil type	Liquid limit (%)	Effective stress (kPa)	Void ratio $e$
CH-clay, soft	41	1.5 28.7 53.9 101.3 214.5 312.1 218.8 107.5 210.3 312.1 445.2 1772.4 445.2 1.5	1.350 1.335 1.326 1.301 1.260 1.236 1.242 1.259 1.248 1.231 1.184 0.746 0.821 1.189

TABLE E5

Soil type	Liquid limit (%)	Effective stress (kPa)	Void ratio $e$
CL-clay, soft	81	1.5 25.5 190.5 56.0 10.9 24.0 99.3 277.2 454.1 871.0 1637.9 445.2 105.4 1.5	0.920 0.905 0.835 0.839 0.858 0.858 0.842 0.820 0.779 0.674 0.604 0.611 0.638 0.805

TABLE E6

Soil type	Liquid limit (%)	Effective stress (kPa)	Void ratio $e$
ML-sandy silt	31	1.5 1.9 9.5 24.5 53.9 99.3 202.2 256.2 107.5 65.6 190.5 271.8 436.5 1605.9 436.5 91.8 1.3	0.841 0.835 0.821 0.810 0.794 0.780 0.760 0.750 0.752 0.754 0.752 0.745 0.723 0.623 0.637 0.645 0.718

TABLE E4

Soil type	Liquid limit (%)	Effective stress (kPa)	Void ratio $e$
CL-clay, firm	50	1.5 26.0 186.8 107.5 53.9 27.0 16.2 53.9 256.2 463.1 1574.5 436.5 101.3 1.5	1.005 0.991 0.947 0.953 0.960 0.963 0.968 0.966 0.937 0.882 0.643 0.658 0.694 0.815

TABLE E7

Soil type	Effective stress (kPa)	Void ratio $e$
H28-1-1 CP2	2.0 13.7 25.4 49.9 114.9 140.2 164.3 204.4 393.6 385.9 204.4 47.0 25.4 2.0 13.2 45.2 102.0 200.4 378.3 820.7 335.8 100.0 42.6 23.5 11.9 2.0	13.926 13.946 13.864 13.659 12.982 11.547 10.337 8.942 6.399 6.296 6.460 6.850 7.055 7.609 7.527 7.301 7.096 6.789 6.235 4.656 4.840 5.230 5.373 5.537 5.620 5.763

**TABLE E8**

Soil type	Effective stress (kPa)	Void ratio $e$
H28-1-2 CP1	2.0	11.772
	15.5	11.731
	28.6	11.690
	57.3	11.547
	129.5	10.439
	230.3	7.117
	443.4	5.250
	221.3	5.291
	129.5	5.373
	12.2	6.009
	1.8	6.460

**TABLE E9**

Soil type	Effective stress (kPa)	Void ratio $e$
H28-1-2 CP1	1.8	6.686
	26.4	6.460
	50.9	6.276
	119.6	5.948
	221.3	5.537
	452.3	5.004
	981.3	3.733
	1816.1	2.564
	3567.5	1.846
	5100.3	1.641
	1375.3	1.661
	672.9	1.702
	292.2	1.805
	96.1	1.928
	13.2	2.010
	2.0	2.010

8. Same as Exercise 1 but for the data of Table E8.
9. Same as Exercise 1 but for the data of Table E9.
10. By using the equations of linear isotropic elasticity, derive the elastic relation between void ratio and effective stress for the one-dimensional loading of the consolidation test. What is the relation between the compressibility coefficient, Young's modulus, and the Poisson ratio?
11. Plot the following  $e-\sigma'$  curves and determine the preconsolidation pressures and compression and swelling indices. CP3 is a remolded sample from CP1. What is the effect of remolding on the consolidation properties?

Soil type	Effective stress (kPa)	Void ratio $e$
CP1	1.8	0.954
	15.3	0.916
	29.5	0.898
	69.6	0.867
	129.8	0.812
	272.1	0.748
	580.3	0.663
	1099.8	0.590
	1137.4	0.583
	590.1	0.596
	281.5	0.605
	136.5	0.620
	31.1	0.653
	1.8	0.743

Soil type	Effective stress (kPa)	Void ratio $e$
CP3	1.8	0.639
	7.9	0.634
	16.1	0.629
	30.5	0.620
	74.5	0.607
	151.0	0.573
	322.0	0.513
	652.8	0.459
	1258.2	0.394
	2728.4	0.340
	1196.3	0.346
	316.6	0.365
	78.4	0.382
	33.8	0.396
	17.2	0.408
	1.7	0.447

12. Plot the following  $e-\sigma'$  curve and determine the preconsolidation pressures and compression and swelling indices. By using the Casagrande method, determine the preconsolidation pressure in the reloading section of the  $e-\sigma'$  curve and compare it to the stress where unloading took place.
13. Plot the compression index versus liquid limit for the data in Table 1, and

Effective stress (kPa)	Void ratio $e$
58.3	0.368
105.0	0.365
203.5	0.359
424.3	0.347
792.4	0.335
1714.1	0.310
3201.3	0.284
1682.9	0.283
837.3	0.285
373.1	0.289
792.4	0.289
1622.2	0.287
3260.6	0.274
5762.9	0.250
12933.1	0.223
5762.9	0.228
3445.4	0.233
1652.3	0.238
25.5	0.256

compare the data points to the approximate relations between compression index and liquid limit.

14. For the data of Table E10, calculate the consolidation coefficient  $C_v$  and secondary compression coefficient  $C_{\alpha z}$ . The initial height is 1.899 cm and corresponds to the dial reading equal to 0.6350. Use the both square-root-time and log-time methods.
15. Same as Exercise 14 but for the data set of Table E11.
16. For the data of Table E12, calculate the consolidation coefficient  $C_v$  and secondary compression coefficient  $C_{\alpha z}$ . The initial height is 1.899 cm and corresponds to a dial reading of 0.6350. Use the generalized square-root-time method with  $U_s = 90\%$  and  $99\%$ .
17. Same as Exercise 16 but for the data set of Table E13.

TABLE E10

Elapsed time (min)	Displacement dial gage (cm)
0.00	0.6350
0.10	0.6342
0.25	0.6340
0.57	0.6337
1.00	0.6335
1.57	0.6333
2.25	0.6332
3.07	0.6330
4.00	0.6328
6.25	0.6327
9.00	0.6325
12.25	0.6324
16.00	0.6323
25.00	0.6322
36.00	0.6320
49.00	0.6318
64.00	0.6315
100.00	0.6312

TABLE E11

Elapsed time (min)	Displacement dial gage (cm)
0.00	0.5288
0.25	0.5161
0.57	0.5118
1.00	0.5077
1.57	0.5033
2.25	0.4994
3.07	0.4959
4.00	0.4931
6.25	0.4883
9.00	0.4851
12.25	0.4826
16.00	0.4806
25.00	0.4778
36.00	0.4757
49.00	0.4737
64.00	0.4722
100.00	0.4700

TABLE E12

Elapsed time (min)	Displacement dial gage (cm)
0.00	0.6312
0.10	0.6307
0.25	0.6307
0.57	0.6306
1.00	0.6304
1.57	0.6302
2.25	0.6301
3.07	0.6300
4.00	0.6300
6.25	0.6299
9.00	0.6299
12.25	0.6299
16.00	0.6299
25.00	0.6299
36.00	0.6298
49.00	0.6297
64.00	0.6294
100.00	0.6292

**TABLE E13**

Elapsed time (min)	Displacement dial gage (cm)
0.00	0.6292
0.10	0.6279
0.25	0.6276
0.57	0.6271
1.00	0.6266
1.57	0.6261
2.25	0.6259
3.07	0.6256
4.00	0.6252
6.25	0.6248
9.00	0.6246
12.25	0.6243
16.00	0.6241
25.00	0.6238
36.00	0.6229
49.00	0.6228
64.00	0.6227
100.00	0.6227
900.00	0.6224

**TABLE E14**

Elapsed time (min)	Displacement dial gage (cm)
0	0.6224
0.25	0.6199
0.57	0.6193
1.00	0.6186
1.57	0.6181
2.25	0.6175
3.07	0.6172
4.00	0.6167
6.25	0.6161
9.00	0.6157
12.25	0.6152
16.00	0.6149
25.00	0.6144
36.00	0.6142
49.00	0.6140
64.00	0.6139
100.00	0.6137
200.00	0.6131

**TABLE E15**

Elapsed time (min)	Displacement dial gage (cm)
0.00	0.5983
0.25	0.5921
0.57	0.5916
1.00	0.5906
1.57	0.5895
2.25	0.5880
3.07	0.5872
4.00	0.5867
6.25	0.5860
9.00	0.5853
12.25	0.5850
16.00	0.5847
25.00	0.5843
36.00	0.5838
49.00	0.5835
64.00	0.5834
100.00	0.5829

18. Same as Exercise 16 but for the data set of Table E14.
19. Same as Exercise 16 but for the data set of Table E15.
20. For the data of Table E16, calculate the consolidation coefficient  $C_v$  and secondary compression coefficient  $C_{ae}$  for the following data set. The initial height is 1.899 cm and corresponds to a dial reading of 0.6350. Calculate the compression ratios.
21. Same as Exercise 20 but for the data of Table E17.
22. Same as Exercise 20 but for the data of Table E18.

**TABLE E16**

Elapsed time (min)	Displacement dial gage (cm)
0.00	0.5829
0.25	0.5867
0.57	0.5872
1.00	0.5871
1.57	0.5878
2.25	0.5880
3.07	0.5883
4.00	0.5884
6.25	0.5886
9.00	0.5887
12.25	0.5887
16.00	0.5888
25.00	0.5890
36.00	0.5890
49.00	0.5891
64.00	0.5891
100.00	0.5892
900.00	0.5892

**TABLE E17**

Elapsed time (min)	Displacement dial gage (cm)
0.00	0.5916
0.25	0.5875
0.57	0.5861
1.00	0.5848
1.57	0.5838
2.25	0.5829
3.07	0.5824
4.00	0.5820
6.25	0.5814
9.00	0.5810
12.25	0.5834
16.00	0.5806
25.00	0.5804
36.00	0.5801
49.00	0.5799
64.00	0.5799
100.00	0.5797
110.00	0.5796
940.00	0.5789

**TABLE E18**

Elapsed time (min)	Displacement dial gage (cm)
0.00	0.2986
0.10	0.2796
0.25	0.2764
0.57	0.2690
1.00	0.2619
1.57	0.2553
2.25	0.2494
3.07	0.2440
4.00	0.2398
6.25	0.2337
9.00	0.2298
12.25	0.2272
16.00	0.2254
25.00	0.2228
36.00	0.2210
49.00	0.2190
64.00	0.2178
100.00	0.2161
1000.00	0.2060

## 6-2 Consolidation Test

### OBJECTIVE

The consolidation (oedometer) test is used to determine the compression index  $C_c$ , swelling index  $C_s$ , and preconsolidation pressure  $\sigma'_p$ , which define the soil compressibility; the coefficient of consolidation  $C_v$ , which characterizes the rate of primary compression; and the secondary compression coefficient  $C_a$ , which defines the creep properties. We present only the conventional consolidation test (ASTM 2435).

### EQUIPMENT

The equipment for the consolidation test includes:

- Consolidation loading device (see Figs. 1 and 2)
- Consolidation cell (see Figs. 3 and 4).
- Specimen trimmer and accessories (miter box, wire saw, and knives).
- Device for placing specimen in container.
- Balance sensitive to 0.1 g.
- Drying oven.
- Dial indicator or displacement transducer with a range of 10 mm and an accuracy of 0.002 mm.
- Timer.
- Moisture content cans.

#### Loading Devices

The most commonly used loading devices are the beam-and-weight mechanism and the pneumatic device (Fig. 1). Both devices apply a sudden axial load to the specimen and maintain it constant after that. Figure 2 shows the operating principle.

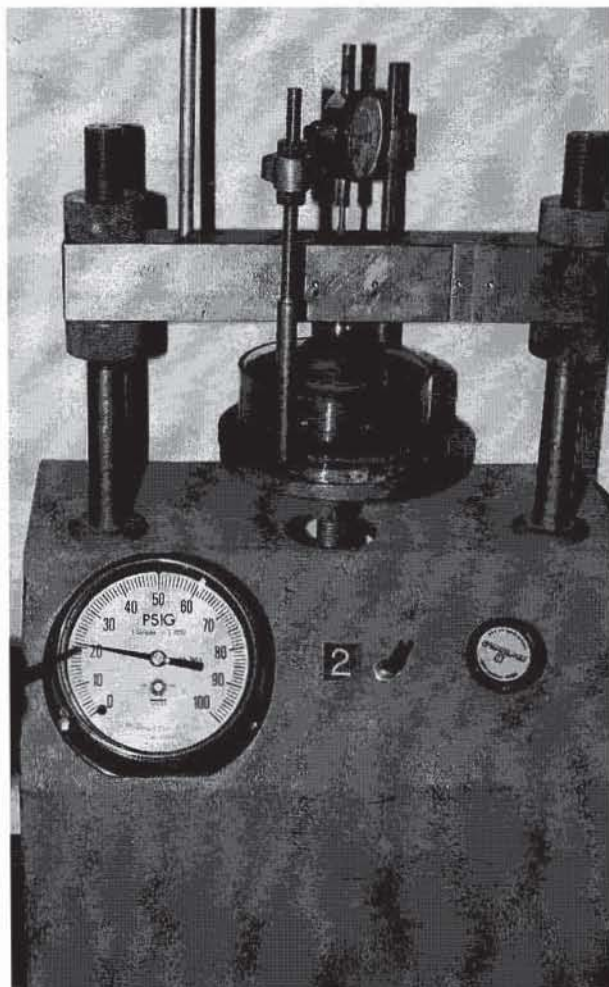
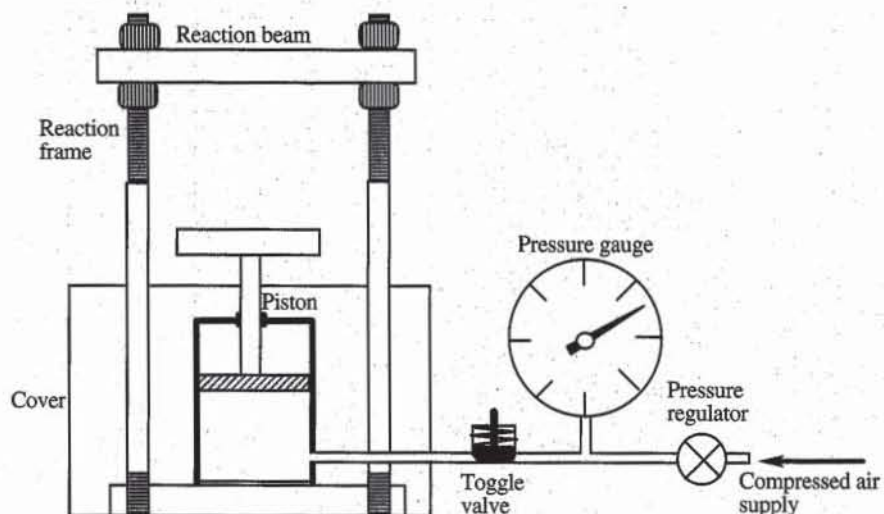


Figure 1 Equipment for the consolidation test.

ple of the pneumatic device of Fig. 1. The pressurized piston squeezes the sample against the reaction beam. The air pressure is adjusted with the pressure regulator and is controlled with the pressure gage. The toggle valve is useful to control the load increments. When the toggle valve is closed, the incoming air pressure is adjusted to the desired value with the air regulator, while the air pressure inside the piston remains constant. Then the toggle valve is released to transmit the new pressure to the sample.

### Consolidation Cells

As shown in Figs. 3 and 4, there are two commonly used types of consolidation cells: fixed-ring and floating-ring cells. In the fixed-ring cell of Fig. 3, the specimen moves downward in relation to the ring, which generates friction drag on the sidewall. As described in Chapter 4-3, the fixed-ring cell may also be used as a falling head permeameter for measuring the soil permeability. In the floating-ring container of Fig. 4, compression occurs toward the middle from both top and bottom. The effect of friction between the container wall and the soil specimen is smaller than that of the fixed-ring container. However, unlike the fixed-ring container, the floating-ring cell cannot be used for permeability tests.



**Figure 2** Pneumatic loading device for the consolidation test.

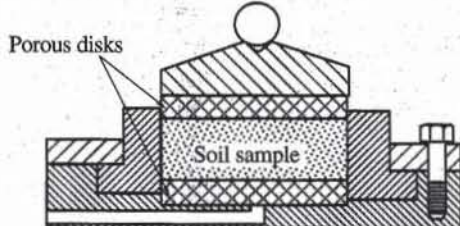


**Figure 3** Fixed-ring consolidation cell.

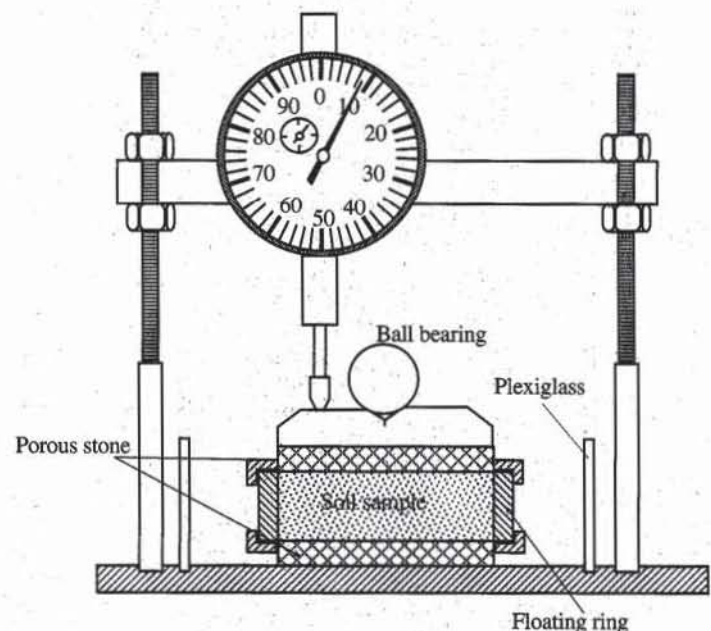


**Figure 4** Floating-ring consolidation cell. The dial indicator can also be replaced by a displacement transducer.

## PREPARATION OF SPECIMENS

Several types of devices may be used to trim and place the test specimen in the consolidation cell. Figures 5 to 8 show an example of sample preparation.

### Measuring Devices

Dial indicators can be replaced by displacement transducers (e.g., LVDT) with similar or even better range and accuracy. Displacement transducers are usually



**Figure 5** A stack of rings of identical diameter is pushed into the soil mass. The lowest ring has a cutting edge. The other cylinders are oedometer floating rings.

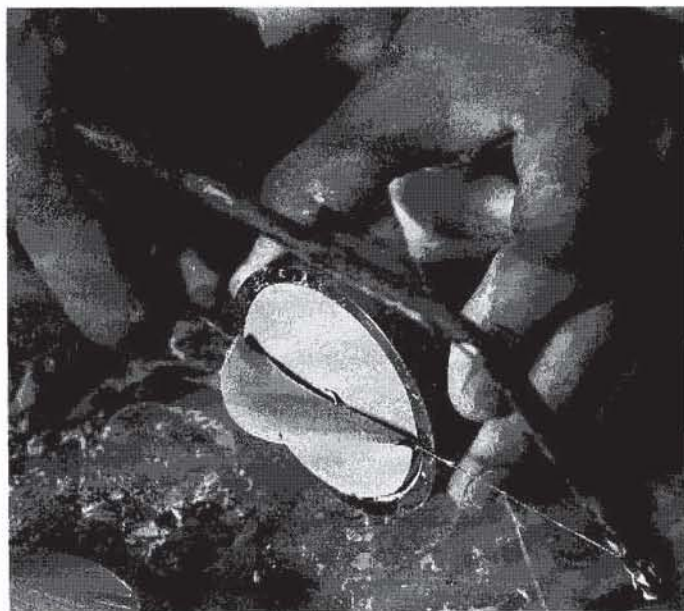


**Figure 6** After removing the stack of rings filled with soil, the wire saw is inserted in the interstices between two rings, and the soil excess is cut off.



**Figure 7** A small coating of vacuum or silicon grease is applied to the upper and lower edges of the ring, and the two external rings are added.



**Figure 8** Filter papers are added to the top and bottom surfaces of the specimen. Then the floating ring is placed on the bottom porous stone and the top porous stone is positioned.

connected to a signal conditioner which supplies and processes electrical signals, and a readout unit which displays the transducer output. They can also be connected to an Analog/Digital (A/D) converter for computer data acquisition. It is very important that displacement transducers be calibrated and positioned in their normal working range. Their output must vary linearly with the displacement that is measured from a dial indicator. When a readout unit or A/D converter is available, it is recommended to scale the displacement transducers output so it can easily be interpreted in terms of length (e.g., 1 output unit = 1 mm).

### SELECTION OF LOADING SEQUENCE

The loading sequence of the consolidation test depends not only on the soils tested but also on the types of engineering applications. As shown in Fig. 9, a typical loading sequence generally has a low initial value, which increases logarithmically to a maximum value and then decreases rapidly toward zero. For the particular sequence of Fig. 9, the applied stresses are 50, 100, 200, 400, 800, 1600, 400, and 50 kPa. In general, the range of applied stress should completely cover the effective stresses that are needed for settlement calculations. This range should encompass the smallest and largest effective stresses in the field, which depend on depth, foundation loads, and excavations.

The duration of each load application depends on the rate of consolidation of the soil. Ideally, the load should only be changed after the degree of consolidation  $U$  reaches 100%. In practice, the load is changed at convenient times provided that  $U$  exceeds 90%. When the soil exhibits a large amount of secondary compression, the load should be sustained even longer to determine the secondary compression coefficient.

### PROCEDURE

1. Measure the weight  $W_{\text{ring}}$  and diameter  $D$  of consolidation ring.
2. Measure the initial height  $h_0$  of the specimen and the weight  $W_{w0}$  of the initial specimen and ring.

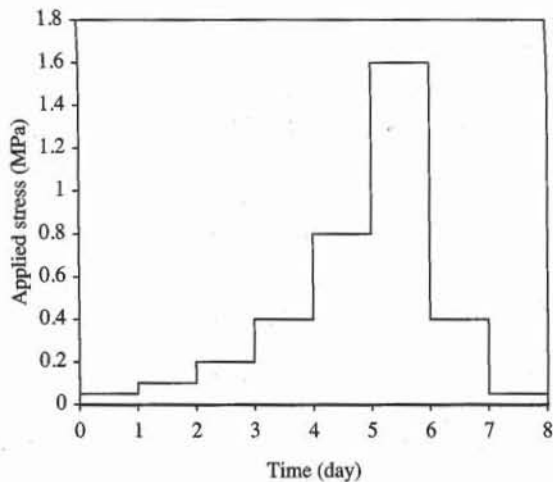
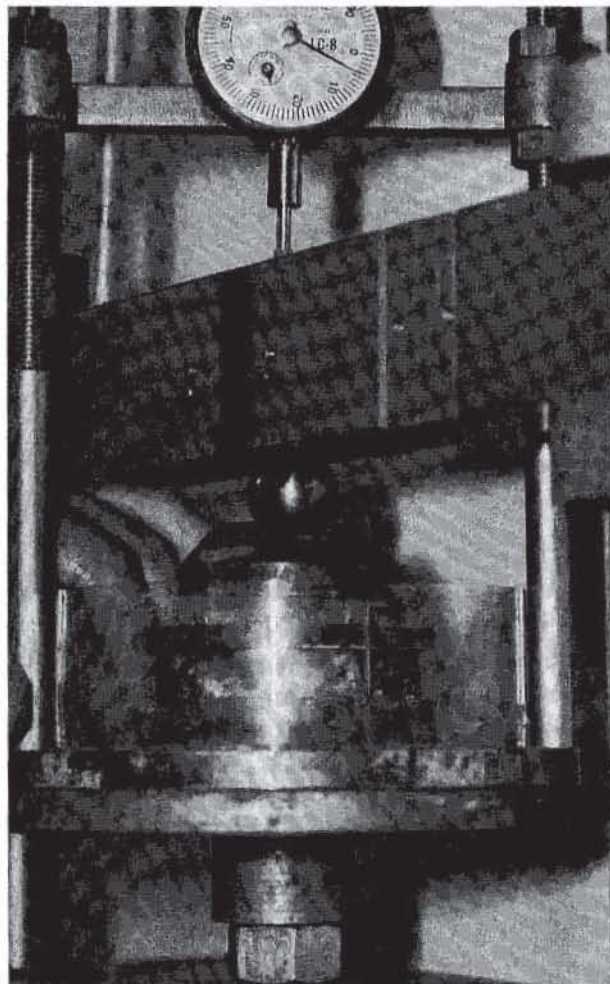
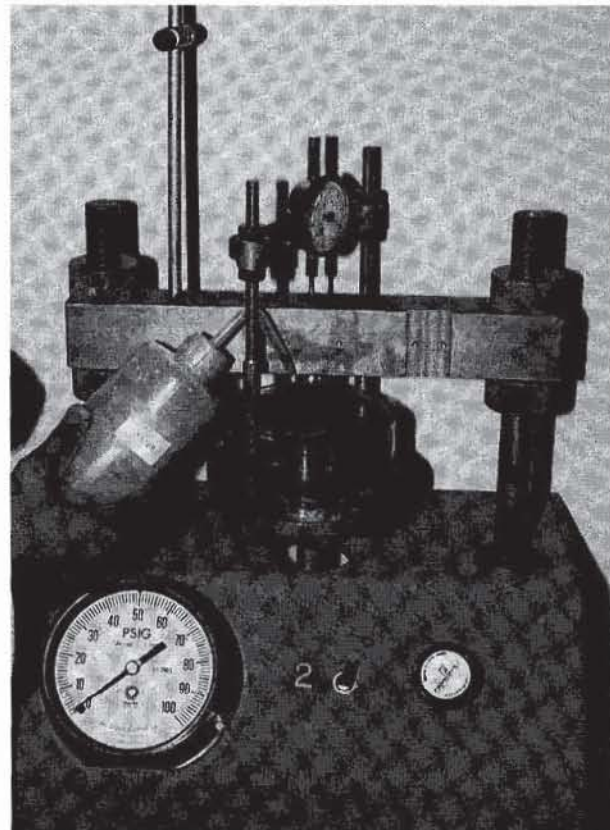


Figure 9 Example of loading sequence for consolidation test.



**Figure 10** The floating-ring cell is mounted on the loading plate. A rigid cap and a steel ball are added on top of the porous stone. The plate of the pneumatic oedometer is raised very slowly by increasing the air pressure and is adjusted so that the ball slightly touches the reaction beam.



**Figure 11** The load on the sample is changed by closing the toggle valve, adjusting the air pressure to the desired value with the pressure regulator, and then releasing the toggle valve.

3. Mount the consolidation cell in the loading unit. Set the vertical displacement dial so that its full range is available during compression (see Fig. 10).
4. Adjust the loading pressure to the first value of the pressure series (see Fig. 11) and measure the vertical displacement at selected time intervals. The vertical displacement gage should be measured at time intervals of 0, 0.1, 0.25, 0.5, 1, 2, 4, 8, 15, 30, 60 min and 2, 4, 8, and 24 h after application of the load increment. In practice, readings can be stopped when the degree of consolidation  $U$  exceeds 90% ( $U = 90\%$  may be detected by using the square-root-time method).
5. After 24 h, or after  $U$  exceeds 90%, the applied load can be changed to its next value, and the vertical displacement is measured as in step 4.
6. Repeat step 5 until all the loading steps are completed.
7. After unloading the specimen completely, record the final dial reading.
8. Quickly dismantle the consolidometer cell and weigh the wet sample.
9. Dry the specimen in the oven and measure its dry weight  $W_d$ .

## COMPUTATIONS

### Soil Characteristics

The initial state of the soil is characterized by its initial water content  $w_0$ , void ratio  $e_0$ , degree of saturation  $S_{r0}$ , and dry unit weight  $\gamma_{d0}$ . The initial dry unit weight  $\gamma_{d0}$  and initial void ratio  $e_0$  are

$$\gamma_{d0} = \frac{W_d - W_{\text{ring}}}{V_0} \quad \text{and} \quad e_0 = \frac{G_s \gamma_w}{\gamma_{d0}} - 1 \quad (1)$$

where  $W_d$  is the weight of the dry sample and ring,  $W_{\text{ring}}$  the weight of the ring,  $V_0 = \pi D^2 h_0 / 4$  the initial sample volume,  $D$  the sample diameter,  $h_0$  the initial sample height,  $G_s$  the soil specific gravity, and  $\gamma_w$  the unit weight of water. The initial water content  $w_0$  is

$$w_0 = \frac{W_{w0} - W_d}{W_d - W_{\text{ring}}} \times 100 \quad (\%) \quad (2)$$

where  $W_{w0}$  is the weight of initial wet sample and ring. The initial degree of saturation  $S_{r0}$  is

$$S_{r0} = \frac{G_s w_0}{e_0} \quad (3)$$

$S_{r0}$  should be close to 100% for fully saturated specimens. If  $S_{r0}$  is much smaller than 100%, the results for the first consolidation loading steps are doubtful.

The water content  $w_f$  and void ratio  $e_f$  after the consolidation test are calculated similarly to the initial quantities by using the sample height  $h$  and weight  $W_{wf}$  of wet sample after the test.  $h_f$  is obtained after completely removing the load, and letting the sample expand freely while keeping it covered with water.

The specific gravity  $G_s$  is calculated by assuming that the sample is completely saturated after the test (i.e.,  $S_{rf} = 100\%$ ):

$$G_s = \frac{\gamma_{df}}{\gamma_w - w_f \gamma_{df}} \quad (4)$$

where  $\gamma_{df} = \gamma_{d0} h_0 / h_f$  is the final dry unit weight.

### Amplitude of Settlement

The sample height  $h$  at time  $t$  is

$$h = h_0 - d_0 + d(t) - h_c(\sigma) \quad (5)$$

where  $h_0$  is the initial height of sample,  $d_0$  the dial reading corresponding to the sample height  $h_0$ ,  $d(t)$  the dial reading at time  $t$ , and  $h_c$  the correction due to loading-frame compliance.  $h_c(\sigma)$ , which accounts for the deformation of the loading frame when the applied load varies, is obtained by loading a very rigid steel block and recording the variation of dial reading  $h_c$  with pressure  $\sigma$ . For rigid loading frames and small pressures,  $h_c$  is negligible compared to  $d(t)$ .

The void ratio  $e$  of the specimen of height  $h$  is

$$e = e_0 - \frac{h_0 - h}{h_0} (1 + e_0) \quad (6)$$

where  $e_0$  is the initial void ratio for  $h = h_0$ .

### Rate of Settlement

The coefficient of primary consolidation  $C_v$  and secondary compression  $C_{\alpha}$  are calculated for a few selected steps by using one of the procedures (e.g., square-root-time or log-time method) described in Chapter 6-1.

### Determination of Permeability

As described in Eq. 27.6-1, the permeability  $k$  is related to  $m_v$  and  $C_v$  through

$$k = C_v m_v \gamma_w \quad (7)$$

Therefore,  $k$  can be determined from the measured values of  $C_v$ , and the compression and swelling indices  $C_c$  and  $C_s$ . However, this indirect method for determining  $k$  gives less accurate values of  $k$  than the falling-head permeability test (see Chapter 4-3).

## PRESENTATION OF RESULTS

The consolidation test report presents the  $\log \sigma' - e$  curve, the swelling index  $C_s$ , the compression index  $C_c$ , the preconsolidation pressure  $\sigma'_p$ , and the variation of the consolidation coefficient  $C_v$  versus effective stress  $\sigma'$ . The compression ratios  $r_i$ ,  $r_p$ , and  $r_s$  are also reported to indicate the relative proportion of the initial, primary, and secondary compressions. When the secondary compression ratio  $r_s$  is large, the secondary compression coefficient  $C_\alpha$  is also reported. The calculations of  $C_s$ ,  $C_c$ ,  $\sigma'_p$ ,  $C_v$ ,  $r_i$ ,  $r_p$ ,  $r_s$ , and  $C_\alpha$  are detailed in Chapter 6-1. The compressibility  $m_v$  and permeability coefficient  $k$  may also be reported for particular stresses.

## EXAMPLES

Figures 12 to 24 cover parts of a complete data set of the consolidation test of a silty clay. The rest of the data set is unprocessed in Table E1. Figure 14

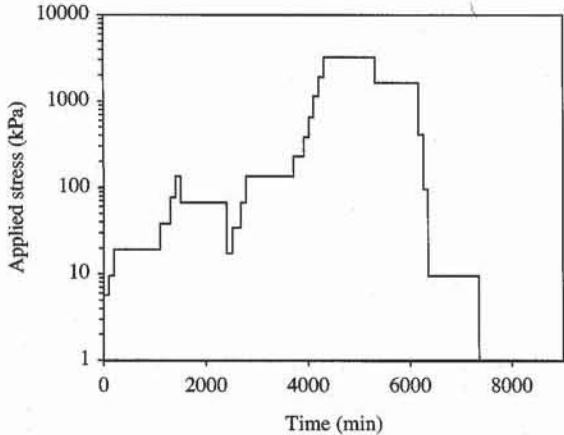


Figure 12 Loading sequence of consolidation test of Fig. 14.

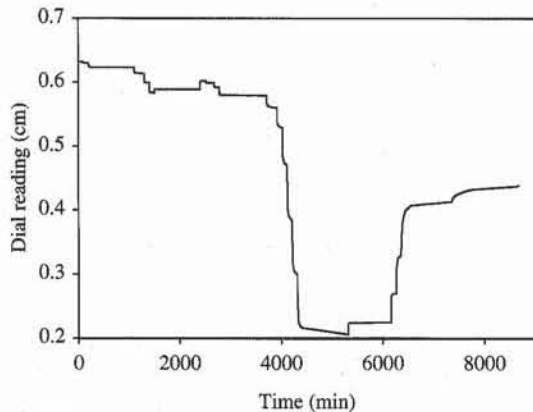


Figure 13 Dial reading corresponding to the loading sequence of Fig. 14.

	A	B	C	D	E	F	G	H	I
1	<b>Consolidation test</b>								
2	Analyst : Shiva Karimi								
3	Test date: 11-12-1986								
4	Sample description: Boston gray silty gray (13.5 m depth)								
5	Initial sample height $h_0 = 1.899$ cm								
6	Sample diameter $d_0 = 6.314$ cm								
7	Initial sample weight $W_{w0} = 113.08$ g								
8	Final sample weight $W_w = 108.46$ g								
9	Final weight of dry sample $W_d = 80.83$ g								
10	Initial dial reading $d_i = 0.635$ cm								
11	Final dial reading $d_f = 0.438$ cm								
12	Initial water content $w_0 = 39.90\%$								
13	Initial dry unit weight $\gamma_{d0} = 13.32$ kN/m <sup>3</sup>								
14	Initial void ratio $e_0 = 1.316$								
15	Initial degree of saturation $S_{r0} = 95.44\%$								
16	Assumed final degree of saturation $S_r = 100.00\%$								
17	Estimated specific gravity $G_s = 3.15$								
18	Final water content $w = 34.18\%$								
19	Final dry unit weight $\gamma_d = 14.86$ kN/m <sup>3</sup>								
20	Final void ratio $e = 1.076$								
21	Liquid limit LL = 55.30%								
22	Plastic limit PL = 24.20%								
23	Preconsolidation pressure $\sigma_p = 313.91$ kPa								
24	Compression index $C_c = 0.47$								
25	Swelling index $C_s = 0.03$								
26									
27	Load number	Vertical stress (kPa)	Dial reading (cm)	System deflection (cm)	Vertical strain (%)	Void ratio	$C_v$ (cm <sup>2</sup> /sec)	$C_{ce}$ (%)	Elapsed time (min)
28		d	hc	eps					
29	1	5.7	0.63122	0.00025	0.21	1.311	0.00208	0.07	100
30	2	9.6	0.62921	0.00040	0.33	1.309	0.00309	0.05	100
31	3	19.2	0.62243	0.00080	0.70	1.300	0.00218	0.04	900
32	4	38.3	0.61311	0.00135	1.22	1.288	0.00189	0.07	200
33	5	76.6	0.59830	0.00230	2.05	1.269	0.00166	0.09	100
34	6	134.1	0.58293	0.00325	2.91	1.249	0.00208	0.10	100
35	7	67.0	0.58918	0.00270	2.56	1.257	0.00231	0.01	900
36	8	17.2	0.60201	0.00225	1.86	1.273	0.00199	0.07	120
37	9	34.5	0.59888	0.00222	2.02	1.270	0.00220	0.02	160
38	10	67.0	0.59157	0.00194	2.39	1.261	0.00240	0.04	100
39	11	134.1	0.57887	0.00282	3.10	1.244	0.00281	0.05	940
40	12	229.8	0.56007	0.00445	4.18	1.220	0.00183	0.17	200
41	13	383.0	0.52883	0.00550	5.88	1.180	0.00159	0.27	100
42	14	651.2	0.47003	0.00705	9.06	1.107	0.00124	0.69	100
43	15	1149.1	0.38354	0.00915	13.72	0.998	0.00131	0.83	100
44	16	1915.2	0.29972	0.01150	18.26	0.893	0.00154	0.66	100
45	17	3255.8	0.20599	0.01500	23.38	0.775	0.00220	0.65	1000
46	18	1627.9	0.22492	0.01205	22.23	0.801	0.00246	0.03	840
47	19	407.0	0.27064	0.00795	19.61	0.862	0.00171	0.13	100
48	20	95.8	0.32896	0.00540	16.40	0.936	0.00067	0.49	100
49	21	9.6	0.41351	0.00340	11.84	1.042	0.00014	0.44	1000
50	22	1.0	0.43818	0.00290	10.52	1.073	0.00003	0.62	1315
51	Preconsolidation pressure with Casagrande method								
52	Slope = 0.07								
53	Preconsolidation pressure = 409.4 kPa								

Figure 14 Example of data set for the consolidation test.

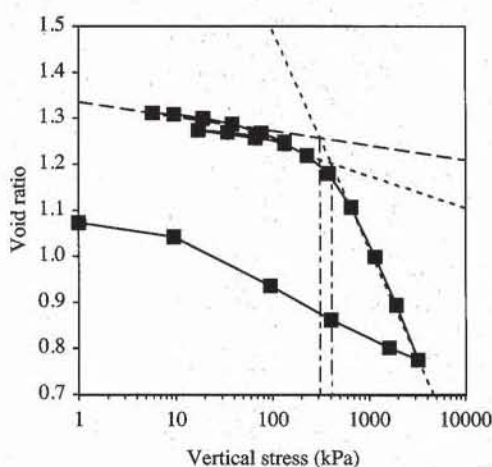


Figure 15 Consolidation curve for Fig. 14.

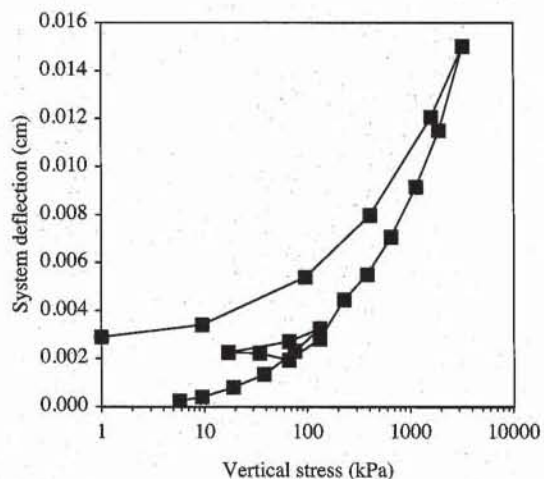


Figure 16 System deflection versus applied pressure.

C	D	E
12 Initial water content $w_0 = (W_w - W_d)/W_d$		
13 Initial dry unit weight $\gamma_{d0} = W_d/(h_0 \cdot PI) / 4 \cdot d_0^2 \cdot 9.8$		kN/m <sup>3</sup>
14 Initial void ratio $e_0 = G_s \cdot PI \cdot d_0^2 / 4 \cdot h_0 / W_d - 1$		
15 Initial degree of saturation $S_{r0} = G_s \cdot w_0 / e_0$		
16 Assumed final degree of saturation $S_r = 1$		
17 Estimated specific gravity $G_s = gd / (9.8 \cdot w \cdot gd)$		
18 Final water content $w = (W_w - W_d)/W_d$		
19 Final dry unit weight $\gamma_d = gd \cdot h_0 / (h_0 - d_i + d_f)$		kN/m <sup>3</sup>
20 Final void ratio $e = G_s \cdot w$		
21 Liquid limit LL = 0.553		
22 Plastic limit PL = 0.242		
23 Preconsolidation pressure $\sigma_p = 10^{((F45+Cc \cdot LOG(B45)-F29-Cs \cdot LOG(B29)) / (Cc-Cs))}$ kPa		
24 Compression index $C_c = -SLOPE(F42:F45, LOG(B42:B45))$		
25 Swelling index $C_s = -SLOPE(F34:F39, LOG(B34:B39))$		
C	E	F
27 Vertical strain (%)		Void ratio
28 eps		
29 $= (d_i - d + h_c) / h_0 \cdot 100 = e_0 - \text{eps} / 100 \cdot (1 + e_0)$		
30 $= (d_i - d + h_c) / h_0 \cdot 100 = e_0 - \text{eps} / 100 \cdot (1 + e_0)$		
C	D	
51 Preconsolidation pressure with Casagrande method		
52 Slope = $-SLOPE(F39:F41, LOG(B39:B41)) / 2$		
53 Preconsolidation pressure = $10^{((F45+Cc \cdot LOG(B45)-F40-D52 \cdot LOG(B40)) / (Cc-D52))}$		

Figure 17 Formulas used in Fig. 14.

summarizes the experimental measurements and processed results. The liquid and plastic limits were obtained from tests which are not reported here.

As shown in Fig. 12, the consolidation test lasted for about 6 days and had 22 loading steps (i.e., more steps than usual tests). The soil sample was taken from the field at a depth of 13.5 m. Assuming that the water table in the field is at the ground surface, the initial vertical effective stress  $\sigma'_v$  at

	A	B	C	D	E	F	G	H
1	Measured			Fitted displacement				
2	Load (kPa)	Time (min)	Displacement dial gage (cm)	Primary only (cm)	Primary and secondary (cm)			
3	t	d	dp	dps				
4	5.7	0.00	0.6350	0.6344	0.6344			
5		0.10	0.6342	0.6341	0.6341			
6		0.25	0.6340	0.6340	0.6340			
7		0.57	0.6337	0.6337	0.6337			
8		1.00	0.6335	0.6335	0.6335			
9		1.57	0.6333	0.6333	0.6333			
10		2.25	0.6332	0.6331	0.6331			
11		3.07	0.6330	0.6329	0.6329			
12		4.00	0.6328	0.6328	0.6328			
13		6.25	0.6327	0.6326	0.6326			
14		9.00	0.6325	0.6325	0.6325			
15		12.25	0.6324	0.6324	0.6324			
16		16.00	0.6323	0.6324	0.6324			
17		25.00	0.6322	0.6324	0.6321			
18		36.00	0.6320	0.6324	0.6319			
19		49.00	0.6318	0.6324	0.6317			
20		64.00	0.6315	0.6324	0.6316			
21		100.00	0.6312	0.6324	0.6313			
22								

Figure 18 Experimental and calculated data for the first loading step of the consolidation test in Fig. 14.

	B	C	D	E	F	G	H
1	Measured			Fitted displacement			
2	Time (min)	Displacement dial gage (cm)	Primary only (cm)	Primary and secondary (cm)			
3	t	d	dp	dps			
4	0.00	0.5892	0.5910	0.5910			
5		0.5921	0.5923	0.5923			
6		0.5929	0.5930	0.5930			
7		0.5942	0.5940	0.5940			
8		1.00	0.5949	0.5950	0.5950		
9		1.57	0.5959	0.5960	0.5960		
10		2.25	0.5968	0.5969	0.5969		
11		3.07	0.5975	0.5978	0.5978		
12		4.00	0.5981	0.5985	0.5985		
13		6.25	0.5990	0.5996	0.5996		
14		9.00	0.5997	0.6001	0.6002		
15		12.25	0.6003	0.6004	0.6006		
16		16.00	0.6008	0.6005	0.6008		
17		25.00	0.6012	0.6005	0.6012		
18		36.00	0.6015	0.6005	0.6014		
19		49.00	0.6016	0.6005	0.6016		
20		64.00	0.6018	0.6005	0.6017		
21		100.00	0.6020	0.6005	0.6020		
22		120.00	0.6020	0.6005	0.6021		

Figure 19 Experimental and calculated data for the first unloading step of the consolidation test in Fig. 14.

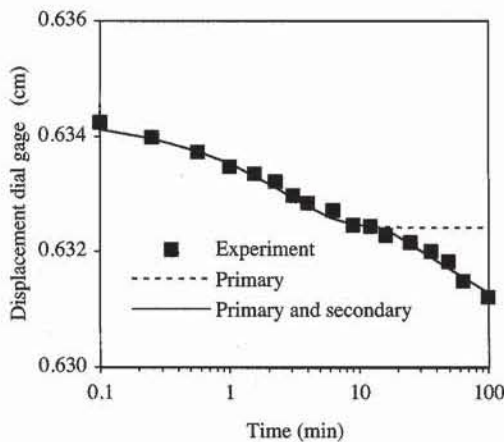


Figure 20 Experimental and fitted data for the first loading step.

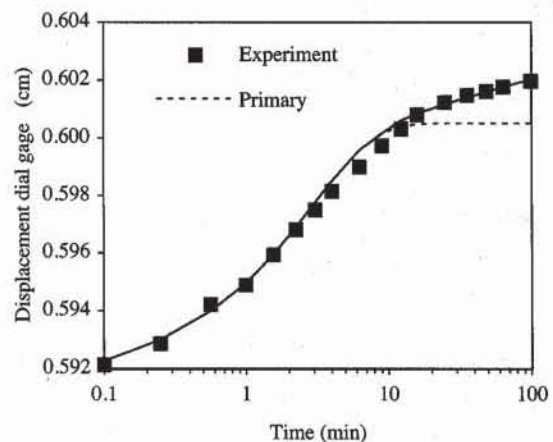


Figure 21 Experimental and fitted data for the first unloading step.

F	G	H
3	<b>Primary consolidation</b>	
4	Initial height $h_0 = 1.899$	cm
5	Starting time for fitting, $t_b = -B6$	min
6	Ending time for fitting, $t_e = -B9$	min
7	Degree of consolidation of method $U_s = 0.99$	
8	Time corresponding to $U_s$ , $t_s = =Conso(t,d,h0,tb,te,Us)$	min
9	Dial reading corresponding to $U_s$ , $d_s = =Conso(t,d,h0,tb,te,Us)$	cm
10	Dial reading at beginning of primary consolidation $d_0 = =Conso(t,d,h0,tb,te,Us)$	cm
11	Dial reading at 100% of primary consolidation $d_{100} = =Conso(t,d,h0,tb,te,Us)$	cm
12	Average drainage distance $d_m = =Conso(t,d,h0,tb,te,Us)$	cm
13	Coefficient of consolidation $C_v = =Conso(t,d,h0,tb,te,Us)$	cm <sup>2</sup> /min
14	Initial compression ration $r_i = =Conso(t,d,h0,tb,te,Us)$	
15	Primary compression ratio $r_p = =Conso(t,d,h0,tb,te,Us)$	
16	Secondary compression ratio $r_s = =Conso(t,d,h0,tb,te,Us)$	
17	<b>Secondary consolidation</b>	
18	Slope of secondary compression $ss = =SLOPE(C16:C21,LOG(B16:B21))$	
19	Intercept of secondary compression $is = =INTERCEPT(C16:C21,LOG(B16:B21))$	
20	Height at beginning of secondary compression $h_s = =h0-INDEX(d,1)+d_{100}$	cm
21	Time at beginning of secondary compression $t_s = =10^{(d_{100}-is)/ss}$	min
22	Coefficient of secondary compression $C_{ss} = =ABS(ss/h_s)$	

D	E
1	Fitted displacement
2	Primary only (cm)
3	Primary and secondary (cm)
4	$dp = d0+(d_{100}-d0)*U(Cv*t/dm^2)$
5	$dps = IF(t>ts,dp-Cae*hs*LOG(t/ts),dp)$

Figure 22 Formulas used in Fig. 18.

13.5 m depth is about 123 kPa for this soil, which has a saturated unit weight of 18.9 kN/m<sup>3</sup>. In the consolidation test, the lowest pressure was 5.7 kPa and the largest pressure was 3256 kPa. A small unloading was performed at 134.1 kPa. Each load was maintained for at least 100 min and for a few loading steps was kept constant during 1000 min ( $\approx 17$  h).

Figure 13 shows the variation of dial reading during the entire test.

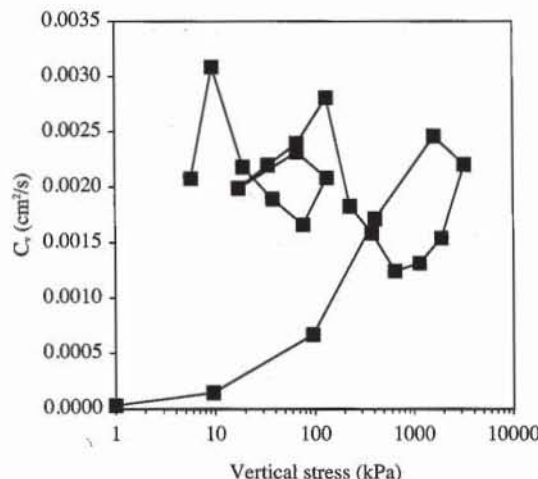


**Figure 23** Variation of consolidation coefficient versus effective stress.

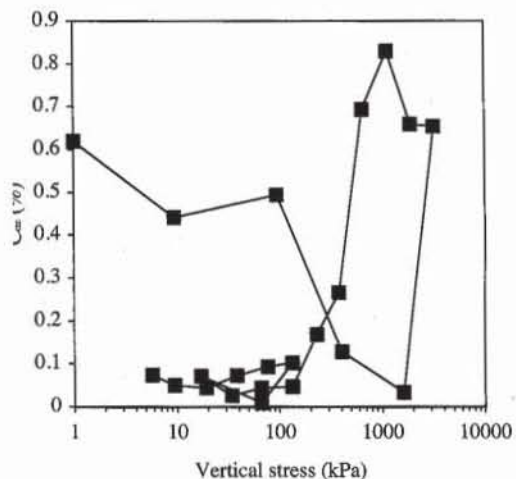


**Figure 24** Variation of secondary compression coefficient  $C_{\alpha e}$  versus effective stress.

Figure 15 shows the consolidation curve corresponding to the data points of Fig. 13. Each point corresponds to the dial readings after each loading step. The system deflection  $h_c(\sigma)$  shown in Fig. 16 was obtained by subjecting a very stiff dummy sample to the same loading sequence as the soil sample.  $h_c(\sigma)$  is nonlinear and slightly irreversible. Figure 17 lists the formulas used in Fig. 14 to calculate the compression and swelling indices  $C_c$  and  $C_s$  and the preconsolidation pressure  $\sigma'_p$ .  $\sigma'_p$  was calculated using methods a and b described in Chapter 6-1. Method a gives  $\sigma'_p = 409$  kPa, whereas method b yields  $\sigma'_p = 314$  kPa. Both values are higher than the estimated vertical effective stress  $\sigma_v' = 123$  kPa.

The coefficient of consolidation  $C_v$  was calculated for each loading step (i.e., 22 times). Figures 18 to 21 show only two particular determinations of  $C_v$ , at the first loading and unloading.  $C_v$  and the initial, primary, and secondary compression ratios are calculated by using the generalized square-root-time method with  $U_s = 99\%$  and the user-defined function CONSO. The secondary compression coefficient  $C_{\alpha e}$  is calculated using linear regression after the end of the primary compression. The dial reading  $d_s$  at the beginning of the secondary compression is assumed to be equal to  $d_{100}$ . In Figs. 18 and 19, the fitted dial readings include the primary consolidation only and the cumulated primary and secondary compressions. As shown in Figs. 20 and 21, there is very good agreement between the experimental and fitted values, which indicates that the coefficients  $C_v$  and  $C_{\alpha e}$  are determined completely. As shown in Fig. 23,  $C_v$  varies from 0.0013 to 0.003  $\text{cm}^2/\text{s}$  during loading and becomes as small as 0.0003  $\text{cm}^2/\text{s}$  during unloading. As shown in Fig. 24,  $C_{\alpha e}$  varies from 0.01 to 0.82%. The secondary compression cannot be neglected for this particular silty clay.

## REFERENCES

See Introduction for references to ASTM procedures (pages 4 to 6).

**REVIEW QUESTIONS**

1. Which material parameters are measured in the consolidation test?
2. What are the log-time and square-root-time methods?
3. Describe two different types of consolidation cells. What are their respective advantages and shortcomings?
4. Name two common types of loading devices used in the consolidation test.
5. On which basis should a loading sequence in the consolidation test be defined?
6. What is the typical time distribution of readings for determining the consolidation coefficient? Why such a sequence?
7. Why do we measure the final height of the sample after the consolidation test?
8. Why do we have to keep the sample fully saturated during the consolidation test?
9. What is the effect of the system deflection during the consolidation test?

**EXERCISES**

1. Calculate the coefficients of consolidation and secondary compression for one of the loading steps in the data set of Table E1. This data set completes the one in Fig. 14. Refer to Fig. 14 for additional data.
2. By using the square-root-time and log-time methods, calculate the coefficient of consolidation for one of the loading steps in the data set of Table E1. This data set completes the one in Fig. 14. Compare your results.

**TABLE E1**

Load (kPa)	Elapsed time (min)	Displacement dial gage (cm)	Load (kPa)	Elapsed time (min)	Displacement dial gage (cm)	Load (kPa)	Elapsed time (min)	Displacement dial gage (cm)
5.7	0.00	0.6350	9.6	0.00	0.6312	19.2	0.00	0.6292
	0.10	0.6342		0.10	0.6307		0.10	0.6279
	0.25	0.6340		0.25	0.6307		0.25	0.6276
	0.57	0.6337		0.57	0.6306		0.57	0.6271
	1.00	0.6335		1.00	0.6304		1.00	0.6266
	1.57	0.6333		1.57	0.6302		1.57	0.6261
	2.25	0.6332		2.25	0.6301		2.25	0.6259
	3.07	0.6330		3.07	0.6300		3.07	0.6256
	4.00	0.6328		4.00	0.6300		4.00	0.6252
	6.25	0.6327		6.25	0.6299		6.25	0.6248
	9.00	0.6325		9.00	0.6299		9.00	0.6246
	12.25	0.6324		12.25	0.6299		12.25	0.6243
	16.00	0.6323		16.00	0.6299		16.00	0.6241
	25.00	0.6322		25.00	0.6299		25.00	0.6238
	36.00	0.6320		36.00	0.6298		36.00	0.6229
	49.00	0.6318		49.00	0.6297		49.00	0.6228
	64.00	0.6315		64.00	0.6294		64.00	0.6227
	100.00	0.6312		100.00	0.6292		100.00	0.6227
							900.00	0.6224

TABLE E1 (cont.)

Load (kPa)	Elapsed time (min)	Displacement dial gage (cm)	Load (kPa)	Elapsed time (min)	Displacement dial gage (cm)	Load (kPa)	Elapsed time (min)	Displacement dial gage (cm)	
38.3	0.00	0.6224	67.0	0.00	0.5829	67.0	0.00	0.5989	
	0.25	0.6199		0.25	0.5867		0.25	0.5964	
	0.57	0.6193		0.57	0.5872		0.57	0.5959	
	1.00	0.6186		1.00	0.5871		1.00	0.5950	
	1.57	0.6181		1.57	0.5878		1.57	0.5944	
	2.25	0.6175		2.25	0.5880		2.25	0.5939	
	3.07	0.6172		3.07	0.5883		3.07	0.5933	
	4.00	0.6167		4.00	0.5884		4.00	0.5931	
	6.25	0.6161		6.25	0.5886		6.25	0.5928	
	9.00	0.6157		9.00	0.5887		9.00	0.5926	
	12.25	0.6152		12.25	0.5887		12.25	0.5924	
	16.00	0.6149		16.00	0.5888		16.00	0.5923	
	25.00	0.6144		25.00	0.5890		25.00	0.5921	
	36.00	0.6142		36.00	0.5890		36.00	0.5919	
	49.00	0.6140		49.00	0.5891		49.00	0.5918	
	64.00	0.6139		64.00	0.5891		64.00	0.5918	
	100.00	0.6137		100.00	0.5892		100.00	0.5916	
	120.00	0.6137		900.00	0.5892				
	200.00	0.6131							
76.6	0.00	0.6131	17.2	0.00	0.5892	134.1	0.00	0.5916	
	0.25	0.6074		0.10	0.5921		0.25	0.5875	
	0.57	0.6063		0.25	0.5929		0.57	0.5861	
	1.00	0.6053		0.57	0.5942		1.00	0.5848	
	1.57	0.6045		1.00	0.5949		1.57	0.5838	
	2.25	0.6035		1.57	0.5959		2.25	0.5829	
	3.07	0.6027		2.25	0.5968		3.07	0.5824	
	4.00	0.6022		3.07	0.5975		4.00	0.5820	
	6.25	0.6012		4.00	0.5981		6.25	0.5814	
	9.00	0.6005		6.25	0.5990		9.00	0.5810	
	12.25	0.6001		9.00	0.5997		12.25	0.5834	
	16.00	0.5998		12.25	0.6003		16.00	0.5806	
	25.00	0.5994		16.00	0.6008		25.00	0.5804	
	36.00	0.5991		25.00	0.6012		36.00	0.5801	
	49.00	0.5989		36.00	0.6015		49.00	0.5799	
	64.00	0.5987		49.00	0.6016		64.00	0.5799	
	100.00	0.5983		64.00	0.6018		100.00	0.5797	
				100.00	0.6020		110.00	0.5796	
				120.00	0.6020			940.00	0.5789
134.1	0.00	0.5983	34.5	0.00	0.6020	229.8	0.00	0.5789	
	0.25	0.5921		0.25	0.6013		0.25	0.5745	
	0.57	0.5916		0.57	0.6010		0.57	0.5729	
	1.00	0.5906		1.00	0.6006		1.00	0.5715	
	1.57	0.5895		1.57	0.6003		1.57	0.5699	
	2.25	0.5880		2.25	0.6001		2.25	0.5689	
	3.07	0.5872		3.07	0.5999		3.07	0.5676	
	4.00	0.5867		4.00	0.5997		4.00	0.5669	
	6.25	0.5860		6.25	0.5995		6.25	0.5655	
	9.00	0.5853		9.00	0.5994		9.00	0.5648	
	12.25	0.5850		12.25	0.5994		12.25	0.5644	
	16.00	0.5847		16.00	0.5992		16.00	0.5639	
	25.00	0.5843		25.00	0.5992		25.00	0.5631	
	36.00	0.5838		36.00	0.5992		36.00	0.5624	
	49.00	0.5835		49.00	0.5991		49.00	0.5620	
	64.00	0.5834		64.00	0.5990		64.00	0.5617	
	100.00	0.5829		100.00	0.5989		100.00	0.5609	
				120.00	0.5989			200.00	0.5601
				140.00	0.5989				
				160.00	0.5989				

TABLE E1 (cont.)

Load (kPa)	Elapsed time (min)	Displacement dial gage (cm)	Load (kPa)	Elapsed time (min)	Displacement dial gage (cm)	Load (kPa)	Elapsed time (min)	Displacement dial gage (cm)
383.0	0.00	0.5601	1915.2	0.00	0.3835	407.0	0.00	0.2249
	0.25	0.5527		0.25	0.3660		0.25	0.2457
	0.57	0.5502		0.57	0.3556		0.57	0.2464
	1.00	0.5476		1.00	0.3518		1.00	0.2497
	1.57	0.5453		1.57	0.3477		1.57	0.2530
	2.25	0.5432		2.25	0.3401		2.25	0.2560
	3.07	0.5413		3.07	0.3325		3.07	0.2586
	4.00	0.5398		4.00	0.3284		4.00	0.2607
	6.25	0.5377		6.25	0.3213		6.25	0.2638
	9.00	0.5357		9.00	0.3165		9.00	0.2659
	12.25	0.5344		12.25	0.3131		12.25	0.2672
	16.00	0.5335		16.00	0.3106		16.00	0.2680
	25.00	0.5321		25.00	0.3073		25.00	0.2689
	36.00	0.5310		36.00	0.3051		36.00	0.2695
	49.00	0.5302		49.00	0.3034		49.00	0.2698
	64.00	0.5293		64.00	0.3022		64.00	0.2701
	100.00	0.5288		100.00	0.2997		100.00	0.2706
651.2	0.00	0.5288	3255.8	0.00	0.2986	95.8	0.00	0.2706
	0.25	0.5161		0.10	0.2796		0.25	0.2823
	0.57	0.5118		0.25	0.2764		0.57	0.2840
	1.00	0.5077		0.57	0.2690		1.00	0.2870
	1.57	0.5033		1.00	0.2619		1.57	0.2901
	2.25	0.4994		1.57	0.2553		2.25	0.2932
	3.07	0.4959		2.25	0.2494		3.07	0.2963
	4.00	0.4931		3.07	0.2440		4.00	0.2992
	6.25	0.4883		4.00	0.2398		6.25	0.3047
	9.00	0.4851		6.25	0.2337		9.00	0.3094
	12.25	0.4826		9.00	0.2298		12.25	0.3134
	16.00	0.4806		12.25	0.2272		16.00	0.3168
	25.00	0.4778		16.00	0.2254		25.00	0.3200
	36.00	0.4757		25.00	0.2228		36.00	0.3246
	49.00	0.4737		36.00	0.2210		49.00	0.3265
	64.00	0.4722		49.00	0.2190		64.00	0.3276
	100.00	0.4700		64.00	0.2178		100.00	0.3290
1149.1	0.00	0.4700		100.00	0.2161			
	0.25	0.4470		1000.00	0.2060			
	0.57	0.4412						
	1.00	0.4382						
	1.57	0.4298						
	2.25	0.4239						
	3.07	0.4191						
	4.00	0.4145						
	6.25	0.4079						
	9.00	0.4026						
	12.25	0.4006						
	16.00	0.3980						
	25.00	0.3928						
	36.00	0.3903						
	49.00	0.3882						
	64.00	0.3866						
	100.00	0.3835						
			1627.9	0.00	0.2060	9.6	0.00	0.3290
				0.25	0.2202		0.25	0.3376
				0.57	0.2212		0.57	0.3383
				1.00	0.2220		1.00	0.3403
				1.57	0.2225		1.57	0.3424
				2.25	0.2228		2.25	0.3444
				3.07	0.2230		3.07	0.3467
				4.00	0.2231		4.00	0.3489
				6.25	0.2234		6.25	0.3534
				9.00	0.2235		9.00	0.3581
				12.25	0.2236		12.25	0.3627
				16.00	0.2238		16.00	0.3666
				25.00	0.2240		25.00	0.3744
				36.00	0.2240		36.00	0.3815
				49.00	0.2240		49.00	0.3876
				64.00	0.2242		64.00	0.3927
				94.00	0.2242		100.00	0.3999
				100.00	0.2243		200.00	0.4074
				200.00	0.2245		1000.00	0.4135
				840.00	0.2249			

TABLE E1 (cont.)

Load (kPa)	Elapsed time (min)	Displacement dial gage (cm)
1.0	0.00	0.4135
	0.25	0.4141
	0.57	0.4144
	1.00	0.4146
	1.57	0.4149
	2.25	0.4151
	3.07	0.4153
	4.00	0.4155
	6.25	0.4161
	9.00	0.4166
	12.25	0.4171
	16.00	0.4178
	25.00	0.4191
	36.00	0.4199
	49.00	0.4211
	64.00	0.4219
	100.00	0.4242
	300.00	0.4300
	400.00	0.4324
	1275.00	0.4372
seating	1315.00	0.4382

# 7

# Shear Strength

- 7-1** Shear strength of soils
- 7-2** Principles of the unconfined compression test
- 7-3** Unconfined compression test
- 7-4** Principles of direct shear tests
- 7-5** Direct shear test
- 7-6** Principles of triaxial tests
- 7-7** Triaxial tests on coarse-grained soils
- 7-8** Triaxial tests on fine-grained soils

## INTRODUCTION

Soils like any other materials fail at some point when they are subjected to increasing shear stresses. They cannot withstand a shear stress larger than their shear strength and deform extensively when the applied shear stress approaches their shear strength. Shear strength is a very important soil property to determine the stability of foundations, retaining walls, slopes, and embankments.

## FAILURE THEORY

### Peak and Residual Failures of Soils

Figure 1 illustrates the typical stress-strain response of soils during the unconfined compression test (Chapter 7-3). The sample, which has no lateral support, is compressed by gradually increasing the axial displacement (*displacement-controlled loading*). When the axial strain  $\epsilon$  is increased, the axial stress  $\sigma$  first increases, reaches a maximum value, and then decreases to a residual value. From this stress-strain curve, two types of failure are defined: peak failure and residual failure. The *peak failure* corresponds to the *peak strength*  $\sigma_p$  at point A. The *residual failure* corresponds to the *residual strength*  $\sigma_r$  at point B sustainable at large strain.

If the axial load, instead of the axial displacement, is gradually increased (*load-controlled loading*), the sample of Fig. 1 becomes unstable at the peak failure (segment AC). For instance, when subjected to the increasing weight of Fig. 1c, the sample cannot withstand the applied load and collapses at peak failure. The soil residual strength cannot be measured with such a load-controlled system.

The strength of soils is usually described in terms of the Mohr-Coulomb theory, which originates from the Coulomb friction theory (Coulomb, 1776).

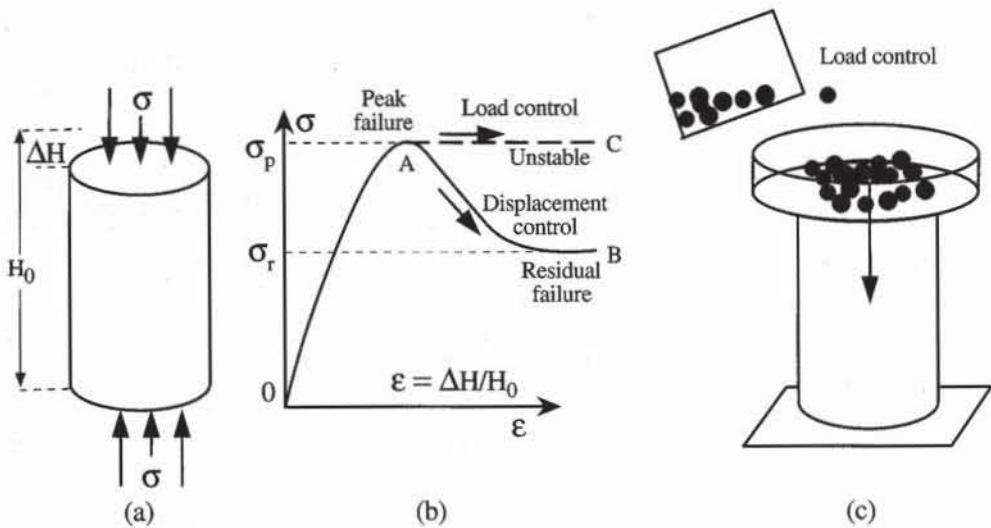


**Figure 1** Typical stress-strain responses of soil sample during the unconfined compression test with displacement control and load control.

### Coulomb Friction Theory

Figure 2a illustrates the Coulomb friction theory by considering two wooden blocks subjected to the normal force  $N$  and the shear force  $T$ .  $N$  is a constant force applied by a dead weight, and  $T$  is gradually increased. At first, the top block does not move when  $T$  is small; then starts to slide when  $T$  exceeds some particular value  $T_{\max}$ . The experiment can be repeated for various values of  $N$ , and the corresponding  $T_{\max}$  can be measured. As shown in Fig. 2b, the points  $(N, T_{\max})$  are aligned along a straight line that intercepts the  $T$  axis at  $C$  and makes the slope  $\mu$  with the  $N$  axis:

$$T_{\max} = C + \mu N \quad (1)$$

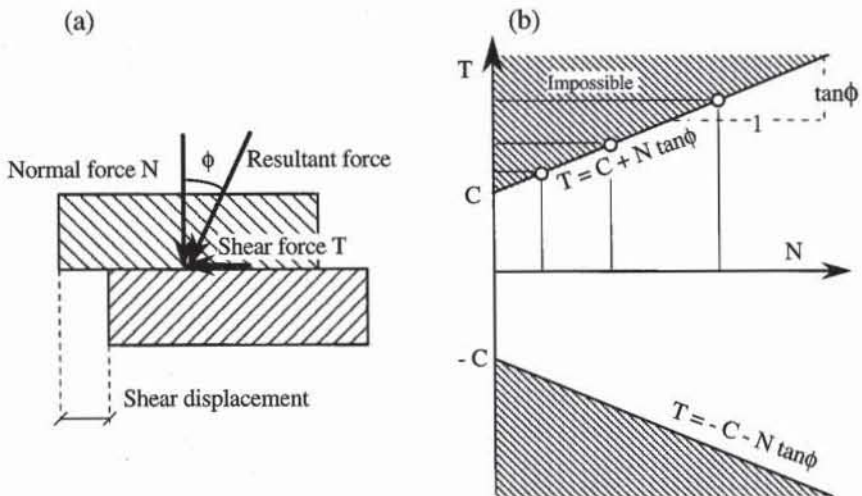


**Figure 2** Coulomb friction theory with (a) sliding blocks and (b) possible states in  $N$ - $T$  space.

The *cohesive force*  $C$  is the value of  $T$  that is required to obtain sliding when  $N = 0$ . The *friction coefficient*  $\mu$  is dimensionless and characterizes the increase in  $T_{\max}$  with  $N$ . The *friction angle*  $\phi$  is defined as  $\phi = \tan^{-1}(\mu)$ .

Both parameters  $C$  and  $\phi$  depend on the material and the surface texture of the sliding blocks. In general, large values of  $C$  and  $\phi$  correspond to rough surfaces and hard materials, whereas low values of  $C$  and  $\phi$  are associated with smooth surfaces and weak materials. The largest absolute value of  $T$  is independent of the loading direction;  $|T|$  never exceeds  $T_{\max} = C + N \tan \phi$ . The point  $(N, T)$  always stays between the lines  $T = C + N \tan \phi$  and  $T = -C - N \tan \phi$ . The impossible domain for point  $(N, T)$  is shaded in Fig. 2b. When  $C = 0$ , the vertical inclination of the resultant force acting on the block is always smaller or equal to  $\phi$  (i.e.,  $\tan^{-1}(T/N) \leq \phi$ ).

### Mohr-Coulomb Failure Theory

The Mohr-Coulomb failure theory generalizes the Coulomb friction theory in  $\sigma-\tau$  space. The normal stress  $\sigma$  and shear stress  $\tau$  are

$$\sigma = \frac{N}{A} \text{ and } \tau = \frac{T}{A} \quad (2)$$

where  $A$  is the contact area. Using stresses instead of forces, Eq. 1 becomes

$$\tau_{\max} = c + \sigma \tan \phi \quad (3)$$

where  $\tau_{\max}$  is the *shear strength*,  $c = C/A$  is the *cohesion*, or *cohesion intercept*, and  $\phi$  is the *friction angle*. The Mohr-Coulomb failure theory requires that  $|\tau| \leq \tau_{\max}$ . As shown in Chapter 5-1, the point  $(\sigma, \tau)$  generates the Mohr circle when the surface inclination varies. Therefore,  $|\tau| \leq \tau_{\max}$  is verified on any surface, provided that the Mohr circle is entirely located between the lines  $\tau = \pm(c + \sigma \tan \phi)$ .

As shown in Fig. 3, when the Mohr circle is strictly included between the failure lines, there is no surface on which  $\tau$  is large enough to create a slip (i.e.,  $|\tau| < \tau_{\max}$ ). When the Mohr circle intersects the failure lines, there are several surfaces on which  $|\tau| \geq \tau_{\max}$ , which is unacceptable in the Mohr-Coulomb theory.

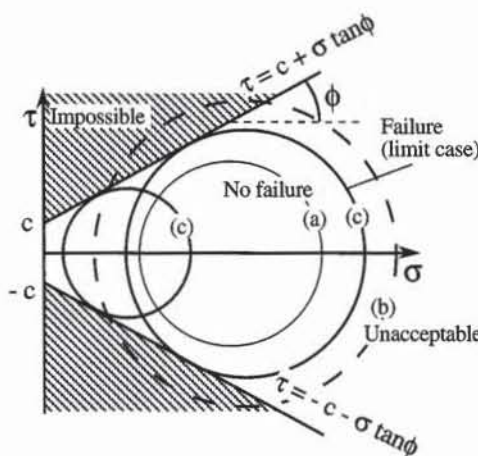


**Figure 3** Acceptable, failure, and unacceptable Mohr circles in Mohr-Coulomb failure theory.

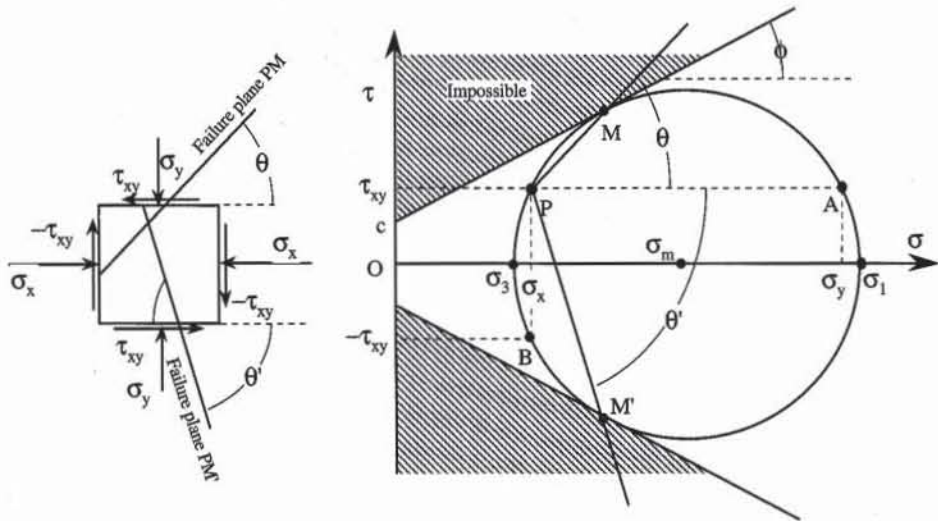


**Figure 4** Inclination of failure planes in Mohr-Coulomb failure theory.

As shown in Fig. 4, in the limiting case when the Mohr circle is tangent to the failure lines at points  $M$  and  $M'$  (i.e.,  $|\tau| = \tau_{\max}$ ), the failure takes place on surfaces parallel to  $PM$  and  $PM'$ , where  $P$  is the pole of the Mohr circle.

The failure line (Eq. 3) can also be expressed in terms of the major and minor principal stresses  $\sigma_1$  and  $\sigma_3$  as follows

$$\sigma_1(1 - \sin \phi) - \sigma_3(1 + \sin \phi) - 2c \cos \phi = 0 \quad (4)$$

When  $c = 0$ , Eq. 4 becomes

$$\sin \phi = \frac{\sigma_1 - \sigma_3}{\sigma_1 + \sigma_3} \quad (5)$$

### MOHR-COULOMB FAILURE IN S-T SPACE

As described in Chapter 5-1, the Mohr circle is also defined in  $s-t$  space. Therefore, the failure line (Eq. 3) can be represented in  $s-t$  space as well. As shown in Fig. 5, the failure envelope is defined by points  $D$  and  $E$  in  $s-t$  space, and by points  $A$  and  $B$  in  $\sigma-\tau$  space. In  $s-t$  space the failure line is

$$|t| = a + s \tan \xi \quad (6)$$

where

$$\tan \xi = \sin \phi \quad \text{and} \quad a = c \cos \phi \quad (7)$$

The  $s-t$  and  $\sigma-\tau$  failure lines have different slopes and intercepts but have a common intersection point  $F$  with the horizontal axis.

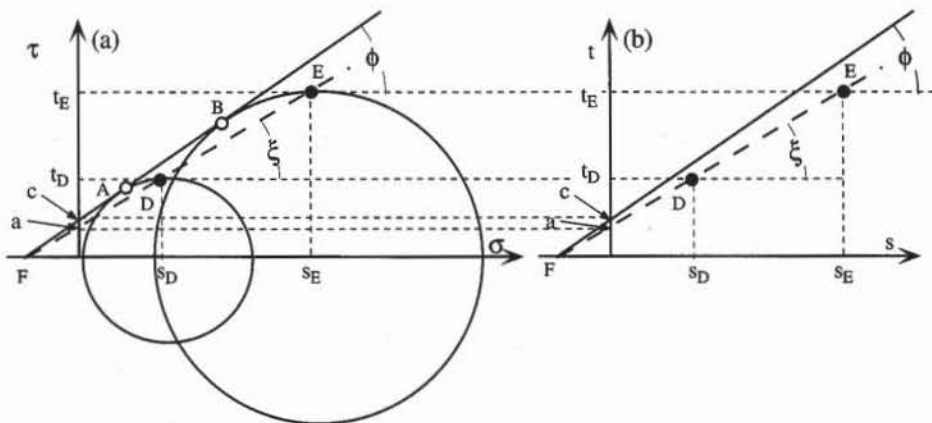


**Figure 5** Mohr-Coulomb failure line in (a)  $\sigma$ - $\tau$  space and (b)  $s$ - $t$  space.

### Mohr-Coulomb Failure in $p$ - $q$ Space

As described in Chapter 5-1, stresses can be represented in terms of  $p$  and  $q$  under axisymmetric conditions. In  $p$ - $q$  space, the Mohr-Coulomb failure line becomes

$$q = \frac{6 \sin \phi}{3 - \sin \phi} p + \frac{6 \cos \phi}{3 - \sin \phi} c \quad \text{if } q > 0 \quad (8)$$

$$q = -\frac{6 \sin \phi}{3 + \sin \phi} p - \frac{6 \cos \phi}{3 + \sin \phi} c \quad \text{if } q < 0$$

In contrast to  $\sigma$ - $\tau$  and  $s$ - $t$  failure lines, the  $p$ - $q$  failure lines in compression ( $q > 0$ ) and tension ( $q < 0$ ) are not symmetric about the  $p$  axis.

### Three-dimensional Mohr-Coulomb Failure Surface

The Mohr-Coulomb failure line (Eq. 4) can be generalized into a failure surface for three-dimensional stress states which are difficult to represent with the Mohr circle (see Chapter 5-1). The shear strength is assumed to be independent of the intermediate principal stress  $\sigma_2$ . After expressing the major and minor principal stresses  $\sigma_1$  and  $\sigma_3$  in terms of the stress invariants  $I_1$ ,  $I_2$  and  $I_3$  (see Eq. 46.5-1), the Mohr-Coulomb surface is

$$\sqrt{I_1^2 - 3I_2} \left( \sqrt{3} \sin(\theta + \pi/3) - \sin \phi \cos(\phi + \pi/3) \right) - I_1 \sin \phi = 3c \cos \theta \quad (9)$$

where  $\theta$  is given in Eq. 47.5-1. In the case of purely cohesive materials with  $\phi = 0$ , Eq. 9 becomes

$$\sqrt{I_1^2 - 3I_2} \sin(\theta + \pi/3) = \sqrt{3}c \quad (10)$$

which is referred to as the Tresca failure surface. The von Mises surface is another failure surface for purely cohesive materials

$$\sqrt{I_1^2 - 3I_2} = 2c \quad (11)$$

Figure 6 shows the surfaces of Eqs. 9 to 11 in the principal stress space of coordinates  $\sigma_1$ ,  $\sigma_2$  and  $\sigma_3$ . The Mohr-Coulomb surface is a cone with six faces when  $\phi \neq 0$ , and becomes the Tresca hexagonal cylinder centered on the axis  $\sigma_1 = \sigma_2 = \sigma_3$  when  $\phi = 0$ . The von Mises surface is a circular cylinder centered on

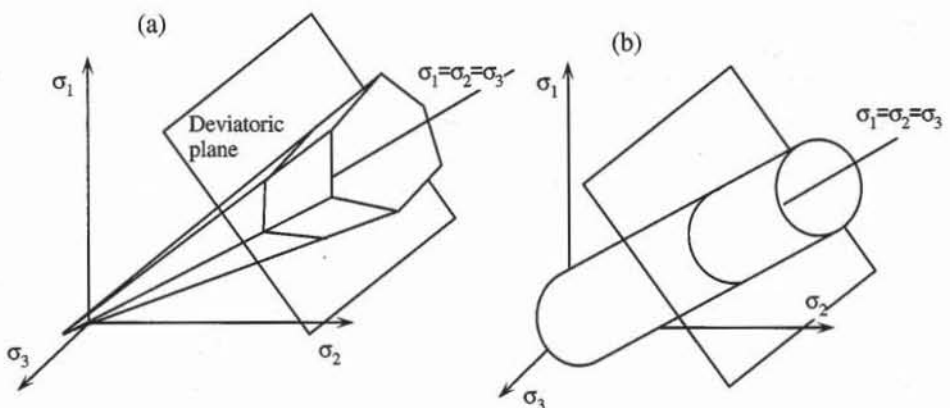


**Figure 6** Failure surfaces in principal stress space: (a) Mohr-Coulomb and (b) von Mises.

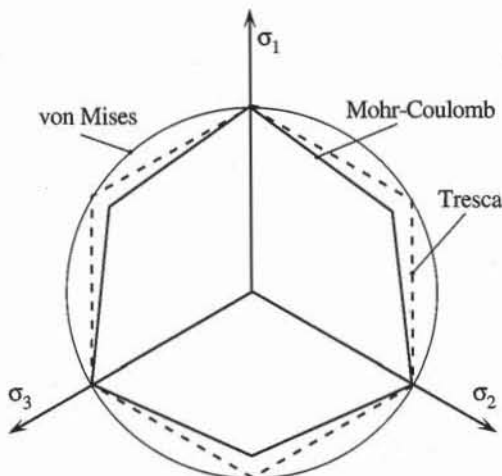


**Figure 7** View of Mohr-Coulomb, Tresca and von Mises failure surfaces in deviatoric plane.

the axis  $\sigma_1 = \sigma_2 = \sigma_3$  and contains the Tresca surface. Figure 7 shows a deviatoric view of these three surfaces (i.e., their intersection with a plane perpendicular to the axis  $\sigma_1 = \sigma_2 = \sigma_3$ ).

### Failure Envelope of Soils

The *failure envelope* (or *shear strength envelope*) of a soil describes the boundary between the stress states it can sustain and those it cannot sustain. This envelope can be expressed in terms of total and effective stresses (see Chapter 5-1). Hereafter, it is defined in terms of effective stress; this approach is more versatile and reliable than the total stress description presented at the end of this section. To avoid confusion between effective and total stresses, we denote the *effective cohesion intercept* by  $c'$ , and the *effective friction angle* by  $\phi'$ . The effective shear strength envelope is defined in  $s'-t$  space by introducing the parameter  $a'$  and  $\xi'$  which are related to  $c'$  and  $\phi'$  through Eq. 7. We also introduce the *peak friction angle*  $\phi'_p$  and the *residual friction angle*  $\phi'_r$ , which corresponds to the peak and residual failures, respectively, as defined in Fig. 1.

The shear strength envelope of soils can be determined by using various types of laboratory experiments, including direct shear tests, triaxial tests, simple

**TABLE 1**

Relations between MIT, Cambridge and principal stress notations.

Parameter or function	Principal stress space	MIT notation $s-t$ and $s'-t$ space	Cambridge notation $p-q$ and $p'-q$ space
First component of total stress - effective stress	$\sigma_1 = \sigma'_1 + u$ $\sigma'_1 = \sigma_1 - u$	$s = \frac{1}{2}(\sigma_1 + \sigma_3) = s' + u$ $s' = \frac{1}{2}(\sigma'_1 + \sigma'_3) = s - u$	$p = \frac{1}{3}(\sigma_1 + 2\sigma_3) = p' + u$ $p' = \frac{1}{3}(\sigma'_1 + 2\sigma'_3) = p - u$
Second component of total stress - effective stress	$\sigma_3 = \sigma'_3 + u$ $\sigma'_3 = \sigma_3 - u$	$t = \frac{1}{2}(\sigma_1 - \sigma_3)$ $t' = t = \frac{1}{2}(\sigma'_1 - \sigma'_3)$	$q = \sigma_1 - \sigma_3$ $q' = q = \sigma'_1 - \sigma'_3$
Major principal effective stress	$\sigma'_1$	$\sigma'_1 = s' + t$	$\sigma'_1 = p' + \frac{2}{3}q$
Minor principal effective stress	$\sigma'_3$	$\sigma'_3 = s' - t$	$\sigma'_3 = p' - \frac{1}{3}q$
Mohr-Coulomb failure line in compression	$\sigma'_1(1 - \sin \phi')$ $-\sigma'_3(1 + \sin \phi') = 2c' \cos \phi'$	$t = c' \cos \phi' + s' \sin \phi'$ $t = a' + s' \tan \xi'$	$q = Mp' + q_c$ $q = \frac{6 \sin \phi'}{3 - \sin \phi'} p' + \frac{6 \cos \phi'}{3 - \sin \phi'} c'$
Stress path during $K_0$ consolidation	$\sigma'_3 = K_0 \sigma'_1$	$t' = \frac{1 - K_0}{1 + K_0} s'$	$q = 3 \frac{1 - K_0}{1 + 2K_0} p'$
Stress path during isotropic test	$\sigma'_1 = \sigma'_3$	$t' = 0$	$q = 0$
Stress path during drained triaxial compression	$\sigma'_3 = \sigma'_0$	$t' = s'_0 + s'$	$p = p_0 + \frac{1}{3}q$

shear, cubical, and torsional tests (see Chapter 5-4). It can be represented in the  $\sigma'-\tau$ ,  $s'-t$ , and  $p'-q$  spaces. Table 1 summarizes some useful relations between  $s'-t$  and  $p'-q$  notations.

### Failure Envelope in $\sigma'-\tau$ Space

Figure 8 shows the effective shear strength envelopes of various types of soils in  $\sigma'-\tau$  space. As illustrated in Fig. 9a for the particular case of London clay, the

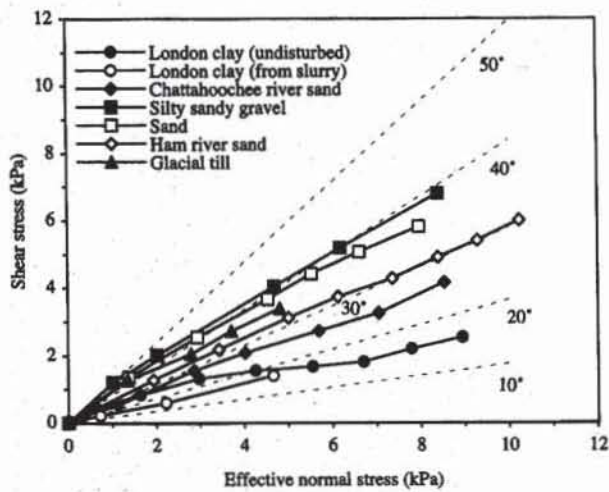
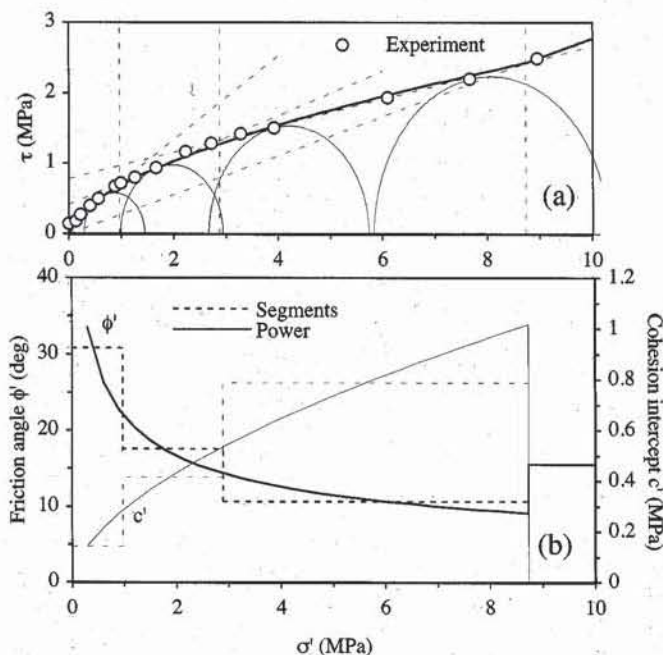


Figure 8 Failure envelopes in  $\sigma'-\tau$  space for various soils (Bishop, 1966).



**Figure 9** Shear strength envelope of undisturbed London clay in  $\sigma'$ - $\tau$  space: (a) approximation of curved envelope with segments and power relation, and (b) corresponding variations of  $c'$  and  $\phi'$  with  $\sigma'$  (data after Bishop, 1966).

$\sigma'$ - $\tau$  failure line is constructed as the envelope of the Mohr circles at failure for various ranges of effective normal stress  $\sigma'$ .

As shown in Fig. 8, over a large range of  $\sigma'$ , the failure envelope is curved, and not straight as assumed in Eq. 3. The curved failure line can be approximated by several straight segments, each having a different slope (i.e.,  $\tan \phi'$ ) and cohesion intercept  $c'$ . As shown in Fig. 9b and Table 1, in the case of London clay,  $c'$  and  $\phi'$  must vary abruptly with  $\sigma'$  to fit the curved envelope.

**TABLE 2**

Variation of cohesion  $c'$ , friction angle  $\phi'$ , and parameters  $\xi'$  and  $a'$  with normal effective stress  $\sigma'$ , for undisturbed London clay (data after Bishop, 1966)

$\sigma'$ (MPa)	$c'$ (MPa)	$\phi'$ (deg)	$a'$ (MPa)	$\xi'$ (deg)
$0 < \sigma' < 1$	0.14	30.8	0.12	27.1
$1 < \sigma' < 2.9$	0.42	17.5	0.40	16.8
$2.9 < \sigma' < 8.7$	0.79	10.6	0.77	10.4
$8.7 < \sigma'$	0.00	15.5	0.00	15.0

An alternate way to approximate curved failure envelope is to use nonlinear relations such as the power relation

$$\tau = A\sigma'^m \quad (12)$$

As shown in Fig. 9, Eq. 12 applies to London clay with  $m = 0.6$ , and  $A = 0.69$ . In this case,  $\phi'$  and  $c'$  over a small stress range about  $\sigma'$  are

$$\tan \phi' = \frac{d\tau}{d\sigma'} = Am\sigma'^{m-1} \quad \text{and} \quad c' = \tau - \frac{d\tau}{d\sigma'} \sigma' = A(1-m)\sigma'^m \quad (13)$$

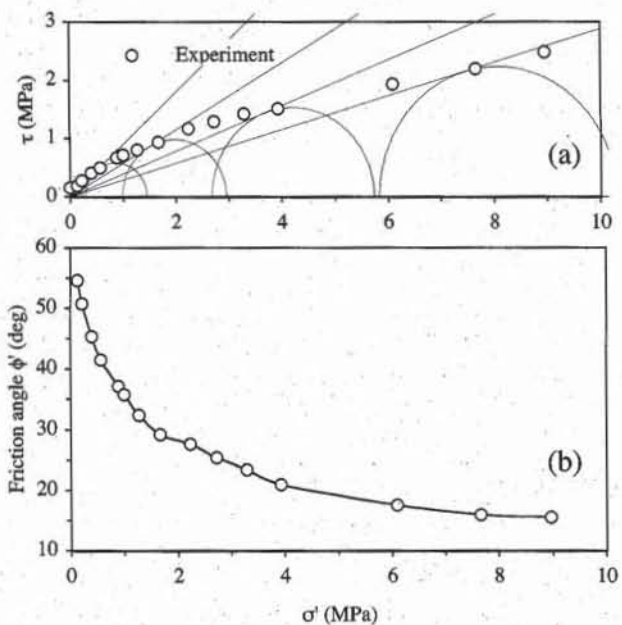


**Figure 10** Shear strength envelope of undisturbed London clay in  $\sigma'$ - $\tau$  space: (a) approximation of curved envelope with segments originating from stress origin and (b) corresponding variations of  $\phi'$  with  $\sigma'$  (data after Bishop, 1966).

As shown in Fig. 9b, in contrast to  $c'$  and  $\phi'$  obtained by linear interpolation,  $c'$  and  $\phi'$  calculated from Eq. 13 varies continuously with  $\sigma'$ .

A third way to describe curved failure surfaces is to introduce the friction angle  $\phi'$  as follows

$$\tan \phi' = \frac{\tau}{\sigma'} \quad (14)$$

and to assume that  $c' = 0$ . Figure 10 shows the variation of  $\phi'$  with  $\sigma'$  which Eq. 14 gives for London clay. The variation of  $\phi'$  with  $\sigma'$  is comparable to those in Fig. 9b, except for small values of  $\sigma'$  at which  $\phi'$  becomes excessively large.

In summary, the shear strength of soils varies nonlinearly with the effective normal stress  $\sigma'$ . There are different ways to define the friction angle  $\phi'$  and cohesion intercept  $c'$ , which yield similar failure  $\sigma'$ - $\tau$  envelopes. Over a large range of  $\sigma'$ ,  $\phi'$  and  $c'$  vary with  $\sigma'$  to approximate the nonlinear shear strength of soils. It is only in a limited range of  $\sigma'$  that constant values of  $\phi'$  and  $c'$  can be used to describe nonlinear shear strength envelopes.

Soils are *cohesionless* when their curved failure envelope goes through the stress origin (i.e.,  $\sigma' = \tau = 0$ ), and *cohesive* when their curved failure envelope intercepts the  $\tau$  axis above the origin. Coarse grained soils without plastic fines are usually cohesionless. For most cohesive soils, at the exception of cemented soils, partially saturated soils, and heavily consolidated clays, the intercept of the curved failure envelope with the  $\tau$  axis is generally small.

### Failure Envelope in $s'$ - $t$ Space

Like the  $\sigma'$ - $\tau$  failure envelope, the  $s'$ - $t$  failure envelope is also curved. As shown in Fig. 11, it is constructed from points  $B$  which are obtained from the Mohr cir-

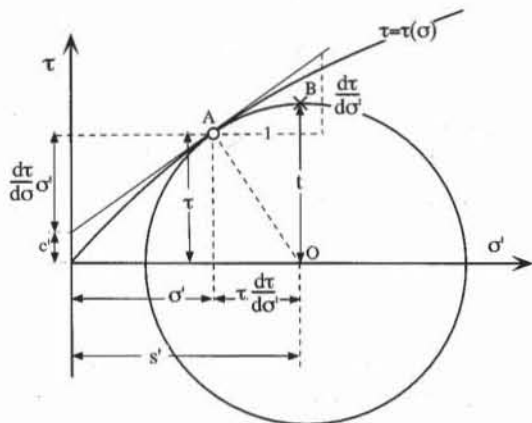


**Figure 11** Definition of failure envelope in  $s'$ - $t$  space based on failure line in  $\sigma'$ - $\tau$ ' space.

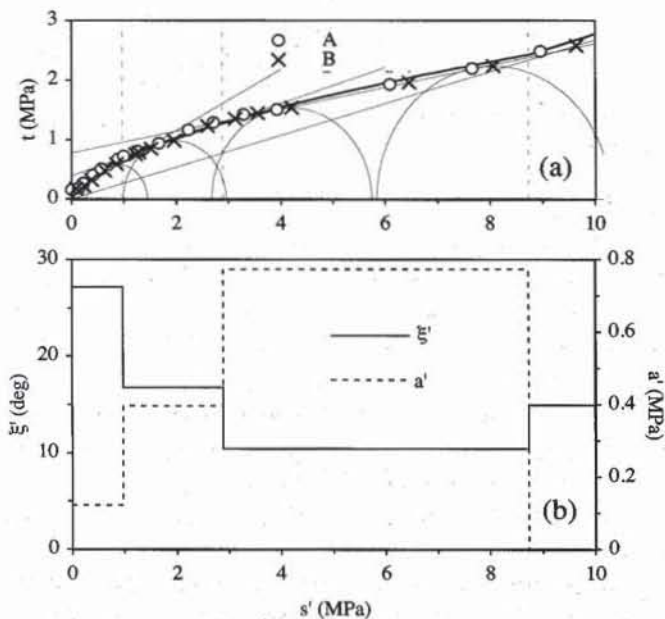


**Figure 12** Shear strength envelope of undisturbed London clay in  $s'$ - $t$  space: (a) construction of curved envelope from data points B, and (b) corresponding variations of  $a'$  and  $\xi'$  with  $s'$  (data after Bishop, 1966).

cles at failure. If the  $\sigma'$ - $\tau$  failure envelope is given by the relation  $\tau = \tau(\sigma')$ , then the  $s'$ - $t$  envelope is generated by varying  $\sigma'$  as follows

$$s' = \sigma' + \tau(\sigma') \frac{d\tau}{d\sigma'}, \quad \text{and} \quad t = \tau(\sigma') \sqrt{1 + \left( \frac{d\tau}{d\sigma'} \right)^2} \quad (15)$$

In a few cases such as a straight failure line (Eq. 3),  $\sigma'$  can be eliminated from Eq. 15 to yield an explicit relation between  $s'$  and  $t$ . Figure 12a shows the construction of the failure line by using points B in  $s'$ - $t$  space, and its approximation with segments for London clay. The corresponding values of  $a'$  and  $\xi'$  are listed in Table 2 and plotted in Fig. 12b.

### Failure Envelope in $p'$ - $q$ Space

The failure envelope of soils can be constructed in the  $p'$ - $q$  space. As shown in Fig. 13 for London clay, it is curved like the failure lines in  $\sigma'$ - $\tau$  and  $s'$ - $t$  spaces. The friction angle  $\phi'$ , can be computed from the  $p'$ - $q$  failure envelope by using Eq. 8.

## SHEAR STRENGTH OF COARSE-GRAINED SOILS

The shear strength characteristics of coarse-grained soils (e.g., sands and gravels) are introduced by examining the stress-strain response of a particular sand—Sacramento river sand—which was extensively tested in the laboratory under CD and CU triaxial compressions.

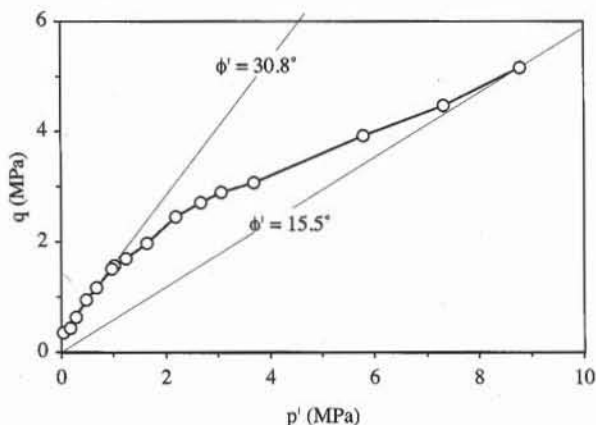


**Figure 13** Shear strength envelope of undisturbed London clay in  $p'-q$  (data after Bishop, 1966).

### Isotropic Compression on Sacramento River Sand

In the triaxial tests, the shear loading is usually preceded by a consolidation phase such as an isotropic loading to recreate in the laboratory the initial stresses in the field (see Chapter 5-4). Figure 11 shows the change in void ratio of loose and dense Sacramento River sands subjected to loading-unloading cycles of isotropic pressure. The sand response is nonlinear and irreversible like that of fine-grained soils subjected to consolidation tests (see Chapter 6-1).

### CD Triaxial Compression on Sacramento River Sand

Figures 15 and 16 show the results of CD triaxial compression tests on loose and dense samples of Sacramento River sand. The initial void ratio  $e_0$  and relative density  $D_r$  of the dense sand samples are  $e_0 = 0.61$  and  $D_r = 100\%$ , and those of the loose sand samples are  $e_0 = 0.87$  and  $D_r = 38\%$ . Each test has a different confining pressure  $\sigma'_3$  ranging from 0.1 to 11.8 MPa, a very large range of pressure which corresponds to depths from 10 to 1000 m.

The peak failure, which is noticeable in all dense samples, appears only in loose samples for  $\sigma'_3 < 1.9$  MPa. The value of  $\sigma'_1/\sigma'_3$  at peak failure depends on density and decreases with  $\sigma'_3$ . However, the value of  $\sigma'_1/\sigma'_3$  at residual failure is independent of  $\sigma'_3$  and density. The loose and dense specimens share the same residual strength.

The loose samples except for those at 0.1 and 0.2 MPa compact in contrast to the dense samples which all dilate. This compaction and dilation is caused by shear and depends on the initial density and confining pressure. The dilatation is the largest in dense sand at low confining pressure, while the compaction is the largest in loose sands at high confining pressure. Figure 17 shows another representation of the variation of void ratio during triaxial compressions. At the beginning of each test, the state  $(p'-e)$  is initially on the isotropic compression curves of Fig. 14. During shear, the points  $(p'-e)$  move away from the isotropic compression line and tend toward a common line, which is referred to as the *critical state line* or *steady state line*. In Fig. 7, the complete convergence to the critical state line is not observed due to the inaccuracy in the measurement of volume changes in sands. Recent experimental results (e.g., Biarez and Hicher, 1994; and Ishihara,

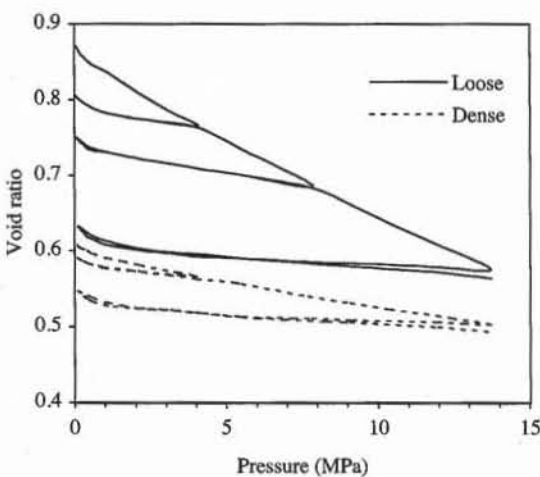


**Figure 14** Variation of void ratio versus confining pressure during isotropic test on loose and dense Sacramento River sand (Lee and Seed, 1967).

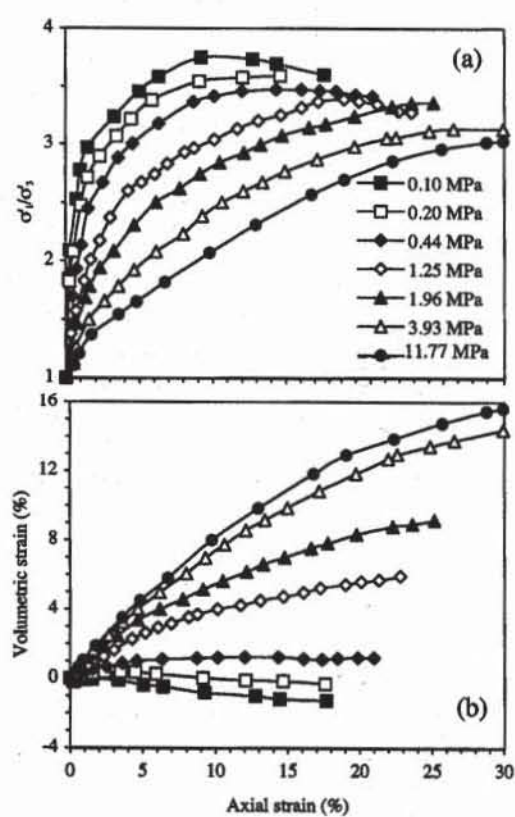


**Figure 15** Results of CD triaxial compression tests on loose ( $D_r = 38\%$ ) Sacramento River sand at various confining pressures: (a) variation of effective stress ratio versus axial strain, and (b) variation of volumetric strain with axial strain (Lee and Seed, 1967).

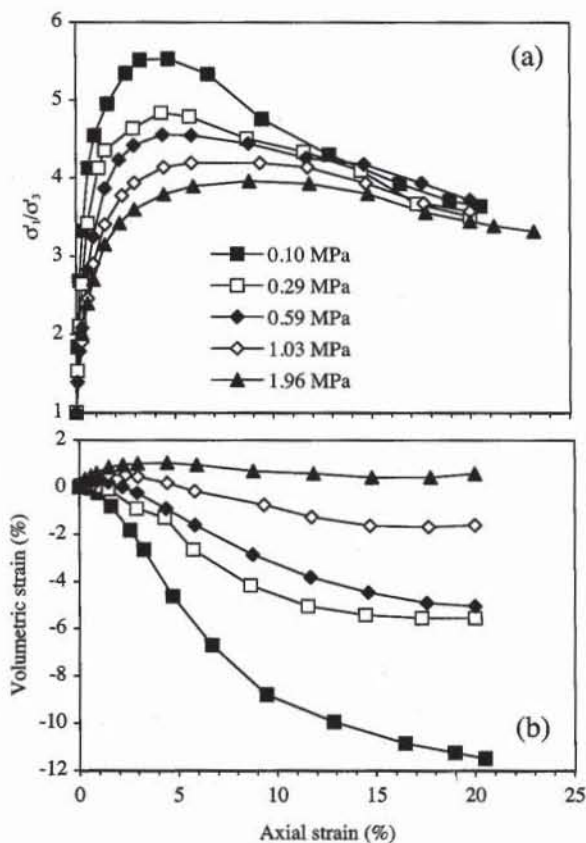


**Figure 16** Results of CD triaxial compression tests on dense ( $D_r = 100\%$ ) Sacramento River sand at various confining pressures: (a) variation of effective stress ratio versus axial strain, and (b) variation of volumetric strain with axial strain (Lee and Seed, 1967).